Title
Tracing Interfacial Reactivity of Lithium Transition Metal Oxides Through Outgassing

Author
Renfrew, Sara

Publication Date
2019

Peer reviewed|Thesis/dissertation

Tracing Interfacial Reactivity of Lithium Transition Metal Oxides Through Outgassing

by

Sara E Renfrew

A dissertation submitted in partial satisfaction of the

requirements for the degree of

Doctor of Philosophy

in

Chemical Engineering

in the

Graduate Division

of the

University of California, Berkeley

Committee in charge:

Professor Bryan D. McCloskey, Chair
Professor Roya Maboudian
Professor Mark Asta

Spring 2019

Tracing Interfacial Reactivity of
Lithium Transition Metal Oxides Through Outgassing
Sara E Renfrew

Abstract

Tracing Interfacial Reactivity of
Lithium Transition Metal Oxides Through Outgassing

by

Sara E Renfrew

Doctor of Philosophy in Chemical Engineering

University of California, Berkeley

Professor Bryan D. McCloskey, Chair

Lithium transition metal oxides are Li host structures used as cathodes for Li-ion batteries. Li is removed (deintercalated) from the oxide during charge and is inserted (intercalated) on discharge. The reversibility of the process is enabled by the transition metal redox and relative stability of the oxide. The achievable reversible capacities of typical Li-ion cathodes are only approximately half of the total possible capacity, as calculated by the total Li content. Attempts to increase the capacity, i.e., intercalate and deintercalate more Li from the oxide host, lead to poor cycling stability and limited working lifetime of the battery due to inherent instabilities at the cathode/electrolyte interface at high potentials and/or high extents of delithiation (charge). These instabilities include loss of active material due to decomposition, transition metal dissolution, particle cracking and isolation, irreversible surface reconstruction, as well as resistive surface film formation.

Many of these interfacial instabilities evolve signature gases. This dissertation aims to trace these fundamental instabilities by monitoring outgassing and quantifying surface changes during electrochemical modification. The main technique used in this work is differential electrochemical mass spectrometry (DEMS), which allows detection and quantification of gases evolved in-situ during electrochemical measurements. Additionally, the DEMS is modified to also quantify gases evolved from ex-situ acid titrations, which allow identification and quantification of surface changes of cathode materials after electrochemical modification.

One difficulty in understanding the fundamental reactivity of the cathode/electrolyte interface is the uncertainty in surface structure of lithium transition metal oxides. Due to incomplete sold-state reaction in synthesis or even inevitable reaction with atmospheric H_2O and CO_2, the surface of lithium transition metal oxides are contaminated with metal hydroxides and carbonates.

A major result of this dissertation is that rigorous quantification of surface contaminants is needed to understand outgassing mechanisms of the cathode/electrolyte interface. For example, in the first charge-discharge (deintercalation-intercalation) cycle of lithium

transition metal oxides, the surface contaminant Li_2CO_3 decomposes above 3.8 V vs. Li/Li^+ to CO_2 and, depending on the identity of the electrolyte, can directly account for 15–100 % of the total evolved CO_2 in the first cycle.

To that end, isotopic labeling of the cathode with ^{18}O is used throughout this work to distinguish the cathode from the electrolyte and the outgassing exhibited by electrolyte degradation, cathode surface degradation, and any mixed cathode/electrolyte reactivity. This dissertation introduces titration protocols that allow accurate determination of the ^{18}O-enrichment of surface carbonates on lithium transition metal oxides.

In addition, also presented is a new titration that quantifies surface peroxo-like character of lithium transition metal oxides that arises due to irreversible surface reconstruction, which has been traditionally measured by electron microscopy techniques. Use of this new peroxide titration shows that in the first cycle the irreversible transformation on the surface of lithium transition metal oxides is due to the extent of delithiation (charge capacity) and is a material property of the prepared oxide that largely does not depend on the identity of the electrolyte. It also shows that some extent of the peroxo-like character developed on charge is reversible, allowing a new quantification of near-surface oxygen redox.

Lastly, this dissertation explores the effects of surface modifications of lithium transition metal oxides on the cathode/electrolyte reactivity. Surface contaminants and local defects fundamentally alter electrolyte decomposition and the irreversible surface reconstruction of lithium transition metal oxides. The main conclusions are that increased contaminants and increase lithium defects on the surface of lithium transition metal oxides increase the electrolyte decomposition.

Contents

List of Figures

List of Tables

1 | Introduction to Li-ion batteries

1.1 Li-ion Battery Basics

After discovery in 1980 and commercialization in the 1990s, the layered $LiCoO_2$ and its derivatives have played a major role in the cathode market in both commercial and research environments for Li-ion batteries. In the most common configuration, a Li-ion cell consists of a graphitic anode, a lithium transition metal oxide cathode (e.g., $LiCoO_2$), a lithium ion conducting electrolyte with linear and cyclic carbonate solvents and a lithium salt, and a polymer separator to physically and electrically separate the electrodes.[1] A simplified schematic is shown below in Figure 1.1.*

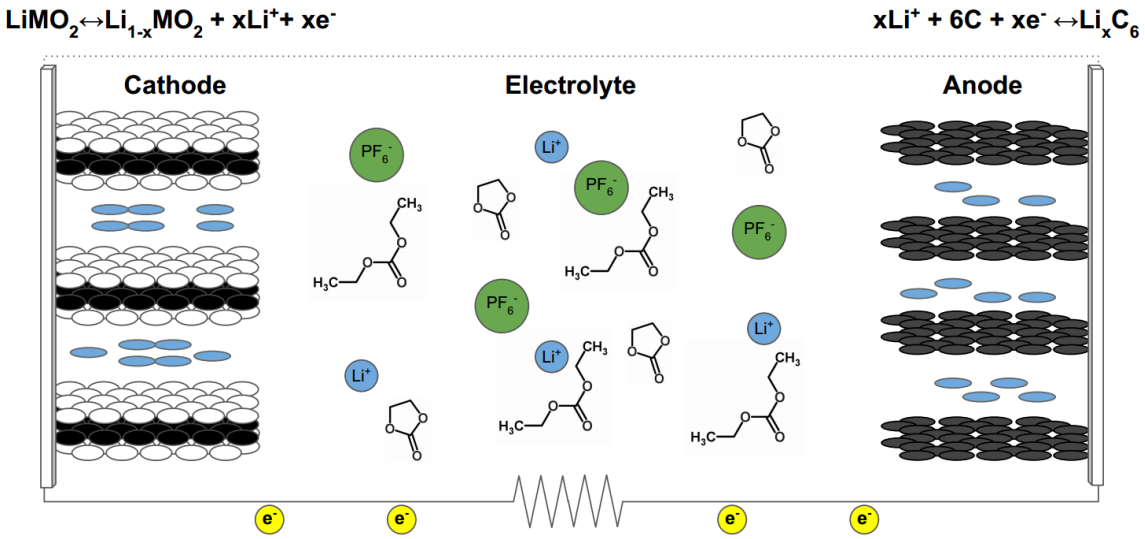

Figure 1.1: Li-ion battery schematic.

*portions of this chapter adapted from the author's qualifying exam manuscript entitled *Transition Metal Oxides: Accommodating Lithium* submitted on September 22, 2015

In the operation of the secondary Li-ion battery, Li ions shuttle between the anode and the cathode, while the energy of the electrons in the external circuit facilitate useful work on discharge. To illustrate, for a general transition metal M, the ideal electrochemical reactions during charge are as follows:

$$\text{Anode:} \quad xLi^+ + xe^- + 6\,C \longrightarrow Li_xC_6 \tag{1.1}$$

$$\text{Cathode:} \quad LiMO_2 \longrightarrow Li_{1-x}MO_2 + xLi^+ + xe^- \tag{1.2}$$

$$\text{Net:} \quad LiMO_2 + 6\,C \longrightarrow Li_{1-x}MO_2 + Li_xC_6 \tag{1.3}$$

The process is reversed on discharge. For the general transition metal M, the M^{3+}/M^{4+} redox couple allows the reaction to proceed reversibly. If M is solely responsible for charge compensation within the oxide, then the formal oxidation state of M is +3 in the fully discharged state ($x = 0$) to accommodate the insertion of Li and theoretically +4 in the fully charged state ($x = 1$) to accommodate the loss of Li.

Layered $LiCoO_2$ adopts the α-$NaFeO_2$ structure, which is a derivative of the rocksalt NaCl structure, as shown in Figure 1.2(b). In this crystal structure the largest ions, the oxygen anions, form a cubic close-packed array (ccp/fcc) as in Figure 1.2(a) and the transition metal and Li ions fully occupy the octahedral sites. Viewing along the [111] direction reveals the "layered" (111) planes of alternating metal and O ions. With Li and M fully ordered and existing in a 1:1 ratio, the stacking becomes O–Li–O–M–O–Li$\cdots$ as shown in Figure 1.2(c). Due to the existence of lithium planes, Li^+ transport is two dimensional.

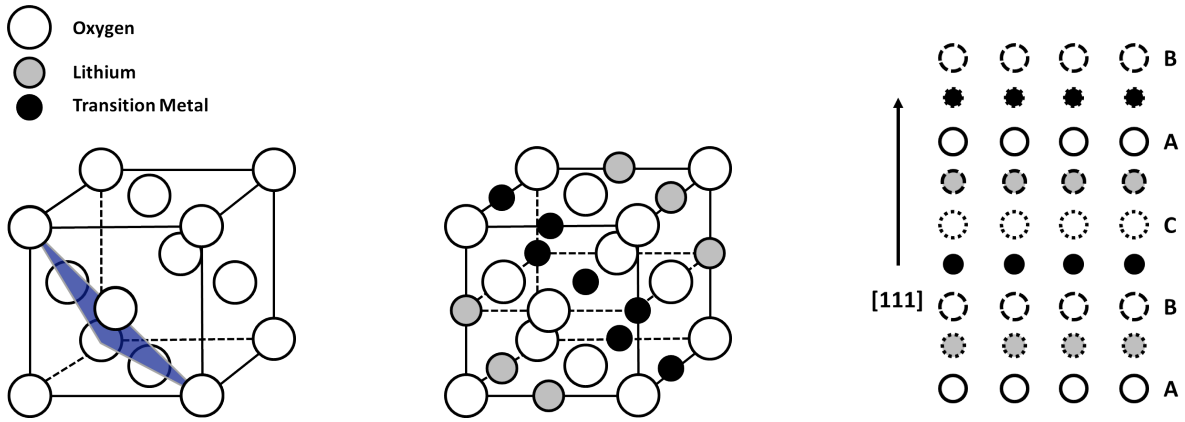

Figure 1.2: Rocksalt layered structure.

(a) The fcc oxygen anion sublattice and (111) plane. (b) The rocksalt layered structure with full occupation of the octahedral sites. Only the fcc unit cell is shown, not the full repeat unit for the layered structure. (c) A schematic of the projected view onto the $(11\bar{2})$ plane showing the alternating stacking in the [111] direction, with the ABC stacking of the oxygen planes labeled. The dashed atoms are projected from above or below and do not lie on the plane of the paper.

Due to instabilities, the full capacities of transition metal oxide cathodes cannot be realized. The practical gravimetric capacities of transition metal oxides are significantly lower than

those of carbon anodes. Graphite, for example, is fully charged as LiC_6 with one Li for every 6 C atoms; this capacity can be written as a gravimetric capacity of 372 mAh g^{-1}, which is near the practical achievable capacity. As a comparison, capacities of a few cathode materials are summarized in Table 1.1. The full, theoretical capacity is the capacity achieved if all of the Li is able to be deintercalated on charge and reintercalated on discharge. The reversible (i.e., practical) capacities are approximate values and are based on typical capacities achieved with normal operating conditions. The reversible capacities are given both in gravimetric units, as well as in Li units.

Material	Full Capacity (mAh g^{-1})	Reversible Capacity	
		(mAh g^{-1})	(Li units)
$LiCoO_2$	274	140	0.5
$Li_{1/2}MnO_2$ ($LiMn_2O_4$)	148	125	0.4
$LiNiO_2$	274	140	0.5
$Li(NiMnCo)_{1/3}O_2$	278	180	0.6

Table 1.1: Full and reversible capacities of various Li-ion cathode active materials.

Though a major revolution in batteries, $LiCoO_2$ suffers from incomplete Li extraction, material degradation, as well as toxicity and prohibitive cost. Naturally, the search for appropriate Li hosts was extended to other transition metals. Though Mn-based oxides can be prepared as $Li_{1-x}MnO_2$, this material suffers a phase transition at $x = 1/2$, and instead $LiMn_2O_4$, a spinel, is used. This material has a lower gravimetric capacity, but is less toxic and has more abundant precursors. However, Mn-ion dissolution is a well documented problem that limits the practical performance in full cells. The equivalent Ni-based oxide, $LiNiO_2$, is isostructural to $LiCoO_2$, when able to be prepared with an ordered structure. Ni redox occurs at a lower potential, thus allowing more lithium utilization without needing to go to higher potentials where electrolyte degradation may occur. While Ni is appealing due to its lower cost and toxicity, $LiNiO_2$ is difficult to synthesize and suffers from low thermal stability and material degradation.

1.2 Increasing the Capacity

There are two potentially viable routes to increase the capacity and energy density of Li-ion cathodes: (i) increase the lithium content and (ii) increase the potential window.

1.2.1 Lithium content. To address the capacity limitation of oxide–based cathodes, we can imagine that a simple solution may be to add lithium, thereby "enriching" the oxide from one stoichiometric in Li and M. This is termed "Li-rich" compared to the "Li-stoichiometric"

$LiMO_2$. By replacing some of the heavy transition metals of the M-layer with Li, the specific capacity is increased by two routes: by lowering the molecular weight and by increasing the lithium content (even if all of the Li is not utilized). If we take the M layer and incrementally replace M with Li, neglecting details of crystal structure, we get:

$$\mathrm{Li[M]O_2, Li[Li_{1/3}M_{2/3}]O_2, \cdots, Li[Li_{(n-2)/n}M_{2/n}]O_2, \cdots, Li[Li]O_2,} \tag{1.4}$$

which is written to show the change in the M–layer in brackets. In this formalism, the metal in each sequential formula has a formal oxidation state incremented by one. In other words, for the positive integer $n \geq 2$, the formal oxidation state of M in the discharged (fully lithiated) state corresponds to $+(n+1)$. There are two major limitations of this route:

Limits of transition metal redox. The common 3d transition metals of stoichiometric $LiMO_2$—Ni, Mn, Co—have accessible oxidation states typically only to +4. In Eqn 1.4, the formal oxidation state of M required in the fully charged state (if all Li is extracted) is $+(2n)$. 4d or more exotic transition metals are needed for metal redox-mediated charge compensation, and it is readily apparent that transition metal redox alone is not practical or even, in some cases, possible.

Instability of oxygen lattice. Due to the limitation of transition metal redox, reversible oxygen redox is required for any significant capacity of any $n = 3$ Li-rich materials (Li_2MO_3) with 3d transition metals (or $n > 3$ for 4d and higher). However, reversible oxygen redox is not guaranteed. As illustrated by the extreme case of Li enrichment, letting $n \to \infty$ gives us Li_2O_2, lithium peroxide. Li_2O_2 has a theoretical capacity of 1170 mAh g^{-1} and is a wide band gap insulating white powder that evolves oxygen gas when charged (delithiated).

1.2.2 Potential window. As seen in Table 1.1, the practical, reversible capacity of $LiMO_2$ is less than the stoichiometric 1 Li possible. Theoretically, a higher cut-off voltage could be used to extract more Li and increase the charge capacity, bringing us closer to the maximum theoretical capacity. This strategy is limited, however, by the rapid decline in performance for stoichiometric lithium transition metal oxides seen with higher cut-off voltages. This decline is due to high-voltage instabilities that lead to capacity loss and voltage fade, limiting the long-term performance. At the particle and molecular level, these instabilities include transition metal dissolution, oxygen loss, particle cracking, phase change, surface transformation, and electrolyte degradation.

1.3 Monitoring Instabilities

Both strategies to increase the attainable capacities have pitfalls. By introducing oxygen redox via increased lithium content, an increased Li_2O_2 character will lead to O_2 gas release

during electrochemical delithiation. By increasing the potential window, which may be needed for both Li-stoichiometric and Li-rich cathodes, there is increased concern of anodic decomposition of the electrolyte leading to gaseous products. Gas release in Li-ion cells is concerning for two main reasons: (1) swelling which can lead to cell failure and significant safety hazards and (2) irreversible capacity losses from undesirable side reactions.

However, outgassing from Li-ion batteries is, for a researcher, an invaluable tool to study to detect, quantify, and, with appropriate labeling, distinguish decomposition of the Li-ion battery components like the electolyte and the positive electrode. In this dissertation differential electrochemical mass spectrometry (DEMS) is used extensively to trace reactivity in Li-ion cathodes systems. DEMS as used in this dissertation is described in Appendix A. Described briefly, DEMS is an in-situ technique that allows quantification of gases while an electrochemical cell is operating. Isotopic labeling is used throughout this work to distinguish the cathode from the electrolyte and other cell components, using the DEMS to trace volatile ^{18}O products. The ^{18}O-enrichment procedure is described in Appendix B.

The aim of this dissertation is to shed light on the anodic instabilities of the cathode/electrolyte. Chapter 2 highlights the similarities seen in the outgassing of both Li-rich and Li-stoichiometric transition metal oxides and introduces the importance of the surface contaminant Li_2CO_3. The rest of this dissertation focuses on Li-stoichiometric oxides. In Chapter 3 a new titration technique is introduced to quantify the irreversible surface changes that occur in the first electrochemical cycle. Additional details of this technique are given in Appendix C. Expanding on these surface changes, Chapter 4 explores the role of the electrolyte in these transformations and Chapter 5 explores how intentional surface modification changes the behavior exhibited by outgassing.

2 | The role of Li_2CO_3 in outgassing during the first charge of layered lithium transition metal oxides

2.1 Abstract

In the prior literature, the role of residual lithium carbonate in the electrochemistry and outgassing of lithium transition-metal oxides (TMOs) had been largely overlooked and underestimated. In this chapter, by combining in-situ gas analysis, isotopic labeling, and a surface carbonate titration, we show that the presence of residual lithium carbonate (Li_2CO_3) on the surface of both Ni-rich Li-stoichiometric (specifically $LiNi_{0.6}Mn_{0.2}Co_{0.2}O_2$) and Li-rich ($Li_{1.2}Ni_{0.15}Co_{0.1}Mn_{0.55}O_2$) TMOs has a direct correlation with the amount of CO_2 and CO evolved and has a relationship with O_2 evolved from the TMO lattice on the first charge. By selectively isotopically labeling the residual surface Li_2CO_3, which remains in small quantities ($\approx$ 0.1 wt%) after synthesis, and not the carbonate electrolyte, we further show that, up to 4.8 V vs. Li/Li^+ on the first charge, carbonate electrolyte degradation negligibly contributes to gas evolution. These key conclusions warrant a reassessment of our notion of oxidative decomposition of carbonate electrolytes on TMO surfaces and, more generally, the reactivity of TMO surfaces.*

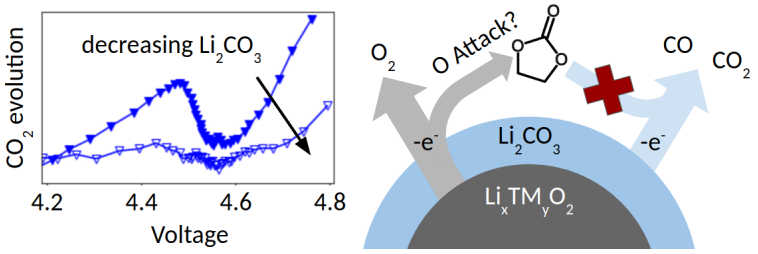

*This chapter largely adapted from previously published work in: S.E. Renfrew; B. D. McCloskey. *J. Am. Chem. Soc.* **2017**, *139*, 17853–17860 and N. Mahne; S. E. Renfrew; B. D. McCloskey; S. A. Freunberger. *Agnew. Chem. Int. Ed.* **2018**, *57*, 5529–5533.

2.2 Introduction

Understanding the high voltage instabilities of Li-ion battery materials is a prerequisite step to increasing the reversible potential window and thus the attainable capacity of Li-ion batteries.[2] As the cathode is the limiting electrode, we then wish to quantify the individual and coupled high voltage decomposition and transformations of the cathode, a lithiated transition-metal oxide (TMO), and the electrolyte, which is most commonly carbonate blends [ethylene carbonate (EC), diethyl carbonate (DEC), propylene carbonate (PC), dimethyl carbonate (DMC), etc.] with fluorinated salts. The most widely studied TMOs are layered $Li_{(1+x)}TM_{(1-x)}O_2$, with $0 \leq x \leq 1/3$, where TM is commonly a blend of Ni, Mn, and Co transition metals and where $x = 0$ represents the Li-stoichiometric TMOs, while $x > 0$ represents the Li-rich TMOs with excess lithium in the transition-metal layer. Despite numerous observations of high voltage decomposition, namely, TMO surface reconstruction, TM dissolution, electrolyte degradation, and formation of surface species (see as examples in refs [3–9] and references therein), the picture is still incomplete, with the curious dependence on electrolyte and TMO composition not yet fully understood. In-situ mass spectrometry techniques, such as differential/operando electrochemical mass spectrometry (DEMS/OEMS), are invaluable tools that allow real-time quantification of volatile products while the potential and/or current are monitored, and they complement the previous observations of high voltage instability.

Pioneering DEMS work on the oxidative stability of carbonate electrolytes on TMOs showed a discrepancy in the outgassing behavior of $LiNiO_2$ cells compared to conductive carbon and the cathode materials $LiMn_2O_4$ and $LiCoO_2$.[10] No significant difference in the onset potential ($\approx$ 4.8 V vs. Li/Li^+) of CO_2 and other characteristic electrolyte decomposition fragments from carbonate electrolyte oxidation was seen in $LiMn_2O_4$, $LiCoO_2$, and carbon cells; however, for $LiNiO_2$ cells with both PC- and EC/DMC-based electrolytes, CO_2 was evolved at lower potentials ($\approx$ 4.2 V), with significantly higher rates and without the other characteristic decomposition fragments [e.g., PC oxidation products of $m/z = 58$ (propanal) and $m/z = 87$ (2-ethyl-4-methyl-dioxalane)]. This difference was attributed to the different electrocatalytic reactivity of the $LiNiO_2$ surface.

Work following this research has attempted to further quantify the surface reactivity/instability anomaly seen in $LiNiO_2$, particularly with the recent renewed interest in Ni-rich TMOs. In the large set of DEMS/OEMS work since then, relatively low voltage onset of CO_2 evolution ($\leq$ 4.4 V) has been observed for a number of Li-TMOs on charge, both Li-stoichiometric[10–19] and Li-rich.[5,16,20–26] Despite distinct voltage profiles, Li-rich and Li-stoichiometric oxides exhibit similar gas evolution characteristics on charge. For both materials, CO_2/CO begins to evolve starting at $\approx$ 3.8–4.2 V and is sustained until the high voltage regime of $\approx$ 4.3–4.6 V, where there is a sudden onset of O_2 evolution, as well as a marked increase in CO_2 evolution accompanied by CO evolution.

There are several sources of C and O in a Li-ion battery that could contribute to this outgassing; however, we can rule out direct contribution of the conductive carbon based on two recent studies.[24,27] The binder (polyvinylidene fluoride, PVDF) also does not directly participate, due to the lack of volatile fluorine species detected. The polypropylene separator can also be ruled out, as CO_2 is also detected with glass fiber separators.[16] This leaves us with three sources of C and O:

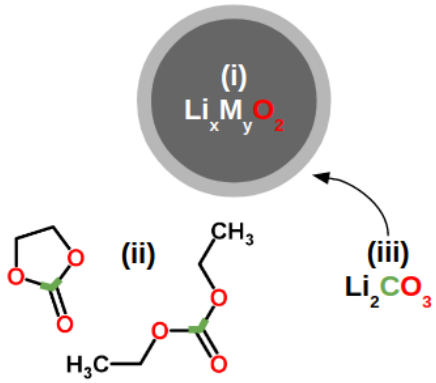

Figure 2.1: Main sources of C and O that could contribute to observed outgassing during active material (de)lithiation.

(i) the TMO

(ii) the carbonate electrolytes, and

(iii) lithium carbonate, Li_2CO_3.

Li_2CO_3 is inevitably present as a contaminant on TMO surfaces[28,29] among other salts as a result of TMO synthesis procedures that use Li_2CO_3 as a precursor or from reactions of other lithium salts and/or the lithiated TMO with atmospheric O_2, H_2O, and/or CO_2.[30] Even after calcination procedures, trace amounts of Li_2CO_3 persist on TMO surfaces, as we show later. While it is well agreed that the O_2 evolution is from irreversible charge compensation by the oxygen lattice from overdelithation of the Li-stoichiometric TMOs on overcharge[17] and from what is often called the activation of the Li_2MnO_3 domains of the Li-rich TMOs,[5] the source of the CO/CO_2 evolution in both the low and high voltage regimes has been debated.

The overarching conclusion from recent DEMS/OEMS studies is that the surface of TMOs, both Li-stoichiometric and Li-rich, facilitates carbonate electrolyte decomposition, which is claimed to be the main source of the high voltage CO/CO_2 evolution. There are three common variations of this conclusion:

(i) the TMO surface acts as a catalyst to lower the onset potential of CO_2 evolution to $\approx$ 4 V and does not participate in the reaction (i.e., no TMO surface oxygen in CO/CO_2);[5,10,17]

(ii) there is coupled TMO-electrolyte decomposition (i.e., TMO surface oxygen incorporates in CO/CO_2) throughout the entire voltage window where CO_2 evolution is observed, before and during O_2 evolution;[15,16,20–23,25,26] and

(iii) there is either electrolyte decomposition or coupled TMO-electrolyte decomposition only in the high voltage region where O_2 evolution is observed and the low voltage ($\approx$ 4–4.4 V) CO_2 is only from electro-oxidation and/or chemical decomposition of the residual surface Li_2CO_3.[11–13,18,19,24]

In the current chapter, we provide compelling evidence that most, if not all, CO_2/CO evolution during the first charge, regardless of the voltage region, is a result of residual Li_2CO_3 oxidation and not electrolyte oxidation. By isotopically enriching Li-rich and Li-stoichiometric TMOs with ^{18}O via a procedure that enriches the O atoms in the residual surface Li_2CO_3 and TMO oxide lattice discriminately, we found that the O isotope composition in the CO_2/CO evolved during the first charge is statistically identical to that of the residual Li_2CO_3. Furthermore, the total CO_2/CO evolved is similar to the amount of Li_2CO_3 initially present. By performing a gentle acid wash, a portion of Li_2CO_3 can be removed from the TMO surface, and in doing so, a proportionately smaller amount of CO_2 is observed to evolve from these "washed" TMOs. Intriguingly, O_2 evolution from the TMO lattice oxygen is also observed to decrease after a portion of the Li_2CO_3 is removed from the TMO surface, implying that oxygen release from these materials is likely related to Li_2CO_3 oxidation through a yet unconfirmed mechanism. The end of this chapter discusses evidence of singlet oxygen generation from the electrochemical oxidation of Li_2CO_3 and the implications of this for stability of TMOs on charge.

2.3 Results and Discussion

As CO_2 could come from either carbonate source—the electrolyte or the residual surface contaminant—and both have evidence of decomposition at similar oxidative potentials, it is clear we must decouple the electrolyte, the surface carbonate, and the TMO surface. To distinguish the cathode components from the electrolyte, we performed an isotopic enrichment with ^{18}O on the TMO. The basic principle of the enrichment is similar to that presented by Luo et al.,[20,21] wherein the TMO is heated under an $^{18}O_2$ headspace; however, we alter the setup to be able to estimate the total enrichment by performing an oxygen balance on the ^{18}O. The surface carbonate oxygen inevitably also exchanges with the headspace oxygen, so to quantify the amount of surface carbonate as well as its isotopic enrichment, we performed a carbonate titration[31] similar to that described initially by Thotiyl et al.,[32] which provides an accurate quantification of the total Li_2CO_3 per unit weight of TMO powder as well as the carbonate O isotopic distribution. See Appendix A for a description of DEMS, B for description of the ^{18}O-enrichment and sample calculations, C for detail of the carbonate titration, and D for description of the electrochemical cells and testing.

The rest of this chapter focuses on the low and high-voltage decomposition products for two ^{18}O-labeled oxides:

(i) $LiNi_{0.6}Mn_{0.2}Co_{0.2}O_2$, Li-stoichiometric and Ni-rich, hereby referred to as NMC, and

(ii) $Li_{1.2}Ni_{0.15}Co_{0.1}Mn_{0.55}O_2$, Li- and Mn-rich, hereby referred to as LMR.

The ^{18}O-labeled NMC and LMR had radically different oxygen exchange kinetics during the ^{18}O enrichment procedure. From our upper bound estimates described in Appendix

B, both the NMC and LMR had similar total enrichments of < 4–6 % ^{18}O. However, the NMC had 23 % ^{18}O surface enrichment, which we infer from the isotope composition of oxygen released at high potentials during a galvanostatic charge (discussed later), while the LMR had only 2 % ^{18}O surface enrichment, suggesting that the ^{18}O is concentrated at the surface of the NMC, while it is more uniformly distributed throughout the LMR particles. Both the LMR and NMC had surface residual carbonate that became enriched in ^{18}O as well, with enrichments of 9 % for both materials. The total amount of surface carbonate on ^{18}O-NMC is 33 µmol g^{-1}, or 0.25 wt%, and the total amount of surface carbonate on ^{18}O-LMR is 15 µmol g^{-1}, or 0.11 wt%. Of note is that the ^{18}O enrichment procedure mimics calcination at high temperatures (800 °C), and even after this thermal treatment, detectable surface carbonate remains. In other words, thermal treatments cannot be assumed to fully remove surface carbonate. Depending on the particular synthesis method, there could be in principal a mixture of various metal carbonates left after calcination; however, for this chapter we simplify the nomenclature and refer to the surface carbonate herein as Li_2CO_3. The distributions of $C^{16,16}O_2$, $C^{16,18}O_2$, and $C^{18,18}O_2$ detected from the carbonate titration in both samples are not well-described by binomial distributions, with the deviations indicating a nonuniformity in the isotopic labeling of the surface Li_2CO_3. Some nonuniformity likely exists due to competing factors: during heating there is a balance between Li_2CO_3 oxygen and headspace oxygen exchange, degradation of Li_2CO_3, and precipitation from any bulk Li_2CO_3 deposits.

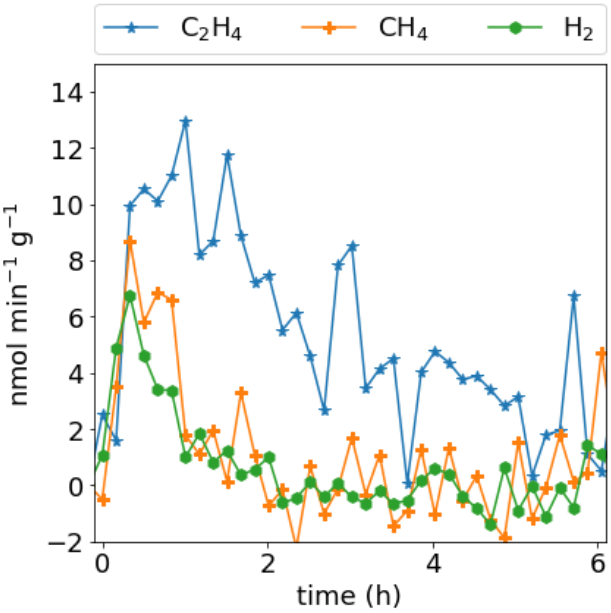

Figure 2.2: Gas evolution rates from the Li counter electrode during delithiation of ^{18}O-NMC. Gases evolved during the first portion of charging shown later in Figure 2.3. Other than CO, CO_2, and O_2, the only other gases detected were trace H_2, C_2H_4, and CH_4 from electrolyte reduction and SEI formation on Li at the very beginning of charge. Compared to SEI formation on carbon, these gas evolution rates are small. Compare to ref. [11] for electrolyte reduction in full cells.

To study the low and high voltage volatile decomposition reactions seen on oxidation, we galvanostatically charged the ^{18}O-NMC and ^{18}O-LMR to 4.8 V vs. Li/Li$^+$ at a rate of 0.1 Li$^+$ h^{-1} (27.65 mA g^{-1} for NMC and 31.44 mA g^{-1} for LMR) and allowed them to rest, all while monitoring the gases that evolved with time. The main gases evolved were CO, CO_2, and O_2, with only trace H_2, C_2H_4, and CH_4 ($\lesssim$ 10 nmol min^{-1} g^{-1}) as shown in Figure 2.2 detected at the very beginning of charge from reduction of the electrolyte at the Li metal electrode. Figure 2.3 summarizes the DEMS results for the first charge of ^{18}O-NMC.

Figure 2.3a) shows the gas evolution data for ^{18}O-labeled NMC, plotting the net rate of evolution of all of the isotopic configurations of O_2, CO, and CO_2. CO_2 and CO evolution begins at $\approx$ 3.8 V and is sustained throughout the blue-shaded region. In the red-shaded region, commencing at about $\approx$ 4.45 V, oxygen evolution is detected, as well as a marked increase in CO_2 and CO evolution. Unlike other studies, we did not detect any other gases (e.g., POF_3) nor did we detect any substantial H_2 evolution at high voltages.[16,26] The presence of ^{18}O is detected in only CO_2, CO, and O_2. The O_2 evolution decays during the rest period in a manner consistent with the tail of a typical galvanostatic DEMS measurement (i.e., O_2 evolution ceases once current is shut off); however, the CO_2/CO evolution is elevated during the rest period, during which the voltage stays above 4.6 V. This potential-mediated CO_2/CO evolution resembles a corrosion reaction, giving evidence that the CO_2/CO evolution does not originate from an NMC charge compensation reaction.

	total (nmol)	Distribution (%)			^{18}O content (%)
		$C^{16,16}O_2$	$C^{16,18}O_2$	$C^{18,18}O_2$	
Li_2CO_3	940 ± 60	85 ± 3	13 ± 2	2 ± 0.5	9 ± 2
CO_2	810 ± 10	82 ± 0.3	16 ± 0.3	2 ± 0.1	10 ± 0.2
		$C^{16}O$		$C^{18}O$	
CO	160 ± 7	91 ± 2		9 ± 2	9 ± 2
		$^{16,16}O_2$	$^{16,18}O_2$	$^{18,18}O_2$	
O_2	53 ± 3	59 ± 2	35 ± 2	6 ± 0.6	23 ± 1

Table 2.1: ^{18}O-NMC total surface Li_2CO_3 and gas evolution.

Residual Li_2CO_3 initially present on the as-prepared ^{18}O-NMC as predicted from the carbonate titration and total CO_2, CO, and O_2 evolution, along with isotopic composition, over the entire first charge and subsequent relaxation period for a cathode with 28 mg (290 µmol) total ^{18}O-NMC.

The total O_2 evolved during the first charge and subsequent rest is 53 nmol (Table 2.1), which corresponds to 0.02 % of the total oxide content of the NMC. From the distribution of $^{16,16}O_2$, $^{16,18}O_2$, and $^{18,18}O_2$, we can calculate that the total ^{18}O enrichment is 23 %, which is substantially higher than the ^{18}O enrichment in evolved CO_2/CO (9–10 %, Table 2.1) or

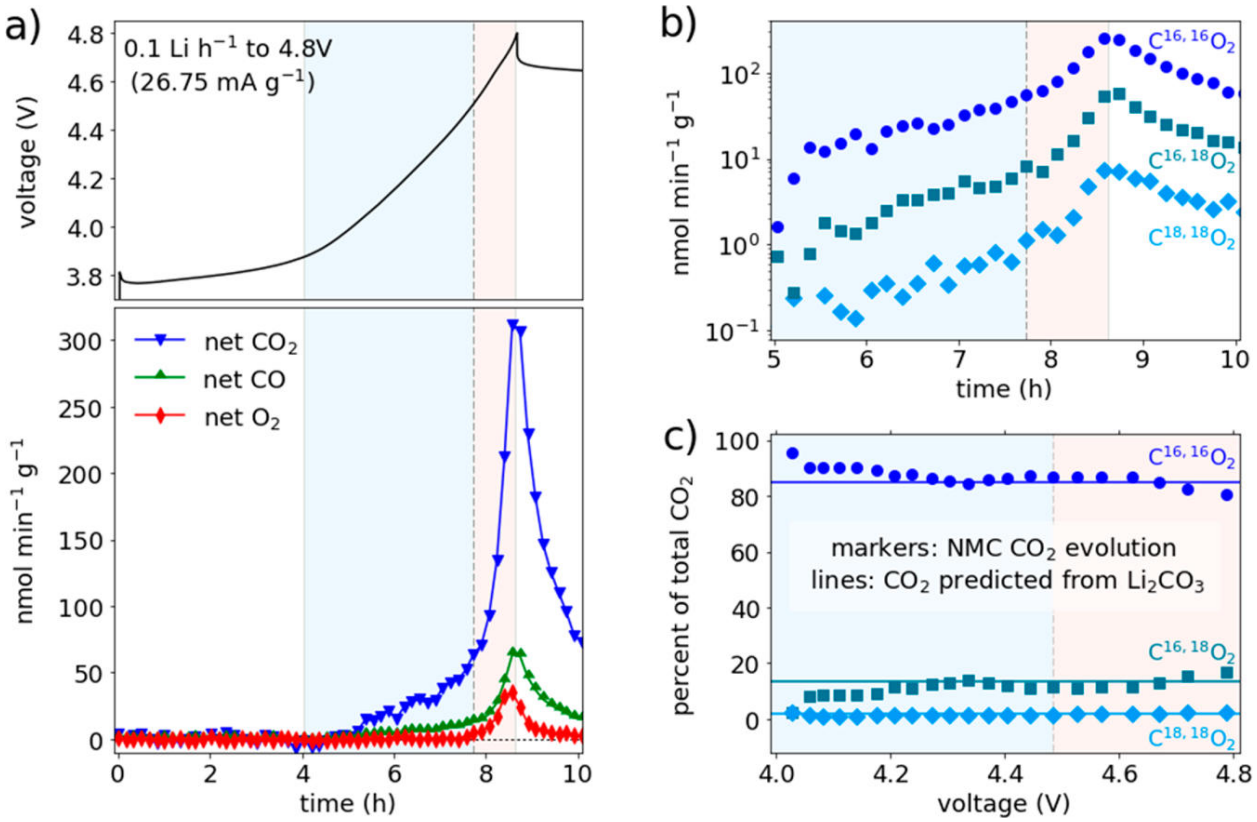

Figure 2.3: Rates of gas evolution for ^{18}O-NMC.

The blue-shaded regions represent the regime where CO_2/CO evolution is detected and the red-shaded regions indicate O_2 evolution in addition to elevated CO_2/CO evolution. **a)** Net gas evolution for all CO_2, CO, and O_2 isotopes for the first charge of ^{18}O-NMC followed by a rest period. The lines are to guide the eye. **b)** Detail of $C^{16,16}O_2$, $C^{16,18}O_2$, and $C^{18,18}O_2$ evolution plotted on a partial log scale, showing detection of all isotopes in each region. **c)** Distribution of the CO_2 evolution versus voltage, with the lines representing the predicted distribution from Li_2CO_3 degradation. Summaries of these data are included in Table 2.1. The cell was allowed to rest after charge until all gas evolution was at or near attenuation; however, for clarity only 2 h of the rest period is plotted. The cell was assembled with a Li foil anode, polypropylene (Celgard) separator, 80 µL EC/DEC (1:1, v/v) 1 M $LiPF_6$ electrolyte, and a cathode with 28 mg ^{18}O-NMC (cast on stainless steel mesh with ≈ 90 wt% ^{18}O-NMC, 5 wt% PVDF, and 5 wt% Super P).

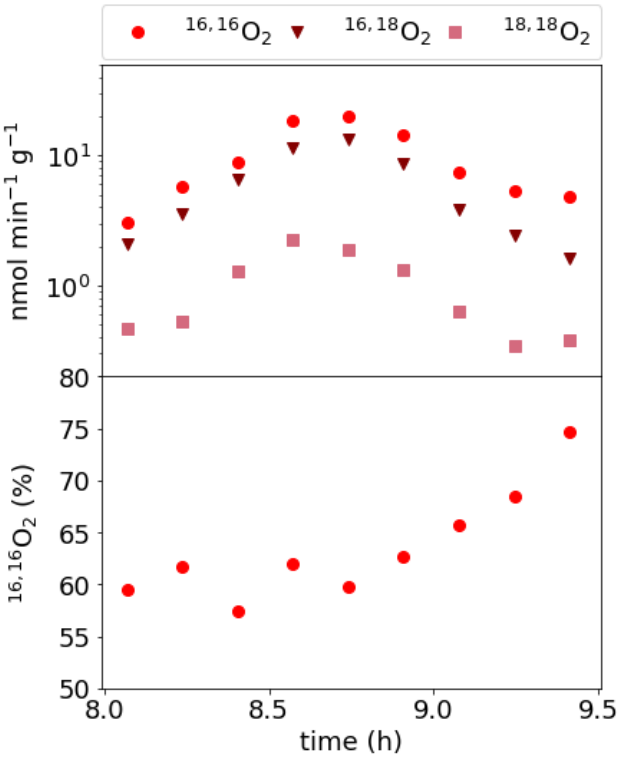

Figure 2.4: Rates of O_2 evolution from ^{18}O-labeled NMC.

Oxygen release during the red region of charging and subsequent rest shown in Figure 2.3. The top panel shows the O_2 evolution rates plotted on a partial log scale. All isotopes were detected. The bottom panel shows the percent of the total O_2 evolution that is from $^{16,16}O_2$. The fraction of ^{16}O isotopes increases with oxygen extraction from the NMC lattice, implying that the NMC enrichment is anisotropic. Contrast to Figure 2.7, which shows an analogous measurement for ^{18}O-labeled LMR.

residual Li_2CO_3 (9 %). The O_2 evolution data is well-described by a binomial distribution (Figure 2.4), suggesting that the ^{18}O is concentrated and uniformly distributed in the NMC surface oxide layer. These results strongly infer that all O_2 is evolved from the NMC lattice oxygen and does not involve Li_2CO_3 or electrolyte degradation, where the ^{18}O content in the evolved O_2 would otherwise be approximately equivalent or less than the ^{18}O composition observed in the residual Li_2CO_3.

During the first charge and subsequent rest, the total CO_2 evolved is 810 nmol and the total CO evolved is 160 nmol (Table 2.1), whereas the total residual Li_2CO_3 initially present was 940 nmol, indicating that, within error, all CO_2/CO evolution could be accounted for by Li_2CO_3 degradation; this theory is bolstered by further evidence described below. Figure 2.3b) shows the CO_2 isotopic data in the charge and rest period plotted on a log scale for

clarity. Figure 2.3c) plots the CO_2 evolution distribution versus charging voltage, with the shaded regions indicating the same regions as in Figure 2.3a) and b). We can see that the isotopic distribution is nearly constant over the whole region and that there is no sudden change with the onset of O_2 evolution. To compare the isotope composition of evolved CO_2 to that of the residual Li_2CO_3, as measured using the carbonate titration, the lines plotted in Figure 2.3c) indicate the average CO_2 ratios predicted if the CO_2 evolution solely came from Li_2CO_3 degradation. Very close agreement between these two values is observed throughout the charge, with only minor deviations at the beginning and end of charge that likely result from the nonuniform isotope labeling of the Li_2CO_3. In fact, the total ^{18}O enrichment in evolved CO_2/CO is statistically identical to that of the Li_2CO_3 ^{18}O enrichment (Table 2.1). As seen in Figure 2.4, as oxygen is extracted from the NMC there is a decrease in ^{18}O content due to the anisotropic labeling of the NMC. If O in CO_2 came from the NMC lattice, we would expect to see the same trend with time, namely, a decrease in the ^{18}O content in the CO_2 distribution with time. The opposite trend is observed in Figure 2.3c). Although we cannot entirely exclude the possibility of some minority electrolyte degradation, as suggested previously,[11,20,21] we propose that our data are entirely consistent with that of Li_2CO_3 degradation, accounting for all CO_2 and CO evolution. We bolster this claim later in this chapter by removing a portion of the surface Li_2CO_3; however, for now we move to the ^{18}O-LMR DEMS results.

Figure 2.5 shows gas evolution data for the ^{18}O-LMR, with Table 2.2 providing a summary of the total residual Li_2CO_3 initially present on the cathode active material, and the total gas evolution during the first charge and rest, including isotope compositions. Like ^{18}O-NMC, trace H_2, C_2H_4, and CH_4 ($\lesssim$ 10 nmol min^{-1} g^{-1}, Figure 2.6) were also detected at the very beginning of charge of ^{18}O-LMR, with no POF_3 throughout and no H_2 evolution at high voltages. Similar to ^{18}O-NMC, the presence of ^{18}O is detected in CO_2, CO, and O_2, with again all possible isotopic configurations of $^{16}O/^{18}O$ detected. Figure 2.5a) plots the net rate of CO_2, CO, and O_2 for all isotopes with the blue-shaded region starting at $\approx$ 4.1 V indicating the detection of only CO and CO_2 and the red-shaded region starting at 4.55 V indicating the onset of O_2 evolution along with an increase in CO/CO_2 evolution. The total oxygen evolved is 0.31 % of the total oxide content, an order of magnitude increase compared to the ^{18}O-NMC oxygen release. The isotopic distribution of the O_2 detected is constant with time/voltage above 4.55 V and during the rest period (see Figure 2.7), suggesting that the ^{18}O enrichment is uniform throughout the region of the LMR particles where the O_2 is lost, consistent with our conclusions based on the exchange data (see Figure 2.7). After the current is shut off, the CO_2 evolution is sustained, similar to that detected in the NMC. Additionally, the O_2 evolution is also sustained in the rest period, as noted by other authors,[24] which additionally questions the notion that the O_2 release from LMR is solely from a charge compensation reaction, instead of or in addition to a phase transformation.[9,24]

Figure 2.5b) plots the CO_2 isotopes on a partial log scale, with a decrease in the CO_2 evolution rate seen during the plateau, consistent with other studies.[16,20–22,24] Figure 2.5c) plots the distribution of the CO_2 detected with voltage, with the solid lines again indicating the predicted average distribution if the CO_2 evolution came solely from the Li_2CO_3 degradation. There is a greater deviation in the blue region from the predicted average

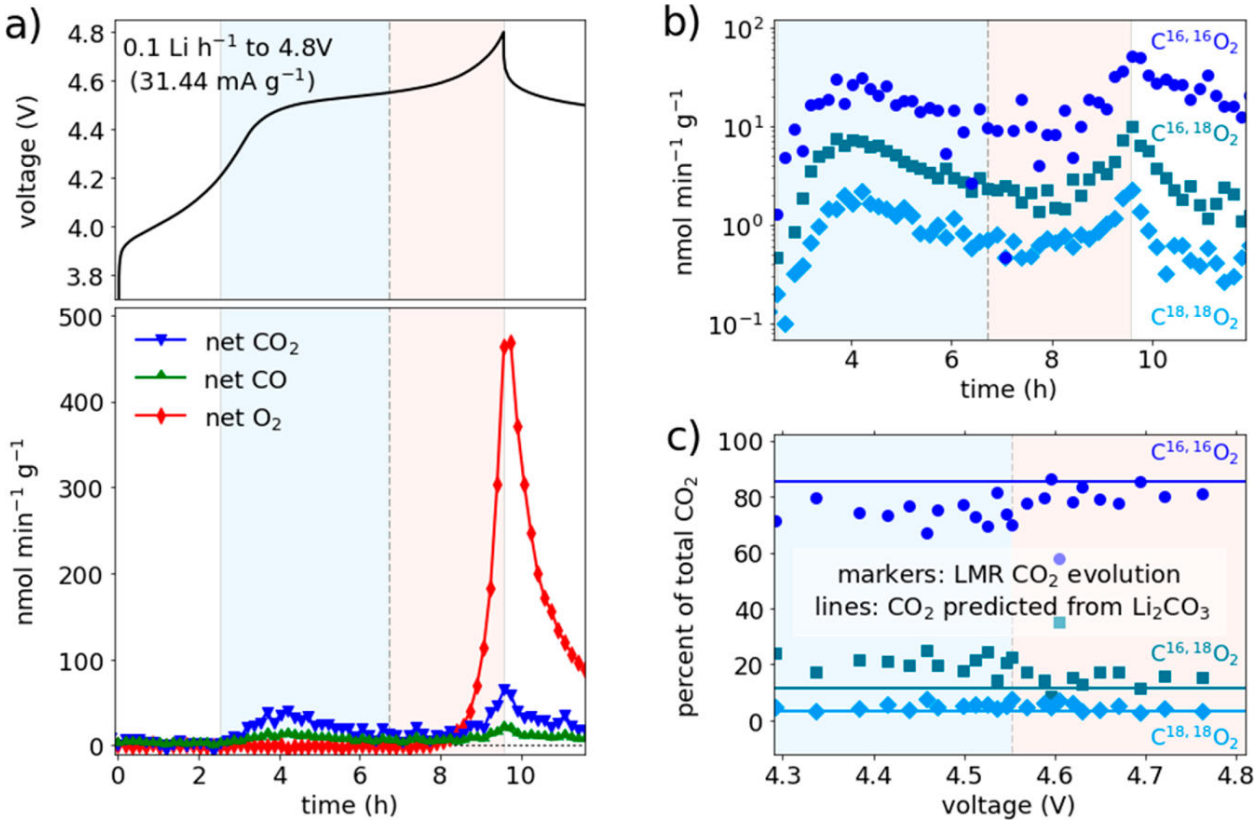

Figure 2.5: Rates of gas evolution for ^{18}O-LMR.

The blue-shaded regions represent the regime where only CO_2/CO evolution is detected, and the red-shaded regions indicate O_2 evolution in addition to elevated CO_2/CO evolution. **a)** Net gas evolution for all CO_2, CO, and O_2 isotopes for the first charge of ^{18}O-NMC followed by a rest period. The lines are to guide the eye. **b)** Detail of $C^{16,16}O_2$, $C^{16,18}O_2$, and $C^{18,18}O_2$ evolution plotted on a partial log scale, showing detection of all isotopes in each region. **c)** Distribution of the CO_2 evolution versus voltage, with the lines representing the predicted distribution from Li_2CO_3 degradation. Summaries of these data are included in Table 2.2. The cell was allowed to rest after charge until all gas evolution was at or near attenuation; however, for clarity only 2 h of the rest period is plotted. The cell was assembled with a Li foil anode, polypropylene (Celgard) separator, 80 µL EC/DEC (1:1, v/v) 1 M $LiPF_6$ electrolyte, and a cathode with 36 mg ^{18}O-LMR (cast on stainless steel mesh with ≈ 90 wt% ^{18}O-LMR, 5 wt% PVDF, and 5 wt% Super P).

	total (nmol)	Distribution (%)			^{18}O content (%)
		$C^{16,16}O_2$	$C^{16,18}O_2$	$C^{18,18}O_2$	
Li_2CO_3	540 ± 30	85 ± 2	12 ± 1	3 ± 0.9	9 ± 2
CO_2	450 ± 50	81 ± 2	15 ± 3	4 ± 0.4	12 ± 1
		$C^{16}O$		$C^{18}O$	
CO	130 ± 20	90 ± 1		10 ± 1	10 ± 1
		$^{16,16}O_2$	$^{16,18}O_2$	$^{18,18}O_2$	
O_2	1300 ± 2	96.5 ± 0.1	3.3 ± 0.1	0.2 ± 0.1	2 ± 0.1

Table 2.2: ^{18}O-LMR total surface Li_2CO_3 and gas evolution.

Residual Li_2CO_3 initially present on the as-prepared ^{18}O-LMR as predicted from the carbonate titration and total CO_2, CO, and O_2 evolution, along with isotopic composition, over the entire first charge and subsequent relaxation period for a cathode with 36 mg (420 µmol) total ^{18}O-LMR.

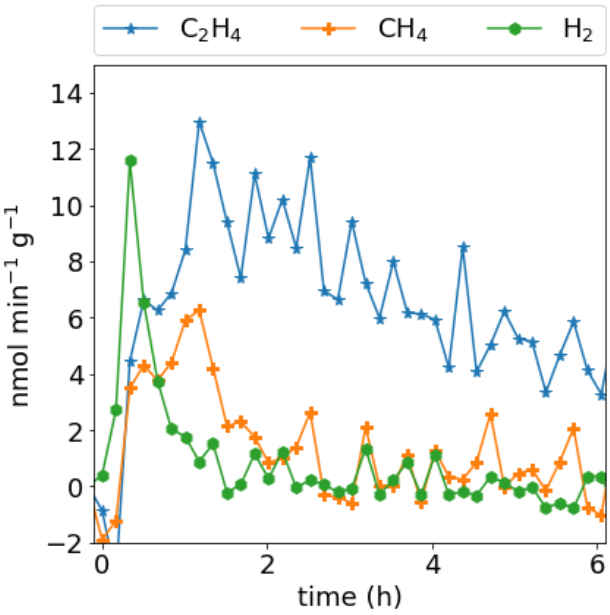

Figure 2.6: Gas evolution rates from the Li counter electrode during delithiation of ^{18}O-LMR. Gases evolved during the first portion of charging shown in Figure 2.5. Other than CO, CO_2, and O_2, the only other gases detected were trace H_2, C_2H_4, and CH_4 from electrolyte reduction and SEI formation on Li at the very beginning of charge.

distribution if Li_2CO_3 oxidation accounted for CO_2 evolution, with a larger amount of ^{18}O-enriched CO_2 detected. Noting again that limited ^{18}O enrichment was observed in the LMR [2 %; see Figure 2.7 and Table 2.2] such that the surface Li_2CO_3 is the only significant source of ^{18}O in the system, a mechanism with any significant involvement of the LMR oxygen in CO_2/CO evolution would result in CO_2/CO that is almost exclusively ^{16}O isotopes. As the electrolyte carbonates have a natural abundance isotopic distribution, there is not a significant source of ^{18}O in the electrolyte, and hence, a dramatic, and perhaps sudden, change in ^{18}O enrichment in the red region would be expected if lattice oxygen release significantly contributed to CO_2 evolution.

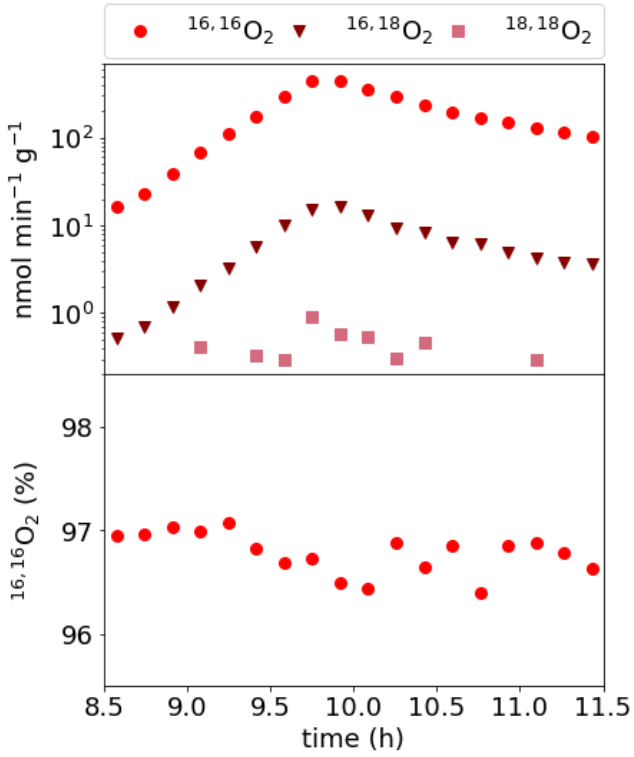

Figure 2.7: Rates of O_2 evolution from ^{18}O-labeled LMR.

Oxygen release during the red region of charging and subsequent open circuit potential shown in Figure 2.5 The top panel shows the O_2 evolution rates plotted on a partial log scale. All isotopes were detected, however $^{18,18}O_2$ was only distinguishable from noise near the peak of the O_2 evolution. The bottom panel shows the percent of the total O_2 evolution that is from $^{16,16}O_2$. The fraction of ^{16}O isotopes is nearly constant in LMR, implying that the LMR enrichment is nearly uniform. Contrast to Figure 2.4, which shows an analogous measurement for the ^{18}O-labeled NMC material.

This strongly suggests that Li_2CO_3 accounts for all CO_2/CO evolution in the blue region of Figure 2.5 and that the isotopic deviation observed in the blue region of Figure 2.5c) is a

result of nonuniform isotopic exchange throughout the Li_2CO_3. However, this deviation likely is also partially a result of the low rate of CO_2 evolution (< 25 nmol min^{-1} g^{-1}) throughout the region, which reduces the accuracy of such a measurement due to detection limits. We note that the cumulative CO_2 evolved in the blue region of Figure 2.5 is less than half of the total amount of CO_2 evolved.

By performing different enrichment procedures, the ^{18}O-LMR in this work ($Li_{1.2}Ni_{0.15}Co_{0.1}Mn_{0.55}O_2$) and the similar ^{18}O-Li,Mn-rich samples (specifically $Li_{1.2}Ni_{0.13}Co_{0.13}Mn_{0.54}O_2$ and the Co-free $Li_{1.2}Ni_{0.2}Mn_{0.6}O_2$) in references [21] and [20] respectively, both by Luo et al. have distinct TMO surface enrichments—2 % in this chapter and 15 % in Luo et al. However, the detected CO_2 distribution presented by Luo et al. (87 % $C^{16,16}O_2$, 13 % $C^{16,18}O_2$, 0 % $C^{18,18}O_2$) is similar to our measured CO_2 evolution data and surface Li_2CO_3 enrichment data, which is further evidence that the LMR surface does not significantly participate in the CO_2/CO evolution reactions. Overall, even with large O_2 release above 4.55 V in LMR, a significant portion of the CO_2 release must come from Li_2CO_3 degradation, not from reactive oxygen-mediated electrolyte decomposition. This observation is particularly evident in our data, as the isotopic distribution of the evolved CO_2/CO is nearly identical to the residual Li_2CO_3 isotope composition during the voltage/capacity range where O_2 is evolved (red region of Figure 2.5). It is also worth noting that even with an order of magnitude higher O_2 evolution rate in LMR compared to NMC, the CO_2/CO evolution rate in LMR is lower than in NMC, as is consistent with the relative amounts of residual Li_2CO_3 in each material (0.11 wt% in LMR and 0.25 wt% in NMC).

Within error, the ^{18}O enrichment of CO and CO_2 match for each material despite the remarkably different TMO surface oxide enrichments and overall O_2 release. These results are highly suggestive that the majority of the CO_2/CO evolution comes from degradation of the surface Li_2CO_3 for both materials, as the residual Li_2CO_3 isotopic distribution in each material is similar (Tables 2.1 and 2.2). Any electrolyte degradation stemming from attack from energetic oxygen release from the TMO surface does not manifest itself as significant CO or CO_2 evolution up to 4.8 V vs. Li/Li^+. Given our results, the overall CO_2/CO evolution rate from related TMO samples will be primarily influenced by the residual Li_2CO_3 content and not by O release from the TMO lattice.

On the basis of our observation that the CO/CO_2 evolution is consistent with Li_2CO_3 degradation for both oxides, we predict that if the ^{18}O-NMC and ^{18}O-LMR materials had less surface carbonate, the rate of CO/CO_2 evolution and total CO/CO_2 evolved would be lower and the distribution of ^{18}O detected would continue to match that detected from the surface carbonate titration. To study the effect of the amount of surface Li_2CO_3 on CO/CO_2 evolution, we chemically removed the surface carbonate by rinsing the ^{18}O-LMR and ^{18}O-NMC powders with a mild acid, ensuring the same ^{18}O enrichments on the TMO surfaces. Other washing methods reported suspend TMO particles in aqueous solutions for long times (20 min) and report some delithiation of the TMO lattice.[33] In our method, we vacuum-rinsed and filtered the TMO particles to limit aqueous exposure. See the SI for a full description of the procedure. After drying the surface-treated (ST) samples, we performed

carbonate titrations on both, finding a reduction of ≈ 65–80 % of surface Li_2CO_3 in the ST compared to the pristine samples. We additionally quantified their isotopic enrichments and found in both cases that the ^{18}O enrichment of the Li_2CO_3 in the ST samples was lower than the pristine enriched samples, consistent with our assertion that the enrichment of the Li_2CO_3 in the pristine samples was not uniform.

From XRD data[34–36] and our own charge profiles in Figure 3b) and d), we see that the bulk properties of LMR and NMC are not affected by the surface treatment. The effect of aqueous treatment on the surface of TMO oxides has been mostly studied in either long-term soaking treatments or long-term aging of materials exposed to moisture and atmosphere (O_2 and CO_2). These rather harsh conditions have been shown to increase the Li_2CO_3 layer from reaction with atmosphere and delithiation of the surface.[33,34] The ^{18}O enrichment of the remaining Li_2CO_3 films after our surface treatment is still over an order of magnitude higher than natural abundance, leading us to conclude that we did not remove the entire Li_2CO_3 layer in our surface treatment and that the remaining carbonate is a portion of the original carbonate layer, not growth of a new layer stemming from reaction with atmosphere and delithiation of the TMO.

Figure 2.8 summarizes the rate of CO_2 evolution of the pristine and ST ^{18}O-NMC and ^{18}O-LMR samples, with the Li_2CO_3 and CO_2 isotopic distributions and cumulative amounts summarized in Table 2.3.

ST ^{18}O–NMC	total (nmol)	Distribution (%)			^{18}O content (%)
		$C^{16,16}O_2$	$C^{16,18}O_2$	$C^{18,18}O_2$	
Li_2CO_3	210 ± 10	95 ± 0.2	4 ± 0.1	1 ± 0.2	3 ± 0.2
CO_2	220 ± 9	95 ± 0.5	4 ± 0..5	1 ± 0.1	3 ± 0.2
ST ^{18}O–LMR	total (nmol)	Distribution (%)			^{18}O content (%)
		$C^{16,16}O_2$	$C^{16,18}O_2$	$C^{18,18}O_2$	
Li_2CO_3	190 ± 10	96 ± 0.2	4 ± 0.2	n/a	2 ± 0.1
CO_2	150 ± 10	95 ± 0.8	5 ± 0.8	n/a	3 ± 0.4

Table 2.3: Total surface Li_2CO_3 and gas evolution for ST ^{18}O-LMR and ST ^{18}O-NMC. Residual Li_2CO_3 remaining after the surface treatment as predicted from the carbonate titrations and total CO_2, CO, and O_2 evolution, along with isotopic composition, over the entire first charge and subsequent relaxation period for ST ^{18}O-NMC (27 mg, 280 µmol) and ^{18}O-LMR (35 mg, 410 µmol).

For both materials we see that CO_2 evolution was reduced after removing a portion of the surface carbonate. In both cases, the CO and $C^{18}O$ signals had decreased and could not be resolved from noise, so though we cannot quantify the decrease, we can state that reduction

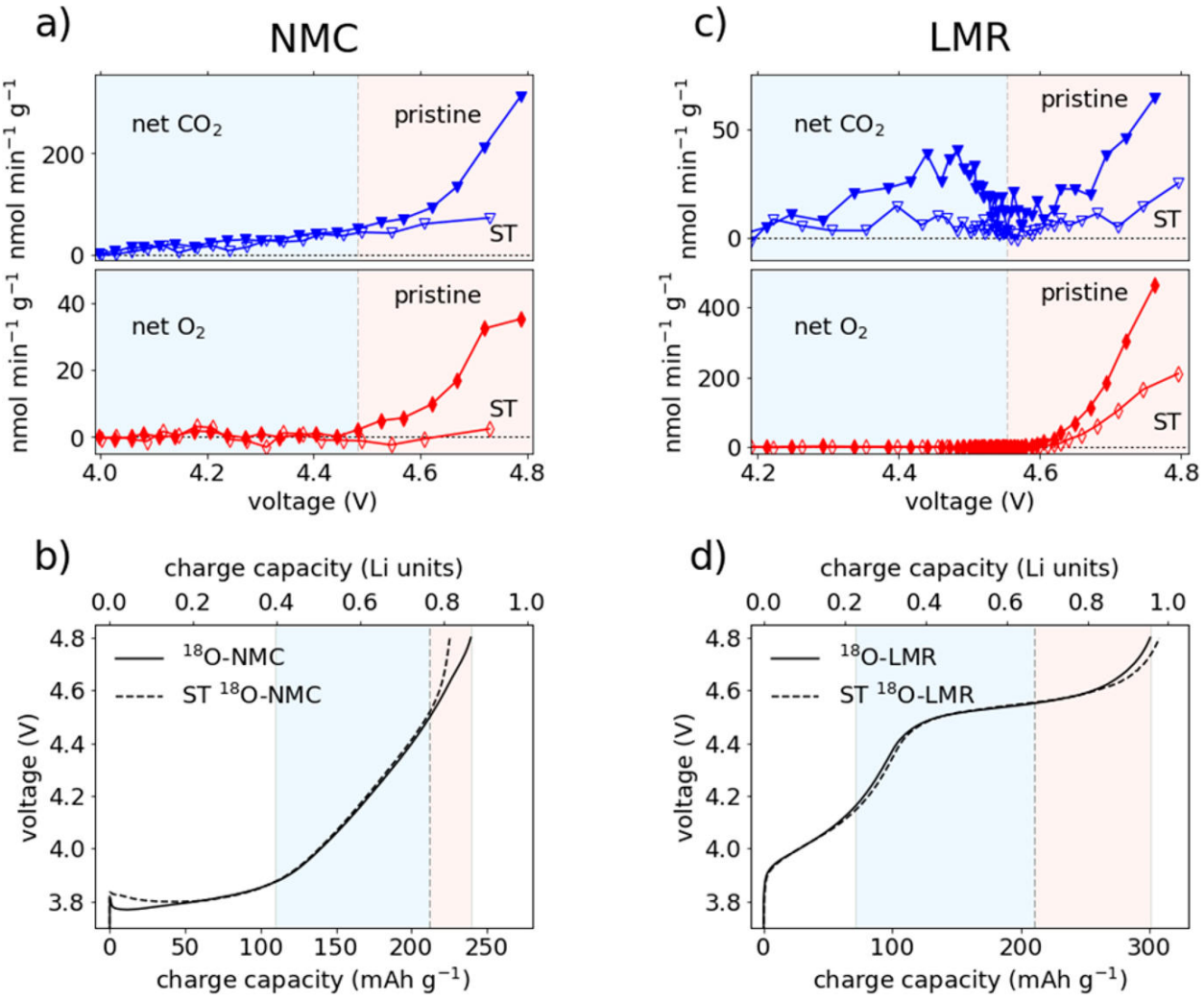

Figure 2.8: Rates of gas evolution for pristine and surface treated (ST) ^{18}O-NMC and ^{18}O-LMR.

Gas evolution rates for the first charge to 4.8 V (0.1 Li^+ h^{-1} removal rate) comparing the pristine (untreated) ^{18}O-NMC and ^{18}O-LMR samples to the ST samples after removal of a portion of the surface Li_2CO_3. The blue- and red-shaded areas indicate regions in the pristine samples where only CO/CO_2 is observed and where O_2 is observed, respectively. **a)** Plots of the O_2 and CO_2 evolution for the ST and pristine ^{18}O-NMC, showing attenuation of both the CO_2 and O_2 evolution rates after removal of a portion of Li_2CO_3. **b)** Comparison of the charge profiles for the pristine and ST NMCs. **c)** Plots of the O_2 and CO_2 evolution for the ST and pristine ^{18}O-LMR, also showing attenuation of both the CO_2 and O_2 evolution rates after removal of a portion of Li_2CO_3. **d)** Comparison of the charge profiles for the pristine and ST LMRs. Of note, no observable CO was detected in either ST measurement. Summaries of these data are included in Table 2.3. Cells were assembled with Li foil anodes, polypropylene (Celgard) separators, 80 µL EC/DEC (1:1, v/v) 1 M $LiPF_6$ electrolyte, and cathodes with either 27 mg ST ^{18}O-NMC or 35 mg ST ^{18}O-LMR (both cast on stainless steel mesh with ≈ 90 wt% active, 5 wt% PVDF, and 5 wt% Super P).

of the surface carbonate reduces the rate of CO evolution. We can, however, quantify the extent of the diminished CO_2 evolution. From the carbonate titration the ST ^{18}O-NMC had 7.8 µmol of Li_2CO_3 g^{-1}, a reduction of 76 ± 2 % compared to the pristine ^{18}O-NMC, and the total CO_2 evolution of the ST ^{18}O-NMC after the charge and rest was reduced by 72 ± 2 % compared to the pristine sample. With a similar trend, the ST ^{18}O-LMR had 5.3 µmol of Li_2CO_3 g^{-1}, a reduction of 65 ± 3 % compared to the pristine ^{18}O-LMR, and the total CO_2 evolved from the ST ^{18}O-LMR was reduced by 67 ± 4 % compared to the pristine sample. Within error, the reduction of surface Li_2CO_3 produced a near concomitant reduction in the total CO_2 evolved for both LMR and NMC. The isotopic distributions and total ^{18}O enrichment presented in Table 2.3 are also nearly identical for the Li_2CO_3 and evolved CO_2 for each material.

A remarkable additional observation is that the O_2 released from the lattice in the ST ^{18}O-NMC was suppressed and the O_2 released from the lattice in the ST ^{18}O-LMR was diminished (from 36 to 15 µmol g^{-1}) compared to the pristine materials, despite their very similar charge profiles. Accounting for the uncertainty in the mass loadings of the cathodes, the ST and pristine ^{18}O-LMR had nearly identical charge capacities, while the ST and pristine ^{18}O-NMC were nearly identical to the point of oxygen release in the red region. While our observation of a positive relationship with O_2 release and CO_2 evolution (i.e., surface Li_2CO_3) is initially puzzling, this observation is not unique to this work and is apparent in a number of other DEMS/OEMS studies.

As other authors have noted, there is a curious positive trend with O_2 and CO_2/CO release. However, as we have demonstrated that the majority of the CO_2 and CO data for TMO half-cells stems from Li_2CO_3 degradation, this allows us to reassess previous observations on other TMOs. A recent study from Streich et al.[15] concluded that for Li-stoichiometric TMOs, Ni-content controls not only O_2 release but CO_2 release as well, echoing the conclusions from Imhof and Novák's study[10] that the Ni-content controls the surface reactivity. However, other recent studies on Ni-containing Li-stoichiometric TMOs by Jung et al.[11,19] found that CO_2/CO release had a positive correlation with O_2 evolution, which was, however, independent of Ni and Co content. Additionally, as noted in several studies, O_2 and CO_2 detected for a given TMO have a dependence on electrolyte[14,15] and water content.[23] An intriguing possibility of a link between TMO lattice oxygen release and surface Li_2CO_3 degradation leads us to question our current understanding of Li_2CO_3 degradation.

The electrochemical oxidation of Li_2CO_3 has been studied mostly in the Li-air field, with the proposed reaction given below:

$$Li_2CO_3 \longrightarrow 2\,Li^+ + 2\,e^- + CO_2 + \frac{1}{2}\,O_2 \text{ (3.82 V vs. } Li/Li^+) \tag{2.1}$$

While CO_2 and CO have been observed, in prior research no O_2 has been detected originating from the carbonate.[37–39] Our results for Li_2CO_3 degradation on LMR and NMC surfaces, show both CO_2 and CO originating from the carbonate, with no other volatile products. The absence of O_2 detected, the so-called "missing oxygen," implies that O_2 does not form

as in Equation 2.1 and that the ultimate product is not volatile. This could stem from a number of forms of reactive oxygen which react with other cell components and thus are not detected as molecular oxygen.

A few mechanisms have been proposed for Li_2CO_3 (electro)chemical oxidation. The thermal decomposition reaction, $Li_2CO_3 \longrightarrow CO_2 + Li_2O$, will not occur at room temperature and can be excluded. From a study of $LiCoO_2$-catalyzed decomposition of Li_2CO_3, CO_2 and CO were, in agreement with our results, determined to originate from Li_2CO_3 with no O_2 detected.[39] In contrast to Reaction 2.1, the researchers proposed indirect generation of CO_2, with first a reaction that produced carbon and an unspecified form of reactive O_2, with the O_2 and C then reacting to produce only CO and CO_2, as listed below in Reactions 2.2 and 2.3:

$$Li_2CO_3 \longrightarrow 2\,Li^+ + 2\,e^- + C + \frac{3}{2}\,O_2 \tag{2.2}$$

$$(1+x)C + O_2 \longrightarrow (1\text{-}x)CO_2 + 2\,xCO \;\; (0 \leq x \leq 1) \tag{2.3}$$

Chemical decomposition mechanisms via acid contaminants present in the electrolyte have also been proposed.[40] By preparing Li_2CO_3 in $LiPF_6$ electrolyte solutions and heating, CO_2 and POF_3 were detected as the main gaseous products, which the researchers proposed to be analogs to reactions that would occur in actual electrochemical cells. They also tested LiTFSI [lithium bis(trifluoromethanesulfonyl)imide] electrolytes with Li_2CO_3 at elevated temperature and found insignificant CO_2 evolution, as expected due to the decreased tendency of LiTFSI to form acidic contaminants.

In another proposed mechanism, Yang et al. suggest that instead of Reaction 2.1, superoxide radicals are formed as below in Reaction 2.4:[27]

$$Li_2CO_3 \longrightarrow 2\,Li^+ + CO_2 + \frac{1}{2}\,{O_2}^{\bullet-} + \frac{3}{2}\,e^-, \tag{2.4}$$

with ${O_2}^{\bullet-}$ proposed to then react with the electrolyte to form volatile species. In reference [27] the formation of ${O_2}^{\bullet-}$ was not directly or indirectly detected, and it was only shown that ${O_2}^{\bullet-}$ *could* decompose the electrolyte if it were present.

In the remaining portion of this chapter, we give compelling evidence that molecular oxygen, superoxide, and peroxide are not generated as proposed in Reactions 2.1–2.4 when Li_2CO_3 is electrochemically oxidized. We propose instead that singlet oxygen, $^1O_2$, is generated when Li_2CO_3 is electrochemically oxidized as below in Reaction 2.5:

$$Li_2CO_3 \longrightarrow 2\,Li^+ + 2\,e^- + CO_2 + \frac{1}{2}\,{}^1O_2. \tag{2.5}$$

Due to its highly reactive nature, direct detection of singlet oxygen can be difficult, however

$^1O_2$ can be indirectly detected and distinguished from molecular oxygen, superoxide, and peroxide with chemical probes that selectively react with $^1O_2$. The reacted chemical probes can then be quantified using various spectroscopic techniques. Practically, to study electrochemical Li_2CO_3 detection, a chemical probe that is soluble and stable in the electrolyte could react chemically with any $^1O_2$ that may be generated, thus acting as an indirect $^1O_2$ detector.

A singlet oxygen probe for Li_2CO_3 detection must be stable to all cell components during charging. Additionally, as Li_2CO_3 oxidation occurs above 3.8 V vs. Li/Li^+, any chemical probe should ideally be stable to potentials above 4 V. 9,10-dimethylanthracene (DMA) has been previously shown to selectively form its endoperoxide form (DMA-O_2) when exposed to $^1O_2$ (Reaction 2.6) and is stable against superoxide and other reactive oxygen species, with both DMA and DMA-O_2 both electrochemically stable to above 4 V vs. Li/Li^+.[41]

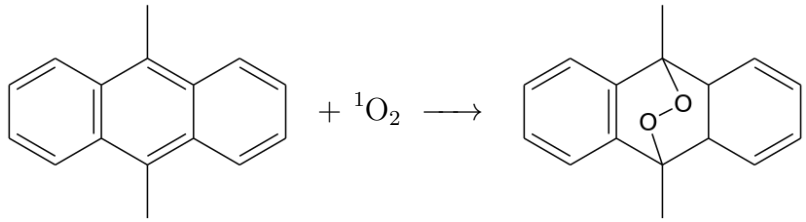

(2.6)

To understand the mechanism of Li_2CO_3 oxidation without the additional complication of a TMO lattice and minor CO_2 evolution from electrolyte carbonate oxidation, as well as to minimize any HF content, in collaboration with researchers at TU Graz we studied Li_2CO_3-packed electrodes with conductive carbon black and PTFE binder in TEGDME (tetraethylene glycol dimethyl ether) or DME (1,2-dimethoxyethane) electrolytes with LiTFSI as the salt. Additionally, to remove any gas evolution from reduction reactions at/with the Li anode, lithium iron phosphate ($LiFePO_4$, LFP) was used as the counter/reference electrode (3.45 V vs. Li/Li^+). Carbon and Li_2CO_3 were ball-milled together before mixing with PTFE to ensure good contact with and utilization of insulating Li_2CO_3.

To confirm that DMA is a suitable probe to study Li_2CO_3 electrochemical oxidation, a TEGDME electrolyte with 1 M LiTFSI and 30 mM DMA was exposed separately to Li_2CO_3, O_2, CO_2, and Li_2O_2, as well as Li_2O_2 with CO_2. DMA-O_2 was not detected in any of these cases, showing its selectivity for $^1O_2$ and suitability to study Li_2CO_3 oxidation. DMA and DMA-O_2 can be distinguished by HPLC (references in the bottom of Figure 2.9a)), which was also confirmed by ^{1}H-NMR.

With 30mM DMA in the DME electrolyte, the Li_2CO_3 cells were held at various potentials from 3.8–4.2 V (vs. Li/Li^+) until a charge capacity of 0.064 mAh was attained. The electrolyte was then extracted and subject to HPLC analyses to quantify the conversion of DMA to DMA-O_2 as in Reaction 2.6. These results are shown in Figure 2.9a). Starting

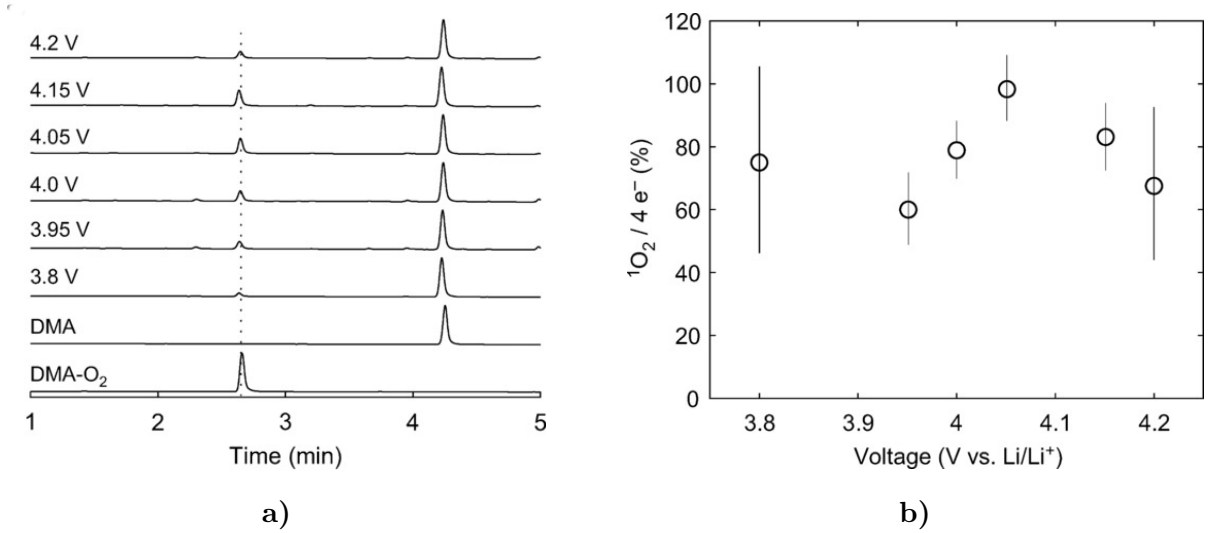

a) **b)**

Figure 2.9: Formation of DMA-O_2 from oxidation of Li_2CO_3 and quantification of $^1O_2$. **a)** Detection and distinction of DMA and DMA-O_2 controls and after extraction by HPLC at the listed voltage hold for cells with Li_2CO_3 packed electrodes [82 wt% carbon black, 9 wt% Li_2CO_3, 9 wt% polytetrafluoroethylene (PTFE)] in 1M LiTFSI DME with 30mM DMA. **b)** Total amount of inferred $^1O_2$ (from DMA-O_2, as quantified by integration of HPLC peaks) compared to the charge passed up to each voltage hold.

at 3.8 V vs. Li/Li^+, DMA-O_2 is observed by HPLC, with the DMA-O_2 peak growing in intensity until higher voltages, where DMA-O_2 begins to be unstable. As a control, identical cell configurations without Li_2CO_3 that were polarized similarly did not yield any quantifiable DMA-O_2.

To quantify the total $^1O_2$ produced at each voltage hold, the HPLC peaks for DMA and DMA-O_2 were integrated and compared to the charge capacity. According to Reaction 2.5, we expect 4 e^- per $^1O_2$. Plotted in Figure 2.9b) is the voltage hold versus percent of $^1O_2$ compared to the charge capacity. There is good agreement across all voltages that nearly theoretical amounts of $^1O_2$ were detected. The quantification of $^1O_2$ from this method is inevitably a lower bound estimate for several reasons: (i) not all $^1O_2$ will react with DMA to form DMA-O_2, (ii) the electrolyte cannot be completely extracted, and (iii) at higher voltages ($\approx$ 4.2 V) DMA-O_2 is unstable and will degrade. With these caveats in mind, we find Figure 2.9b) to be evidence that most, if not all of the "missing oxygen" is generated as $^1O_2$ and is thus not detected as molecular oxygen.

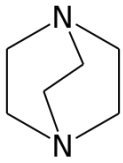

1,4-diazabicyclo[2.2.2]octane (DABCO).

$^1O_2$ can be quenched by a number of pathways. As molecular O_2 is not detected from Li_2CO_3, $^1O_2$ is likely quenched by detrimental reactions with cell components. We propose that if $^1O_2$ could be quenched to $^3O_2$ before reacting with cell components, then gaseous oxygen would be detected during electrochemical oxidation of Li_2CO_3 and these unknown side reactions would be prevented. Suitable quenchers that are stable at higher voltages are not known, but as a proof of concept we use 1,4-diazabicyclo[2.2.2]octane (DABCO, above), which has been previously used as a quencher in nonaqueous environments.[42] DABCO is anodically unstable above 3.9 V vs Li/Li^+, but with suitable excess DABCO, diffusion from the anode may provide enough fresh DABCO to show an effect.

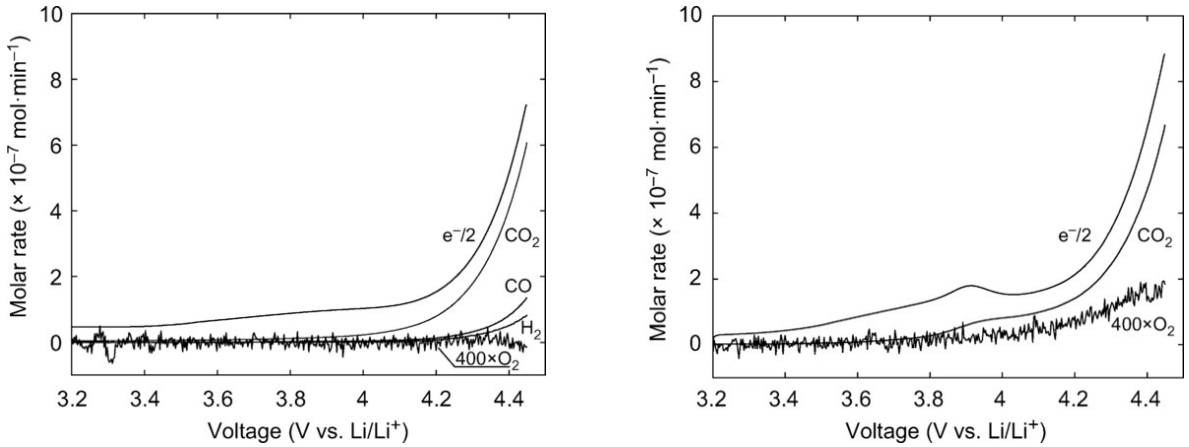

Figure 2.10: Rates of gas evolution from oxidation of Li_2CO_3 with and without DABCO. **a)** CO_2, CO, H_2, and O_2 evolution of Li_2CO_3 packed electrodes [82 wt% carbon black, 9 wt% Li_2CO_3, 9 wt% polytetrafluoroethylene (PTFE)] oxidatively scanned to 4.45 V vs. Li/Li^+ (1 V vs. $LiFePO_4$) in 1 M LiTFSI TEGDME with applied current. **b)** CO_2 and O_2 evolution of Li_2CO_3 packed electrodes [82 wt% carbon black, 9 wt% Li_2CO_3, 9 wt% polytetrafluoroethylene (PTFE)] in 1M LiTFSI TEGDME with 30 mM of the quencher DABCO oxidatively scanned to 4.45 V vs. Li/Li^+ (1 V vs. $LiFePO_4$) with applied current. Note that the peak at $\approx$ 3.9 V is due to DABCO decomposition. O_2 evolution is clearly evident in **b)** with the addition of DABCO compared to no detectable O_2 evolution with the electrolyte without DABCO in **a)**.

In Figure 2.10 we show the gas evolution from Li_2CO_3-packed electrodes in a 1 M LiTFSI TEGDME electrolyte without a) and with b) the addition of DABCO. a) shows that the majority of gas evolution is CO_2, starting at above 3.8 V and is consistent with a 2 e^-

process. CO and H_2 are also present at higher voltages, but no O_2 is detected. In b), with the addition of 30 mM DABCO, we see that CO_2 is still the dominant gas however there is now detectable O_2 evolved. Note that the anodic peak corresponds to DABCO oxidation. Although only a small part of the total $^1O_2$ is evolved as $^3O_2$, this shows that if a suitable $^1O_2$ quencher could be found, the detrimental effects of $^1O_2$ could be avoided and molecular oxygen would be evolved instead.

For oxidation of pure Li_2CO_3, our results with DMA as a $^1O_2$ trap show that up to stoichiometric amounts of $^1O_2$ are evolved as according to Reaction 2.5, which explains the absence of gas phase molecular oxygen detection in previous research. With an appropriate quencher the possible deleterious effects of singlet oxygen could be prevented by $^1O_2 \rightarrow {}^3O_2$. As Li_2CO_3 is a universal passivating agent on TMOs as Li-ion cathodes, it is a fundamental aspect in the interfacial reactivity in the operation of Li-ion batteries. The detection of $^1O_2$ thus strongly suggest that Li_2CO_3 formation, even at impurity levels, will have a deleterious affect on the stability of TMOs as Li-ion cathodes.

That said, the link between residual Li_2CO_3 on the surface of TMOs and the long-term stability/cyclability of TMOs is still not fully understood, though Li_2CO_3 and other lithium compounds have long been blamed for poor cycling performance.[40,43] This has implications for the two sources of surface Li_2CO_3: (i) growth of films due to inevitable aging of TMO surfaces after exposure to atmosphere, delithiating the TMO lattice,[30,44] and (ii) true residual Li_2CO_3 from unreacted Li precursors[29,45] (Li_2CO_3 as well as Li_2O/LiOH, which can react with atmospheric CO_2). It has been shown that with greater excess Li_2CO_3 used in synthesis, there is a larger amount of residual Li_2CO_3 on the surface of TMOs,[29,46] and with our results this implies greater rates of gas evolution, likely sustained over multiple cycles. This is particularly relevant for Ni-rich TMOs that necessarily use excess Li sources in synthesis to limit Ni/Li mixing.[36,47] Kim et al.[35] showed that after repeated washing/calcination cycles it was possible to remove a large portion of the native Li_2CO_3 from a Li-stoichiometric TMO, which displayed decreased gas evolution and improved cycling characteristics. With a similar conclusion, Bi et al.[40] chemically converted surface Li_2CO_3 to LiF on $LiNi_{0.8}Mn_{0.1}Co_{0.1}O_2$ and found an improvement in cycling performance in the LiF samples compared to the Li_2CO_3 samples. However, Li_2CO_3 has also been proposed to be a beneficial insulator that protects the TMO surface.[46] These prior observations combined with our results show that there is a need for further research to fully understand the effect of Li_2CO_3 on the surface of TMOs.

Important for this future work will be the study of the mechanism of Li_2CO_3 degradation on the surface of TMOs. Our results for pure Li_2CO_3 will guide future work, however the morphology of Li_2CO_3 on TMOs will inevitably be different than that of the ball-milled Li_2CO_3 in our studies. The distribution of Li_2CO_3 on TMOs may also change depending on the synthesis method and air exposure. In addition to morphology, another important future consideration may be defects. As proposed by theoretical calculations on Li_2CO_3, due to the insulating nature of Li_2CO_3 defects of either lithium vacancies (V'_{Li}) or lithium ion interstitials ($Li_i^{\bullet}$) will be the dominant charge carrier, depending on the voltage regime.[48] The ball-milled Li_2CO_3 likely induced additional defects that enhanced its conductivity, and thus

influenced its decomposition. From the typical synthesis procedures of TMOs, there is the possibility of additional site defects in Li_2CO_3 due to other metal impurities, as well as any defects at the Li_2CO_3-TMO interface. All of these possible differences between ball-milled Li_2CO_3 and Li_2CO_3 on TMO surfaces highlight the need for future detailed studies.

2.4 Conclusions

In summary, by combining quantitative analysis of the gaseous charge products of isotopically labeled TMOs with residual carbonate titration results, we have shown that for both Li-rich and Li-stoichiometric TMOs the overwhelming majority of CO and CO_2 evolution comes from oxidation of residual surface carbonate contaminants and does not originate from TMO-mediated electrolyte decomposition, up to 4.8 V vs. Li/Li^+. A surprising link between residual surface Li_2CO_3 and O_2 release from TMO surfaces questions our current understanding of the mechanism of Li_2CO_3 degradation and oxygen release from TMOs. A possible explanation for this was shown by using a singlet oxygen trap to show that the electrochemical oxidation of pure lithium carbonate generates singlet oxygen. This work has wide-reaching implications on our understanding of the stability of TMO surfaces and indicates a need for further quantitative study of the effect of surface Li_2CO_3 on the cycling performance of TMOs, as well as a need to develop strategies to remove/limit Li_2CO_3.

2.5 Acknowledgments

This work was supported by the Assistant Secretary for Energy Efficiency and Renewable Energy, Office of Vehicle Technologies of the U.S. Department of Energy under Contract No. DE-AC02-05CH11231, under the Advanced Battery Materials Research (BMR) Program. The author gratefully acknowledges support from the Department of Defense (DoD) through the National Defense Science & Engineering Graduate Fellowship (NDSEG) Program. We thank Umicore for receipt of the NMC powder.

3 | Quantification of surface oxygen depletion and solid carbonate evolution during the first cycle of $LiNi_{0.6}Mn_{0.2}Co_{0.2}O_2$

3.1 Abstract

By combining differential electrochemical mass spectrometry (DEMS) with titrations of electrochemically modified $LiNi_{0.6}Mn_{0.2}Co_{0.2}O_2$ (NMC622), we find that coinciding with the onset of CO_2 evolution above $\approx$ 3.9 V vs. Li/Li^+ anodic cut-off potentials are several phenomena: (i) degradation of the native surface Li_2CO_3, (ii) degradation of the electrolyte evolving CO_2, (iii) formation of a film of carbonate-like electrolyte degradation products on charge which are (iv) largely reduced and desorb on discharge, (v) near-surface oxygen charge compensation during charge, and (vi) irreversible formation of a transition metal-reduced, oxygen-depleted layer on the surface of NMC622 that persists after discharge. CO_2 stemming from electrolyte degradation and Li_2CO_3 decomposition begins to evolve above $\approx$ 3.9 V on charge, discharge, and rest, and results from a corrosion-like process involving the NMC622, which appears to be distinct from the process that evolves O_2. As measured using titrations that quantify surface peroxo-like character, the disordered surface layer that forms during cycling extends deeper into the oxide bulk than would be anticipated simply from the total O_2 evolved. The analyses reported in this chapter could be used to quantify the role of the electrolyte, surface contaminants, and transition metal oxide composition on outgassing, electrolyte decomposition, and transition metal oxide surface degradation.*

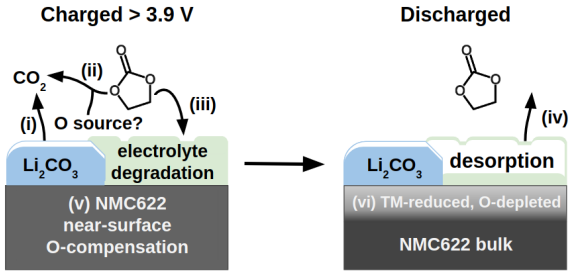

*This chapter largely adapted from previously published work in: S.E. Renfrew; B. D. McCloskey. *ACS Appl. Energy Mater.* **2019**, DOI: 10.1021/acsaem.9b00459.

3.2 Introduction

3.2.1 The benefits and challenges of Ni-rich transition metal oxides as cathode materials. Ni-rich stoichiometric transition metal oxides (TMOs) as next-generation cathodes for Li-ion batteries, though desirable for their high theoretical capacities, lower cost, and lower toxicity than their Co-rich counterparts, are limited in their practical use by performance degradation, leading to limited cycle life. Pure $LiNiO_2$ suffers most dramatically from irreversible bulk phase changes, however all Ni-rich compounds, typically with Ni content > 33 % of the total transition metal content, exhibit large first cycle irreversible capacity, disordered rocksalt surface layers, particle cracking, difficulty in synthesis, and particular sensitivity and reactivity to the atmosphere.[36,47,49–56]

The size similarity of Ni^{2+} and Li^{+} leads to Li/Ni site mixing in synthesis and strict controls are needed to optimize the stoichiometry and calcination temperature and time.[52] Additionally, increased site mixing and loss of the layered structure on the surface of Ni-rich materials has been observed after extended cycling[49,50,53,54,57–61] and even after only a single electrochemical cycle.[49,53,62–65] By closely examining the electronic structure, distinct redox behavior is observed for the bulk and the disordered surface, with the surface transition metals reduced compared to the bulk.[49] Relative to the bulk layered structure, this transition metal-reduced layer can equally be described as an oxygen-depleted layer, both referring generally to a rocksalt-like structure. Though the existence of the surface layer has been verified by many independent reports using electron energy loss spectroscopy (EELS), high-resolution transmission electron microscopy (HRTEM), and X-ray techniques, among others, the exact nature, origin, as well as the surface layers specific role in the performance degradation of Ni-rich materials are still debated. Although questions remain, it is theorized that the formation and reactivity of the surface layer is intimately tied to the identity of the electrolyte, leading to coupled TMO surface/electrolyte degradation with the formation of soluble and insoluble surface species and gaseous products.[49,57,58]

3.2.2 Monitoring outgassing as a technique to trace reactivity of Li-ion cathodes. To study these degradation mechanisms, gas analyses using differential/operando electrochemical mass spectrometry (DEMS/OEMS) has been employed to identify and quantify instabilities of Ni-rich materials during electrochemical cycling, showing a general trend of increased gas evolution (like CO_2 and O_2) compared to materials like $LiCoO_2$ and $LiMn_2O_4$.[15,19] The interpretation of outgassing of Ni-rich materials is complicated, however, by the uncertainty of their surface structures. Reactivity with the atmosphere, which will change the surface structure of the oxide and increase the surface lithium/nickel compounds, including hydroxides, bicarbonates, and carbonates, generally increases with Ni content. Additionally, as excess Li compounds are needed to synthesize phase-pure Ni-rich materials, increased unreacted Li precursors remain on the surface of Ni-rich oxides.[36,47] These surface compounds can increase the interfacial resistance and react with the electrolyte. In particular, with collaborators we have previously shown[42] in Chapter 2 that Li_2CO_3 can

decompose electrochemically, releasing singlet oxygen, $^1O_2$, and CO_2.

It has been proposed that Ni content in Ni-rich layered TMOs determines lattice instability and O_2 release, in turn controlling the magnitude of the CO_2 evolution.[11,15,66,67] Comparing available DEMS data of O_2 and CO_2 evolution from Ni-rich TMOs within and among different research groups, there is no simple O_2/CO_2 relationship that unifies the observations made, suggesting more complex relationships govern the outgassing. Nonetheless, it has been proposed that lattice O_2 is released in part as singlet oxygen, $^1O_2$, which has previously been shown to have a significantly negative effect on cell performance.[19,42,66] $^1O_2$ has been detected at high potentials in the first cycle for several Li-rich and Li-stoichiometric TMOs.[68] In the referenced study, however, the surface Li_2CO_3 present on these materials was not accounted for, and given that $^1O_2$ has been also detected from the electrochemical oxidation of Li_2CO_3,[42] the source of the $^1O_2$ is not clear. What remains further debated are the roles of the electrolyte (solvent, salt, and contaminants), the delithiated TMO, and any reactive oxygen on the mechanisms of Li_2CO_3 and carbonate electrolyte degradation. Particularly so, as a recent study found decomposition of surface Li_2CO_3 to CO_2 during cycling of $LiNi_{0.6}Mn_{0.2}Co_{0.2}O_2$ in an all-solid-state electrochemical cell.[67]

3.2.3 Prior results and the importance of Li_2CO_3 impurities. In our previous work[69] in Chapter 2 we employed isotopic labeling and DEMS to illustrate the similarities in gas evolution between Li-rich and Li-stoichiometric TMOs due to surface Li_2CO_3. Despite the starkly contrasting oxygen activities and oxygen release exhibited in these two classes of Li-ion cathodes, we found that the isotopic distributions of CO and CO_2 detected during the first charge was nearly identical for both. Furthermore, the magnitude of gas evolution for each material was largely determined by the magnitude of each materials surface Li_2CO_3, which we quantified using an acid titration that involved monitoring CO_2 evolution from TMOs immersed in aqueous H_2SO_4 ($\approx$ 1000:1 H_2SO_4 to Li_2CO_3). The Li,Mn-rich oxide ($Li_{1.2}Ni_{0.15}Co_{0.1}Mn_{0.55}O_2$, referred to here on as LMR) had approximately half the surface Li_2CO_3 as the Li-stoichiometric oxide ($LiNi_{0.6}Mn_{0.2}Co_{0.2}O_2$, referred to here on as NMC622) and, illustratively, the total CO_2 evolved for LMR during the first charge was approximately half that of NMC622 for the same applied current rate (0.1 Li^+ h^{-1}). When both samples were washed with H_2O to remove a portion of the native Li_2CO_3, a nearly concomitant reduction in CO_2 evolution was observed for both.

The LMR and NMC622 were labeled by exchanging the lattice and surface Li_2CO_3 oxygen with ^{18}O by heating under an $^{18}O_2$ headspace (see Appendix B). The isotopic enrichments of the lattices were confirmed by examining the O_2 evolution during charge [this has been confirmed valid for Li-rich materials by secondary ion mass spectrometry (SIMS)[20,21]]. For the determination of the ^{18}O enrichment of the Li_2CO_3 we used an acid titration method employing an excess of approximately 1000:1 H_2SO_4 to Li_2CO_3 to decompose Li_2CO_3 to quantifiable CO_2. By using both the total amount of CO_2 evolved as well as the distribution of ($C^{16,16}O_2$, $C^{16,18}O_2$, $C^{18,18}O_2$), we were able to predict the total amount of surface Li_2CO_3 per mass and the total ^{18}O-enrichment for both LMR and NMC, finding that the Li_2CO_3 on

both materials had an enrichment of about 10 % ^{18}O.

We found that the ^{18}O-enrichment of the evolved CO and CO_2 on the first charge matched that as predicted by the carbonate titration for both LMR and NMC, with the cumulative CO_2 evolved in the first charge and rest approximately equal to the total surface Li_2CO_3 for both materials. This observation held as well for the water-washed samples with reduced surface lithium carbonate. With these observations we concluded that the majority of the CO and CO_2 evolved stemmed from direct Li_2CO_3 oxidation and that the electrolyte degradation only marginally contributed to volatile products in the first charge. With our results, we stressed that surface contaminants should be more rigorously quantified and accounted for when studying cathode/electrolyte degradation mechanisms.

As a side note worthy of discussion at the beginning of this chapter, since publication of our original results a number of other researchers have studied the role of contaminants and surface defects in the performance of Li-stoichiometric materials.[51,52,66,67,70,71] Outgassing studies on NMC622 include using complementary isotopic techniques to distinguish Li_2CO_3 from the other cell components, including ^{13}C-labeled ethylene carbonate (EC) as the electrolyte[66] and growing ^{13}C-labeled Li_2CO_3 on the surface of NMC622.[67] Though these studies did indeed find that Li_2CO_3 contributed directly to a portion of the CO_2 outgassing, they questioned our conclusion that it was directly responsible for the majority of the CO and CO_2. With 1.5 M $LiPF_6$ ^{13}C-EC as the electrolyte, Jung et al. found that Li_2CO_3 accounted for directly $\approx$ 33 % of the CO_2 evolution in the first cycle (removing hydrolysis products) and none of the evolved CO.[66] Hatsukade et al. found that for 1 M $LiPF_6$ in EC/EMC (ethyl methyl carbonate) (3:7, w/w), the grown ^{13}C-labeled Li_2CO_3 accounted for $\approx$ 50 % of the direct CO_2 evolution on the first cycle and none of the evolved CO (in other words, no ^{13}CO was detected).[67] Searching for the discrepancy between our results with those of references [66] and [67], we found that our original carbonate titration method, though it accurately predicted the amount of Li_2CO_3, did not accurately predict the ^{18}O-enrichment of Li_2CO_3. For an extensive discussion see Appendix C, however, in short we found that 1000:1 H_2SO_4 to Li_2CO_3 was not sufficient excess acid for the titration, and an isotope exchange during the titration resulted in systematically underpredicting the total ^{18}O-enrichment of the surface Li_2CO_3. With an improvement to our titration method, namely an increase in H_2SO_4 concentration, we find now that the ^{18}O-enrichment of the CO_2 evolved during delithiation of the NMC622 is about half of that of the native Li_2CO_3 ^{18}O-enrichment, as is described later in this article. The significant increase in the proportion of ^{16}O isotopes in the evolved CO_2 compared to Li_2CO_3 implies that another source of C-^{16}O bonds must participate in the CO_2 evolution reaction. As all other sources have been excluded by previous studies,[11] the CO_2 evolved must in part originate from the electrolyte. We must revise our original interpretation of Chapter 2, which now becomes inline with observations from other groups using complementary isotopic labeling techniques, and conclude that direct Li_2CO_3 degradation accounts for 33–50 % of the CO_2 evolution in the first cycle, depending on the electrolyte/NMC622 contaminants and applied current rate. As the total CO evolved is typically only $\approx$ 1/5 the total CO_2 evolved and always follows a similar profile to CO_2 evolution, we do not focus on or report it in this chapter, but combining our results with those of references [66] and [67] we can conclude that the CO carbon must originate from

the electrolyte and the oxygen must come in part from the NMC622 particle—be it from the lattice, surface defects, and/or surface contaminants.

With this in mind, while the mechanisms of electrolyte and Li_2CO_3 degradation remain debated, more generally lacking are clear connections of gas-evolving electrolyte and surface contaminant degradation reactions to the detrimental effects on cell performance and to established observations from microscopic/spectroscopic techniques. A reduced surface layer, where the transition metal oxidation states are reduced compared to the bulk, has been observed in many studies on Ni-rich TMOs. This oxygen-depleted layer is theorized to form from reaction with the electrolyte,[58] which may produce detectable volatile products and cause a build-up of electrolyte degradation products on the surface of Ni-rich TMOs. Although this surface layer and the electrolyte degradation products have been blamed for poor cyclability, others have found that the extent of the surface layer is limited and can be relithiated on discharge, and instead blame particle cracking or other electrolyte processes for the bulk of the performance degradation observed at high voltages.,[50,59,60] Our goal is then to understand the evolution of the NMC622 surface, as determined by outgassing from the degradation of the native Li_2CO_3, the NMC622 surface, and the electrolyte.

As we will detail in the rest of this chapter, by combining DEMS with titrations of electrochemically modified isotopically-labeled NMC622, we find that the irreversible formation of the reduced surface layer coincides with the onset of CO_2 evolution above ≈ 3.9 V. At this same onset potential, we also detect the degradation of the native surface Li_2CO_3 and the carbonate electrolyte, as well as the formation of carbonate-like electrolyte degradation products which, however, are largely reduced and desorb from the NMC622 surface during discharge. We find that the electrolyte and Li_2CO_3 degradation evolves CO_2 via a similar mechanism involving the delithiated NMC622 that is distinct from O_2 evolution. By comparing ^{18}O-enrichment we also conclude that the reconstruction layer extends deeper into the oxide bulk than would be anticipated from the O_2 evolved during cycling alone. In other words, the ^{18}O-enrichment of the oxygen-depleted layer is lower than that of the O_2 evolved during cycling. Isotopic labeling also implies that O_2 evolved from the NMC622 lattice is spatially correlated to the surface contaminant, Li_2CO_3. A limited number of comparisons are made in this chapter, but we report here analyses that could be used to quantify outgassing differences between Li-ion cells of differing composition, as well as to quantify solid deposited carbonates and the depleted oxygen layer that may form during cell cycling of high energy Li-ion cathode materials.

3.3 Results and Discussion

3.3.1 The evolution of the NMC622 surface during the first cycle. To understand the evolution of the NMC622 surface that occurs in the first cycle, ^{18}O-NMC622/Li cells with 1 M $LiPF_6$ EC/DEC (diethyl carbonate) (1:1, v/v, see Appendix D) were charged on the DEMS (see Appendix A) to anodic cut-off voltages of 3.9, 4.2, 4.4, 4.65, and 4.8

V; discharged to 2.8 V without rest between the charge and discharge steps; and then the cathodes were extracted and acid titrated. Briefly, the acid titration infers the amount of surface carbonate by quantifying the total CO_2 (and other gases) evolved after exposing the extracted cathode to 10 M H_2SO_4; for full details of the acid titration method see Appendix C. All cells tested, regardless of anodic cut-off potential, exhibited irreversible capacity losses of 0.11 ± .01 Li units on the first cycle, leading to a final assumed average formula of $Li_{0.89}Ni_{0.6}Mn_{0.2}Co_{0.2}O_2$. ^{18}O-labeled NMC622 was prepared by heating to 800 °C under an $^{18}O_2$ atmosphere as described in Appendix B. Using the carbonate titration we found the ^{18}O-NMC622 surface to have 28.5 ± 1.7 µmol Li_2CO_3 per g ^{18}O-NMC622 (0.21 ± 0.01 wt%) with an ^{18}O-enrichment of 20.6 ± 0.2 %. The distribution of ($C^{16,16}O_2$, $C^{16,18}O_2$, $C^{18,18}O_2$) as detected by the carbonate titration is given in the first row of Table 3.1 and was found to be well-described by a binomial distribution, implying that at 800 °C the ^{18}O uniformly enriches the Li_2CO_3 surface layer.

Gas evolution during the first cycle of a NMC622 electrode. Figure 3.1a) summarizes the gas evolution behavior seen in the cell charged to 4.8 V and immediately discharged to 2.8 V, and 1b) shows a representative voltage profile. Beginning at ≈ 3.9 V, CO_2 begins to evolve, increasing in rate with potential. At ≈ 4.45 V, O_2 is released from the NMC622 lattice. As indicated by the stars in Figure 3.1b), we cycled cells to before the onset of any gases (3.9 V), after the onset of CO_2 but before the onset of O_2 (4.2 and 4.4 V), and after the onset of O_2 evolution (4.65 and 4.8 V). The gases evolved during discharge are shown with open markers. There is hysteresis in O_2 evolution between charge and discharge while CO_2 evolution exhibits a symmetric profile with capacity. The CO_2 evolution exhibits a single peak with a maximum at the top of charge while the O_2 shows two distinguishable peaks: one on charge and a smaller on discharge, which is consistent with O_2 loss due to a phase transition at high states of delithiation. The second O_2 peak on discharge can be seen more clearly when data from Figure 3.1 are replotted as a function of time, as given in Figure 3.2, with the O_2 evolved on discharged highlighted in gray.

We will start by discussing first the results for the 4.8 V anodic cut-off potential. The cumulative gases evolved for the 4.8–2.8 V cycle are given in Table 3.1. The total CO_2 evolved is 25.0 µmol g^{-1}, less than the total Li_2CO_3 initially present but with an ^{18}O-enrichment of 9.3 %, less than half of that compared to the Li_2CO_3 enrichment of 20.6 %. As seen in the distribution given rows 8–10 of Table 3.1, the evolved O_2 during the first cycle has a comparable oxygen isotope distribution to the surface Li_2CO_3, which indicates that the source of the evolved O_2 is limited to the outermost surface, spatially where the surface Li_2CO_3 is located. Additionally, in Table 3.1 the evolved O_2 is split into that from charge and that evolved on discharge (as highlighted by gray in Figure 3.2). As the O_2 evolved on discharge has a nearly identical ^{18}O distribution to that on charge, this suggests that this oxygen on discharge originates from the ^{18}O-NMC622 directly and not from another source.

To interpret the CO_2 evolution and its isotopic distribution, we must be able to decouple direct Li_2CO_3 oxidation from the rest of the CO_2 evolution. If we assume a portion of the carbonate electrolyte degradation is initiated by some reactive oxygen species, we can

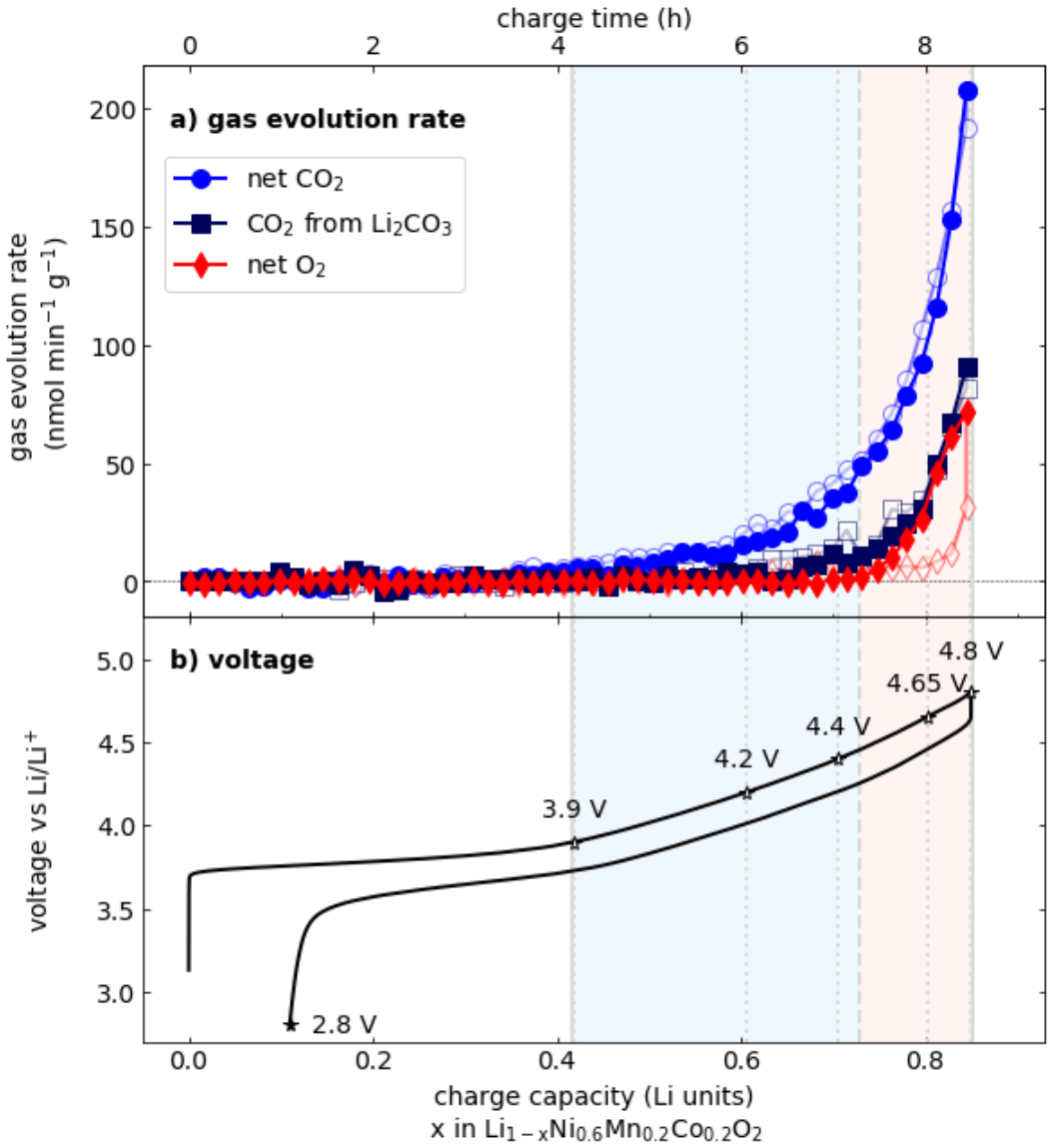

Figure 3.1: CO_2 and O_2 evolution rates and voltage profile for the first cycle of ^{18}O-NMC622. ^{18}O-NMC622 with 1 M $LiPF_6$ in EC/DEC (1:1, v/v) charged at a rate of 0.1 Li^+ h^{-1} (27.65 mA g^{-1}) to 4.8 V and immediately discharged to 2.8 V. a) Closed markers indicate gas evolution on charge and open markers indicate gas evolution on discharge. The blue shaded region indicates the region where only CO and CO_2 evolution is observed on charge and the red shaded region indicates the region where O_2 evolution is also observed. b) Starred voltages on the charge profile indicate all anodic cut-off voltages tested in this chapter.

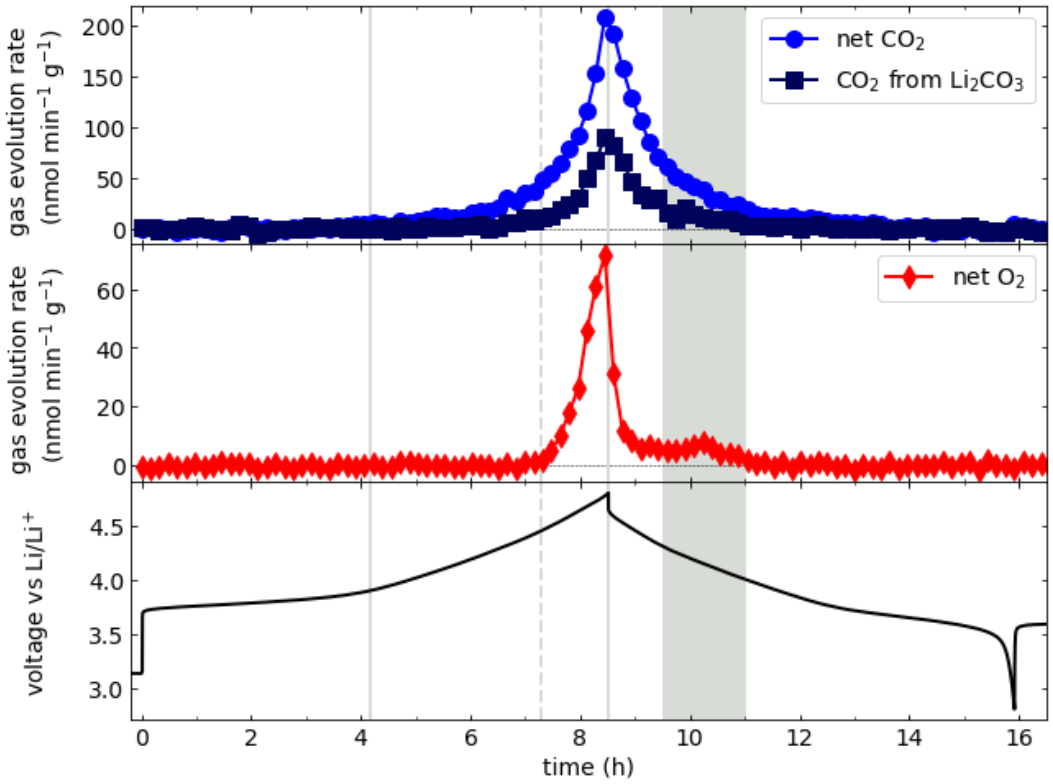

Figure 3.2: CO_2 and O_2 evolution rates vs. time for the first cycle of ^{18}O-NMC622. These data are the same as those used for Figure 3.1, but plotted as a function of time rather than extent of delithiation to further highlight differences in O_2 and CO_2 outgassing profiles.

speculate on the nature of its CO_2 products with the electrolyte. Writing a generic reactive oxygen species which originates from the ^{18}O-NMC622 particle, including from lattice, surface defect, or impurity, as $^*O_2$, we can consider possible mechanisms for its reaction with the natural abundance carbonate electrolytes. As conductive carbon is not involved in this reaction,[11,27] we make the assumption that no, or at least a negligibly small fraction of, CO_2 will be evolved as C^*O_2, as it would be highly unusual for carbon atoms in electrolyte molecules to dissociate from all bonds (e.g., C-H and C-O bonds) within the molecule and reassociate only with the $^*O_2$. This is supported by Li-O_2 isotopic studies with carbonate electrolytes,[38] as well as with proposed mechanisms.[72] As the only possible source of ^{18}O beyond natural abundance in the system is from the ^{18}O-NMC622 particle—be it from the lattice, surface defects, and/or surface contaminants—if little to no C^*O_2 is evolved this implies that effectively no $C^{18,18}O_2$ is evolved from electrolyte degradation involving ^{18}O-NMC622-originating reactive oxygen. This allows us to then make the assumption that the vast majority of $C^{18,18}O_2$ evolved is due to direct Li_2CO_3 oxidation, which further allows us to infer the flow rates of $C^{16,16}O_2$ and $C^{16,18}O_2$ due to direct Li_2CO_3 oxidation using the distribution predicted by the carbonate titration. As discussed earlier, the ^{18}O is taken to be uniformly distributed in the surface Li_2CO_3.

^{18}O-NMC622 4.8–2.8 V	Distribution (%)			^{18}O (%)	µmol g^{-1}
	$C^{16,16}O_2$	$C^{16,18}O_2$	$C^{18,18}O_2$		
initial native Li_2CO_3	*63.2 ± 0.3*	*32.4 ± 0.3*	*4.4 ± 0.1*	*20.6 ± 0.2*	*28.5 ± 1.7*
Total CO_2 evolved	82.9 ± 0.2	15.6 ± 0.2	1.5 ± 0.1	9.3 ± 0.1	25.0 ± 0.2
from Li_2CO_3	63.2 ± 0.3	32.4 ± 0.3	4.4 ± 0.1	20.6 ± 0.2	8.3 ± 0.3
from electrolyte	92.7 ± 0.4	7.3 ± 0.4	n/a	3.7 ± 0.2	16.7 ± 0.4
Post-cycle titration CO_2	67.2 ± 0.2	28.9 ± 0.2	3.9 ± 0.1	18.3 ± 0.2	22.8 ± 0.2
from Li_2CO_3	63.2 ± 0.3	32.4 ± 0.3	4.4 ± 0.1	20.6 ± 0.2	20.3 ± 0.6
from electrolyte	100 ± 0.6	0.0 ± 0.6	n/a	0.0 ± 0.3	2.5 ± 0.6
	$^{16,16}O_2$	$^{16,18}O_2$	$^{18,18}O_2$	^{18}O (%)	µmol g^{-1}
Total O_2 evolved	63.5 ± 0.4	32.2 ± 0.3	4.3 ± 0.2	20.4 ± 0.3	3.8 ± 0.1
from charge	63.2	32.4	4.4	20.6	3.2
from discharge	64.7	31.3	3.9	19.6	0.5
Post-cycle titration O_2	69.9 ± 0.3	27.1 ± 0.2	3.0 ± 0.2	16.6 ± 0.3	8.5 ± 0.1

Table 3.1: CO_2 and O_2 evolution and isotopic distribution from DEMS and post-cycle titration for ^{18}O-NMC622. The data presented correspond to Figures 3.1 and 3.2.

Using $C^{18,18}O_2$ as a marker for direct Li_2CO_3 oxidation, we can perform a calculation based on this assumption and split the evolved CO_2 into two components: (i) that stemming from direct Li_2CO_3 oxidation and (ii) the remaining CO_2 involving degradation of the carbonate electrolytes. As given in the 3rd and 4th rows of Table 3.1, we find that of the total 25 µmol g^{-1} of CO_2 evolved, 8.3 µmol g^{-1} is from direct Li_2CO_3 degradation ($\approx$ 33 %) and the remaining 16.7 µmol g^{-1} ($\approx$ 66 %) stems from electrolyte degradation. Using this principle, the inferred rate of direct Li_2CO_3 degradation is also plotted in Figure 3.1. Based on these results, we predict that 20.2 ± 1.7 µmol g^{-1} Li_2CO_3 remains on the surface of the ^{18}O-NMC622 after the first full delithiation-lithiation 4.8–2.8 V cycle.

Solid carbonate deposition and oxygen depletion on NMC622 electrode surfaces after the first charge-discharge cycle. We extracted the 4.8–2.8 V-cycled ^{18}O-NMC622 cathode after discharge and performed a carbonate titration (for details of this procedure see Appendix C). As shown in the fifth row of Table 3.1, this titration gives 22.8 µmol g^{-1} carbonate species on the surface of the cycled ^{18}O-NMC622 with a similar, yet slightly ^{16}O-enriched oxygen isotope distribution compared to the pristine ^{18}O-NMC622 Li_2CO_3. Using the same reasoning as given earlier, we can split this total carbonate into a native Li_2CO_3 portion and a portion originating from electrolyte degradation, finding 20.3 µmol g^{-1} native Li_2CO_3 and 2.5 µmol g^{-1} originating from the electrolyte. Comparing 20.2 to 20.3 µmol g^{-1}, we find good agreement between the remaining surface Li_2CO_3 as predicted from decoupling the CO_2 evolution, as described in the prior paragraph, and from direct measurement of Li_2CO_3 remaining on the cycled cathode, and we also find a small amount

^{18}O-NMC622 x–2.8 V	Distribution (%)			^{18}O (%)	µmol g^{-1}
	$C^{16,16}O_2$	$C^{16,18}O_2$	$C^{18,18}O_2$		
initial native Li_2CO_3	*63.2 ± 0.3*	*32.4 ± 0.3*	*4.4 ± 0.1*	*20.6 ± 0.2*	*28.5 ± 1.7*
4.65 V: CO_2	83.8 ± 0.3	14.9 ± 0.2	1.3 ± 0.1	8.8 ± 0.1	8.4 ± 0.1
from Li_2CO_3	63.2 ± 0.3	32.4 ± 0.3	4.4 ± 0.1	20.6 ± 0.2	2.6 ± 0.1
from electrolyte	92.8 ± 0.4	7.2 ± 0.4	n/a	3.6 ± 0.2	5.8 ± 0.2
Post-cycle titration CO_2	65.0 ± 0.1	30.8 ± 0.1	4.2 ± 0.1	19.6 ± 0.1	25.4 ± 0.1
4.4 V: CO_2	86.3 ± 0.4	12.8 ± 0.4	0.9 ± 0.1	7.3 ± 0.2	4.2 ± 0.1
from Li_2CO_3	63.2 ± 0.3	32.4 ± 0.3	4.4 ± 0.1	20.6 ± 0.2	0.9 ± 0.1
from electrolyte	92.2 ± 0.4	7.8 ± 0.4	n/a	3.9 ± 0.2	3.3 ± 0.2
Post-cycle titration CO_2	64.6 ± 0.1	31.2 ± 0.1	4.2 ± 0.1	19.8 ± 0.1	27.2 ± 0.1
4.2 V: CO_2	86.8 ± 1.2	13.2 ± 1.2	below detection	6.6 ± 0.6	1.4 ± 0.1
Post-cycle titration CO_2	64.2 ± 0.1	31.7 ± 0.1	4.1 ± 0.1	20.0 ± 0.1	28.8 ± 0.1
3.9 V: no gas detected	n/a	n/a	n/a	n/a	0
Post-cycle titration CO_2	63.6 ± 0.1	32.3 ± 0.1	4.1 ± 0.1	20.3 ± 0.1	28.8 ± 0.1

Table 3.2: CO_2 evolution and isotopic distribution from DEMS and post-cycle titrations for ^{18}O-NMC622 charged to the listed anodic cut-off potentials and discharged to 2.8 V.

of electrolyte decomposition products that remain on the surface after the first cycle, which may be inevitable as adsorbed/chemisorbed species on nearly fully lithiated NMC622.[73,74] We performed gas analysis and post-cycle titrations for the other anodic cut-off potentials of 3.9, 4.2, 4.4, and 4.65 V. This near agreement between the decrease in the surface Li_2CO_3 as predicted by the gas evolution analysis and that observed by the post-cycle titration data is observed for all cut-off potentials tested for the first cycle of ^{18}O-NMC622; this is tabulated for the anodic cut-off potentials of 3.9, 4.2, 4.4, and 4.65 V in Table 3.2.

As listed in the final row of Table 3.1, in addition to CO_2, 8.5 µmol g^{-1} O_2 is evolved during the titration of the 4.8–2.8 V-cycled ^{18}O-NMC622. No O_2 is evolved during the titration of pristine ^{18}O-NMC622 powder, implying that it does not originate from Li_2CO_3 or fully lithiated pristine NMC622; however, for full cycles to every anodic cut-off potential $\geq$ 4.2 V and discharged back to 2.8 V, molecular O_2 with a large ^{18}O-enrichment of $\approx$ 14–18 % was evolved during the titration of extracted electrodes. This is tabulated for the remaining anodic cut-off potentials tested in Table 3.3. Though all anodic cut-off potentials exhibited the same degree of irreversible capacity, the extent of the O_2 evolved from the post-cycle titrations increased in magnitude with cut-off potentials. As molecular O_2 is observed from titrated cycled electrodes that are charged and then relithiated back to a composition of approximately $Li_{0.89}Ni_{0.6}Mn_{0.2}Co_{0.2}O_2$, we posit that the O_2 released in the titration is due to the decomposition of peroxo-like domains at the surface, in a similar fashion to O_2 release

^{18}O-NMC622 x–2.8 V	Distribution (%)			^{18}O (%)	µmol g^{-1}
	$^{16,16}O_2$	$^{16,18}O_2$	$^{18,18}O_2$		
4.65 V: O_2	62.9 ± 1.4	32.3 ± 1.2	4.8 ± 0.8	21.0 ± 1.0	0.8 ± 0.1
Post-cycle titration O_2	67.4 ± 0.3	28.8 ± 0.3	3.8 ± 0.3	18.2 ± 0.3	6.3 ± 0.1
4.4 V: no O_2 detected	n/a	n/a	n/a	n/a	0
Post-cycle titration O_2	67.6 ± 0.7	28.4 ± 0.7	4.0 ± 0.7	18.2 ± 0.7	2.7 ± 0.1
4.2 V: no O_2 detected	n/a	n/a	n/a	n/a	0
Post-cycle titration O_2	68.7 ± 2.1	31.3 ± 2.1	below detection	15.6 ± 1.1	0.6 ± 0.1
3.9 V: no gas detected	n/a	n/a	n/a	n/a	0
Post-cycle titration O_2	n/a	n/a	n/a	n/a	0

Table 3.3: O_2 evolution and isotopic distribution from DEMS and post-cycle titrations for ^{18}O-NMC622 charged to the listed anodic cut-off potentials and discharged to 2.8 V.

from pure lithium peroxide as below in Reaction 3.1:

$$Li_2O_2 + H_2O \longrightarrow 2\,LiOH + \frac{1}{2}\,O_2 \tag{3.1}$$

These domains likely originate from Li/Ni mixing and surface structural loss in part induced by metal vacancies that are relithiated on discharge. We believe this is a complementary quantitative measurement of the reduced surface/rocksalt disordered layer as observed more traditionally by microscopy and spectroscopy methods. To compare our measurement to others, it is necessary to convert the evolved O_2 to a depth of the ^{18}O-NMC622 particle surface.

To estimate the oxygen surface layer thickness, we first calculate a characteristic radius of the ^{18}O-NMC622 particles using the crystallographic density (4.78 g cm^{-3}), calculated from a unit cell volume of 101.0 $\mathring{A}^3$) and BET surface area of 0.3 m^2 g^{-1}.[50] Assuming spherical particles, the surface area S, characteristic particle radius r, and density ρ are related as below:

$$S = \frac{4\pi r^3}{\frac{4}{3}\pi r^3 \rho} = \frac{3}{r\rho}. \tag{3.2}$$

Using the stoichiometry given in Reaction 3.1, given n_i total moles of ^{18}O-NMC622 initially

present and n_{O_2} moles of molecular O_2 detected from the titration of the cycled electrode, the surface oxygen thickness, r_s, is then estimated by:

$$\frac{\frac{4}{3}\pi(r-r_s)^3}{\frac{4}{3}\pi r^3} = \frac{n_i - 2n_{O_2}}{n_i}, \tag{3.3}$$

which, after applying the relation in Equation 3.2, is rearranged to give:

$$r_s = r\left[1-\left(1-\frac{2n_{O_2}}{n_i}\right)^{\frac{1}{3}}\right] = \frac{3}{S\rho}\left[1-\left(1-\frac{2n_{O_2}}{n_i}\right)^{\frac{1}{3}}\right]. \tag{3.4}$$

Note that the oxygen detected in the titration of the cycled electrodes, and not the oxygen loss as detected by DEMS during the electrochemical cycle, was used in the estimation. The titration oxygen directly measures the remaining formed surface layer, while the O_2 lost in the electrochemical cycle could form/alter the surface layer.

That stated, the estimation in Equation 3.3 does not explicitly account for O_2 loss as seen during electrochemical testing of the ^{18}O-NMC622 in the total lattice oxygen nor the oxygen content of the impurity Li_2CO_3 phase, as if accounted for this would only negligibly change the estimation of the surface layer thickness in Equation 3.4. As the ^{18}O-enrichment process only enriches the total NMC622 oxygen by an upper bound of a few percent, this change in weight was ignored for this calculation.[69]

Using this estimation, we can calculate the depth of this oxygen-depleted layer formed by a single 4.8–2.8 V electrochemical cycle to be $\approx$ 1.1 nm. This estimate is reasonable given that a recent study on an identical batch of NMC622 used HRTEM to find a reduced surface layer of 2–3 nm after 100 cycles for both anodic cut-off potentials of 4.5 and 4.8 V.[50]

In the same report, an amorphous layer of alkyl and metal carbonate species of $\approx$ 4 nm in depth was found above the reduced oxygen/rocksalt layer only in the 4.8 V-100-cycled NMC622, with no consistent surface layer observable in the 4.5 and 4.2 V-100-cycled electrodes. As stated earlier, we did not observe significant decomposition products from the electrolyte for the 4.8–2.8 V-cycled titration. As shown in Appendix C.3.1, post-cycle titrations of dimethyl carbonate (DMC)-rinsed and unrinsed ^{18}O-NMC622 electrodes show that rinsing with DMC does not remove any carbonate-like decomposition products from cycled electrodes. Given that surface electrolyte decomposition products including organic and metal carbonates have been observed in addition to the reduced surface/rocksalt layer by a number of independent reports using, for example, XPS and Raman spectroscopy,[63,75,76] and that electrolyte-originating CO_2 was observed in the outgassing of ^{18}O-NMC622, it is surprising that nearly no (2.5 µmol g^{-1}, Table 3.1, line 7) carbonate-like solid electrolyte decomposition products were observed on the cathode surface after a full 4.8–2.8 V cycle.

3.3.2 The evolution of the NMC622 surface during the first charge and subsequent open circuit voltage. However, titrations on electrodes that are only charged, and not cycled, to various voltages indicated by stars in Figure 3.1a) indicate that solid carbonates originating from the electrolyte are in fact deposited on the electrode surface. To understand the evolution of the NMC622 surface that occurs in the first charge, identical ^{18}O-NMC622/Li cells as earlier were charged on the DEMS to cut-off voltages of 3.9, 4.2, 4.4, 4.65, and 4.8 V; allowed to rest for 4 hours; and then the cathodes were extracted and titrated. As before, we will begin by discussing the results for the 4.8 V anodic cut-off potential.

Gas evolution during a 4 h rest period following charge to various cutoff potentials. Before discussing these titration results, a few interesting observations can be gleaned from analyzing gas evolution during the 4 hour rest period, which is plotted in Figure 3.3 along with the associated voltage profile for the 4.8 V charge and subsequent 4 h open circuit voltage period. The gas evolution characteristics during charge are identical as previously stated for the cycled ^{18}O-NMC622: CO_2 evolution begins at $\approx$ 3.9 V and O_2 evolution begins at $\approx$ 4.45 V. However, the gas evolution during the rest period after charge is distinct; during rest the O_2 evolution decays rapidly while the CO_2 evolution—both from Li_2CO_3 and electrolyte-originating—is elevated during rest without an applied current. This is indicative of a corrosion or self-discharge-like reaction which occurs due to the high state of charge of the electrode. This behavior is consistent as well with the 4.8–2.8 V-cycled data presented in Figure 3.1, where the CO_2 evolution is symmetric about the state of charge during charge and discharge while O_2 exhibits hysteresis.

Similarly as before, we can split the total CO_2 evolution into Li_2CO_3 and electrolyte-originating components. The gas data for the 4.8 V-charged + 4h rest (called 4.8 V-charge in the text from here on out) electrode are presented in Table 3.4. Comparing the tabulated data, we see that more CO_2 (both electrolyte and Li_2CO_3) is evolved while less oxygen is released for the 4.8 V-charge compared to the 4.8–2.8 V-cycle. This gives further evidence that the oxygen release mechanism and the CO_2 evolution mechanisms are distinct. The ^{18}O-distribution of CO_2 and the relative ratios of direct Li_2CO_3 and electrolyte-originating CO_2 are similar but not identical to those seen in the 4.8–2.8 V-cycle presented earlier.

Solid carbonate deposition and oxygen depletion on NMC622 electrode surfaces after the first charge. Although the gases evolved are similar, the titration of a NMC622 electrode charged to 4.8 V is notably different than the 4.8–2.8 V-cycle titration. As seen in Table 3.4, instead of detecting a distribution predominantly like the remaining native ^{18}O-Li_2CO_3 as was seen in the 4.8–2.8 V-cycle titration, the carbonate-like species detected in the 4.8 V-charge titration are predominantly ^{16}O, indicating the deposition of a significant amount of electrolyte decomposition products. With a similar logic as presented earlier, splitting the detected carbonate into a Li_2CO_3 and electrolyte portion, we see that 45 µmol g^{-1} of electrolyte-based products, likely solid alkyl carbonates, are detected on the surface with only 1 % ^{18}O-enrichment. As these sorbed electrolyte degradation products are largely

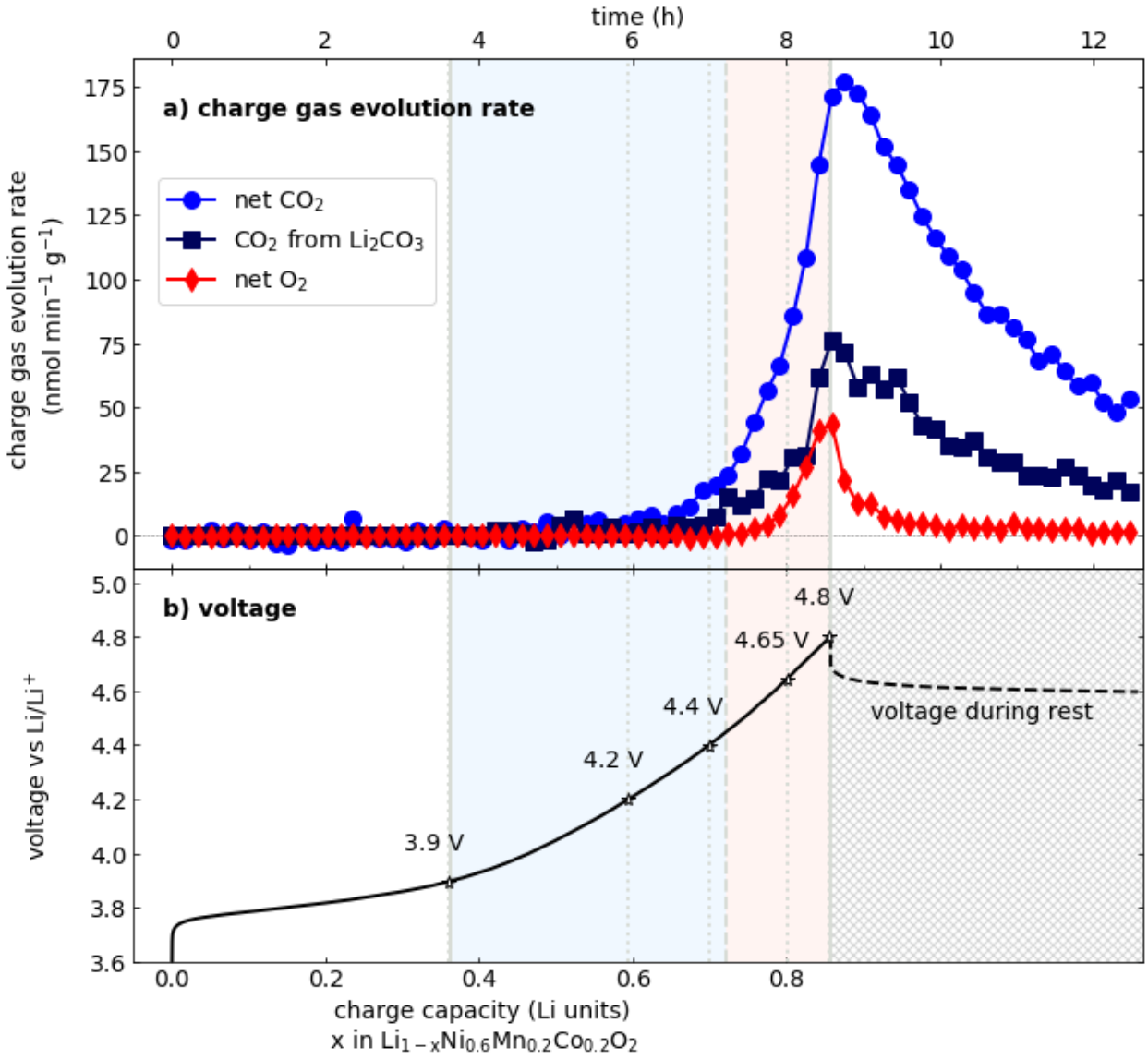

Figure 3.3: Rates of gas evolution and voltage profile for the first charge of ^{18}O-NMC622. ^{18}O-NMC622 with 1 M $LiPF_6$ in EC/DEC (1:1, v/v) charged at a rate of 0.1 Li^+ h^{-1} (27.65 mA g^{-1}) to 4.8 V and allowed to rest for 4 h. a) The blue shaded region indicates the region where only CO and CO_2 evolution is observed on charge and the red shaded region indicates the region where O_2 evolution is also observed. Note that CO_2 continues to evolve during the rest after charge, during which the open circuit voltage remains above 4.6 V. b) Starred voltages on the charge profile indicate all anodic cut-off voltages tested in this chapter.

^{18}O-NMC622 4.8 V + 4 h rest	Distribution (%)			^{18}O (%)	µmol g^{-1}
	$C^{16,16}O_2$	$C^{16,18}O_2$	$C^{18,18}O_2$		
initial native Li_2CO_3	*63.2 ± 0.3*	*32.4 ± 0.3*	*4.4 ± 0.1*	*20.6 ± 0.2*	*28.5 ± 1.7*
Total CO_2 evolved	81.9 ± 0.1	16.5 ± 0.1	1.6 ± 0.1	9.9 ± 0.1	31.5 ± 0.2
from Li_2CO_3	63.2 ± 0.3	32.4 ± 0.3	4.4 ± 0.1	20.6 ± 0.2	11.7 ± 0.3
from electrolyte	92.8 ± 0.3	7.2 ± 0.3	n/a	3.6 ± 0.1	19.7 ± 0.4
Post-cycle titration CO_2	94.3 ± 0.1	5.2 ± 0.1	0.5 ± 0.1	3.1 ± 0.1	49.9 ± 0.2
from Li_2CO_3	63.2 ± 0.3	32.4 ± 0.3	4.4 ± 0.1	20.6 ± 0.2	5.2 ± 0.5
from electrolyte	97.9 ± 0.6	2.1 ± 0.6	n/a	1.0 ± 0.3	44.7 ± 0.5
	$^{16,16}O_2$	$^{16,18}O_2$	$^{18,18}O_2$	^{18}O (%)	µmol g^{-1}
Total O_2 evolved	64.1 ± 0.4	31.8 ± 0.4	4.1 ± 0.3	20.0 ± 0.3	2.6 ± 0.1
Post-cycle titration O_2	87.3 ± 0.1	11.4 ± 0.1	1.3 ± 0.1	7.0 ± 0.1	21.6 ± 0.1

Table 3.4: CO_2 and O_2 evolution and isotopic distribution from DEMS and post-charge titration for ^{18}O-NMC622. The data presented correspond to Figure 3.3.

not detected after full and partial discharges to 4.0, 2.8, and 2.0 V (see Appendix C.3.2) and are not detected after extended rest before discharge (see Appendix C.3.3), we conclude that the electrolyte degradation products are desorbed by relithiation of ^{18}O-NMC622. As given by Table 3.5, this behavior is seen for all anodic cut-off potentials tested above 3.9 V.

Also notable is how little original Li_2CO_3 remains on the ^{18}O-NMC622 surface after charge to 4.8 V and rest. Based on the DEMS data it is expected that 16.8 µmol Li_2CO_3 g^{-1} would remain on the surface, yet by the post-charge titration only 5.2 µmol g^{-1} (Table 3.4 row 5) is detected. As seen in Table 3.5, this discrepancy is seen for all anodic cut-off potentials above 4.2 V, showing larger extents of "missing" Li_2CO_3 with higher cut-off potentials. As the Li_2CO_3 and electrolyte continue to react at open circuit after charge as a function of potential, they necessarily must continue to react during the time needed to transfer the charged ^{18}O-NMC622 electrodes to the glove box and may potentially even continue to react after rinsing with DMC to remove the entrained electrolyte. As shown Appendix C.3.1, rinsing a charged ^{18}O-NMC622 electrode slows this corrosion reaction while leaving the entrained electrolyte accelerates decomposition of the native surface Li_2CO_3 and deposition of solid electrolyte decomposition products.

The O_2 evolved from the titration of the 4.8 V-rest electrode is approximately three times that evolved from the 4.8–2.8 V-cycle electrode with a significantly lower ^{18}O-enrichment of 7 % compared to 14 %. The O_2 evolved from titrations of charged ^{18}O-NMC622 for all anodic cut-off potentials tested is given in Table 3.6 and shows an increase in amount of O_2 and ^{16}O-content as the anodic cut-off potential increases. The O_2 released on the titration of charged electrodes likely follows a similar reaction as cycled electrodes as given earlier in Reaction 3.1. We posit that this O_2 released during the titration of charged electrodes

^{18}O-NMC622 x + 4 h rest	Distribution (%)			^{18}O (%)	µmol g^{-1}
	$C^{16,16}O_2$	$C^{16,18}O_2$	$C^{18,18}O_2$		
initial native Li_2CO_3	*63.2 ± 0.3*	*32.4 ± 0.3*	*4.4 ± 0.1*	*20.6 ± 0.2*	*28.5 ± 1.7*
4.65 V: CO_2	81.6 ± 0.2	16.9 ± 0.2	1.5 ± 0.1	9.9 ± 0.1	12.4 ± 0.1
from Li_2CO_3	63.2 ± 0.3	32.4 ± 0.3	4.4 ± 0.1	20.6 ± 0.2	4.3 ± 0.2
from electrolyte	91.4 ± 0.3	8.6 ± 0.3	n/a	4.3 ± 0.2	8.0 ± 0.2
Post-cycle titration CO_2	86.9 ± 0.1	11.7 ± 0.1	1.4 ± 0.1	7.2 ± 0.1	43.3 ± 0.2
from Li_2CO_3	63.2 ± 0.3	32.4 ± 0.3	4.4 ± 0.1	20.6 ± 0.2	13.5 ± 0.5
from electrolyte	97.7 ± 0.6	2.3 ± 0.6	n/a	1.1 ± 0.3	29.8 ± 0.5
4.4 V: CO_2	85.7 ± 0.4	13.4 ± 0.3	0.9 ± 0.1	7.6 ± 0.2	5.4 ± 0.1
from Li_2CO_3	63.2 ± 0.3	32.4 ± 0.3	4.4 ± 0.1	20.6 ± 0.2	1.1 ± 0.1
from electrolyte	92.4 ± 0.3	7.6 ± 0.3	n/a	3.8 ± 0.2	4.3 ± 0.2
Post-cycle titration CO_2	77.5 ± 0.1	20.1 ± 0.1	2.4 ± 0.1	12.5 ± 0.1	39.8 ± 0.1
from Li_2CO_3	63.2 ± 0.3	32.4 ± 0.3	4.4 ± 0.1	20.6 ± 0.2	21.9 ± 0.6
from electrolyte	94.9 ± 1.0	5.1 ± 1.0	n/a	2.5 ± 0.5	17.9 ± 0.6
4.2 V: CO_2	87.1 ± 0.5	12.4 ± 0.5	0.5 ± 0.1	6.7 ± 0.3	4.0 ± 0.1
from Li_2CO_3	63.2 ± 0.3	32.4 ± 0.3	4.4 ± 0.1	20.6 ± 0.2	0.4 ± 0.1
from electrolyte	89.9 ± 0.4	10.1 ± 0.4	n/a	5.1 ± 0.2	3.6 ± 0.1
Post-cycle titration CO_2	67.2 ± 0.1	28.9 ± 0.1	3.9 ± 0.1	18.3 ± 0.1	29.5 ± 0.2
from Li_2CO_3	63.2 ± 0.3	32.4 ± 0.3	4.4 ± 0.1	20.6 ± 0.2	26.3 ± 0.6
from electrolyte	99.6 ± 0.5	0.4 ± 0.5	n/a	0.2 ± 0.2	3.2 ± 0.5
3.9 V: no gas detected	n/a	n/a	n/a	n/a	0
Post-cycle titration CO_2	64.4 ± 0.1	31.5 ± 0.1	4.1 ± 0.1	19.8 ± 0.1	28.6 ± 0.1

Table 3.5: CO_2 evolution and isotopic distribution from DEMS and post-cycle titrations for ^{18}O-NMC622 charged to the listed anodic cut-off potentials and discharged to 2.8 V.

quantifies the lattice instability due to charge compensation seen for deintercalation of more than 0.6 Li. After relithiation the lattice stability is substantially recovered for the bulk but only partially recovered on the surface.

3.3.3 The effect of a 4.8 V potentiostatic hold In addition to the galvanostatic experiments described earlier we also charged and cycled ^{18}O-NMC622 with a 4.8 V potentiostatic hold instead of a higher anodic cut-off potential, allowing extraction of 0.94 Li without the inevitable direct electrolyte degradation above ≈ 5 V. Figure 3.4 shows the gas evolution and associated voltage and current profiles for the potentiostatic hold cycle experiment, highlighting the divergent behavior between CO_2 and O_2 evolution observed during the 4.8 V hold compared to the galvanostatic experiments.

^{18}O-NMC622 x + 4 h rest	Distribution (%)			^{18}O (%)	µmol g^{-1}
	$^{16,16}O_2$	$^{16,18}O_2$	$^{18,18}O_2$		
4.65 V: O_2	63.1 ± 1.3	32.6 ± 1.1	4.3 ± 0.7	20.6 ± 0.9	0.8 ± 0.1
Post-cycle titration O_2	70.4 ± 0.1	27.6 ± 0.1	2.0 ± 0.1	15.8 ± 0.1	12.9 ± 0.1
4.4 V: no O_2 detected	n/a	n/a	n/a	n/a	0
Post-cycle titration O_2	69.5 ± 0.5	30.5 ± 0.5	below detection	15.2 ± 0.3	3.1 ± 0.1
4.2 V: no O_2 detected	n/a	n/a	n/a	n/a	0
Post-cycle titration O_2	65.3 ± 1.0	34.7 ± 1.0	below detection	17.3 ± 0.5	1.5 ± 0.1
3.9 V: no O_2 detected	n/a	n/a	n/a	n/a	0
Post-cycle titration O_2	n/a	> 0	n/a	n/a	≈ 0

Table 3.6: O_2 evolution and isotopic distribution from DEMS and post-charge titrations for ^{18}O-NMC622 charged to the listed anodic cut-off potentials and allowed to rest for 4 h.

As before in the galvanostatic experiments presented earlier, CO_2 and O_2 evolution increases in rate with potential until the potentiostatic 4.8 V hold, during which CO_2 and O_2 exhibit diverging behaviors. As shown in panel a) of Figure 3.4 and zoomed in in panel b), the rate of O_2 evolution reaches a maximum at the end of the galvanostatic charge to 4.8 V, dropping during the potentiostatic hold as the current falls, as shown in panel c). Contrastingly, the rate of CO_2 evolution (net and that from Li_2CO_3) continues to rise during the beginning of the potentiostatic hold, doubling in rate from the start of the hold to the maximum rate of CO_2 evolution achieved $\approx$ 1 h during the hold, marked by the dashed vertical line.

As highlighted by the gray panel, there is a similar amount of O_2 released during discharge compared to the cycled data without potentiostatic holds as shown in Figure 3.2. This suggests that near the maximum O_2 possible is released during the potentiostatic hold and that there is a maximum amount of O_2 release possible before transport limitations/depletion. As shown in Table 3.7, note also that the isotopic distribution of the evolved O_2 during the potentiostatic holds is nearly identical to that evolved during the 4.65 and 4.8 V galvanostatic cycles. This indicates that the source of the evolved O_2 is limited to the outermost surface, spatially correlated to the surface Li_2CO_3.

Comparing the CO_2 evolution from the potentiostatic experiments shown in Table 3.8 to the galvanostatic ones given earlier in Tables 3.2 and 3.5, we see that the total CO_2 isotopic distribution as well as the isotopic distribution of the electrolyte-originating portion are comparable among all of the experiments, indicating that the corrosive process that decomposes the electrolyte/Li_2CO_3 does not change significantly with higher states of charge. The main difference between the potentiostatic and galvanostatic experiments is the relative magnitude of the total CO_2/O_2 evolved: there is $\approx$ 180 % more CO_2 and only $\approx$ 50 % more O_2 evolved in the hold experiment compared to the 4.8–2.8 V-cycle.

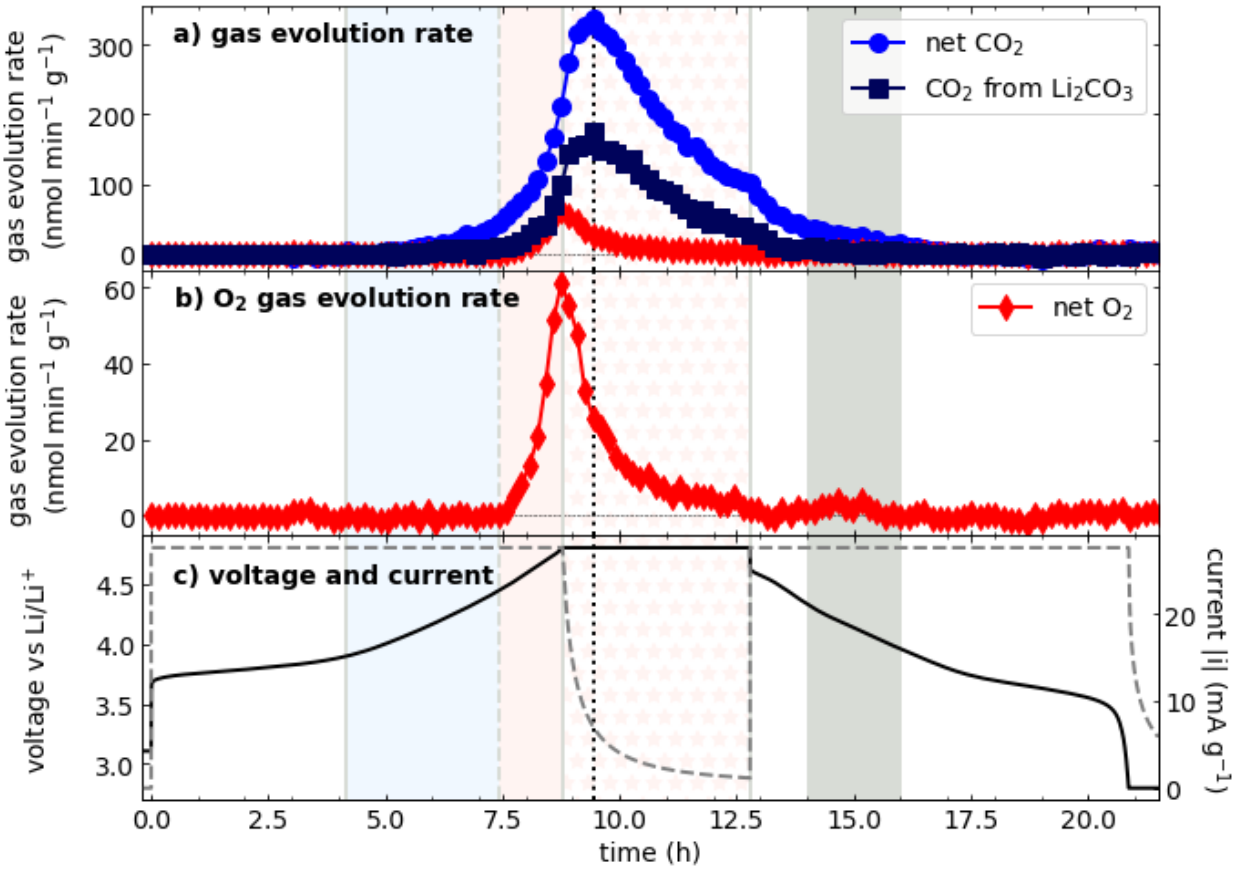

Figure 3.4: Gas evolution rates and corresponding current/voltage profiles for ^{18}O-NMC622 for an additional potentiostatic hold step at 4.8 V.

^{18}O-NMC622 with 1 M $LiPF_6$ in EC/DEC (1:1, v/v) charged at a rate of 0.1 Li^+ h^{-1} (27.65 mA g^{-1}) to 4.8 V, held at 4.8 V for 4 h, and discharged to 2.8 V. a) Total CO_2, CO_2 from Li_2CO_3 degradation, and O_2 evolution rates. The maximum in rate of CO_2 evolution is given by the dashed vertical black line, occurring about 1 h into the 4.8 V hold. The blue shaded region indicates the region where only CO and CO_2 evolution is observed on charge and the red shaded region indicates the region where O_2 evolution is also observed. b) Detail of O_2 evolution showing the decrease in rate during the 4.8 V hold. The maximum O_2 rate of evolution is observed at the end of the galvanostatic charge/beginning of the 4.8 V hold. The gray shaded region shows some O_2 evolution seen during discharge. c) The voltage profile is plotted in black and the absolute value of the current plotted in dashed gray.

What deviates from our predictions is the detected surface carbonate after the potentiostatic cycle. As discussed earlier, in the galvanostatic cycle experiments the remaining surface Li_2CO_3 detected by the titration was in good agreement with that predicted by the analyzing the CO_2 evolved. For the potentiostatic cycle experiment, from the CO_2 evolution we predict that almost all of the native surface Li_2CO_3 is decomposed during the cycle. However, from the post-cycle titration we detect $\approx$ 8 µmol g^{-1} of carbonate-like species with an ^{18}O-enrichment of 14 % on the ^{18}O-NMC622 surface. An explanation for this could be that

^{18}O-NMC622	Distribution (%)			^{18}O (%)	µmol g^{-1}
	$^{16,16}O_2$	$^{16,18}O_2$	$^{18,18}O_2$		
4.8 V hold cycle: O_2	64.9 ± 0.2	31.1 ± 0.2	3.9 ± 0.2	19.5 ± 0.2	5.6 ± 0.1
Post-cycle titration O_2	79.9 ± 0.2	19.2 ± 0.2	0.9 ± 0.1	10.5 ± 0.2	14.5 ± 0.1
4.8 V hold charge O_2	64.5 ± 0.3	31.2 ± 0.2	4.3 ± 0.2	19.6 ± 0.2	5.2 ± 0.1
Post-cycle titration O_2	87.8 ± 0.1	11.3 ± 0.1	0.9 ± 0.1	6.5 ± 0.1	54.0 ± 0.2

Table 3.7: O_2 evolution and isotopic distribution from DEMS and post-experiment titrations for ^{18}O-NMC622 charged to 4.8 V with a 4 h 4.8 V hold and also discharged to 2.8 V with a 4 h 2.8 V hold.

there is another mechanism that produces significant $C^{18,18}O_2$ such that $C^{18,18}O_2$ cannot be used as a "marker," as we have done, to determine ^{18}O-Li_2CO_3 decomposition. If this were the case, we would overestimate the total ^{18}O-Li_2CO_3 decomposed during cycling of ^{18}O-NMC622 and would then have extra ^{18}O-Li_2CO_3 left as detected by the post-cycle titration. As seen in Table 3.8, using the $C^{18,18}O_2$ evolved in the post-hold cycle titration as the marker for the pristine ^{18}O-Li_2CO_3 remaining on the electrode, we predict 1.6 µmol g^{-1} of the original ^{18}O-Li_2CO_3 left on the surface. This is the uncertainty of the actual mass loading of ^{18}O-Li_2CO_3 as predicted by our carbonate titration, so we do not believe that there is another significant source of $C^{18,18}O_2$ as evolved during cycling of ^{18}O-NMC622.

This leaves us with a few possible explanations for the anomalous carbonate species detected on the surface of ^{18}O-NMC622 after the potentiostatic cycle: i) the ^{18}O-enrichment of the surface Li_2CO_3 is not uniform enough to apply the technique used in this chapter to separate the Li_2CO_3 from the electrolyte decomposition, and that as the Li_2CO_3 is degraded the ^{18}O-enrichment changes enough to be significant; ii) there is buried Li_2CO_3 from unreacted precursors that is not as enriched as the original detectable surface Li_2CO_3, which may be initially electrochemically inactive and only exposed due to significant particle morphology changes/cracking induced by the harsh conditions of the potentiostatic experiment; and iii) there is a Li_2CO_3 or alkyl-carbonate-forming reaction, which occurs during the potentiostatic 4.8 V hold and not in the galvanostatic experiments, that must involve a majority of ^{18}O-NMC622 originating oxygen and a minority of electrolyte oxygen to produce the relatively high observed ^{18}O-enrichment of 14 %. Based on the limited experiments presented here we cannot make any conclusions on the origin of this carbonate and its deviation from the galvanostatic experiments, and further experiments are needed to narrow down the origin. That said, from a recent study on NCA ($LiNi_{0.8}Co_{0.15}Al_{0.05}O_2$), no significant reformation of carbonate species was observed from XPS analyses after 10 h potentiostatic holds at various potentials above 4.1 V.[77] As NCA exhibits similar behaviors of O_2 release and surface reconstruction like NMC622, this evidence makes explanation iii) less likely, though not impossible.

^{18}O-NMC622	Distribution (%)			^{18}O (%)	µmol g^{-1}
	$C^{16,16}O_2$	$C^{16,18}O_2$	$C^{18,18}O_2$		
initial native Li_2CO_3	*63.2 ± 0.3*	*32.4 ± 0.3*	*4.4 ± 0.1*	*20.6 ± 0.2*	*28.5 ± 1.7*
4.8 V hold cycle: CO_2	80.9 ± 0.1	17.3 ± 0.1	1.8 ± 0.1	10.4 ± 0.1	70.2 ± 0.3
from Li_2CO_3	63.2 ± 0.3	32.4 ± 0.3	4.4 ± 0.1	20.6 ± 0.2	28.6 ± 0.7
from electrolyte	93.0 ± 0.4	7.0 ± 0.4	n/a	3.5 ± 0.2	41.6 ± 0.8
Post-cycle titration CO_2	72.4 ± 0.4	26.7 ± 0.4	0.9 ± 0.3	14.2 ± 0.4	8.1 ± 0.1
from Li_2CO_3	63.2 ± 0.3	32.4 ± 0.3	4.4 ± 0.1	20.6 ± 0.2	1.6 ± 0.6
from electrolyte	74.8 ± 0.9	25.2 ± 0.9	n/a	12.6 ± 0.4	6.5 ± 0.5
4.8 V hold charge: CO_2	79.6 ± 0.1	18.5 ± 0.1	1.9 ± 0.1	11.2 ± 0.1	58.8 ± 0.3
from Li_2CO_3	63.2 ± 0.3	32.4 ± 0.3	4.4 ± 0.1	20.6 ± 0.2	25.9 ± 0.7
from electrolyte	92.4 ± 0.4	7.6 ± 0.4	n/a	3.8 ± 0.2	32.9 ± 0.7
Post-cycle titration CO_2	96.0 ± 0.1	3.8 ± 0.1	0.2 ± 0.1	2.1 ± 0.1	41.0 ± 0.2
from Li_2CO_3	63.2 ± 0.3	32.4 ± 0.3	4.4 ± 0.1	20.6 ± 0.2	2.1 ± 0.6
from electrolyte	97.7 ± 0.9	2.3 ± 0.9	n/a	1.1 ± 0.4	38.9 ± 0.6

Table 3.8: CO_2 evolution and isotopic distribution from DEMS and post-experiment titrations for ^{18}O-NMC622 charged to 4.8 V with a 4 h 4.8 V hold and also discharged to 2.8 V with a 4 h 2.8 V hold.

3.3.4 Reversible and irreversible changes to NMC622 throughout the first cycle. In this section we will combine the charged and cycled results for all anodic cut-off potentials tested and the 4.8 V potentiostatic hold experiments. In the 4.8–2.8 V cycle we observed that the measured ^{18}O-Li_2CO_3 remaining on the surface after the first cycle agreed well with the prediction made by decoupling the evolved carbon dioxide. In addition to the remaining initial ^{18}O-Li_2CO_3, a small amount of adsorbed/chemisorbed electrolyte was detected. The same behavior was observed for all anodic cut-off potentials with, of course, the lower cut-off potentials exhibiting less ^{18}O-Li_2CO_3 degradation. The formation of the peroxo-like surface character after the first cycle was observed for all anodic cut-off potentials 4.2 V, increasing in magnitude with cut-off potential. As ^{18}O-NMC622 does not evolve O_2 during cycling until above 4.45 V on the first charge, the formation of the reconstruction layer is then detected before O_2 release from delithiation.

In contrast to the 4.8–2.8 V cycled electrode, for the charged 4.8 V-charge electrode, we found that from the post-charge titration there was significant "missing" Li_2CO_3. This was observed for all charged electrodes with anodic cut-off potentials > 4.2 V. In addition, for all charged electrodes > 4.2 V, there was detectable deposition of electrolyte degradation products. Both of these phenomena—"missing" Li_2CO_3 and deposition of electrolyte degradation products—increased in extent with increasing anodic cut-off potential. These electrolyte degradation products are desorbed by the discharge process and were largely not detected on the equivalent electrodes that were discharged to 2.8 V. The O_2 detected from

the post-charge titrations indicates an instability of the lattice after delithiation of > 0.6 Li (> 4.2 V) and partial charge compensation from the oxygen. As the magnitude and ^{16}O-content of the released O_2 in the post-charge titrations increase with increasing charge cut-off potential, this indicates that the peroxo-like character extends deeper into the particle bulk with delithiation extent. That only a small degree of peroxo-like character is detected after discharge indicates that the lattice stability is substantially recovered after relithiation.

These phenomena will be further discussed and visualized in the following sections and figures. The evolution of the ^{18}O-NMC622 surface and associated gas evolution for all anodic cut-off potentials for charged and cycled electrodes is summarized in Figure 3.5. Figure 3.5a) shows the cumulative gas evolution for all cycles tested, notably showing a large amount of CO_2 evolved for the 4.8 V potentiostatic hold as plotted in Figure 3.4. Panels b) and c) of Figure 3.5 show the increase of the peroxo-like oxygen and carbonate-like surface layers after charge to the listed anodic cut-off potentials in open markers, the decrease of these during discharge shown by arrows, and the final values after discharge in closed markers. We propose that the arrows from charge to discharge signify the reversible near-surface oxygen redox or the recurring surface coverage/desorption of solid carbonates from the electrolyte. Irreversible processes include deposition of solid carbonates from electrolyte degradation during charge and anodic hold, as well as those changes that remain after relithiation: formation of the persisting oxygen-depleted surface layer, decomposition of the surface Li_2CO_3, and adsorption/chemisorption of a small amount of electrolyte.

Estimation of disordered, oxygen-depleted layer thickness on the NMC622 surface after the first cycle. Depth-dependent redox behavior has been observed in layered stoichiometric TMOs, with the bulk showing reversible TM and O (via hybridization) redox for $LiCoO_2$ and NMCs.[49,56,78,79] That we observe significant O_2 release in the post-charge titrations agrees with this notion of bulk reversible oxygen participation in stoichiometric TMOs for large degrees of delithiation. After relithiation, the growth of the surface reconstruction layer and increase in its ^{16}O-content with increased charge capacity (see Tables 3.3 and 3.7) is consistent with observations of extended Li/Ni disordered phases that reach deeper into the ^{18}O-NMC622 particle than the outermost surface.[60] As detailed earlier, using the estimation as given in Equation 3.4 the depth of the disordered, oxygen-depleted surface layer can be estimated from the total O_2 released during electrode acid titrations. This calculated disordered surface layer depth is shown in Figure 3.6 and shows significant growth after charge capacities of 0.6 Li units, reaching a maximum of $\approx$ 2 nm after extraction of 0.94 Li on the first charge. This defective disordered phase has been blamed as the source of particle cracking and thereby a catalyst for performance degradation. By noting that the O_2 release detected by DEMS during cycling has a similar ^{18}O-distribution to the native surface ^{18}O-Li_2CO_3, even for the 4.8 V hold (see Table 3.7), this indicates that the O_2 loss during cycling is limited to the outermost layer (spatially correlated to the contaminants) and that the larger surface reconstruction layer does not evolve molecular O_2 with the same mechanism. If this disordered layer also evolved O_2 at high degrees of delithiation it would be observable by a decreased ^{18}O-enrichment of the detected O_2 during cycling.

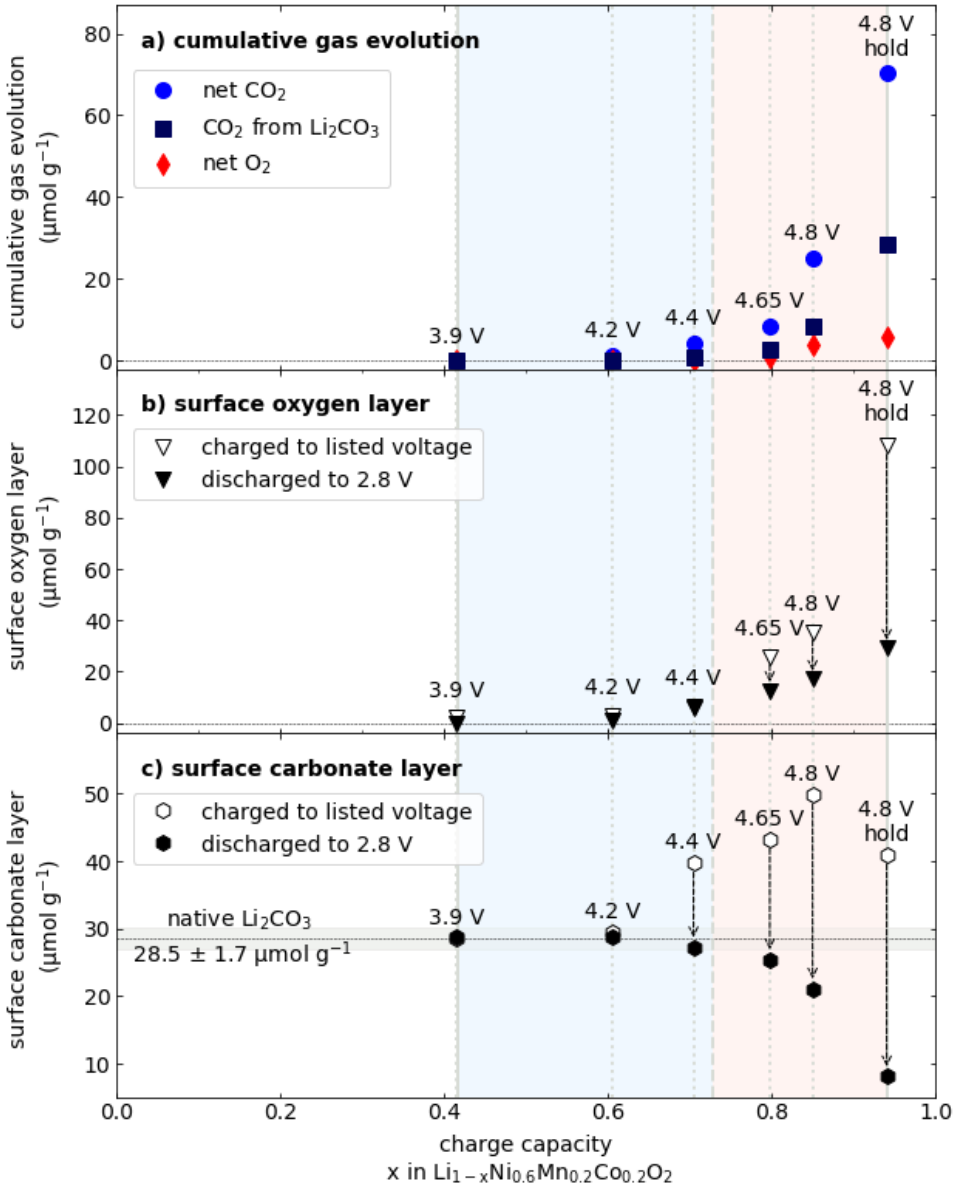

Figure 3.5: Cumulative gas evolution and evolution of the surface oxygen and surface carbonate layers for charged and discharged ^{18}O-NMC622.

Gas evolution and corresponding current/voltage profiles for ^{18}O-NMC622 for an additional potentiostatic hold step at 4.8 V. ^{18}O-NMC622 with 1 M $LiPF_6$ in EC/DEC (1:1, v/v) charged at a rate of 0.1 Li^+ h^{-1} (27.65 mA g^{-1}) and either allowed to rest for 4 h or discharged to 2.8 V. "4.8 V hold" indicates an additional potentiostatic 4 h hold at 4.8 V after the galvanostatic charge. a) Cumulative gas evolution for electrodes cycled to the anodic cut-off potentials listed. The blue shaded region indicates the region where only CO and CO_2 evolution is observed on charge and the red shaded region indicates the region where O_2 evolution is also observed. b) Change in the oxygen-depleted layer as detected by titrations. c) Change in the surface carbonate layer compared to the native Li_2CO_3.

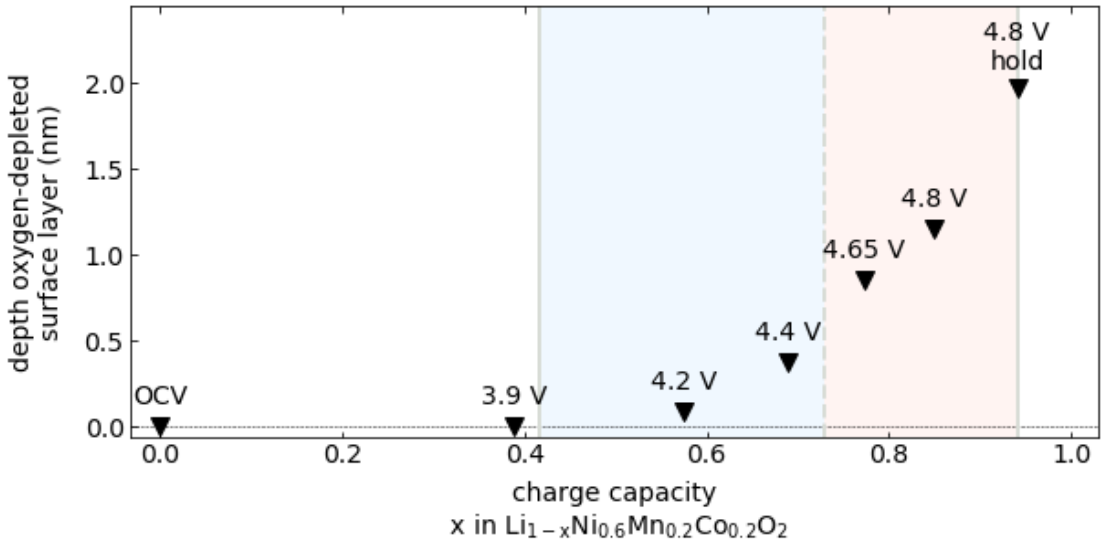

Figure 3.6: Calculated surface thickness after discharge to 2.8 V.

Labels above the points indicate the anodic cut-off potential except for "4.8 V hold," which indicates an additional potentiostatic 4 h hold at 4.8 V after the galvanostatic charge and "OCV," which indicates a pristine ^{18}O-NMC622 electrode. The blue shaded region indicates the region where only CO and CO_2 evolution is observed on charge and the red shaded region indicates the region where O_2 evolution is also observed. Note that the oxygen-depleted surface layer is detected before the onset of O_2 evolution during cycling. The surface thickness was calculated using Equation 3.4.

^{18}O-NMC622 x–2.8 V	charge capacity (Li units)	discharge capacity (Li units)	O_2 loss by DEMS (µmol g^{-1})	O_2 by titration (µmol g^{-1})	est. surface thickness (nm)
3.9 V	0.39	0.28	0	0	0
4.2 V	0.57	0.47	0	0.6	0.1
4.4 V	0.69	0.58	0	2.7	0.4
4.65 V	0.77	0.65	0.8	6.3	0.9
4.8 V	0.85	0.74	3.8	8.5	1.1
4.8 V hold	0.94	0.86	5.6	14.5	2.0

Table 3.9: Oxygen-depleted/rocksalt thickness estimation for cycled electrodes along with capacity and O_2 loss observed by DEMS.

Solid carbonate evolution throughout the first cycle of NMC622 electrodes. Figures 3.5c) and 3.7 show that significant chemisorption of electrolyte decomposition products occurs on charged electrodes above 4.4 V, resulting in a detected increase of ^{16}O-content of the surface carbonate. This is likely due to a larger affinity of the carbonate electrolyte with and increased reactivity of the ^{18}O-NMC622 surface as the state of charge

increases. During discharge the chemisorbed electrolyte species desorb and what largely remains on the ^{18}O-NMC622 surface is the partially decomposed native ^{18}O-Li_2CO_3, as can be clearly observed in Figure 3.7. An important open debate in the field is the mechanism by which Li_2CO_3 decomposes during cycling.

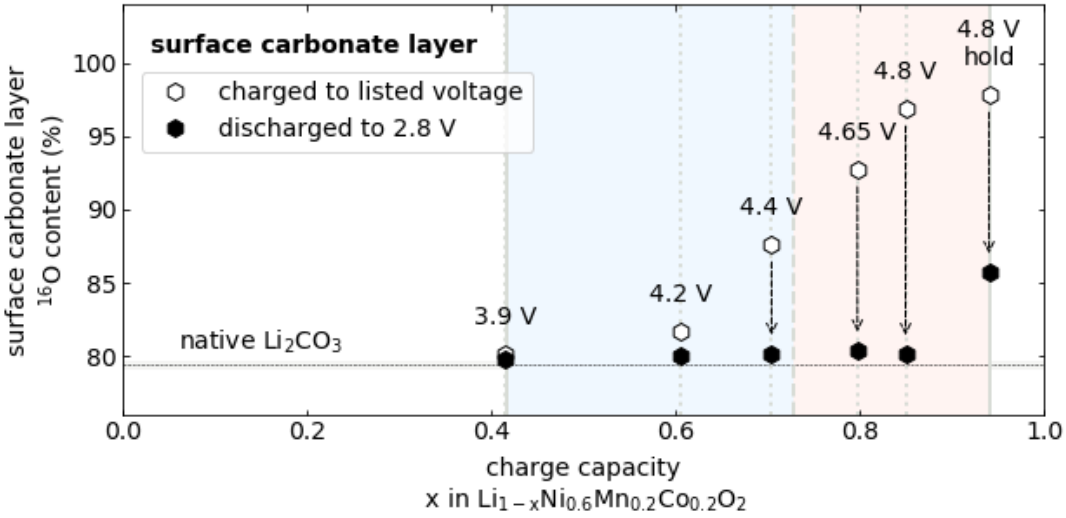

Figure 3.7: ^{16}O-content in the solid carbonate layer for ^{18}O-NMC622

Growth of ^{16}O-content in the solid carbonate layer as measured using ex-situ titrations versus achieved charge capacities of ^{18}O-NMC622. An increase in ^{16}O-content above the native Li_2CO_3 layer indicates the deposition of electrolyte degradation products on the surface of ^{18}O-NMC622. This is a complementary representation of the data presented in Table 3.5 and Figure 3.5c).

Jung et al. have proposed[66] that Li_2CO_3 is degraded by an acid/base reaction from HF impurities via the following: $^1O_2$ from the lattice (partially detected as triplet oxygen, $^3O_2$) reacts with EC to form H_2O_2, H_2O_2 then is oxidized to release volatile $^3O_2$ and protons, these protons then react with the PF_6^- anion to produce PF_5 and HF, which then finally reacts with Li_2CO_3 to produce LiF. As we find that Li_2CO_3 on the surface of NMC622 degrades with a different gas evolution profile than O_2, starts to degrade at $\approx$ 3.9 V (before the onset of O_2 evolution), degrades with also the less acidic LiTFSI as the salt (discussed later in Chapter 4), as well as with non-carbonate based electrolytes with (Chapter 4) and without the presence of TMOs (Chapter 2),[42] and was recently even found to degrade in an all-solid state battery,[70] the proposed series of reactions as the sole mechanism of Li_2CO_3 degradation are not consistent with the observations of this chapter. Although above room temperature, $LiPF_6$-related decomposition products can readily chemically decompose Li_2CO_3 in carbonate electrolytes,[40] we do not detect the $LiPF_6$ decomposition product POF_3 (from H_2O reacting with PF_5) below 5.0 V.

We propose instead that Li_2CO_3 degradation proceeds through a related mechanism to the carbonate electrolyte decomposition via a reaction involving the delithiated ^{18}O-NMC622, resulting in the evolution of CO_2 with similar profiles to the CO_2 evolved from electrolyte degradation.

3.4 Conclusions

In this chapter we introduce the combined analyses of isotopic labeling, gas analysis, and peroxo/carbonate titrations that complement standard microscopy measurements. Using these analyses we quantify the changes that occur during the first cycle of NMC622. Our findings are summarized and labeled visually in the graphic on page 28:

Concomitant with the onset of gas evolution above 3.9 V are:

(i) decomposition of the native surface Li_2CO_3 to CO_2,

(ii) decomposition of the electrolyte to CO_2, this CO_2 involves oxygen from the ^{18}O-NMC622 particle at potentials as low as 3.9 V, below the onset of O_2 lattice loss at 4.45 V,

(iii) deposition of solid carbonates from electrolyte decomposition on charge,

(iv) desorption of these electrolyte degradation products on discharge,

(v) (quasi-)reversible near-surface O redox during charge with however,

(vi) the irreversible formation of the disordered surface layer that persists after discharge.

We observe formation of the peroxo-like surface character before the onset of O_2 evolution seen from cycling > 4.45 V. The CO_2 from both decomposition of the native Li_2CO_3 and the electrolyte have profiles that appear to be distinct from lattice O_2 evolution.

We believe the combination of analysis reported here will allow discrimination of the tunable properties of Li-ion cathode/electrolyte systems including: extent of surface contaminants, electrolyte solvent and salt, cathode composition, and cycling conditions. With additional studies, quantifying these differences will allow further understanding of the complex processes of electrolyte/surface degradation in Li-ion cathodes.

We conclude this chapter with a number of open questions that remain to be addressed, but are outside the scope of this present work, which aimed to present and apply new methods to quantitatively account for reversible and irreversible processes occurring at TMO-based Li-ion cathodes. As shown in Tables 3.1, 3.2, 3.4, 3.5, and 3.8, the electrolyte-originating CO_2 evolved during cycling is composed of both $C^{16,16}O_2$ and $C^{16,18}O_2$, with an ^{18}O-enrichment of ≈ 4 %. What is the mechanism of this electrolyte decomposition such that $C^{16,18}O_2$ is evolved?

As singlet oxygen is predicted to produce CO_2 stemming from ring-opening of EC,[72] in our system any CO_2 originating from that mechanism would produce only natural abundance isotopes of CO_2. This indicates that, while ring opening must be a component of the total

reaction, there is another mechanism that produces $C^{16,18}O_2$ that is as of yet unknown. As there is only one source of ^{18}O in the system, this oxygen must originate from the ^{18}O-NMC622 particle—be it from the lattice, surface defects, and/or surface contaminants. Notable also is that the ^{18}O-enrichment of the electrolyte-originating CO_2 is nearly constant for all anodic cut-off potentials tested, including those below the onset potential of O_2 evolution and the 4.8 V potentiostatic experiments with extensive CO_2 evolution. This suggests that the source of ^{18}O of the electrolyte-originating CO_2 is constant in enrichment and unchanging in mechanism above $\approx$ 3.9 V. As O_2 is not evolved from the NMC622 surface until $\approx$ 4.45 V and exhibits disparate behavior compared to CO_2 as seen in Figures 3.1, 3.3, and 3.4, it is unlikely that lattice oxygen released as O_2 directly contributes to $C^{16,18}O_2$. We however note that since the surface Li_2CO_3 and evolved O_2 have the same ^{18}O-enrichment, definitive discrimination between the two as a possible source of $C^{16,18}O_2$ is not possible in this chapter.

Furthermore, carbonate electrolytes are hypothesized to interact/react with the surface of delithiated TMOs in such a way that eventual O loss reduces TMs, thereby allowing Ni/Li exchange and formation of a disordered surface layer. Does this process cause $C^{16,18}O_2$ evolution at potentials as low as $\approx$ 3.9 V? This formation of the disordered rocksalt surface layer has been shown to depend on the identity of the electrolyte. Compared to baseline carbonate electrolytes, fluorinated carbonates show the least extent of surface layer formation and carbonates with oxidizable additives show the largest extent of formation.[58] What gas evolution markers are associated with the formation of the surface layer? As surface modifications must change the interaction with the electrolyte compared to the bare oxide surface, how does the oxygen-depleted layer formation and interaction with the electrolyte depend on contaminants/defects? We envision that the techniques presented here can be applied to other TMOs, battery compositions, and electrochemical analysis conditions to help answer these questions.

For example, though increased surface contaminants have been shown to increase outgassing during cycling,[67,69] the specific changes in the electrolyte-surface interaction are not known. Some have found that increased Li_2CO_3 does not change the cathode surface $LiPF_6$-originating fluorine and phosphorus compounds,[60] while others have shown the exact opposite.[43] Additionally, increased surface TM reduction and rocksalt formation has been observed after cycling of samples with increased surface Li_2CO_3,[60] suggesting that quantification of surface contaminants is needed to understand the complete evolution of the surface layer formation. This leaves open questions of how surface compounds and defects change the interaction with the electrolyte, the formation of a disordered surface, and moreover how they affect the overall cell performance.

3.5 Acknowledgements

The author gratefully acknowledges support from the Department of Defense (DoD) through the National Defense Science & Engineering Graduate Fellowship (NDSEG) Program. This work was supported by the Assistant Secretary for Energy Efficiency and Renewable Energy, Office of Vehicle Technologies of the U.S. Department of Energy under Contract No. DEAC02-05CH11231. We thank Umicore for receipt of the NMC622 powder.

4 | The role of electrolyte in the first cycle transformations of $LiNi_{0.6}Mn_{0.2}Co_{0.2}O_2$

4.1 Abstract

In this chapter we present the role of the electrolyte in the gaseous electrolyte decomposition, decomposition of the native surface contaminant Li_2CO_3, loss of O_2 from the $LiNi_{O.6}Mn_{0.2}Co_{0.2}O_2$ (NMC622) lattice, and formation of the peroxo-like surface layer on NMC622 in the first cycle. Results are given for the cyclic carbonates ethylene carbonate (EC) and propylene carbonate (PC); the linear carbonates dimethyl carbonate (DMC) and diethyl carbonate (DEC); and the glymes dimethoxyethane (DME) and tetraethylene glycol dimethyl ether (TEGDME). We also make the comparison between the salts lithium bis(trifluoromethanesulfonyl)imide (LiTFSI) and lithium hexafluorophosphate ($LiPF_6$) and the additives vinylene carbonate (VC) and fluoroethylene carbonate (FEC) for the mixed carbonate EC/DEC electrolyte system. Although the gas evolution is distinct for different electrolytes, with exception of DEC, which is unstable as a single solvent electrolyte versus Li, we find that the formation of the peroxo-like surface layer on NMC622 during the first cycle is largely independent of the identity of the electrolyte and tends to increase in magnitude with the attainable charge capacity for each electrolyte. Our results indicate that initial Li/Ni mixing is inevitable at high states of delithiation and is largely a material function of the NMC622. In all cyclic carbonate-based electrolytes except for VC, Li_2CO_3 degradation to CO_2 accounted for the maximum source of carbon dioxide > 4.6 V vs. Li/Li^+ in the first cycle. Additionally, in DME and DMC partial dissolution of the native Li_2CO_3 occurred without reaction to CO_2.

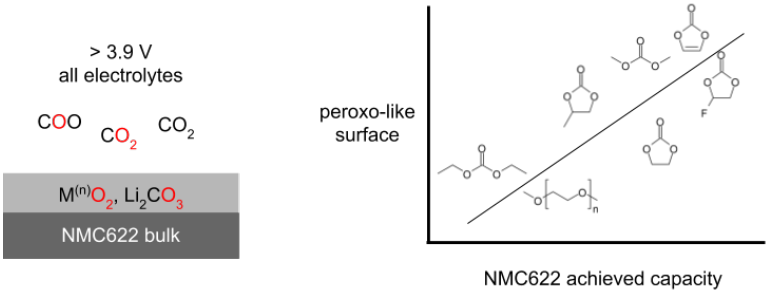

4.2 Introduction

Ni-rich lithium transition metal oxides (TMOs) as next-generation positive electrode materials are limited in their practical use by structural instabilities that manifest as poor cycling performance. Loss of active material can occur via a combination of TM dissolution, bulk and surface transformations, lattice oxygen loss, resistive film formation from reaction with the electrolyte, and material segregation from particle cracking.[47,80] While the exact nature and role of these in cycling performance degradation are debated, it is agreed that greater understanding of the complex processes at the cathode/electrolyte interface is critical to the development of future electrode materials.

The existence of a disordered rocksalt/peroxo-like surface layer on many Ni-based TMOs with depths $\approx$ 10 nm have been observed after extended cycling and even after just one electrochemical cycle.[49,53] The depth of this layer has been shown to depend on the identity of the electrolyte and anodic cut-off potentials after extended cycling.[58,59] However, the function of this surface reconstruction layer has not yet been established. While it has been posited that the growth of the disordered surface is a major factor in performance degradation by acting as a catalyst for larger crack formation, others have found that the layer conducts Li^+ relatively unimpeded and its presence could not explain the differences observed in performance degradation.[54,59] Additionally, factors which control the surface transformation are complicated by the uncertainty in the surface structure of Ni-rich TMOs, as these are contaminated by Li compounds, either residual from synthesis or from reaction with the atmosphere, like hydroxides and carbonates, which can outgas and react with the electrolyte during cell operation.[42,69]

A general strategy to combat lithium TMO surface instability and reactivity with the electrolyte is to create an intermediate passivating layer that allows Li^+ diffusion while however preventing further decomposition of the electrolyte and/or TMO surface. This strategy includes the routes of (i) modifying the near-surface lattice of the TMO and altering the composition with dopants or vacancies;[81] (ii) reducing the outer TMO surface contaminants by removing them or reacting them to create artificial Li^+-conducting coatings;[28,45] and (iii) choosing electrolyte additives that react during the operation of the battery to form a cathode electrolyte interphase (CEI) that should ideally be more stable than the electrolyte to highly oxidative potentials,[82] analogously to the more well-studied concept of the solid electrolyte interphase (SEI) on negative electrode materials.

Without additives, typical Li-ion electrolytes consisting of blends of linear carbonates like dimethyl carbonate (DMC), ethyl methyl carbonate (EMC), or diethyl carbonate (DEC) and a cyclic carbonate like ethylene carbonate (EC) with lithium hexafluorophosphate ($LiPF_6$) as the salt form unstable CEIs consisting of electrolyte decomposition products. These surface deposits are dynamic and change in morphology and composition with cycling of the battery. For example, at higher potentials and higher states of delithiation, LiF and other $LiPF_6$ decomposition products can be depleted from the surface of positive electrodes, only

to reform later during discharge.[77] Inorganic and alkyl carbonates, as impurity species or originating from the electrolyte, may decompose anodically producing gaseous products but may also reform at sufficiently low potentials on discharge if O_2 is present in the headspace.[9] Electrolyte oxidation products originating from the cathode may also migrate to the anode, altering the SEI there.[83] In general, without a stable CEI the electrolyte continues to be consumed during cycling with high anodic cut-off potentials, leading to continuous capacity loss.

With additives that promote polymerization reactions, like fluoroethylene carbonate (FEC), the CEI formed tends to be less diffuse and more effectively passivates the TMO surface. Other additives, like vinylene carbonate (VC), may also act as a sacrificial additive that is consumed preferentially to the main electrolyte. Electrolyte additives may suppress or enhance the extent of surface TM reduction, and thus formation of the disordered rocksalt surface layer after cycling in Ni-rich TMOs.[58,59] That said, most additives react not only with the TMO positive material, but also with the Li or carbonaceous negative electrode.[84] Stabilization of the anode's SEI can prevent deposition of TM on the anode, and thus plays an indirect role in suppression of positive electrode decomposition.

In the previous chapter we demonstrated quantification of the first-cycle surface transformations of $LiNi_{O.6}Mn_{0.2}Co_{0.2}O_2$ (NMC622) with EC/DEC-based electrolytes using the combined analyses of isotopic labeling, differential electrochemical mass spectrometry (DEMS), and peroxo/carbonate titrations–a technique which allows quantification of decomposition of the native surface contaminant Li_2CO_3, deposition of carbonate-like electrolyte decomposition products, and quantification of the irreversible formation of the peroxo-like surface layer on TMOs.[85] In the first cycle of NMC622 we found that with the onset of CO_2 evolution above ≈ 3.9 V vs Li/Li^+ is the irreversible formation of the disordered oxygen-depleted/TM-reduced surface layer up to ≈ 1 nm for an anodic cut-off potential of 4.8 V, decomposition of the native surface contaminant Li_2CO_3, and solid carbonate deposition from electrolyte degradation which, however, desorbs and is largely removed during discharge.

In the present chapter we use these analyses to distinguish the NMC622 reactivity with different carbonate electrolytes, the additives FEC and VC, and glyme electrolytes in the first electrochemical cycle to 4.8 V vs Li/Li^+. Although we find that formation of the peroxo-like surface layer is largely independent of the identity of the electrolyte, both the electrolyte and native Li_2CO_3 decomposition to gaseous species are highly dependent on the identity of the electrolyte. By tracking the NMC622 surface oxygen, in addition to CO_2 evolution from the surface Li_2CO_3, we show that the electrolyte-originating CO_2 involves oxygen from the NMC622 surface at potentials as low as 3.9 V for all electrolytes tested except for TEGDME. In all electrolytes except linear carbonates and with VC as an additive, the rate of Li_2CO_3 degradation was the largest of all forms of carbon dioxide above 4.6 V, showing the importance of quantifying Li_2CO_3 for understanding first cycle outgassing.

4.3 Results and Discussion

The performances of NMC622 for the first cycle for a current rate of 0.1 Li^+ h^{-1} (27.65 mA g^{-1}), anodic cut-off potential of 4.8 V, and cathodic cut-off potential of 2.8 V were compared for the following electrolytes with 1 M $LiPF_6$ as the salt unless indicated:

(i) the cyclic carbonates EC and propylene carbonate (PC);

(ii) the linear carbonates DMC and DEC;

(iii) mixed carbonates EC/DEC (1:1 v/v) with $LiPF_6$ and lithium bis(trifluoromethanesulfonyl)imide (LiTFSI) as the salt

(iv) FEC and VC as additives to EC/DEC;

(v) the glymes dimethoxyethane (DME) and tetraethylene glycol dimethyl ether (TEGDME), both with LiTFSI as the salt. Due to anodic stability limits, TEGDME and DME were both tested to anodic cut-off potentials of 4.65 V.

See Appendix D for further description of the electrochemical cells and electrolytes. To distinguish the NMC622 surface oxygen from the electrolyte oxygen, partially enriched ^{18}O-NMC622 was prepared by heating under a headspace containing $^{18}O_2$ as described in Appendix B, yielding a ^{18}O-NMC622 surface enrichment of 20.7 ± 0.1 % ^{18}O. ^{18}O-NMC622 electrodes had an initial surface Li_2CO_3 amount of 29.3 ± 1.5 µmol g^{-1}. See Appendix C for a full description of the titration.

The achieved charge and discharge capacities for ^{18}O-NMC622 for the first cycle are plotted in Figure 4.1 for all electrolytes. Additionally plotted in open circles and fit with the dashed line are achieved charge/discharge capacities for anodic cut-off potentials of 3.9 (not shown), 4.2, 4.4, 4.65, and 4.8 V for the baseline EC/DEC electrolyte from the previous chapter. Points above the line indicate less irreversible capacity loss, while points below the line indicate greater irreversible capacity loss than the baseline electrolyte. The linear fit has a slope of unity and indicates an irreversible capacity of ≈ 0.11 Li units for the first cycle, regardless of charge cut-off potential above 3.9 V. As seen in Figure 4.1, all EC-based electrolytes with and without additives, with and without linear carbonates, and with both $LiPF_6$ and LiTFSI as the salt achieved first cycle charge/discharges that are in line with our previous results. PC, DME, TEGDME, and DMC single-solvent electrolytes all achieved lower discharge capacities than the baseline electrolyte of 0.03–0.06 Li units, likely due to larger extents of irreversible electrolyte degradation. DEC is not stable as a single solvent electrolyte and exhibited the lowest discharge capacity with 0.21 Li units below the baseline EC/DEC electrolyte. As will be discussed more in depth later, this is likely due to significant parasitic reactions such that the charge capacity is not a good indicator of the true extent of delithiation for DEC.

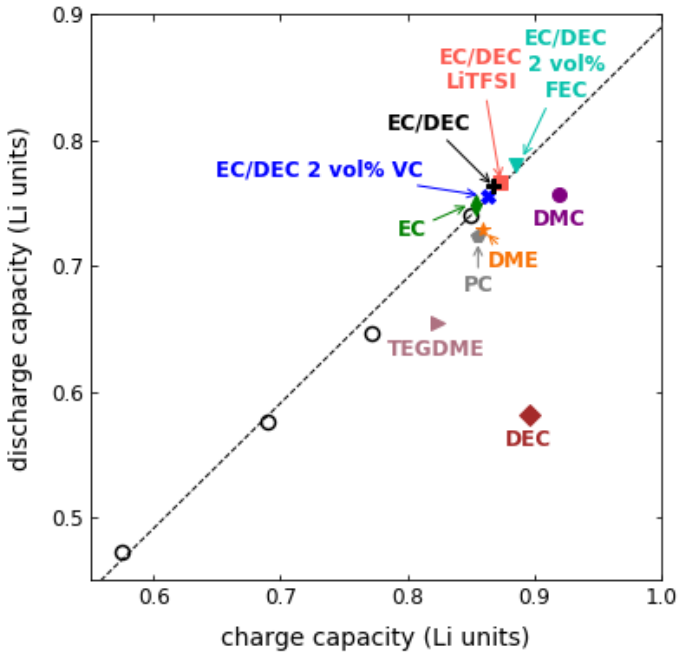

Figure 4.1: First cycle discharge vs. charge capacity for all electrolytes for ^{18}O-NMC622. All cells were charged to 4.8 V and discharged to 2.8 V at a rate of 27.65 mA g^{-1} (0.1 Li^{+} h^{-1}) except for DME and TEGDME, which had anodic cut-off potentials of 4.65 V. All electrolytes had 1 M salt concentrations and unless indicated were prepared with $LiPF_6$, except for DME and TEGDME which had LiTFSI as the salt. The linear fit and open circles are taken from Chapter 3 and are first cycle charge/discharge capacities for anodic cut-off potentials 3.9 (not shown), 4.2, 4.4, 4.65, and 4.8 V from a similarly prepared batch of ^{18}O-NMC622 with EC/DEC as the electrolyte.

4.3.1 Oxygen release and formation of surface reconstruction layer during the first cycle. Previous studies on NMC622 with typical carbonate electrolytes have shown that on charge above $\approx$ 4.45 V ($\approx$ 0.7 Li removed) molecular oxygen is released from the NMC622 surface.[69] This loss of oxygen is predicted to form spinel and/or rocksalt surface layers on Ni-rich TMOs.[11] In the previous chapter we showed that the formation of surface Li/Ni disorder on NMC622 occurs even before the onset of O_2 evolution for anodic cut-off potentials $>$ 3.9 V ($>$ 0.4 Li removed), increasing in extent of disorder with cut-off voltage. As detailed in the previous chapter, this disordered surface is quantifiable by an ex-situ titration that yields detectable molecular oxygen released from peroxo-like domains.

This detected O_2 from the peroxo-like domains is plotted against the O_2 released during the first electrochemical cycle for all electrolytes in Figure 4.2. Also included in open circles are the corresponding data from Chapter 3, as described earlier. The extent of the peroxo-like surface domain is nonlinear in O_2 released during the first cycle. A linear trend would be expected if the formation of the peroxo-like domain were due to lattice oxygen released as molecular O_2 on charge. As presented in Figure 4.2, the data are consistent with first the formation of the peroxo-like layer above 3.9 V, which is then partially released as O_2 from the outermost surface at higher extents of delithiation.

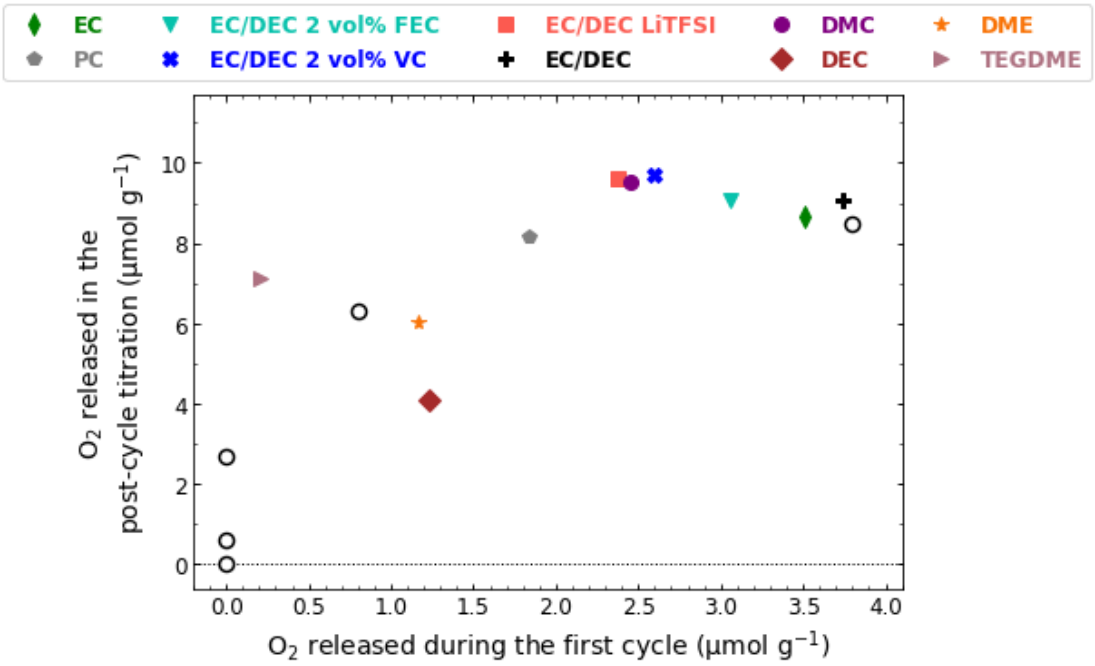

Figure 4.2: The peroxo-like surface layer vs. O_2 release during the first cycle.

Formation of the peroxo-like surface layer on ^{18}O-NMC622 after the first cycle as measured by the post-cycle titration versus O_2 released during the first cycle as measured by DEMS for all electrolytes studied. The open circles are taken from Chapter 3 and are measurements for different anodic cut-off potentials of 3.9, 4.2, 4.4, 4.65, and 4.8 V from a similarly prepared batch of ^{18}O-NMC622 with EC/DEC as the electrolyte.

In Figure 4.3 plotted instead is the extent of the peroxo-like surface layer versus capacity. The extent of this layer is plotted instead as a depth as estimated by the calculations given in Equations 3.2–3.4. Plotted in the left panel is the depth of the surface layer versus the achieved charge capacity, with the linear fit calculated from the baseline EC/DEC electrolyte with different anodic cut-off potentials of 4.2, 4.4, 4.65, and 4.8 V plotted in open markers. The majority of the electrolytes follow the linear trend as for the baseline electrolyte, with DEC exhibiting the largest deviation. Plotted in the right panel of Figure 4.3 is the achieved discharge capacity instead of charge capacity. While the peroxo-like formation for most electrolytes is unchanged in trend, for single solvent electrolytes with lower anodic stability like DEC, DMC, DME, and TEGDME, the achieved discharge capacity is a better measure of the reversible capacity due to (de)intercalation and thus gives a more linear trend.

Figure 4.3 implies that the irreversible formation of the peroxo-like surface layer in the first cycle is a material property of the prepared ^{18}O-NMC622, is formed as a function of the extent of delithiation of the NMC622 lattice for a given current rate, and is largely independent of the identity of the electrolyte. Given that the additives FEC and VC in carbonate blends have been shown to exhibit improved performance and less rocksalt formation after many cycles for Ni-rich TMOs,[58,59] it is then surprising that there is no significant difference in the peroxo-like formation on NMC622 after just the first cycle for all of the electrolytes tested.

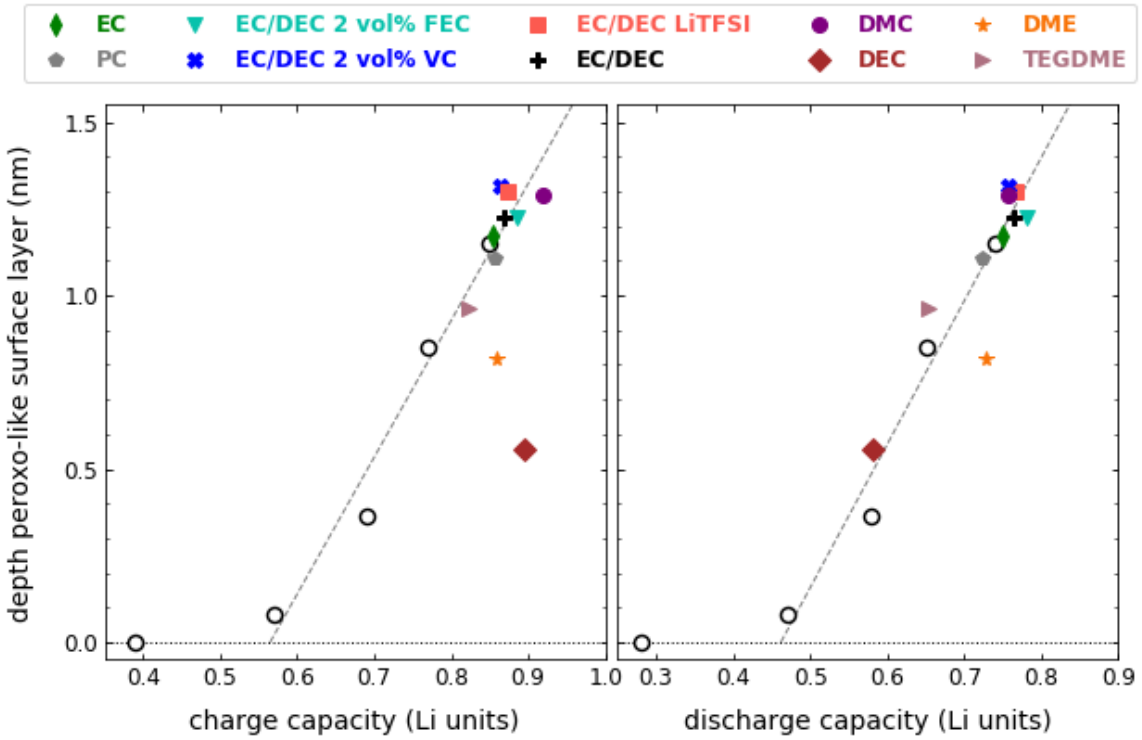

Figure 4.3: Depth of the peroxo-like surface layer vs. achieved capacity.

Estimated depth of the peroxo-like surface layer on ^{18}O-NMC622 after the first cycle as measured by the post-cycle titration for all electrolytes studied. The linear fit (excluding 3.9 V) and open circles are taken from Chapter 3 and are measurements for different anodic cut-off potentials of 3.9, 4.2, 4.4, 4.65, and 4.8 V from a similarly prepared batch of ^{18}O-NMC622 with EC/DEC as the electrolyte.

This suggests that the improved performance shown for choice electrolytes and additives may stem from different stabilizations other than prevention of the initial peroxo-like surface formation on Ni-rich TMOs. For example, stabilization of the anode SEI may have a larger role in long-term positive electrode stabilization by limiting active material loss by preventing TM plating. Additionally, as suggested by others, surface layer transformations on positive electrodes may not significantly negatively impact long-term performance, provided the interphases sufficiently conduct Li^+. Overall, our results suggest that reactions with the electrolyte other than cathode surface transformations may govern the long-term cycling performance.

That stated, undesirable reactions as detected by outgassing are most prominent in the initial formation cycles. Given the surface contaminant Li_2CO_3, inevitable peroxo-like character of the NMC622 surface, and that oxygen is released at high potentials during the initial cycles, the rest of this study focuses on the gaseous byproducts of electrolyte reactivity in the first cycle.

4.3.2 Decomposition as exhibited by outgassing. For TMO/Li cells with carbonate electrolyte the major gases evolved during cycling are CO_2, CO, and O_2. Electrolyte reduction products like ethylene from EC and H_2 on the anode are also evolved but are minor for Li. In the previous chapter we showed that the TMO surface contaminant Li_2CO_3, which is inevitably present from unreacted Li precursors from synthesis or present from reaction with atmospheric CO_2, decomposes during cycling of TMO materials and can directly account for ≈ 30–40 % of the total CO_2 evolution in EC/DEC-based electrolytes in the first cycle. The rest of the CO_2 originates in part from decomposition of the electrolyte.

For Ni-rich and Li-rich TMOs, which release O_2 at high degrees of delithiation, oxidative stability is a major consideration for the performance and safety of the electrolyte. This concern is heightened due to the recent detection of highly reactive singlet oxygen, $^1O_2$, during the first charge of numerous TMOs at high potentials near 5 V[68] and also during the electrochemical oxidation of Li_2CO_3 above 3.8 V.[42] Parasitic reactions with oxygen are speculated to cause poor long-term cell performance and electrolyte decomposition.

To explore the nature of this electrolyte decomposition we must distinguish between the naturally abundant electrolyte oxygen and the enriched ^{18}O-NMC622 surface. As the ^{18}O-NMC622 surface is not fully enriched in ^{18}O, we find it more illustrative to change basis. Writing the generic ^{18}O-NMC622 surface oxygen species as *O and natural abundance oxygen as O, for all electrolytes the evolved carbon dioxide must be a linear combination of C^*O_2, C^*OO, and CO_2. To apply this reasoning, it is necessary to know the ^{18}O-enrichment of the reactive oxygen species *O. As discussed in the previous chapters, as we find that the surface Li_2CO_3 and the surface lattice oxygen (evolved as molecular O_2 during cycling) are uniformly enriched nearly identically in ^{18}O, we can perform the analyses here without restricting the source of the oxygen. In other words we label *O to encompass all types of ^{18}O-NMC622 surface oxygen, which in this study has an enrichment of 20.7 ± 0.1 % ^{18}O. From here out we will label all surface oxygen as *O, for example in referencing the original surface lithium carbonate as $Li_2C^*O_3$. For simplicity, we take natural abundance oxygen to be 100 % ^{16}O. The natural abundance of ^{18}O is ≈ 0.2 %, so its ($C^{16,16}O_2$, $C^{16,18}O_2$, $C^{18,18}O_2$) distribution would be (99.6, 0.4, 0.0), introducing an acceptably low error for this level of analysis. Writing z as the fraction of ^{18}O-enrichment of the surface oxygen, the theoretical distributions of all forms of O, *O carbon dioxide in the directly measurable ^{16}O, ^{18}O basis are given in Table 4.1, again assuming a uniform distribution of ^{18}O.

	$C^{16,16}O_2$	$C^{16,18}O_2$	$C^{18,18}O_2$
C^*O_2	$(1-z)^2$ [62.9 %]	$2z(1-z)$ [32.8 %]	z^2 [4.3 %]
C^*OO	$(1-z)$ [79.3 %]	z [20.7 %]	0
CO_2	1 [100 %]	0	0

Table 4.1: Distributions of C^*O_2, C^*OO, and CO_2 as measurable isotopes of carbon dioxide, given as a function of the ^{18}O-enrichment of ^{18}O-NMC622 surface oxygen, z. Brackets indicate the percentages for this study.

Using the distributions given in Table 4.1 and by denoting the molar evolution rates as r, the transformations from the ^{16}O, ^{18}O basis to the O, *O basis are given below for carbon dioxide:

$$rC^{*}O_2 = \frac{1}{z^2} rC^{18,18}O_2, \tag{4.1}$$

$$rC^{*}OO = \frac{1}{z} rC^{16,18}O_2 - \frac{2(1-z)}{z^2} rC^{18,18}O_2, \tag{4.2}$$

$$rCO_2 = rC^{16,16}O_2 - \frac{1-z}{z} rC^{16,18}O_2 + \frac{(1-z)^2}{z^2} rC^{18,18}O_2. \tag{4.3}$$

Using Equations 4.1–4.3, the rates of carbon dioxide evolution in the O, *O basis are plotted in Figure 4.4 for all electrolytes. The rates for DME are not plotted because the solvent's high volatility gives a significant background signal for m/z= 45 that is 1–2 orders of magnitude larger than for the rest of the electrolytes, meaning the ion current signal for m/z= 44 could not be resolved from noise and $C^{16,16}O_2$ could not be calculated. The rates of oxygen evolution, which is solely evolved as $^{*}O_2$, are also plotted in Figure 4.4.

In our previous work[85] in Chapter 3 we showed that the vast majority of $C^{*}O_2$ evolution is due to direct decomposition of the surface $Li_2C^{*}O_3$, which was confirmed by comparing the measured $Li_2C^{*}O_3$ remaining on the surface with the total $C^{*}O_2$ evolved during the first cycle in EC/DEC-based electrolytes. Thus we consider $C^{*}O_2$ as a marker for surface lithium carbonate decomposition and as can be seen in Figure 4.4, $Li_2C^{*}O_3$ decomposes for all solvents and salts tested in the first cycle.

From other ^{13}C isotopic studies, the remaining CO_2 and $C^{*}OO$ must stem from electrolyte decomposition,[66,67] with CO_2 likely stemming in part from direct ring opening of the carbonate electrolytes and the presence of $C^{*}OO$ indicating a coupled ^{18}O-NMC622 surface/electrolyte degradation. Notable is that for all electrolytes except TEGDME, $C^{*}OO$ is evolved throughout the charge and discharge, indicating that this coupled ^{18}O-NMC622 surface/electrolyte reaction occurs for both linear and cyclic carbonates, with both LiTFSI and $LiPF_6$ as the salt, and with and without FEC and VC additives. The corresponding tabulated cumulative carbon dioxide evolved is given in Table 4.2.

Additionally given in Table 4.2 is the surface $Li_2C^{*}O_3$ that remains after the first cycle as measured by the post-cycle carbonate titration. For all but two of the electrolytes the measured remaining $Li_2C^{*}O_3$ is in good agreement with the predicted $Li_2C^{*}O_3$ remaining, as calculated by the initial amount of 29.3 ± 1.5 µmol g^{-1} minus the total $C^{*}O_2$ evolved. In both DMC and DME electrolytes there is ≈ 10 µmol g^{-1} $Li_2C^{*}O_3$ that is unaccounted for by the $C^{*}O_2$ evolution. Without a higher viscosity solvent or a cyclic carbonate that forms polymeric films on the surface of the TMO, there is likely dissolution or reaction of the native surface $Li_2C^{*}O_3$ that does not result in detectable $C^{*}O_2$ evolution. Surprisingly, DEC did not show similar behavior to DMC. As will be discussed later, during the first cycle DEC decomposed to form insoluble products that covered the ^{18}O-NMC622 surface, likely blocking the $Li_2C^{*}O_3$ dissolution as might be expected.

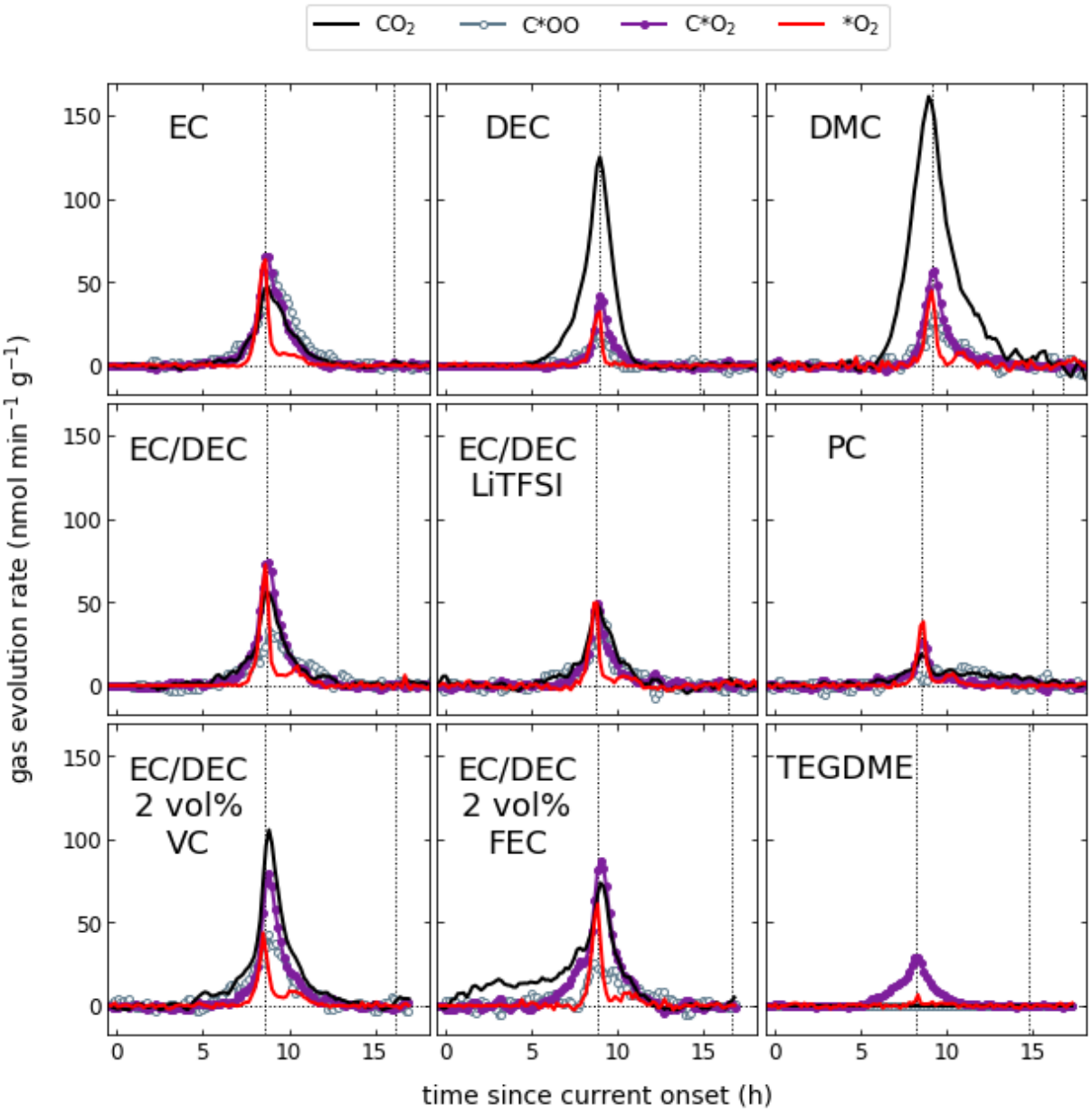

Figure 4.4: Rates of carbon dioxide and $^*O_2$ evolution for all electrolytes.

Carbon dioxide and $^*O_2$ evolution rates during the first charge in the O, *O basis. Cells were charged to 4.8 V and discharged to 2.8 V at a rate of 27.65 mA g^{-1} (0.1 Li^+ h^{-1}) except for DME and TEGDME, which had anodic cut-off potentials of 4.65 V. The start of charge occurs at time = 0 h for all electrolytes and the other vertical lines indicate the onset and completion of discharge for each electrolyte.

electrolyte	cumulative $^*O_2$ (µmol g^{-1})	cumulative carbon dioxide in µmol g^{-1} (fraction of total evolution, %)				$Li_2C^*O_3$ remaining (µmol g^{-1})
		CO_2	C^*OO	C^*O_2	Σ	
PC	1.8	4.2 (41 %)	2.9 (29 %)	3.1 (30 %)	10.1	25.8
EC	3.5	6.5 (28 %)	8.9 (39 %)	7.4 (33 %)	25.4	21.8
DMC	2.5	27.1 (75 %)	4.1 (11 %)	5.2 (14 %)	36.4	*14.9*
DEC	1.2	14.0 (74 %)	2.0 (10 %)	3.0 (16 %)	19.0	26.1
EC/DEC	3.7	7.7 (37 %)	5.8 (27 %)	7.9 (36 %)	21.4	21.4
EC/DEC LiTFSI	2.4	5.9 (39 %)	4.4 (29 %)	4.8 (32 %)	15.1	22.6
EC/DEC 2 vol% FEC	3.1	13.8 (49 %)	4.6 (16 %)	9.6 (34 %)	28.3	19.7
EC/DEC 2 vol% VC	2.6	15.5 (53 %)	6.4 (22 %)	7.5 (26 %)	29.4	21.8
DME	1.1	unresolvable	0.8 (31 %)	1.9 (69 %)	$\geq$ 2.7	*19.1*
TEGDME	0.2	0	0	3.6 (100 %)	3.6	25.8

Table 4.2: Cumulative $^*O_2$ and carbon dioxide evolved during the first cycle of ^{18}O-NMC622 and remaining surface $Li_2C^*O_3$ as measured by the post-cycle titration. Pristine ^{18}O-NMC622 electrodes had initial surface coverage of $Li_2C^*O_3$ of 29.3 $\pm$ 1.5 µmol g^{-1}.

Also given in Table 4.2 is the cumulative $^*O_2$ evolved during the first cycle for each electrolyte. It has been hypothesized that carbon dioxide from carbonate electrolyte degradation is due in part to the released surface $^*O_2$ (which is partially detected as molecular $^*O_2$) reacting with the electrolyte, or in other words, a causal relationship of $^*O_2$ leading to carbon dioxide has been proposed.[11,66,67] We have found, however, that both the peroxo-like surface is formed and that all forms of carbon dioxide are detected before the onset of $^*O_2$ evolution, implying that surface $^*O$ reacts with the electrolyte at relatively low voltages (low extents of delithiation).

We have previously shown[85] in Chapter 3 that in EC/DEC electrolytes above 3.9 V the carbonate electrolyte and the surface $^*O$ form carbonate-like products comprised of both O and $^*O$ on the surface of ^{18}O-NMC622. These alkyl carbonates are quantified by a post-charge acid titration that yields both CO_2 and C^*OO; and these electrolyte-originating surface carbonates are largely desorbed by the discharge process below $\approx$ 4 V. The original contaminant $Li_2C^*O_3$ and these newly formed surface carbonates decompose at high voltages during charge, discharge, and rest after charge, yielding carbon dioxide.

In all carbonate electrolytes tested except for pure DEC, the formed alkyl carbonates deposited on the surface chemically decompose to both CO_2 and C^*OO like the baseline EC/DEC electrolyte. This indicates that all of the carbonate electrolytes decomposed by the surface $^*O$ to form alkyl carbonates with a similar mechanism and may suggest that the

^{18}O-NMC622 surface/electrolyte outgassing mechanisms may also be similar for all carbonate electrolytes tested. In the next subsections we will examine this outgassing behavior by electrolyte class.

Cyclic carbonates. The alkene reduction products of cyclic carbonates during Li plating are well studied: ethylene for EC and propylene for PC. The cyclic carbonate oxidative decomposition products seen in Li-ion batteries, however, are less well understood. Pioneering DEMS studies on oxidative decomposition products of cyclic carbonate electrolytes on carbon electrodes without TMOs detected volatile decomposition products above ≈ 4.8–5 V vs Li/Li$^+$, with PC decomposing to propanal, 2-ethyl-4-methyl-1,3-dioxolane, and CO_2; and EC decomposing to CO_2 along with other volatile, though not identified, higher mass products.[10,86] Early studies also found that water contaminants played a large role in the decomposition of PC/EC.[87,88] While at room temperature nominally anhydrous EC/PC decompose to detectable CO_2 only above ≈ 4.8 V, increased water contamination and temperature shifts the CO_2 onset potential negatively and enhances the rate of CO_2 evolution. Although water contaminants are expected to yield CO_2 and an alkyl glycol from the chemical reaction of EC/PC hydrolysis, the increased decomposition observed in the presence of water contaminants at lower potentials (and higher currents) was explained by electrochemical reduction of water on the counter electrode to form hydrogen and hydroxides, which then decompose PC/EC by a base-driven hydrolysis.[89] This is shown in Scheme 4.1 with the hydroxide colored red to highlight the mechanism of hydrolysis via nucleophilic attack of the carbonyl carbon by the hydroxide anion.

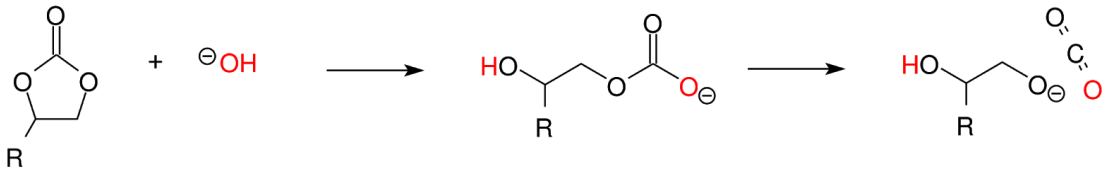

Scheme 4.1: Cyclic Carbonate Hydrolysis. R = H for EC, CH_3 for PC.

The deprotonated glycol may polymerize further with other carbonates.[90] This reaction can in some cases be relevant for practical batteries, as in both NMC622/Li and NMC622/graphite cells for pure EC-based electrolytes. Jung et al. found that with trace water impurities present, CO_2 evolved from the electrolyte at open circuit potential and when the anode was capable of reducing water.[66]

With the addition of a lithiated positive electrode material, the onset of CO_2 evolution on charge in cyclic carbonates shifts negatively in potential compared to the ≈ 4.8 V onset for carbon electrodes in anhydrous electrolytes. In the case of PC, the other anodic decomposition products of propanal and 2-ethyl-4-methyl-1,3-dioxolane are not observed to also negatively shift in potential as with CO_2. As seen in Figure 4.5, carbon dioxide evolution begins at ≈ 3.9 V vs Li/Li$^+$ for EC and ≈ 4.0 V for PC single solvent electrolytes. All forms of carbon dioxide, namely C*O_2, C*OO, and CO_2, are observed to evolve throughout the first cycle. Although we did not detect any significant ethylene/propylene glycol open circuit

decomposition for EC/PC single solvent electrolytes, it is notable that C*OO remains more elevated during discharge compared to C^*O_2 and CO_2.

As CO_2 likely partially stems from direct ring opening of the carbonate electrolyte and C^*O_2 originates from surface lithium carbonate degradation, what is the origin of C*OO? Water impurities would yield hydroxide anions with natural abundance oxygen and could only produce natural abundance CO_2 via Scheme 4.1. If the base instead originated from the ^{18}O-NMC622 surface, new alkyl carbonates could be formed and C*OO could be evolved at higher potentials, yielding a possible source of the C*OO observed.

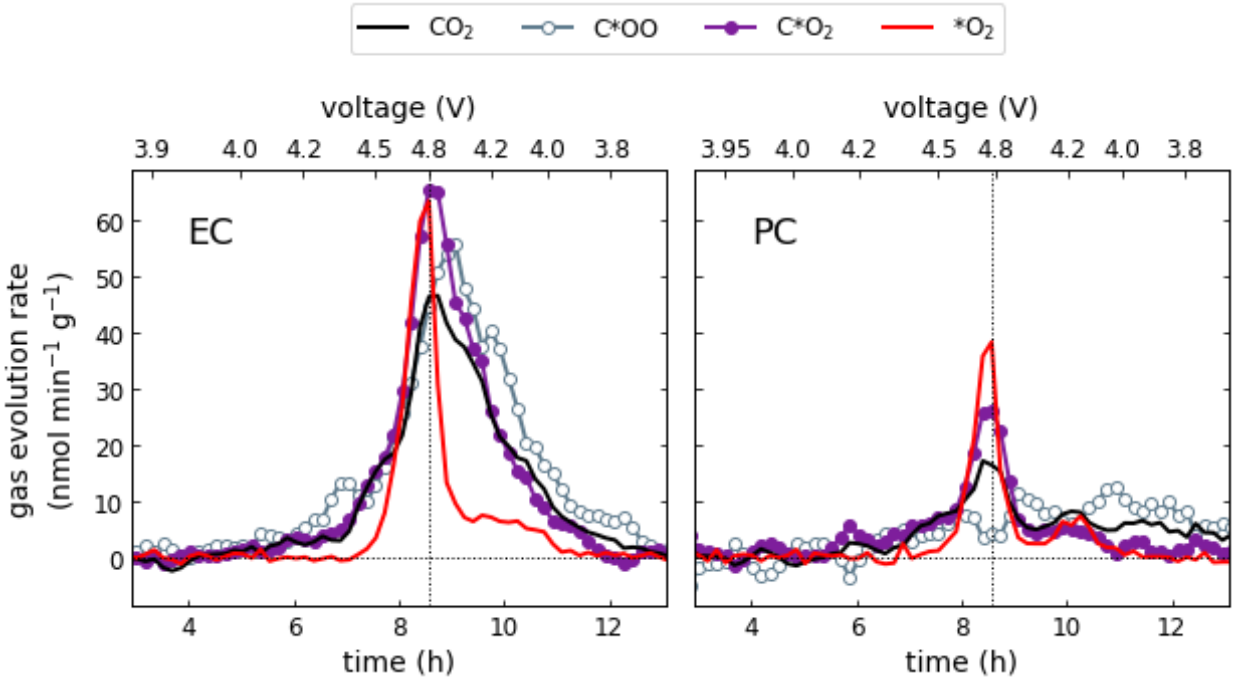

Figure 4.5: Detail of gas evolution rates for EC and PC for the first cycle of ^{18}O-NMC622.

What about the chemical oxidative instability of EC/PC as the source of C*OO? As proposed by Freiberg et al., $^1O_2$ released from the ^{18}O-NMC622 surface—from either surface impurities, defects, or the lattice—would first deprotonate EC to create H_2O_2 and VC. VC may be further oxidized with O_2 or $^1O_2$ as below in Scheme 4.2:

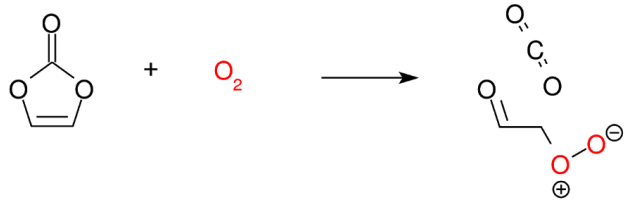

Scheme 4.2: VC oxidation.

with the $OC_2H_3O_2$ zwitterion reacting further to as of yet unknown products.[72] For triplet

or singlet oxygen originating from the ^{18}O-NMC622 surface, natural abundance CO_2 would be directly released from the ring-opening mechanism of Scheme 4.2. As will be discussed later and as seen in Table 4.2, the addition of VC was found to double the CO_2 evolved and slightly enhance the C*OO evolved, giving weight to the possibility of the dipolar $OC_2H_3{}^*O_2$ to produce C*OO in further reactions, although not proportionally.

Linear carbonates. As seen in Table 4.2 the low viscosity linear carbonates DMC and DEC exhibit the largest fraction of natural abundance CO_2 of the total carbon dioxide evolution compared to the rest of the electrolytes studied. As shown in Figure 4.6, the onset of CO_2 evolution is below 4.2 V for both electrolytes, which is below the theoretical anodic stability limit though consistent with other reports on other TMOs.[22]

The rate of $Li_2C^*O_3$ decomposition is comparable for the linear carbonates with the other cyclic carbonate-based electrolytes. It has been proposed surface Li_2CO_3 contaminants are not directly electrochemically decomposed, but rather are chemically decomposed by HF or H^+ from water contaminants that may be either electrochemically or chemically produced from $LiPF_6$ decomposition. Given that others have found larger extents of $LiPF_6$ decomposition (as detectable POF_3) for pure DMC compared to pure EC $LiPF_6$ electrolytes,[22] it may be expected that more surface $Li_2C^*O_3$ would decompose in the linear carbonates if HF decomposition dominated.

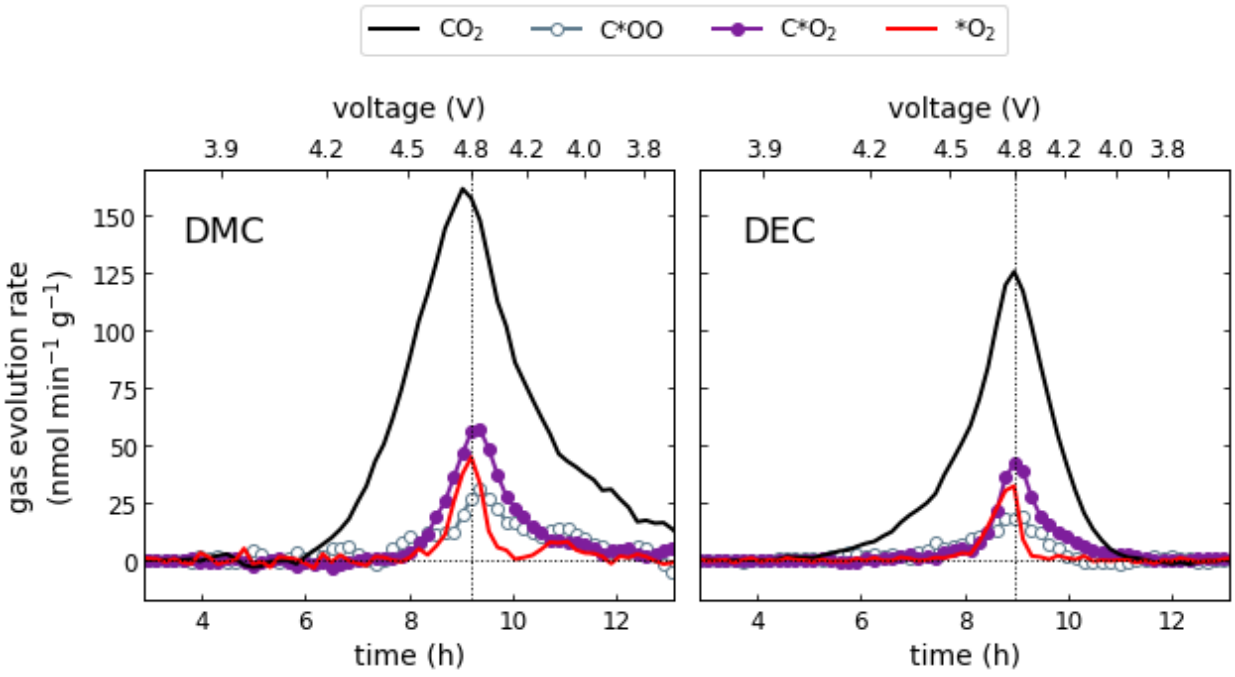

Figure 4.6: Detail of gas evolution rates for DMC and DEC for the first cycle of ^{18}O-NMC622.

As discussed earlier, from the DMC post-cycle titration there was ≈ 10 µmol g^{-1} of unaccounted for $Li_2C^*O_3$. This is likely unrelated to $LiPF_6$ decomposition as missing $Li_2C^*O_3$ was also observed for DME with LiTFSI as the salt. Unlike DMC, the post cycle

titration showed that DEC did not have any unaccounted for $Li_2C^*O_3$ and additionally was the only solvent to show significant electrolyte decomposition products on the surface of ^{18}O-NMC622 after the first cycle. As detailed in Chapter 3, after discharge to below ≈ 4.0 V the majority of the electrolyte decomposition products originating during charge in EC/DEC are desorbed from the surface of ^{18}O-NMC622, leaving surface carbonate that is nearly fully $Li_2C^*O_3$, with little alkyl carbonates originating from electrolyte decomposition. In all electrolytes tested in this study we observed the same behavior except for in pure DEC: 84 µmol g^{-1} of carbonate-like electrolyte decomposition products (as measured by carbon dioxide during the acid titration) with natural abundance were detected on the surface of ^{18}O-NMC622 after the first cycle.

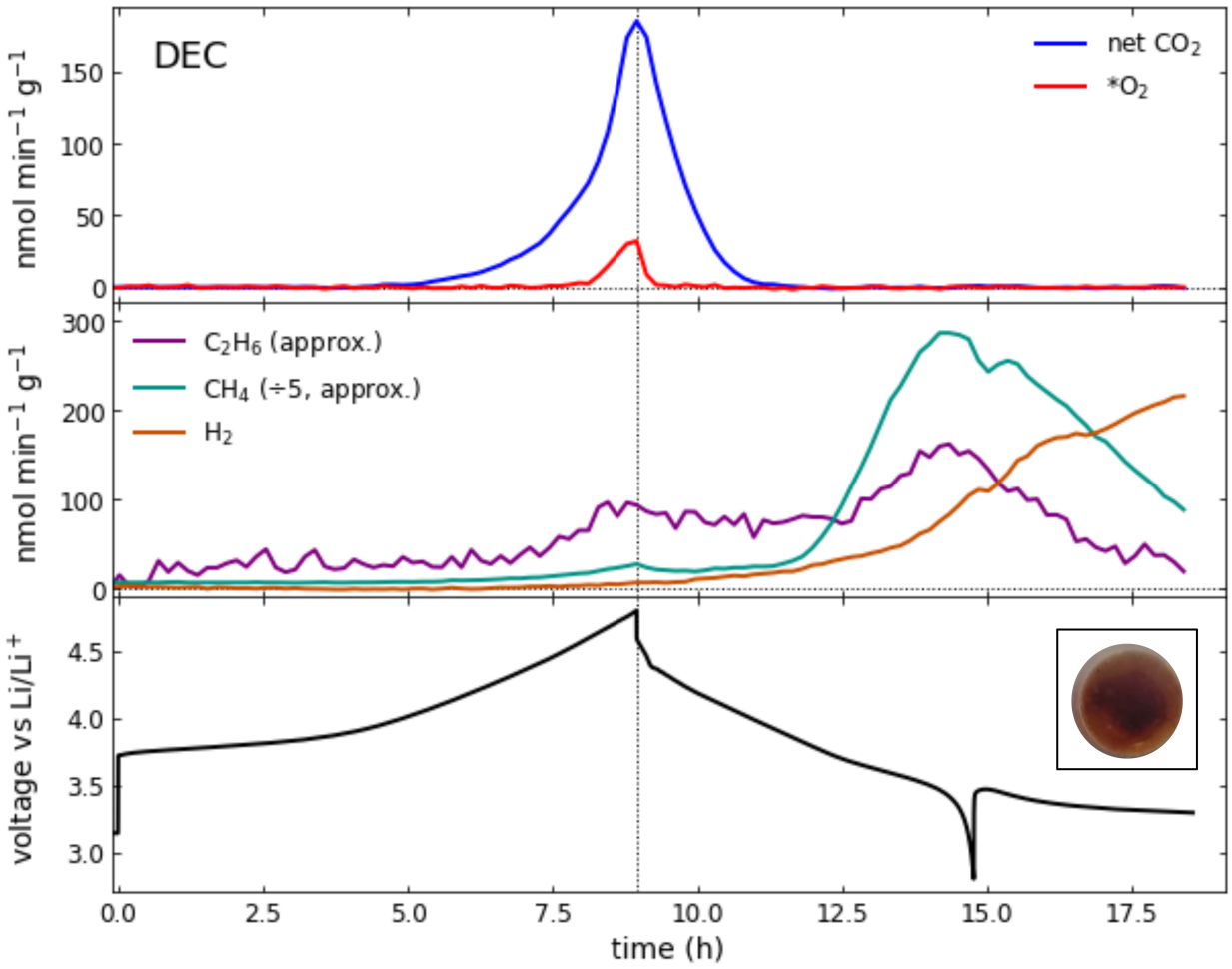

Figure 4.7: DEC gas evolution rates and voltage profile for the first cycle of ^{18}O-NMC622.

DEC was unstable as a single-solvent electrolyte for ^{18}O-NMC622/Li cells. Figure 4.7 shows the voltage profile for DEC for the first cycle as well as the gases evolved from the cathode and anode. As seen in the middle panel, during Li plating at the beginning of charge ethane is evolved as a reduction product. Above 4.2 V we observe an increase in C_2H_6, H_2, and CH_4 evolution that extends into discharge. This is due to significant TM dissolution from the ^{18}O-NMC622 and eventual plating on the Li counter/reference electrode. The voltage

continues to fall during OCV after discharge as the gases continue to evolve from the Li electrode. In the bottom panel inset is an image of the separator/DEC electrolyte on top of the Li electrode, showing a brown/red color uniformly throughout the electrolyte, as has been observed before for thermal decomposition of linear carbonates with $LiPF_6$ as the salt.[91] The particularly aggressive "peculiar decomposition" of DEC as a single solvent compared to DMC has been observed before.[92,93]

Significant TM dissolution for DEC compared to the other electrolytes may be due to the more abstractable hydrogens of the α carbon, eventually leading to creation and dissolution of TM complexes from oxidation of DEC.[7] Additionally unique to DEC is that no $^*O_2$ is evolved during discharge. In every other electrolyte tested, a separate $^*O_2$ peak on discharge is discernible from the main peak evolved on charge, which we previously attributed to a phase change. This lack of discharge oxygen is likely due to significant structural loss/changes at the ^{18}O-NMC622 surface due to the TM dissolution.

C*OO is observed to evolve for both single-solvent linear carbonates tested. In a recent study, DMC exposed to $^1O_2$ was not found to produce carbon dioxide or any other gaseous products, making a ring-opening mechanism similar to that presented in Scheme 4.2 unlikely. From what reaction then does C*OO originate in the linear carbonates?

Transesterification of EMC has been observed to produce DMC, DEC, and larger dicarbonates in the bulk electrolyte after aging, with the largest extent occurring in the first formation cycles.[76,92] The origin of the transesterification products, whether from oxidation or reduction, is debated. Lithium alkoxides formed reductively at the anode are thought to be a source of the transesterification,[92] but transesterification products are also known to be produced from acids originating from salt decomposition, particularly at elevated temperatures.[94] These products have been observed in both half and full cells and it has also been found that increasing the anodic cut-off potential increases the extent of the transesterification products.[95] Correlated to the increase in transesterification products also was an impedance growth on the positive electrode, which was proposed to be related to oxidative decomposition at high potentials on the positive electrode.

One possible source of the transesterification is first a base-driven hydrolysis as shown in Scheme 4.3 for linear carbonates. The produced ROH, with R = CH_3, C_2H_5, could further react to yield transesterification products, which in EMC electrolytes would give DMC, EMC, and DEC as possible products.

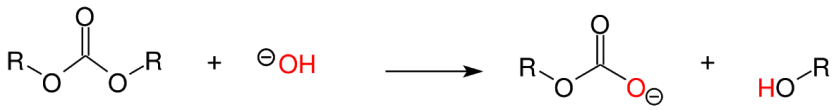

Scheme 4.3: Linear Carbonate Hydrolysis. R = C_2H_5 for DEC, CH_3 for DMC.

If the nucleophile originated from the ^{18}O-NMC622 surface and the RCO_3^- further

decomposed to carbon dioxide at high potentials, C*OO would then be produced much like in Scheme 4.1. In support of this scheme, nucleophilic attack by the TMO surface oxygen on the carbonyl carbon of DEC has been proposed to explain observed surface films of DEC adsorbed onto $LiCoO_2$ as detected by XPS.[96]

Cyclic carbonate additives to EC/DEC. The cyclic additives VC and FEC have been found to prevent transesterification. VC is preferentially consumed and prevents transesterification until depletion of VC, while FEC prevents transesterification by more effective passivation.[76] However, extended cycling beyond initial formation cycles with higher cut-off potentials with FEC will eventually yield transesterification products.[95]

As shown in Figure 4.8 and given in Table 4.2, C*OO is detected in both FEC and VC comparable to that of the baseline EC/DEC electrolyte, slightly suppressed in FEC and slightly elevated in VC. This makes the reaction as given in Scheme 4.3 unlikely to be a significant route for transesterification products, though a possible route for C*OO. It is clear that whatever reaction(s) produce(s) C*OO, the presence of cyclic additives to the concentration of 2 vol% does not have a dramatic effect.

FEC is preferentially reduced during Li plating (charge) to give CO_2[97] and as seen in Figure 4.4 it is the only electrolyte to evolve CO_2 at the onset of Li plating. In addition to CO_2 we observe a small amount of H_2 (0.2 µmol g^{-1}) evolved at just the onset of charge for FEC. The rate of CO_2 evolution is < 20 nmol min^{-1} g^{-1} and the cumulative CO_2 evolved from Li plating accounts for 5.4 µmol g^{-1} of the total CO_2, leaving 8.4 µmol g^{-1} CO_2 stemming from reactions at the positive electrode. FEC is predicted to dimerize and yield CO_2 when reduced, giving rise to a fluorinated SEI on the anode.[98] FEC is however also predicted to produce VC after defluorination yielding LiF on the surface of the anode.[99] Although VC also has been reported to reduce at the anode forming poly(VC) and evolving an amount of CO_2 from the terminal groups, we do not detect an initial or constant plating evolution of CO_2 for VC as for FEC, and so it is assumed that the majority of the detected CO_2 evolved for the VC cell is from the positive electrode. Any solvated CO_2 that may be liberated from VC reduction at the anode could scavenge Li alkoxides produced from electrolyte reduction, which is believed to be a mechanism of VC-mediated transesterification prevention.[100]

As additives, VC and FEC have been shown to also reduce parasitic reactions at the positive electrode.[59,101,102] From a gas analysis perspective, in the first cycle FEC shows an enhanced decomposition of $Li_2C^*O_3$ to C^*O_2 of 1.7 µmol g^{-1} compared to the baseline EC/DEC, which may be to due to better passivation of the ^{18}O-NMC622 surface, or in other words less EC/DEC decomposition, or due to an increase of acidic groups, which would have to be electrochemically formed from decomposition of FEC as there is a voltage dependence of C^*O_2 evolution. FEC also showed less C*OO, which is also consistent with a better passivation of the ^{18}O-NMC622 surface. Additionally, despite an increased attainable capacity, the $^*O_2$ released is lower than baseline. The purely electrolyte originating carbon dioxide of 8.4 µmol g^{-1} CO_2, after subtracting the plating evolution of CO_2, is comparable to the baseline EC/DEC of 7.7 µmol g^{-1} CO_2.

The increased outgassing of CO_2 shows that VC is consumed and decomposed on the ^{18}O-NMC622 surface. Although C*OO is slightly enhanced, both C*OO and C*O_2 evolved are comparable to the baseline EC/DEC electrolyte. This shows that although VC is decomposed, it is not done so preferentially as there is no major change in the other surface reactions, highlighting that VC is not an effective passivating agent for ^{18}O-NMC622. The rate and cumulative $^*O_2$ is decreased in VC compared to the baseline, but this is more likely due to a lower extent of delithiation in the first charge.

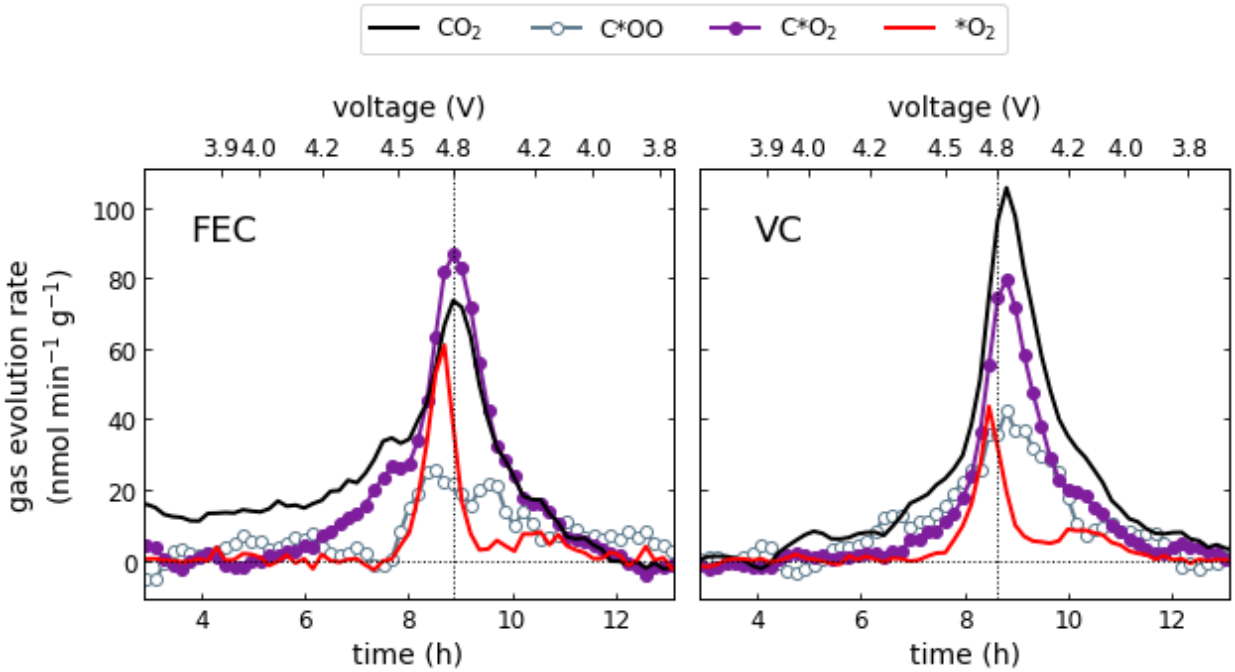

Figure 4.8: Detail of gas evolution rates for FEC and VC additives (2 vol% in EC/DEC 1 M $LiPF_6$) for the first cycle of ^{18}O-NMC622.

LiTFSI vs $LiPF_6$. As LiTFSI-based electrolytes exhibit higher hydrolytic and thermal stability than $LiPF_6$-based electrolytes, due to differing tendencies to dissociate to create Lewis acidic species, it may be expected that LiTFSI and $LiPF_6$-based carbonate electrolytes will exhibit different outgassing behaviors on cycling of ^{18}O-NMC622, measurable by the total CO_2 evolved and its ^{18}O-content. The differences in the rates of carbon dioxide and $^*O_2$ evolution for the salts LiTFSI and $LiPF_6$ are shown in Figure 4.9.

Another view of the outgassing and voltage profiles for the first 4.8–2.8 V-cycle for the two salts are shown below in Figure 4.10. Note that this is not the same batch of ^{18}O-NMC622 used in the rest of this chapter, but is the same batch used in Chapter 3. The voltage profiles and capacities are identical between the two and the general rates of CO_2 and O_2 evolution exhibited are comparable: CO_2 evolution—Li_2CO_3 and electrolyte-originating—begins at $\approx$ 3.9 V, and O_2 is released at $\approx$ 4.45 V. As seen in Table 4.2, the largest difference is the portion of Li_2CO_3 decomposition of the total CO_2 evolution: for $LiPF_6$ direct Li_2CO_3 decomposition is 36 % of the total CO_2 evolution and for LiTFSI 32 % the total CO_2.

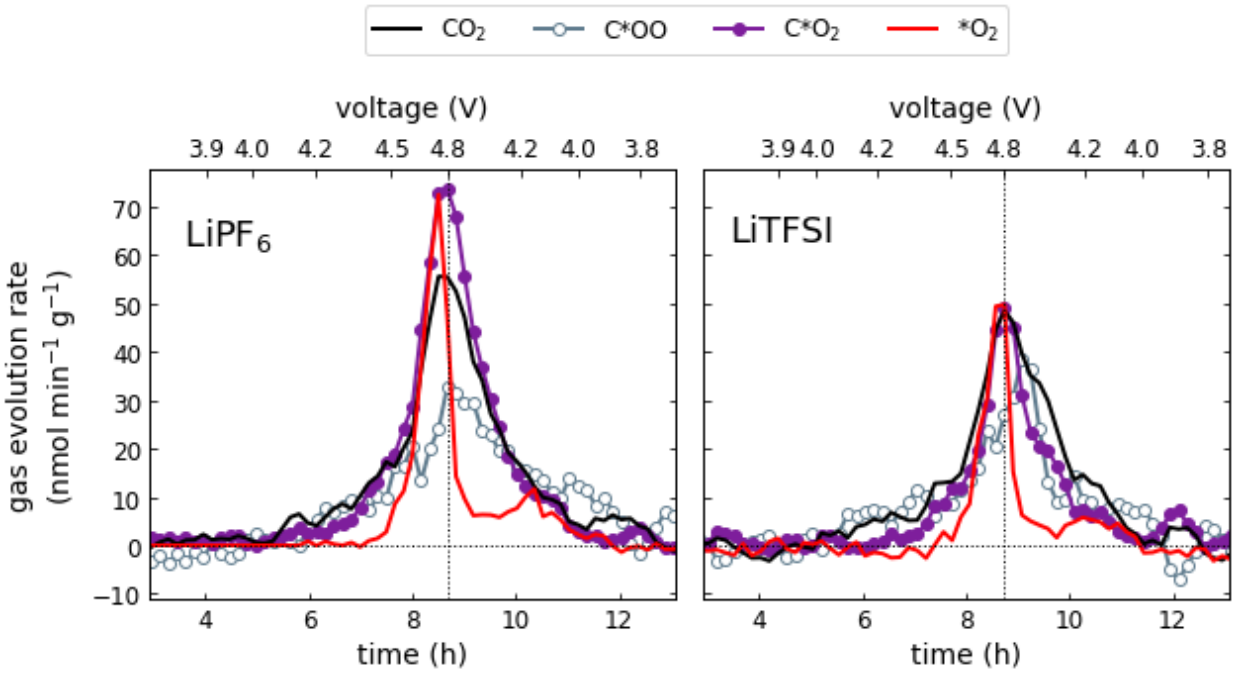

Figure 4.9: Detail of gas evolution rates for electrolytes prepared from either LiTFSI or $LiPF_6$ for the first cycle of ^{18}O-NMC622.

Examining this further, as shown in Table 4.2, the C*OO:CO_2 ratio is comparable for LiTFSI and $LiPF_6$ ($\approx$ 3:4). Although there are differences in the solvation shell compositions of LiTFSI and $LiPF_6$ in mixed carbonate solvents,[103,104] the net result of the electrolyte reactivity as exhibited by outgassing is similar between the two salts.

Although there is generally less gas evolved for the salt LiTFSI compared to $LiPF_6$ (though not in every cell tested; see Figure 4.11), a significant difference is due to the poorer passivation of the Li anode, leading to increased TM dissolution and plating. This difference between the two salts is exhibited in ^{18}O-NMC622 charged to 4.8 V and allowed to rest. Due to the poorer ability of LiTFSI to form a stable SEI on Li, ^{18}O-NMC622 exhibits a larger extent of self-discharge and TM dissolution in LiTFSI, which leads to voltage fade and TM plating on the Li anode, evolving C_2H_4 from EC reduction. As shown in Figure 4.11, the voltage fade in LiTFSI corresponds to increased evolution of C_2H_4 during rest as compared to $LiPF_6$. During charge of LiTFSI, $\approx$ 10 nmol C_2H_4 min^{-1} g^{-1} is evolved due to EC reduction from Li plating. During rest after charge the C_2H_4 evolution rate reaches 30 nmol min^{-1} g^{-1}, with the OCV falling to $\approx$ 4.4 V for LiTFSI compared to 4.6 V for $LiPF_6$, indicating a large extent of self-discharge.

Glymes. Glymes have been explored as cosolvents with cyclic carbonates for Li anodes in early studies[93] and as electrolytes for Li-O_2 cells.[38] Although glyme electrolytes like DME and TEGDME have shown better stability for the reduction of O_2 to Li_2O_2 in Li-O_2 electrochemistry compared to carbonate electrolytes, instabilities exist during charge

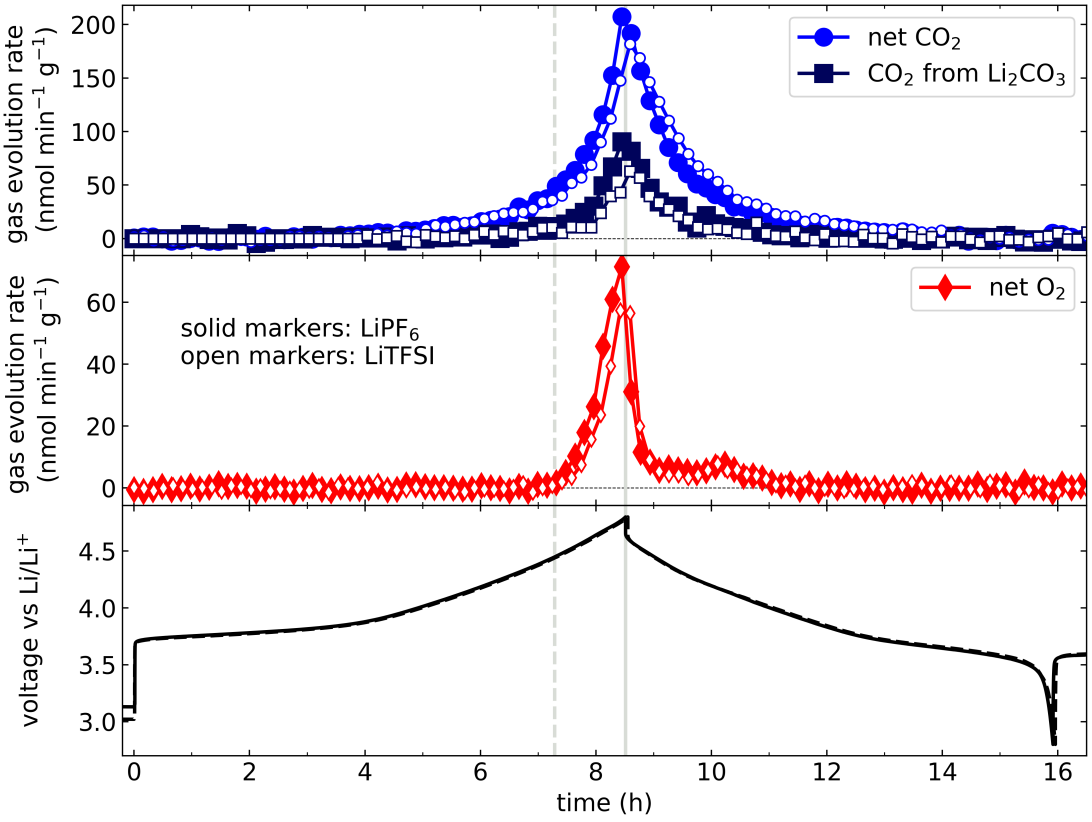

Figure 4.10: Gas evolution from ^{18}O-NMC622 on the first 4.8–2.8 V cycle for LiTFSI and $LiPF_6$ electrolytes. The $LiPF_6$ data were presented in Figures 3.1 and 3.2 and Table 3.1.

of Li_2O_2 to reform O_2. Electrochemical oxidation of Li_2O_2 in glyme electrolytes creates carbonates and formates that at higher potentials decompose to yield volatile CO_2.[31,38]

While in DME both forms of carbon dioxide of C*OO and C*O_2 were observed, in TEGDME only decomposition of $Li_2C^*O_3$ to C*O_2 was detected. As seen in Figure 4.2, the peroxo-like layer formed in the first cycle for TEGDME, but very little $^*O_2$ was evolved compared to what is observed for the same charge capacity in carbonate-based electrolytes. The overall low outgassing for the glyme electrolytes warrants future study for the understanding of the irreversible changes of the ^{18}O-NMC622 surface. For example, highly concentrated DME-based electrolytes have recently been demonstrated to yield promising cycling performance for Li/NMC622 cells.[105]

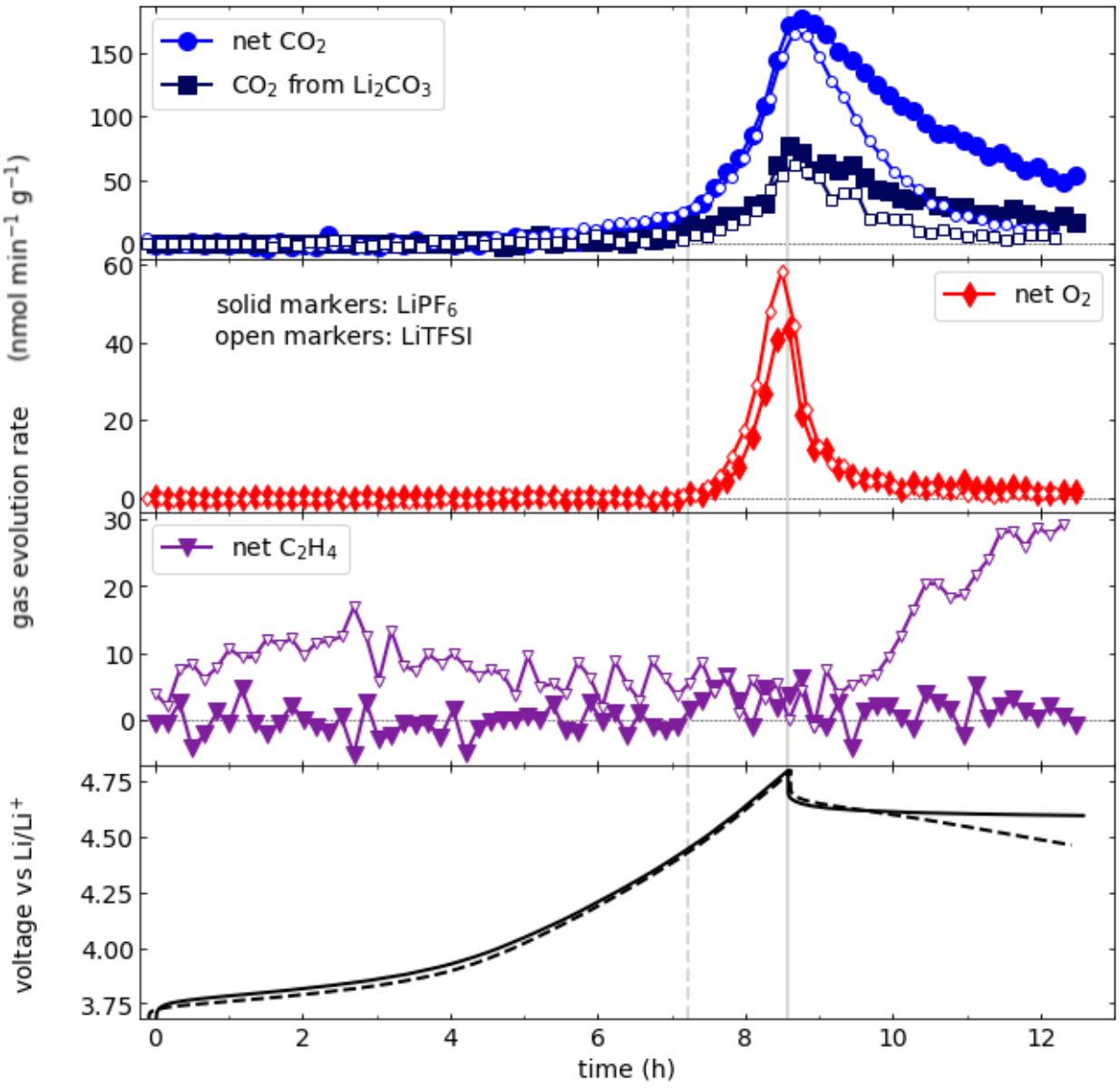

Figure 4.11: Gas evolution from ^{18}O-NMC622 on the first charge to 4.8 V and subsequent rest for LiTFSI and $LiPF_6$ electrolytes. The $LiPF_6$ data is that already presented in Figure 3.3 and Table 3.4.

4.4 Conclusions

In this chapter we have shown that the formation of the peroxo-like surface layer is largely independent of the identity of the electrolyte and is instead a material property of the prepared ^{18}O-NMC622 and, for constant current, is formed as a function of the extent of delithiation. This suggests that electrolyte engineering may be limited in utility for preventing irreversible surface changes of TMOs and that other TMO modifications are

needed to help prevent them. Given that electrolyte additives have been shown to improve cycling performance, our results also suggest that surface transformations of the positive electrode may not govern long-term stability.

We have also shown that in all cyclic carbonate-based electrolytes except that with VC as an additive, surface Li_2CO_3 degradation has the highest rate of evolution of all forms of carbon dioxide at the top of charge above 4.6 V, showing that for the first cycle consideration of Li_2CO_3 degradation is required to understand the reactivity exhibited by gas evolution. Furthermore, in all electrolytes tested except for pure EC, the cumulative C^*OO evolved from the mixed ^{18}O-NMC622 surface/electrolyte reactivity is less than the amount of $Li_2C^*O_3$ degraded to C^*O_2.

That said, electrolyte stability with the ^{18}O-NMC622 surface deserves further consideration. All electrolytes except TEGDME evolved C^*OO originating from a mixed electrolyte/^{18}O-NMC622-surface reaction, which indicates reactive surface $^*O$ that yields potential-dependent carbon dioxide evolution, suggesting electrochemically-initiated or state of charge-dependent decomposition mechanisms other than chemical reactions. The existence of both a peroxo-like surface on NMC622 after just one cycle and the inevitable surface contaminant Li_2CO_3 complicate the determination of the origin of the parasitic reactions, as oxidation of both Li_2CO_3 and Li_2O_2 have been shown to release $^1O_2$.[41,42] To further the understanding of the reactivity of the ^{18}O-NMC622 surface at high states of charge future studies must distinguish between surface contaminants like Li_2CO_3 and the formed peroxo-like surface.

4.5 Acknowledgements

The author gratefully acknowledges support from the Department of Defense (DoD) through the National Defense Science & Engineering Graduate Fellowship (NDSEG) Program. We thank Umicore for receipt of the NMC622 powder.

5 | The influence of altering surface contaminants and defects on $LiNi_{0.6}Mn_{0.2}Co_{0.2}O_2$

5.1 Abstract

By altering the surface of $LiNi_{0.6}Mn_{0.2}Co_{0.2}O_2$ (NMC622) we show that surface defects and contaminants dominate the outgassing and irreversible surface transformations during the first electrochemical cycle. To alter the surface defects and contaminants without changing the bulk structure of the NMC622, we perform mild methanol and water rinses, a water soak, a water rinse and subsequent heat treatment, as well as purposeful increase of the surface Li_2CO_3. By combining isotopic labeling, gas analysis, and peroxide/carbonate titrations, we observe that these alterations change the surface Li_2CO_3, surface hydroxides, and the local defects, which in turn alter the nature and extent of the outgassing to O_2 and CO_2. In particular, by adding additional surface Li_2CO_3, we observe an increase in electrolyte decomposition at high potentials. By increasing the surface lithium vacancies the coupled NMC622 surface/electrolyte reactivity increases. Our results highlight that outgassing of Li-ion cathode materials is highly dependent on the synthesis routes and comparison of varying compositions must take into account these differences to make any meaningful comparisons. We also show that simple rinsing procedures may be an effective route to controlling interfacial reactivity of Li-ion active materials.

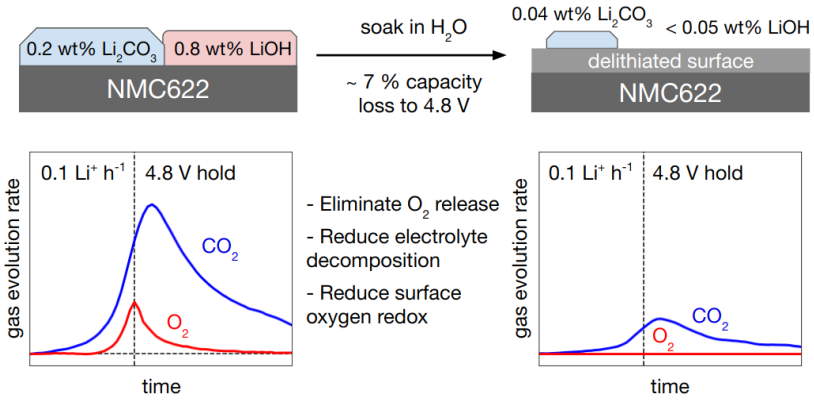

5.2 Introduction

Syntheses of Ni-rich lithium transition metal oxides (TMOs) by calcination are sensitive to the parameters of precursor stoichiometry, O_2 partial pressure, and temperature, and time. With high Ni-content it is difficult to obtain phase-pure compounds with the desired stoichiometry.[47] For example, in the pure Ni limit, $LiNiO_2$ is particularly sensitive, often producing off-stoichiometric $Li_{1-x}Ni_{1+x}O_2$ with Ni in Li sites, which leads to poor performance. To prevent this off-stoichiometry, early studies suggested excess LiOH was needed to produce near stoichiometric $LiNiO_2$, but resulted in large surface deposits of unreacted LiOH. As strongly alkaline impurities lead to poor performance, researchers recommended washing synthesized $LiNiO_2$ with H_2O to remove the surface residual LiOH.[36]

Bulk defects are critical considerations for any TMO's electrochemistry and intrinsic point defects are easily formed at high temperature during synthesis. More modern studies have detailed these bulk defects obtained in the synthesis of Ni-rich TMOs based on stoichiometry and calcination conditions. For Li_2CO_3 as the Li source, insufficient calcination temperatures will leave unreacted surface Li_2CO_3 that will lead to a Li deficient lattice, promoting Li/Ni site defects. For overly high calcination temperatures, Li_2CO_3 will decompose, but selective Li/O loss during the calcination will again lead to Li deficiency and Li/Ni mixing.[52] Experimental observations of Li/Ni mixing have been confirmed by theoretical calculations, showing that the antisite defects Li_{Ni} and Ni_{Li} have favorable formation energetics and that Ni^{3+} is easily reduced to Ni^{2+} at synthesis conditions.[106,107]

The same high temperature bulk defects are relevant for the surface defects seen at room temperature. The surface is easily reduced and the defects there play a major role in outgassing and behavior at high states of delithiation.[107] Even before electrochemical delithiation, surface defects may arise from reconstruction due to reaction with the electrolyte and atmosphere, or due to O_2 loss after prolonged storage in low O_2 partial pressure. The surface may also be contaminated by unreacted Li precursors like Li_2CO_3 and LiOH (which may react with any CO_2 forming $LiHCO_3$ and Li_2CO_3) or from reaction with the atmosphere, leading to near-surface delithiation and even denickelation,[55] forming surface hydroxides, bicarbonates, and carbonates: $Li_{Li}^{\times}, Ni_{Ni}^{\times} -> LiOH, LiHCO_3, NiCO_3$, etc. With surface nonstoichiometry, there can be rearrangement leading to disorder with defects including Li/Ni mixing and rocksalt/spinel like layers, which, when large enough, can impede Li transport and lead to poor cell performance.

With electrochemical delithiation, new surface defects and reconstruction arise. Increasing the anodic cut-off potential, i.e., increasing the extent of delithiation, increases the growth of a disordered surface for Ni-rich materials. This disordered surface can impede Li transport and has been blamed for poor cycling performance of Ni-rich materials. Washing techniques have been used to modify the surface of TMOs without introducing new compounds and in some cases of mild H_2O[35] and alcohol washes,[44] have been found to improve the cycling performance. This is likely due to changes in the local surface defects.

In the previous two chapters we showed that irreversible surface changes, normally observed by electron microscopy techniques, were also quantifiable by an increase in the surface peroxo-like behavior, as measured by a peroxide titration. As shown in Chapter 4, the formation of the peroxo-like surface was largely independent of the identity of the electrolyte and instead was a function of the extent of delithiation. This behavior is likely highly dependent on the surface defects and the surface delithiation extent, and thus we expect washing techniques may give rise to significantly different surface reconstruction.

In this chapter we alter the surface of a pre-synthesized $LiNi_{0.6}Mn_{0.2}Co_{0.2}O_2$ (NMC622) to study the effects of surface modifications without altering the bulk material. We employ a mild wash with H_2O, with and without extra heat treatment steps; mild wash with methanol; a prolonged soak with H_2O; and introduce extra surface Li_2CO_3 to alter the baseline material. We additionally employ isotopic labeling and carbonate/peroxide titrations to tie the outgassing behavior and irreversible surface changes to the initial surface defects and discriminate electrolyte, Li_2CO_3, and other NMC622 surface degradation. We find that these treatments dramatically influence the outgassing behavior of NMC622, with the most striking observation being the nearly complete suppression of outgassing after soaking the NMC622 material in H_2O for 1 h.

5.3 Results and Discussion

In this chapter we employ similar electrochemical tests as in the previous chapters to study how the surface defects and contaminants play a role in the outgassing, degradation of the electrolyte, and irreversible surface reconstruction of the NMC622 surface. These electrochemical tests given in this chapter are: cycling from 4.8–2.8 V, charging to 4.8 V, and cycling from 4.8–2.8 V with a 6 h potentiostatic hold at 4.8 V before discharge.

The following NMC622 materials were prepared:

^{18}O-NMC622: This is considered the baseline material and was prepared similarly to those as detailed in previous chapters. Briefly, the ^{18}O-NMC622 was enriched under $^{18}O_2/N_2$ at 800 °C for 8 h. The ^{18}O-NMC622 surface had an enrichment of 21.7 % ^{18}O with a surface carbonate amount of 24.7 µmol g^{-1}.

For brevity the -NMC622 suffix is dropped from the given names of the following materials:

^{18}O-MeOH: ^{18}O-NMC622 powder was rinsed twice with methanol to selectively remove surface hydroxide species and largely not disturb the surface carbonate species. The MeOH-rinsed powder was first dried under N_2 and then dried under vacuum at 150 °C in the glovebox heated antechamber. The washing and filtering was performed under N_2 and the vacuum filtered powder was brought into the glovebox with < 30 s exposure to air. The rinseate was titrated with HCl to determine that 30 µmol g^{-1} OH^- species were removed

from the ^{18}O-NMC622 surface to yield ^{18}O-MeOH-NMC622. The ^{18}O-MeOH surface had an enrichment of 21.0 % ^{18}O with a surface carbonate amount of 23.1 µmol g^{-1}. Comparing to the surface Li_2CO_3 given earlier for ^{18}O-NMC622, only mild changes to the surface Li_2CO_3 were observed by rinsing with MeOH, as expected.

^{18}O-H_2O: ^{18}O-NMC622 powder was swirled with ultrapure degassed H_2O for 30 s, vacuum filtered, and then dried under vacuum at 150 °C in the glovebox heated antechamber. The washing and filtering was performed under N_2 and the vacuum filtered powder was brought into the glovebox with < 30 s exposure to air. The ^{18}O-H_2O surface had an enrichment of 18.6 % ^{18}O with a surface carbonate amount of 14.1 µmol g^{-1}. The enrichment of the surface carbonate is slightly diminished compared to the unwashed ^{18}O-NMC622. Although this may be due to a small growth due to brief atmospheric exposure, the O_2 released during cycling has the same enrichment as that measured by the carbonate titration.

^{18}O-soak: ^{18}O-NMC622 powder was allowed to soak for in ultrapure degassed H_2O in two 30 min stages to remove the surface hydroxide and carbonate species and allow for sufficient time for some delithiation of the lattice. The powder was then vacuum filtered and dried under vacuum at 150 °C in the glovebox heated antechamber. The soaking and filtering was performed under N_2 and the vacuum filtered powder was brought into the glovebox with < 30 s exposure to air. The ^{18}O-soak surface had an enrichment of 8.0 % ^{18}O with a surface carbonate amount of 4.8 µmol g^{-1}.

H_2O-^{18}O: Pristine NMC622 (without first an ^{18}O enrichment step) was first washed with ultrapure degassed H_2O in two 30 s stages, dried, and then enriched with ^{18}O with the same thermal treatment as given for ^{18}O-NMC622. The H_2O-^{18}O surface had an enrichment of 20.3 % ^{18}O with a surface carbonate amount of 13.4 µmol g^{-1}.

Li_2CO_3-^{18}O: Pristine NMC622 was ground with Li_2CO_3 and then enriched under $^{18}O_2$ with the same thermal treatment as given for ^{18}O-NMC622. The Li_2CO_3-^{18}O surface had an enrichment of 19.9 % ^{18}O with a surface carbonate amount of 78.1 µmol g^{-1}.

5.3.1 Possible surface defects and changes induced by surface modifications. Before analyzing our results for the baseline and surface modified NMC622s we will discuss the possible surface defects and contaminants present on each prepared NMC622. None of the prepared NMC622s had any peroxo-like surface character prior to electrochemical delithiation, though all had surface carbonates.

The surface carbonate and hydroxide present on the baseline ^{18}O-NMC622 material may be a mixture of unincorporated Li precursors from the initial calcination, or carbonates and hydroxides formed from reaction with the atmosphere that, however, do not fully reincorporate during the ^{18}O-enrichment heating step at 800 °C.

Oxygen vacancies, as formed by insufficient oxygen partial pressure in synthesis, have been

correlated with increased Li/Ni mixing in synthesis.[108] One route for charge compensation of the oxygen vacancies is Ni^{3+} reduction to Ni^{2+} as $O_O^{\times} + 2\,Ni_{Ni}^{\times} \longrightarrow V_O^{\bullet\bullet} + 2\,Ni_{Ni}' + \frac{1}{2}\,O_2$, then allowing Ni^{2+}/Li^{+} site mixing.

That stated, oxygen vacancies formed to charge compensate Co vacancies (from intentional deficiency) in synthesis have been shown to decrease the extent Li/Ni mixing, but resulted in increased surface degradation via reaction with the atmosphere as catalyzed by the oxygen vacancies.[81] For metal oxides, even without lithium, slightly reduced surfaces, i.e., surfaces with oxygen vacancies, can accelerate reactions with the atmosphere compared to stoichiometric surfaces.[109] As both studies on oxygen vacancies in references [81] and [108] found increased surface reactions and contaminants for increased oxygen vacancies, this inevitable reactivity is a complicating factor in understanding the surface and defect chemistry of TMOs, as the surfaces will form surface hydroxides and carbonates. This also shows that the degree of site mixing may not be the figure of merit for surface reactivity in Ni-rich materials.

As the surface of Ni-rich TMOs is reduced compared to the bulk after synthesis and lithium vacancies have lower formation energies than most transition metals,[106] we then consider that the likely most populous initial surface defects on the baseline material are hole states on oxygen, oxygen vacancies, lithium vacancies, and increased Ni^{2+} compared to the bulk. None of these give rise to any detectable peroxo-like surface behavior.

In all of the rinsing treatments performed, H_2O will dissolve both carbonates and hydroxides and MeOH will dissolve hydroxides, thereby removing a portion of surface contaminants in all cases. Another possibility is simply that washing with H_2O or MeOH will dissolve nano-sized surface aggregates, thereby reducing the reactivity with the electrolyte.

The short H_2O rinse ($\approx$ 30 s) to create the ^{18}O-H_2O-NMC622 only removed approximately half of the surface carbonate. To our knowledge there are no other studies on surface changes from such short exposures to H_2O. As carbonates are less soluble than hydroxides in water, this short exposure to water will remove more surface hydroxides than carbonates, remove any nano-sized surface aggregates, and may delithiate the outermost surface of the ^{18}O-NMC622 lattice beyond the baseline ^{18}O-NMC622.

The H_2O soak procedure (cumulative 1 h) to create the ^{18}O-soak-NMC622 is comparable to other published washing studies. A recent study on washing and heat treatment methods for $LiCoO_2$ found that after soaking in water for 1 h the surface Co^{2+} compounds were removed and the outermost lattice was delithiated and, though the initial surface carbonates and hydroxides were removed, new CoO(OH) was formed on the surface.[110] Similar behavior is expected for the ^{18}O-soak material.

In the same study (reference [110]), after heating the washed sample to 700 °C, the surface CoO(OH) decomposed to the lithium deficient, densified Co^{2+} containing Co_2O_3. Although this surface modification was found to decrease the extent of deposition of electrolyte degradation products after cycling, the cycling performance was diminished due to the

increased polarization. A more mild heat treatment step to 400 °C was found to form the rocksalt CoO. In this chapter, to prepare the NMC622 H_2O-^{18}O material, the pristine NMC622 is first mildly washed (not allowed to soak in H_2O) and then subject to the heat treatment of the ^{18}O enrichment procedure. Due to the decrease in surface lithium compounds from the H_2O rinsing, the heat treatment will produce surface Li vacancies, potentially accompanied by O loss to charge compensate and back migration, likely creating a densified surface analogously, though not to the same extent, as the aforementioned study.

Rinsing with EtOH has been shown to improve cycling performance and resistance to reaction with atmosphere in Ni-rich TMOs. The improved performance even without atmospheric aging was attributed to decreased electrolyte reaction with surface hydroxides.[44] An additional possibility for improved performance by reducing surface hydroxyl groups could be from diminished reactivity of the surface hydroxides with PVDF during electrode preparation, a reaction which defluorinates the polymer and creates surface fluorides.[111] As rinsing with EtOH was not found to delithate the lattice of $LiNiO_2$,[112] it is not expected that rinsing with MeOH will drastically change the surface lattice defects of NMC622, other than solubility of small surface aggregates.

Lastly, in grinding excess Li_2CO_3 with NMC622 and performing a heat treatment step to create the Li_2CO_3-^{18}O-NMC622, though obviously more Li_2CO_3 is introduced and remains on the surface, the surface Li vacancies are likely diminished by providing excess lithium in the additional calcination step.

5.3.2 Behavior of surface modified NMC622s in the first electrochemical cycle. All NMC622 preparations were tested with EC/DEC (1:1, v/v) 1 M $LiPF_6$ as the electrolyte (Appendix D) and subject to one 4.8–2.8 V electrochemical cycle. The achieved charge, discharge, and irreversible capacities for the first cycle are given in Table 5.1. All NMC622s achieved irreversible capacities of 0.11–0.12 Li units, comparable to that observed in earlier chapters. Although most NMC622 preparations achieved charge and discharge capacities within $\approx$ 0.02 Li of each other, ^{18}O-soak, which was allowed to sit in H_2O for a total of 1 h, had a delithiation capacity of only 0.82 Li units up to 4.8 V, $\approx$ 7 % lower than the rest of the NMC622 materials.

()-NMC622	charge capacity (Li units)	discharge capacity (Li units)	irreversible capacity (Li units)
^{18}O	0.877	0.768	0.109
^{18}O-MeOH	0.859	0.751	0.108
^{18}O-H_2O	0.880	0.773	0.107
^{18}O-soak	0.816	0.710	0.106
Li_2CO_3-^{18}O	0.878	0.758	0.120
H_2O-^{18}O	0.853	0.738	0.115

Table 5.1: Charge, discharge, and irreversible capacities for all NMC622s in the first cycle.

Formation of the peroxo-like surface. In Chapters 3 and 4 we found that the formation of the peroxo-like surface on NMC622 was a function of the extent of delithiation and was largely independent of the choice of electrolyte. After the first 4.8–2.8 V cycle we extracted the NMC622 electrodes and titrated them as explained in previous chapters and Appendix C. The oxygen released, as an indicator of peroxo-like character at the surface, is plotted versus the achieved charge capacity in Figure 5.1. Additionally plotted in open circles are the results for the similarly prepared baseline ^{18}O-NMC622 at various states of delithiation from Chapter 3.[85] The batch of ^{18}O-NMC622 prepared for this chapter is observed to be inline with the previous results, with the extent of the peroxo-like surface close that that predicted by the charge capacity. In contrast, all surface modified NMC622s exhibited lower degrees of peroxo-like surface formation compared to the baseline material.

As an alternate view of the differences exhibited by the surface modifications, the extent of the peroxo-like surface is plotted versus the released lattice oxygen during the first cycle in Figure 5.2. As described in Chapter 3, for the baseline ^{18}O-NMC622 the peroxo-like surface is detected > 3.9 V (≈ 0.4 Li units) and O_2 released is detected above 4.45 V (≈ 0.75 Li

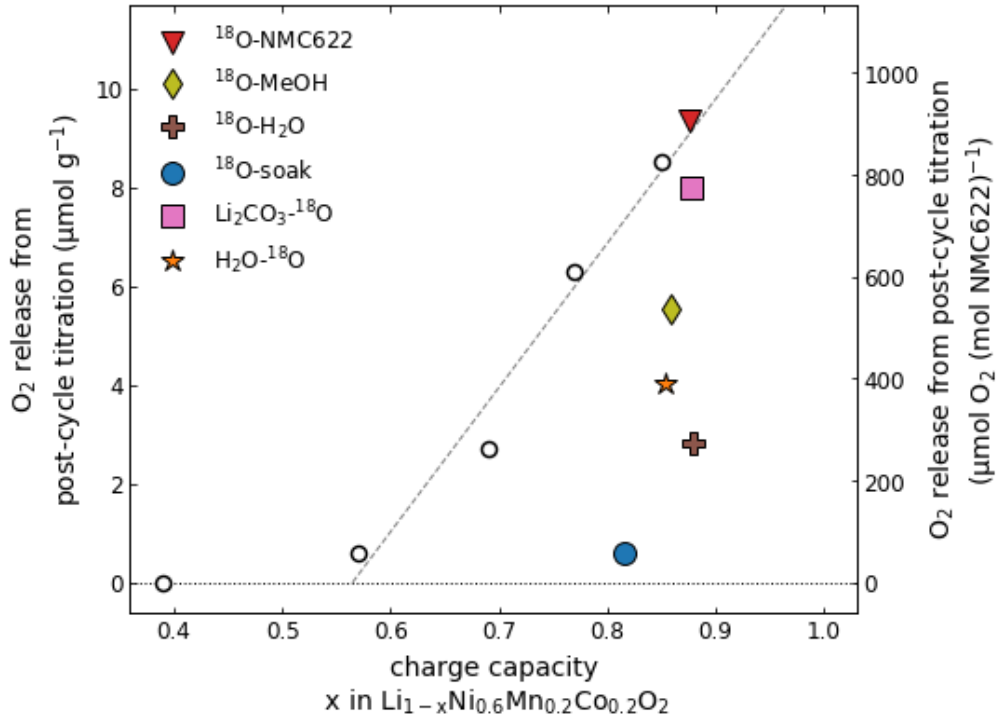

Figure 5.1: Extent of the peroxo-like surface versus achieved charge capacity for all NMC622s. O_2 released during an acid titration as detected after the 4.8–2.8 V-cycle versus the extent of delithiation. The open circles are from Chapter 3 and are titration results for a similarly prepared batch of ^{18}O-NMC622 with 3.9, 4.2, 4.4, 4.65, and 4.8 V as the anodic cut-off potentials. The dashed line is a linear fit for those results, excluding the 3.9 V cut-off potential with a ≈ 0.4 Li charge capacity.

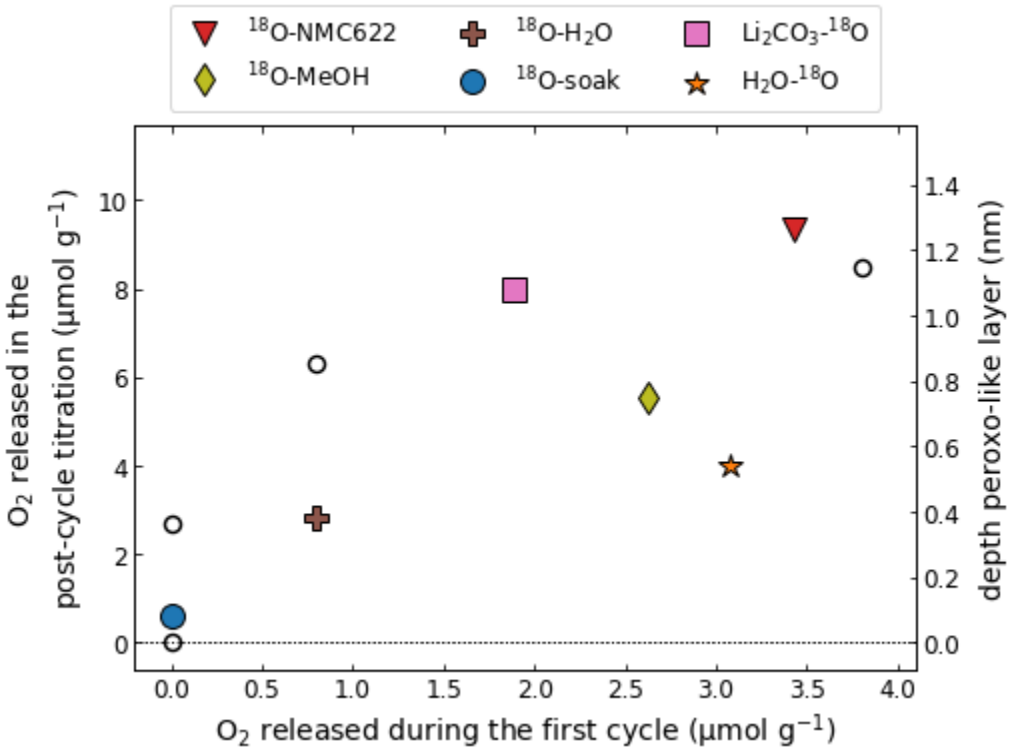

Figure 5.2: Extent/depth of the peroxo-like surface versus O_2 released for all NMC622s. O_2 released as detected from the post-4.8–2.8 V-cycle acid titration versus the extent of delithiation. The open circles are from Chapter 3 and are titration results for a similarly prepared batch of ^{18}O-NMC622 with 3.9, 4.2, 4.4, 4.65, and 4.8 V as the anodic cut-off potentials.

units). This behavior is plotted in the open circles as described for Figure 5.1. Also plotted on the right hand side is the estimated depth of the peroxo-like layer. It was assumed that all NMC622 preparations had identical surface areas for this estimate and although significant changes in the surface area are not expected from washing treatments,[110] this could not be experimentally measured due to insufficient quantities of material. Two of the NMC622s—^{18}O-NMC622 and Li$_2$CO$_3$-^{18}O—exhibit peroxo/O_2 release behavior generally in agreement with the previous results of Chapter 3. For the remaining three washed samples, the peroxo-like surface extent is about half of what is expected given the O_2 released during the cycle. Given that all wash/rinse treatments were found to decrease the formation of the peroxo-like surface character, it may be that H_2O and MeOH soluble surface species play a large role in its formation. For the final NMC622 in particular, ^{18}O-soak is remarkable because for a bulk delithiation of 0.82 Li, the detected surface peroxo-like character is approximately equal to that found for a delithiation of only 0.57 Li (4.2 V) for the baseline material. This near suppression warrants more examination, thus we next more closely examine the outgassing to attempt to understand these differences.

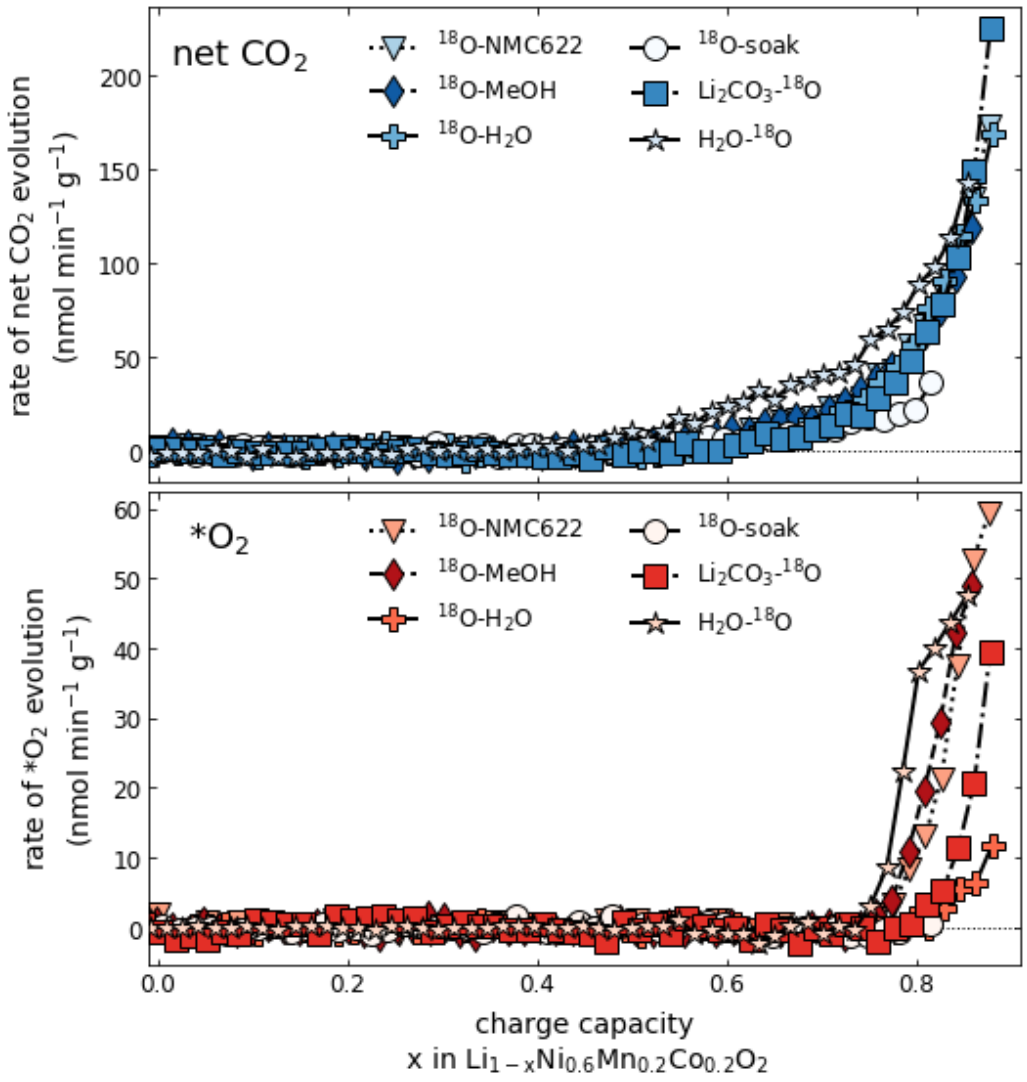

Figure 5.3: Total evolution rates of O_2 and CO_2 for all NMC622s during charge.
All NMC622s were galvanostatically charged at 0.1 Li^+ h^{-1} (26.75 mA g^{-1}) until 4.8 V and then immediately discharged to 2.8 V at the same current rate. The top panel shows the net rate of CO_2 evolution and the bottom panel the net O_2 evolution. All NMC622 preparations evolved CO_2 and all but ^{18}O-soak evolved O_2.

Gas evolution during the first cycle. The corresponding gas evolution rates for the charge portion of the first cycle are given in Figure 5.3, showing the net carbon dioxide evolution rate on top in blue, and net oxygen evolution rates on the bottom in red. Surprisingly, the CO_2 evolution rates are quite similar for all NMC622s, when plotted as a function of delithiation capacity. It can be readily seen, however, that the oxygen evolution rates are significantly different for the different surface modifications of NMC622.

The earliest onset for O_2 evolution occurs in the washed then heated NMC622, H_2O-^{18}O,

at ≈ 0.72 Li units. This is consistent with the speculation that the washing and heating process created surface lithium vacancies, thus creating an artificially high surface state of charge. The baseline ^{18}O-NMC622 and the MeOH-^{18}O both have onsets at ≈ 0.75 Li, the water rinsed, ^{18}O-H_2O, and extra Li_2CO_3 NMC622s both onset at ≈ 0.8 Li, and the water soaked ^{18}O-soak does not exhibit any O_2 evolution during the first cycle, which may be due to the lack of surface peroxo-like character as described earlier.

To understand further the differences exhibited by the surface modifications, it is necessary to distinguish the origins of the carbon dioxide evolved. As shown in the previous two chapters, the evolved carbon dioxide is a mixture of that stemming from direct ring opening of the carbonate electrolytes, direct decomposition of the surface Li_2CO_3, and a mixed electrolyte/NMC622 surface reaction. Using the notation as given in Chapter 4, we use *O to label each NMC622's surface oxygen to distinguish it from the natural abundance electrolyte oxygen. Here the surface oxygen encompasses all oxygen spatially correlated to the outermost surface of the NMC622 and is measured by the ^{18}O-enrichment of the surface Li_2CO_3 and, when possible, checked against the oxygen released during the first cycle. In other words, oxygen release during cycling is evolved solely as $^*O_2$ and carbon dioxide is evolved as a combination of CO_2, C*OO, and C$^*O_2$. As shown in the previous chapters, the majority of C$^*O_2$ evolved comes from decomposition of the original surface lithium carbonate, which we now write as $Li_2C^*O_3$.

Using this notation, the gas evolution rates from Figure 5.3 are replotted individually for each NMC622 material for the first 4.8–2.8 V cycle in Figure 5.4. The corresponding cumulative gas evolution is given in Table 5.2.

()-NMC622	$^*O_2$ (µmol g^{-1})	cumulative carbon dioxide in µmol g^{-1} (fraction of total evolution, %)			$\Sigma(CO_2)$ (µmol g^{-1})
		CO_2	C*OO	C$^*O_2$	
^{18}O	3.4	7.8 (34 %)	6.3 (28 %)	8.5 (38 %)	22.6
^{18}O-MeOH	2.6	6.7 (42 %)	3.3 (21 %)	6.0 (37 %)	16.0
^{18}O-H_2O	0.8	7.0 (35 %)	2.9 (15 %)	10.0 (50 %)	19.9
^{18}O-soak	0.0	1.9 (42 %)	0.6 (13 %)	2.1 (45 %)	4.6
Li_2CO_3-^{18}O	1.9	5.8 (25 %)	4.7 (20 %)	12.9 (55 %)	23.4
H_2O-^{18}O	3.1	9.2 (41 %)	5.4 (24 %)	7.9 (35 %)	22.5

Table 5.2: Cumulative gases evolved for the first 4.8–2.8 V cycle for all prepared NMC622s.

On an absolute scale, all surface modifications tested reduced the amount of evolved C*OO, which originates from a mixed NMC622 surface/electrolyte reaction. As expected, by increasing the amount of surface $Li_2C^*O_3$ there is a larger amount of C$^*O_2$ evolved. The fraction of total carbon dioxide evolution attributable to direct $Li_2C^*O_3$ decomposition is comparable to that found in another study with similar amounts of grown $Li_2{}^{13}CO_3$.[67]

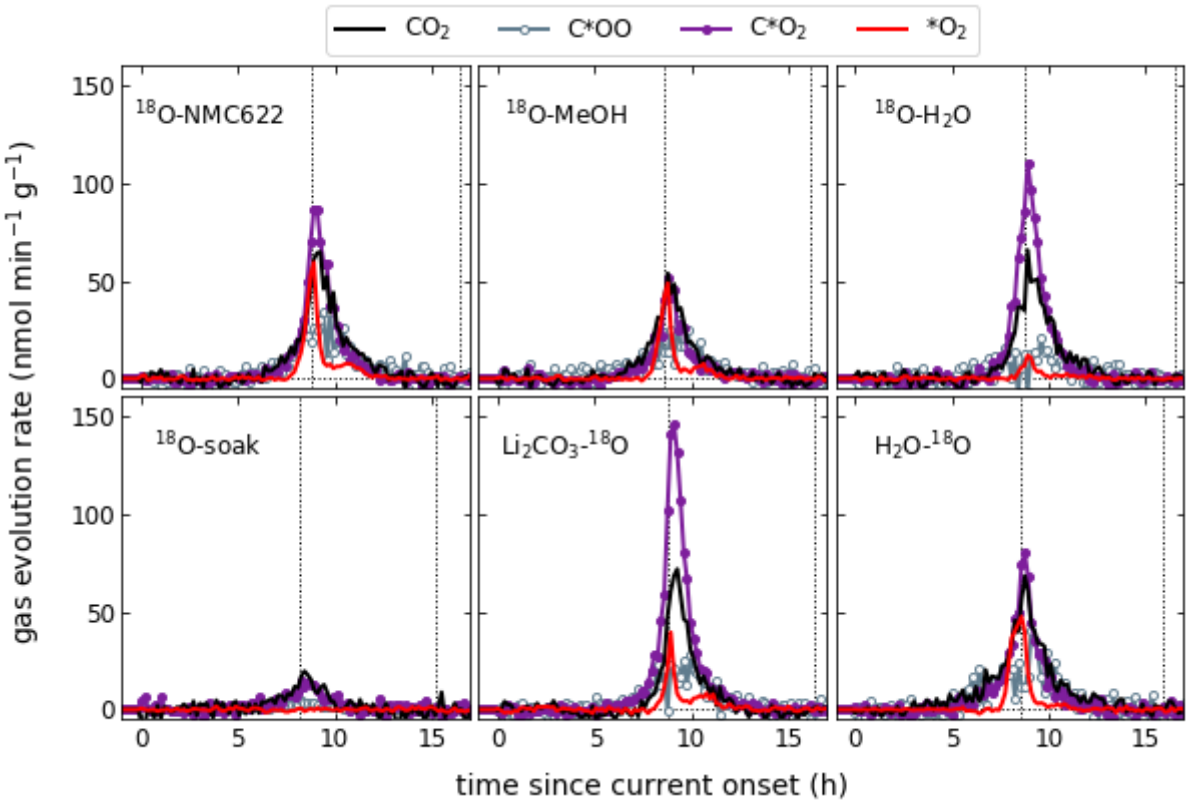

Figure 5.4: Rates of $^{*}O_2$ and carbon dioxide evolution for all NMC622s in the first cycle. All NMC622s were galvanostatically charged at 0.1 Li^+ h^{-1} (26.75 mA g^{-1}) until 4.8 V and then immediately discharged to 2.8 V at the same current rate. Charge begins at time = 0 h and vertical lines indicate changes in the applied current

However, in the water rinsed ^{18}O-H_2O, more $Li_2C^{*}O_3$ is degraded than the baseline ^{18}O-NMC622, despite that the total surface $Li_2C^{*}O_3$ was approximately halved by the rinsing process. As Li_2CO_3 is insulating, this may be due to a simply thinner layer of lithium carbonate that is more easily degraded.

Though there are differences exhibited by the outgassing of the surface modified NMC622s, with the exception of the ^{18}O-soak the cumulative gas evolution is comparable among the materials. To induce the surface degradation mechanisms to a larger extent, with the goal of more readily discriminating between the effect of surface modifications, we added an additional 6 h 4.8 V potentiostatic hold after galvanostatic charge to 4.8 V. We envision that this extreme hold may be considered as a replacement for extended cycling, at least to understand the instabilities at the cathode/electrolyte interface, and has previously been used as such.[58,60] In Chapter 3 we showed that a 4 h potentiostatic hold decomposed nearly all of the native surface $Li_2C^{*}O_3$.

()-NMC622	capacity to 4.8 V (Li units)	hold capacity (Li units)	discharge capacity (Li units)	irreversible capacity (Li units)
^{18}O	0.873	0.945	0.803	0.142
^{18}O-MeOH	0.852	0.936	0.799	0.137
^{18}O-H_2O	0.879	0.951	0.813	0.138
^{18}O-soak	0.815	0.897	0.779	0.118
Li_2CO_3-^{18}O	0.854	0.933	0.789	0.144
H_2O-^{18}O	0.862	0.929	0.791	0.138

Table 5.3: Capacities for all NMC622 materials for the 4.8 V hold cycle.

"Hold capacity" is the total capacity, assuming all charge is due to delithiation, of the galvanostatic delithiation to 4.8 V and the potentiostatic hold at 4.8 V for 6 h.

5.3.3 The effect of surface modification on high voltage outgassing The NMC622s were galvanostatically charged to 4.8 V at the same 0.1 Li^+ h^{-1} (26.75 mA g^{-1}) rate, held at 4.8 V while monitoring the current for 6 h, and then discharged at the same galvanostatic rate to 2.8 V. The obtained capacities of the galvanostatic and potentiostatic portions are given in Table 5.3. As earlier for the galvanostatic cycle, all prepared NMC622s exhibited similar capacities, with the exception of ^{18}O-soak.

The net rates of total carbon dioxide and oxygen evolution rates for all NMC622 preparations are shown in Figure 5.5 spanning 1 h before and the duration of the 6 h 4.8 V potentiostatic hold. With the introduction of the 4.8 V hold, significant differences in the outgassing behavior of the different surface modifications are apparent.

As in Chapter 3, ^{18}O-NMC622, ^{18}O-MeOH, and Li_2CO_3-^{18}O all exhibit maxima in the rates of net CO_2 evolution approximately 1 h into the potentiostatic hold, after the currents have already fallen to $\approx$ 20 % the galvanostatic rate of 0.1 Li^+ h^{-1} (27.65 mA g^{-1}). The two H_2O washed samples exhibit maxima in the rates CO_2 evolution near the onset of the 4.8 V hold. For all NMC622s the rate of oxygen evolution peaks at the end of the galvanostatic charge, falling with the current during the hold. It is interesting to note that even after a charge of 0.9 Li, ^{18}O-soak does not evolve any observable O_2 during the 4.8 V hold.

With the extra 4.8 V hold, the addition of the added Li_2CO_3 has a more apparent effect on the outgassing, with the maximum in net rate carbon dioxide of Li_2CO_3-^{18}O approximately 50 % higher than the baseline ^{18}O-NMC622. Although generally more carbon dioxide is evolved in the order Li_2CO_3-^{18}O > ^{18}O > ^{18}O-MeOH > H_2O-^{18}O $\approx$ ^{18}O-H_2O > ^{18}O-soak, to glean more information we apply the change of basis to (O,*O) as before.

The cumulative $^*O_2$ and all forms of carbon dioxide for the 4.8 V hold cycle are tabulated in Table 5.4 and the corresponding rates are plotted in Figure 5.6. Additionally in Table 5.4 are the initial surface coverages of $Li_2C^*O_3$ as measured by the carbonate titration. For all preparations of NMC622 the total C^*O_2 evolved is comparable to the initial $Li_2C^*O_3$, implying that the majority of the initial carbonate is decomposed by the 4.8 V hold.

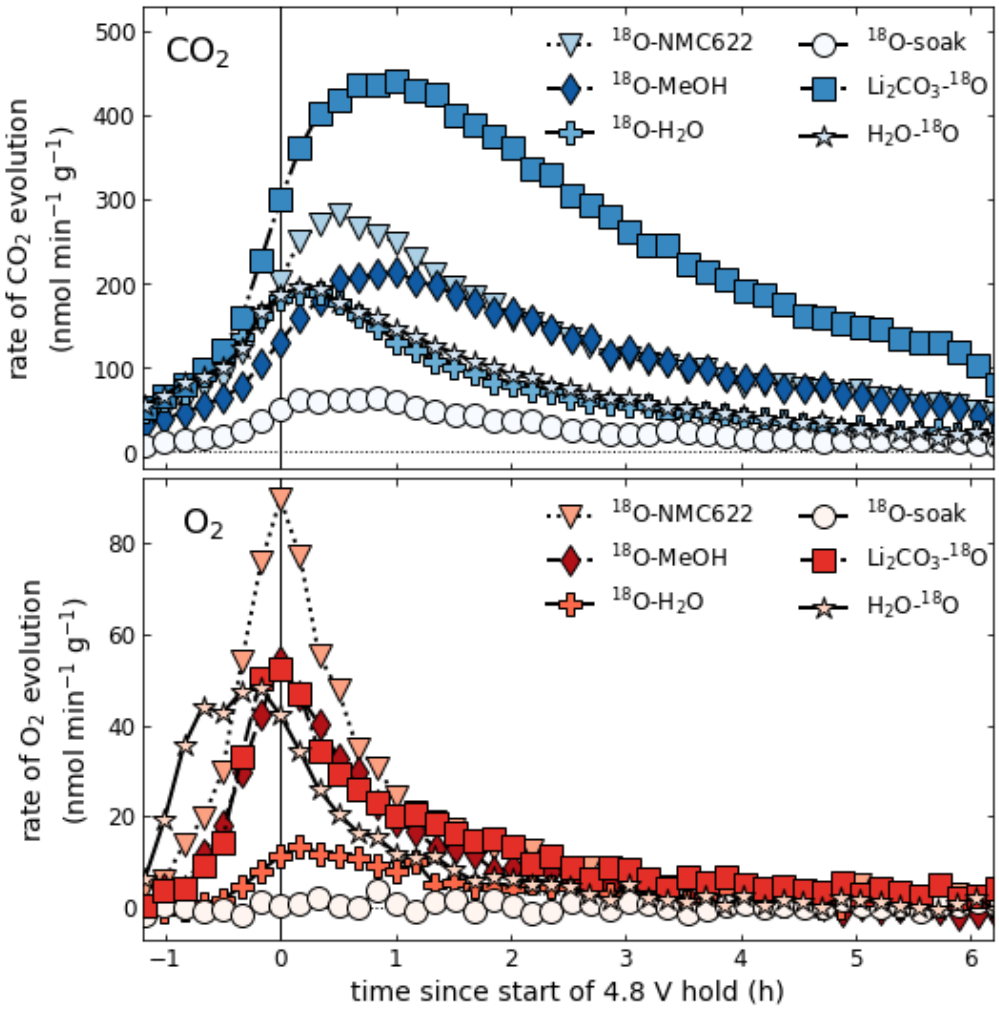

Figure 5.5: Evolution rates of net O_2 and CO_2 for all NMC622s during the 4.8 V hold. All NMC622s were galvanostatically charged at 0.1 Li^+ h^{-1} (26.75 mA g^{-1}) until 4.8 V, potentiostatically held at 4.8 V for 6 h, and then discharged to 2.8 V at 0.1 Li^+ h^{-1} (26.75 mA g^{-1}). The top panel shows the net rate of CO_2 evolution and the bottom panel the net O_2 evolution. Time = 0 h corresponds to the start of the 6 h 4.8 V hold.

Comparing the CO_2, C*OO, and C*O_2 evolved for all of the prepared NMC622s we can see that for Li_2CO_3-^{18}O the majority of the evolved carbon dioxide is from direct decomposition of $Li_2C^*O_3$ ($\approx$ 60 %). Additionally Li_2CO_3-^{18}O exhibits the largest extent of CO_2 evolution, which likely largely stems from direct ring opening of the carbonate electrolyte. As presented in Chapter 2, with collaborators we previously showed that the electrochemical oxidation of Li_2CO_3 generated singlet oxygen, $^1O_2$. As described in the previous chapter, $^1O_2$ is proposed to react with EC and form CO_2 from eventual ring opening.[72] Given that Li_2CO_3-^{18}O evolved less $^*O_2$, which has also been proposed to release in part as singlet oxygen,[11] and C*OO compared to other NMC622 preparations, our results are consistent with the proposition that decomposition of lithium carbonate increases decomposition of the electrolyte.

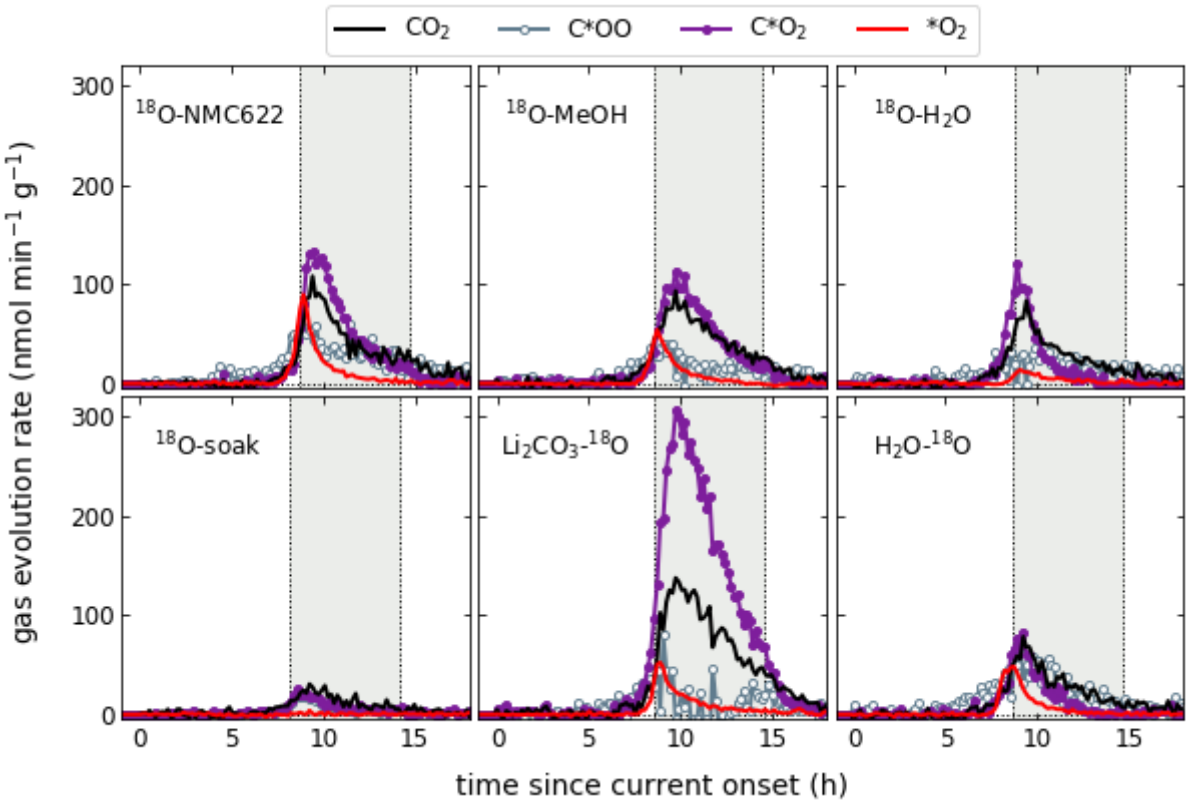

Figure 5.6: Rates of $^*O_2$ and carbon dioxide evolution for all NMC622s for the 4.8 V hold. All NMC622s were galvanostatically charged at 0.1 Li^+ h^{-1} (26.75 mA g^{-1}) until 4.8 V, potentiostatically held at 4.8 V for 6 h, and then discharged to 2.8 V at 0.1 Li^+ h^{-1} (26.75 mA g^{-1}). Charge begins at time = 0 h and the gray shaded region indicates the 6 h 4.8 V hold.

()-NMC622	$^*O_2$ (µmol g^{-1})	cumulative carbon dioxide in µmol g^{-1} (fraction of total evolution, %)			$\Sigma(CO_2)$ (µmol g^{-1})	initial $Li_2C^*O_3$ (µmol g^{-1})
		CO_2	C*OO	C^*O_2		
^{18}O	7.8	21.7 (33 %)	18.6 (29 %)	24.4 (38 %)	64.8	24.7
^{18}O-MeOH	4.9	22.4 (40 %)	10.5 (19 %)	23.5 (41 %)	56.4	23.1
^{18}O-H_2O	1.7	15.7 (39 %)	11.9 (30 %)	12.4 (31 %)	40.0	14.1
^{18}O-soak	0.0	6.2 (41 %)	4.0 (27 %)	4.9 (32 %)	15.1	4.8
Li_2CO_3-^{18}O	6.2	37.7 (31 %)	9.0 (8 %)	73.0 (61 %)	119.7	78.1
H_2O-^{18}O	5.3	15.7 (36 %)	17.1 (39 %)	11.1 (25 %)	43.9	13.4

Table 5.4: Cumulative gases evolved for the 4.8-hold–2.8 V cycle for all prepared NMC622s.

Rinsing with MeOH, H_2O, and heating with extra Li_2CO_3 all decrease the total C*OO evolved, which stems from a coupled NMC622 surface/electrolyte reaction. From the earlier discussion on possible surface defects, we then tentatively assign C*OO evolution to both the presence of surface lithium vacancies and surface hydroxides and/or soluble surface aggregates. In support of this, H_2O-^{18}O, which we predicted to have an increase in surface lithium vacancies due to lack of free surface lithium during the ^{18}O-enrichment treatment, is observed to have the largest fraction of C*OO of the total carbon dioxide evolved of all the NMC622s and near the absolute value of the baseline ^{18}O-NMC622. ^{18}O-soak, on the other hand, has the lowest amount of C*OO evolved.

5.3.4 Electrolyte decomposition as measured after the first charge There is, however, an additional electrolyte decomposition process that may or may not be a significant contributor to outgassing. As described in Chapter 3, carbonate-like electrolyte decomposition products, likely alkyl carbonates,[113] are sorbed to the surface of charged NMC622 electrodes when more than ≈ 0.6 Li is removed from the lattice (> 4.2 V). These electrolyte decomposition products are largely reduced and desorb from the surface when discharged to below 4.0 V. The carbonate titration of these charged electrodes showed that the majority of the carbonate-like species originated from the electrolyte, however when we removed the signal originating from the remaining surface $Li_2C^*O_3$ we detected a portion of the carbonate had oxygen from not only the electrolyte (natural abundance) but also *O from the NMC622 surface.

To understand how the surface contaminants and defects change the sorbed electrolyte decomposition products, if at all, we compared the electrolyte decomposition products on the surfaces after charge to 4.8 V. We charged all of the NMC622 preparations at 0.1 Li^+ h^{-1} (26.75 mA g^{-1}) to 4.8 V, allowed them to rest for 4 h, and then extracted and titrated the electrodes. The $Li_2C^*O_3$ portion was excluded from the detected surface carbonates after charge for all NMC622 preparations and the remaining portion, which must stem from reaction with the electrolyte, was split into two portions: that which evolves CO_2 when titrated with acid and that which evolves C*OO. The presence of C*OO indicates NMC622 surface oxygen participates in the alkyl carbonate formation reaction.

The titration results for the charged NMC622 electrodes are given in Table 5.5. The results for the baseline ^{18}O-NMC622 are similar to those presented in Chapter 3. All surface modifications decrease the NMC622 surface *O contribution to the deposited electrolyte degradation products. As posited in the previous chapter, surface $^*OH^-$ may react with the carbonate electrolyte to form new alkyl carbonates. These $^*OH^-$ are partially removed by MeOH rinsing or replaced by natural abundance OH^- by the H_2O rinsing/washing processes and result in a lower extent of C*OO detected in the post-charge titrations for ^{18}O-MeOH, ^{18}O-H_2O, H_2O-^{18}O, and ^{18}O-soak. These results could also be attributable to a decrease of soluble surface aggregates.

()-NMC622	carbon dioxide from electrolyte degradation products in post-charge titration µmol g^{-1}, (fraction of total evolution, %)		$CO_2 + C^*OO$ (µmol g^{-1})
	CO_2	C^*OO	
^{18}O	38.7 (90 %)	4.5 (10 %)	43.2
^{18}O-MeOH	29.5 (97 %)	1.0 (3 %)	30.5
^{18}O-H_2O	27.3 (93 %)	2.0 (7 %)	29.3
^{18}O-soak	15.7 (100 %)	0 (0 %)	15.7
Li_2CO_3-^{18}O	35.4 (94 %)	2.1 (6 %)	37.5
H_2O-^{18}O	29.7 (5 %)	1.6 (5 %)	31.3

Table 5.5: Carbonate-like electrolyte decomposition products detected on the surface after charge to 4.8 V for all prepared NMC622s.

Although it is not anticipated that Li_2CO_3-^{18}O will have significantly different surface hydroxyl coverage compared to the baseline material, as it was not washed, it also exhibits a lower surface NMC622 surface $^*O$ contribution to the deposited electrolyte degradation products. One possibility is that extra Li_2CO_3 changes the morphology and thus interaction with the electrolyte, so it may simply block hydroxyl contact with the electrolyte. Another is that because excess Li_2CO_3 was ground with NMC622 to prepare Li_2CO_3-^{18}O—approximately 90 µmol g^{-1} Li_2CO_3 was ground with NMC622 and yet the surface Li_2CO_3 was only effectively increased by $\approx$ 50 µmol g^{-1}—that some hydroxyl groups were converted to carbonate by CO_2, as the ^{18}O-enrichment procedure is a closed process.

5.4 Conclusions

By modifying the nature of the surface of NMC622 without altering the bulk structure by performing H_2O rinses with and without heat treatment, a MeOH rinse, a H_2O soak, and by increasing the surface Li_2CO_3, we were able to drastically change the observed outgassing to oxygen and carbon dioxide and also change the depth-dependent irreversible peroxo-like surface reconstruction after the first charge. We additionally found that the surface defects/contaminants changed the nature of the deposited electrolyte degradation products after charge to 4.8 V.

However, we do not observe any clear relationship between the formation and extent of the peroxo-like surface character with outgassing among the NMC622 preparations. The role of the irreversible surface layer formation may be more apparent in performance degradation observed in cycling.

Additionally, although it has been widely published that lattice oxygen release has a causal relationship with CO_2 evolution from both the electrolyte[11,19,67,68,97] and even indirectly from Li_2CO_3,[66] from this study no obvious relationship exists between the NMC622 $^*O_2$ release and evolution of any of the possible carbon dioxides: CO_2, C^*OO, or C^*O_2. Although C^*O_2 stems from $Li_2C^*O_3$ degradation, there are likely several sources of CO_2 and C^*OO, complicating mechanistic identification.

Although this preliminary study does not identify surface defects beyond quantification of the peroxo-like character and surface carbonates, the disparate outgassing behavior for, in some cases, such mild surface modifications warrants future study. A better quantification of the exact surface structure is necessary, however quantification may be difficult to due damages that arise in imaging from beam damage[60] and the likely non-uniform distribution of defects on different exposed facets.[114]

5.5 Acknowledgements

The author gratefully acknowledges support from the Department of Defense (DoD) through the National Defense Science & Engineering Graduate Fellowship (NDSEG) Program. We thank Umicore for receipt of the NMC622 powder.

6 | Conclusion

This dissertation explored the fundamental instabilities of Li-ion cathodes, as exhibited by outgassing, that occur during the first electrochemical cycle and how these instabilities relate to the surface defects and contaminants present.

The first major observation of this work was the similarities exhibited in the CO_2 evolved during the first cycle for two different classes of Li-ion cathode materials. Despite the order of magnitude difference in lattice O_2 release, the CO_2 outgassing behaviors of Li-rich and Li-stoichiometric transition metal oxides tended to depend on the magnitude of their surface contaminants. This observation spurred more detailed analyses on a particular Ni-rich Li-stoichiometric material: $LiNi_{0.6}Mn_{0.2}Co_{0.2}O_2$, NMC622. In addition to quantifying gases evolved during cycling, additional titration methods combined with isotopic labeling were developed to quantify the change in the NMC622 surface carbonates and peroxo-like character.Concurrent with the detection of CO_2 outgassing on the very first cycle are: (i) decomposition of the native Li_2CO_3 at above 3.9 V; (ii) decomposition of the electrolyte above 3.9 V, well below the anodic stability limit of carbonate electrolytes; (iii) deposition of carbonate electrolyte decomposition products; which, however, (iv) reduce and desorb from the surface after discharge. Additionally, by titrating the peroxo-like surface character, changes in the oxygen lattice are detected: (v) near surface oxygen redox is quantified on charge and is largely reversible, except for (vi) the irreversible surface reconstruction that persists after charge.

An important result is that the formation of the persistent surface reconstruction, as measured by the peroxo-like character after the electrode has been discharged, is observed to occur before the onset of lattice oxygen release on cycling. The formation of the surface peroxo-like character occurs $>$ 3.9 V ($>$ 0.4 Li removed) and the O_2 released during charge occurs typically $>$ 4.45 V ($\approx$ 0.75 Li removed). This indicates that the irreversible near-surface lattice transformations occur and then eventually lead to O_2 release. Additionally, the irreversible surface reconstruction is a function of the state of charge (extent of delithiation) and largely does not depend on the choice of the electrolyte. This implies that the tendency to irreversibly form new surface layers is largely a material property.

However, intentional surface modification to change the surface contaminants and defects is a viable method to influence the surface transformations that occur as a function of local

delithiation. By performing various washing and heat treatment steps, the tendency to form irreversible surface peroxo-character is altered and in some cases almost completely suppressed. In addition, the three main classes of CO_2—that from Li_2CO_3, directly from the carbonate electrolyte, and from mixed NMC622/electrolyte decomposition—are all influenced by the extent of the surface contaminants and defects.

Lacking in this work are cycling studies. Specifically of interest are applying the techniques presented here to gain greater insight into how the reversible and irreversible surface transformations change with time and, more importantly, how these effect long-term cycling performance. More generally, clear connections between outgassing in "formation" cycles and long-term performance are still elusive.

Another major consideration for future studies is more systematic understanding of the effects of atmospheric aging. Unreacted residial lithium carbonate differs from grown surface lithium carbonate from atmospheric contamination due to the surface lattice defects that arise in formation of the latter. Delithiation (and even denickelation) occurs to form the surface hydroxides and carbonates in atmospherically exposed materials, arising in surface lithium vacancies and potentially other compensatory defects. Surface defects alter the coupled surface/electrolyte reactivity to CO_2. For the same surface coverage, comparisons should be made between true residual unreacted lithium carbonate (or from unreacted LiOH that converts, $2\,\mathrm{LiOH} + \mathrm{CO_2} \longrightarrow \mathrm{Li_2CO_3} + \mathrm{H_2O}$) and atmospherically grown lithium carbonate.

Bibliography

[1] Goodenough, J. B.; Kim, Y. Challenges for Rechargeable Li Batteries. *Chem. Mater.* **2010**, *22*, 587–603.

[2] Goodenough, J. B.; Park, K.-S. The Li-Ion Rechargeable Battery: A Perspective. *J. Am. Chem. Soc.* **2013**, *135*, 1167–1176.

[3] Lin, F.; Markus, I. M.; Nordlund, D.; Weng, T.-C.; Asta, M. D.; Xin, H. L.; Doeff, M. M. Surface reconstruction and chemical evolution of stoichiometric layered cathode materials for lithium-ion batteries. *Nature Communications* **2014**, *5*, 3529.

[4] Zheng, H.; Sun, Q.; Liu, G.; Song, X.; Battaglia, V. S. Correlation between dissolution behavior and electrochemical cycling performance for $LiNi_{1/3}Co_{1/3}Mn_{1/3}O_2$-based cells. *Journal of Power Sources* **2012**, *207*, 134–140.

[5] Armstrong, A. R.; Holzapfel, M.; Novák, P.; Johnson, C. S.; Kang, S.-H.; Thackeray, M. M.; Bruce, P. G. Demonstrating Oxygen Loss and Associated Structural Reorganization in the Lithium Battery Cathode $Li[Ni_{0.2}Li_{0.2}Mn_{0.6}]O_2$. *J. Am. Chem. Soc.* **2006**, *128*, 8694–8698.

[6] Hausbrand, R.; Cherkashinin, G.; Ehrenberg, H.; Gröting, M.; Albe, K.; Hess, C.; Jaegermann, W. Fundamental degradation mechanisms of layered oxide Li-ion battery cathode materials: Methodology, insights and novel approaches. *Materials Science and Engineering: B* **2015**, *192*, 3–25.

[7] Jarry, A.; Gottis, S.; Yu, Y.-S.; Roque-Rosell, J.; Kim, C.; Cabana, J.; Kerr, J.; Kostecki, R. The Formation Mechanism of Fluorescent Metal Complexes at the $Li_xNi_{0.5}Mn_{1.5}O_{4-\delta}$/Carbonate Ester Electrolyte Interface. *J. Am. Chem. Soc.* **2015**, *137*, 3533–3539.

[8] Banerjee, A.; Shilina, Y.; Ziv, B.; Ziegelbauer, J. M.; Luski, S.; Aurbach, D.; Halalay, I. C. On the Oxidation State of Manganese Ions in Li-Ion Battery Electrolyte Solutions. *J. Am. Chem. Soc.* **2017**, *139*, 1738–1741.

[9] Yabuuchi, N.; Yoshii, K.; Myung, S.-T.; Nakai, I.; Komaba, S. Detailed Studies of a High-Capacity Electrode Material for Rechargeable Batteries, Li_2MnO_3–$LiCo_{1/3}Ni_{1/3}Mn_{1/3}O_2$. *J. Am. Chem. Soc.* **2011**, *133*, 4404–4419.

[10] Imhof, R.; Novák, P. Oxidative Electrolyte Solvent Degradation in Lithium-Ion Batteries: An In Situ Differential Electrochemical Mass Spectrometry Investigation. *J. Electrochem. Soc.* **1999**, *146*, 1702–1706.

[11] Jung, R.; Metzger, M.; Maglia, F.; Stinner, C.; Gasteiger, H. A. Oxygen Release and Its Effect on the Cycling Stability of $LiNi_xMn_yCo_zO_2$ (NMC) Cathode Materials for Li-Ion Batteries. *J. Electrochem. Soc.* **2017**, *164*, A1361–A1377.

[12] Robert, R.; Bünzli, C.; Berg, E. J.; Novák, P. Activation Mechanism of $LiNi_{0.80}Co_{0.15}Al_{0.05}O_2$: Surface and Bulk Operando Electrochemical, Differential Electrochemical Mass Spectrometry, and X-ray Diffraction Analyses. *Chem. Mater.* **2015**, *27*, 526–536.

[13] Berkes, B. B.; Schiele, A.; Sommer, H.; Brezesinski, T.; Janek, J. On the gassing behavior of lithium-ion batteries with NCM523 cathodes. *J Solid State Electrochem* **2016**, *20*, 2961–2967.

[14] Wang, H.; Rus, E.; Sakuraba, T.; Kikuchi, J.; Kiya, Y.; Abruña, H. D. CO_2 and O_2 Evolution at High Voltage Cathode Materials of Li-Ion Batteries: A Differential Electrochemical Mass Spectrometry Study. *Anal. Chem.* **2014**, *86*, 6197–6201.

[15] Streich, D.; Erk, C.; Guéguen, A.; Müller, P.; Chesneau, F.-F.; Berg, E. J. Operando Monitoring of Early Ni-mediated Surface Reconstruction in Layered Lithiated Ni–Co–Mn Oxides. *J. Phys. Chem. C* **2017**, *121*, 13481–13486.

[16] Guéguen, A.; Streich, D.; He, M.; Mendez, M.; Chesneau, F. F.; Novák, P.; Berg, E. J. Decomposition of $LiPF_6$ in High Energy Lithium-Ion Batteries Studied with Online Electrochemical Mass Spectrometry. *J. Electrochem. Soc.* **2016**, *163*, A1095–A1100.

[17] Kumai, K.; Miyashiro, H.; Kobayashi, Y.; Takei, K.; Ishikawa, R. Gas generation mechanism due to electrolyte decomposition in commercial lithium-ion cell. *Journal of Power Sources* **1999**, *8182*, 715–719.

[18] Metzger, M.; Strehle, B.; Solchenbach, S.; Gasteiger, H. A. Origin of H_2 Evolution in LIBs: H_2O Reduction vs. Electrolyte Oxidation. *J. Electrochem. Soc.* **2016**, *163*, A798–A809.

[19] Jung, R.; Metzger, M.; Maglia, F.; Stinner, C.; Gasteiger, H. A. Chemical versus Electrochemical Electrolyte Oxidation on NMC111, NMC622, NMC811, LNMO, and Conductive Carbon. *J. Phys. Chem. Lett.* **2017**, *8*, 4820–4825.

[20] Luo, K.; Roberts, M. R.; Guerrini, N.; Tapia-Ruiz, N.; Hao, R.; Massel, F.; Pickup, D. M.; Ramos, S.; Liu, Y.-S.; Guo, J.; Chadwick, A. V.; Duda, L. C.; Bruce, P. G. Anion Redox Chemistry in the Cobalt Free 3d Transition Metal Oxide Intercalation Electrode $Li[Li_{0.2}Ni_{0.2}Mn_{0.6}]O_2$. *J. Am. Chem. Soc.* **2016**, *138*, 11211–11218.

[22] He, M.; Boulet-Roblin, L.; Borel, P.; Tessier, C.; Novák, P.; Villevieille, C.; Berg, E. J. Effects of Solvent, Lithium Salt, and Temperature on Stability of Carbonate-Based Electrolytes for 5.0 V $LiNi_{0.5}Mn_{1.5}O_4$ Electrodes. *J. Electrochem. Soc.* **2016**, *163*, A83–A89.

[23] Castel, E.; Berg, E. J.; El Kazzi, M.; Novák, P.; Villevieille, C. Differential Electrochemical Mass Spectrometry Study of the Interface of $xLi_2MnO_3 \cdot (1\text{-}x)LiMO_2$ (M = Ni, Co, and Mn) Material as a Positive Electrode in Li-Ion Batteries. *Chem. Mater.* **2014**, *26*, 5051–5057.

[24] Strehle, B.; Kleiner, K.; Jung, R.; Chesneau, F.; Mendez, M.; Gasteiger, H. A.; Piana, M. The Role of Oxygen Release from Li- and Mn-Rich Layered Oxides during the First Cycles Investigated by On-Line Electrochemical Mass Spectrometry. *J. Electrochem. Soc.* **2017**, *164*, A400–A406.

[25] Hong, J.; Lim, H.-D.; Lee, M.; Kim, S.-W.; Kim, H.; Oh, S.-T.; Chung, G.-C.; Kang, K. Critical Role of Oxygen Evolved from Layered Li-Excess Metal Oxides in Lithium Rechargeable Batteries. *Chem. Mater.* **2012**, *24*, 2692–2697.

[26] Streich, D.; Guéguen, A.; Mendez, M.; Chesneau, F.; Novák, P.; Berg, E. J. Online Electrochemical Mass Spectrometry of High Energy Lithium Nickel Cobalt Manganese Oxide/Graphite Half- and Full-Cells with Ethylene Carbonate and Fluoroethylene Carbonate Based Electrolytes. *J. Electrochem. Soc.* **2016**, *163*, A964–A970.

[27] Yang, S.; He, P.; Zhou, H. Exploring the electrochemical reaction mechanism of carbonate oxidation in Li-air/CO_2 battery through tracing missing oxygen. *Energy & Environmental Science* **2016**, *9*, 1650–1654.

[28] Jo, C.-H.; Cho, D.-H.; Noh, H.-J.; Yashiro, H.; Sun, Y.-K.; Myung, S. T. An effective method to reduce residual lithium compounds on Ni-rich $Li[Ni_{0.6}Co_{0.2}Mn_{0.2}]O_2$ active material using a phosphoric acid derived Li_3PO_4 nanolayer. *Nano Res.* **2015**, *8*, 1464–1479.

[29] Noh, H.-J.; Youn, S.; Yoon, C. S.; Sun, Y.-K. Comparison of the structural and electrochemical properties of layered $Li[Ni_xCo_yMn_z]O_2$ (x=1/3, 0.5, 0.6, 0.7, 0.8 and 0.85) cathode material for lithium-ion batteries. *Journal of Power Sources* **2013**, *233*, 121–130.

[30] Haik, O.; Leifer, N.; Samuk-Fromovich, Z.; Zinigrad, E.; Markovsky, B.; Larush, L.; Goffer, Y.; Goobes, G.; Aurbach, D. On the Surface Chemistry of $LiMO_2$ Cathode Materials (M = [MnNi] and [MnNiCo]): Electrochemical, Spectroscopic, and Calorimetric Studies. *J. Electrochem. Soc.* **2010**, *157*, A1099–A1107.

[33] Xiong, X.; Wang, Z.; Yue, P.; Guo, H.; Wu, F.; Wang, J.; Li, X. Washing effects on electrochemical performance and storage characteristics of $LiNi_{0.8}Co_{0.1}Mn_{0.1}O_2$ as cathode material for lithium-ion batteries. *Journal of Power Sources* **2013**, *222*, 318–325.

[34] Zhang, X.; Jiang, W. J.; Zhu, X. P.; Mauger, A.; Qilu; Julien, C. M. Aging of $LiNi_{1/3}Mn_{1/3}Co_{1/3}O_2$ cathode material upon exposure to H_2O. *Journal of Power Sources* **2011**, *196*, 5102–5108.

[35] Kim, J.; Hong, Y.; Ryu, K. S.; Kim, M. G.; Cho, J. Washing Effect of a $LiNi_{0.83}Co_{0.15}Al_{0.02}O_2$ Cathode in Water. *Electrochem. Solid-State Lett.* **2006**, *9*, A19–A23.

[36] Arai, H.; Okada, S.; Ohtsuka, H.; Ichimura, M.; Yamaki, J. Characterization and cathode performance of $Li_{1-x}Ni_{1+x}O_2$ prepared with the excess lithium method. *Solid State Ionics* **1995**, *80*, 261–269.

[37] Meini, S.; Tsiouvaras, N.; Schwenke, K. U.; Piana, M.; Beyer, H.; Lange, L.; Gasteiger, H. A. Rechargeability of Li-air cathodes pre-filled with discharge products using an ether-based electrolyte solution: implications for cycle-life of Li-air cells. *Phys. Chem. Chem. Phys.* **2013**, *15*, 11478–11493.

[39] Fan, L.; Tang, D.; Wang, D.; Wang, Z.; Chen, L. $LiCoO_2$-catalyzed electrochemical oxidation of Li_2CO_3. *Nano Res.* **2016**, *9*, 3903–3913.

[40] Bi, Y.; Wang, T.; Liu, M.; Du, R.; Yang, W.; Liu, Z.; Peng, Z.; Liu, Y.; Wang, D.; Sun, X. Stability of Li_2CO_3 in cathode of lithium ion battery and its influence on electrochemical performance. *RSC Adv.* **2016**, *6*, 19233–19237.

[41] Mahne, N.; Schafzahl, B.; Leypold, C.; Leypold, M.; Grumm, S.; Leitgeb, A.; Strohmeier, G. A.; Wilkening, M.; Fontaine, O.; Kramer, D.; Slugovc, C.; Borisov, S. M.; Freunberger, S. A. Singlet oxygen generation as a major cause for parasitic reactions during cycling of aprotic lithium-oxygen batteries. *Nature Energy* **2017**, *2*, 17036.

[42] Mahne, N.; Renfrew, S. E.; McCloskey, B. D.; Freunberger, S. A. Electrochemical Oxidation of Lithium Carbonate Generates Singlet Oxygen. *Angew. Chem. Int. Ed.* **2018**, *57*, 5529–5533.

[43] Cho, D.-H.; Jo, C.-H.; Cho, W.; Kim, Y.-J.; Yashiro, H.; Sun, Y.-K.; Myung, S.-T. Effect of Residual Lithium Compounds on Layer Ni-Rich $Li[Ni_{0.7}Mn_{0.3}]O_2$. *J. Electrochem. Soc.* **2014**, *161*, A920–A926.

[44] Zheng, X.; Li, X.; Wang, Z.; Guo, H.; Huang, Z.; Yan, G.; Wang, D. Investigation and improvement on the electrochemical performance and storage characteristics of $LiNiO_2$-based materials for lithium ion battery. *Electrochimica Acta* **2016**, *191*, 832–840.

[45] Xu, S.; Du, C.; Xu, X.; Han, G.; Zuo, P.; Cheng, X.; Ma, Y.; Yin, G. A Mild Surface Washing Method Using Protonated Polyaniline for Ni-rich $LiNi_{0.8}Co_{0.1}Mn_{0.1}O_2$ Material of Lithium Ion Batteries. *Electrochimica Acta* **2017**, *248*, 534–540.

[46] Kim, J.; Kim, O.; Park, C.; Lee, G.; Shin, D. Electrochemical Properties of $Li_{1-+}CoO_2$ Synthesized for All-Solid-State Lithium Ion Batteries with Li_2S-P_2S_5 Glass-Ceramics Electrolyte. *J. Electrochem. Soc.* **2015**, *162*, A1041–A1045.

[47] Xu, J.; Lin, F.; M.Doeff, M.; Tong, W. A review of Ni-based layered oxides for rechargeable Li-ion batteries. *Journal of Materials Chemistry A* **2017**, *5*, 874–901.

[48] Shi, S.; Qi, Y.; Li, H.; Hector, L. G. Defect Thermodynamics and Diffusion Mechanisms in Li_2CO_3 and Implications for the Solid Electrolyte Interphase in Li-Ion Batteries. *J. Phys. Chem. C* **2013**, *117*, 8579–8593.

[49] Tian, C.; Nordlund, D.; Xin, H. L.; Xu, Y.; Liu, Y.; Sokaras, D.; Lin, F.; Doeff, M. M. Depth-Dependent Redox Behavior of $LiNi_{0.6}Mn_{0.2}Co_{0.2}O_2$. *J. Electrochem. Soc.* **2018**, *165*, A696–A704.

[50] Ruan, Y.; Song, X.; Fu, Y.; Song, C.; Battaglia, V. Structural evolution and capacity degradation mechanism of $LiNi_{0.6}Mn_{0.2}Co_{0.2}O_2$ cathode materials. *Journal of Power Sources* **2018**, *400*, 539–548.

[51] May, B. M.; Serrano-Sevillano, J.; Dauphin, A. L.; Nazib, A.; Lima, N.; Casas-Cabanas, M.; Cabana, J. Effect of Synthetic Parameters on Defects, Structure, and Electrochemical Properties of Layered Oxide $LiNi_{0.80}Co_{0.15}Al_{0.05}O_2$. *J. Electrochem. Soc.* **2018**, *165*, A3537–A3543.

[52] Duan, Y.; Yang, L.; Zhang, M.-J.; Chen, Z.; Bai, J.; Amine, K.; Pan, F.; Wang, F. Insights into Li/Ni ordering and surface reconstruction during synthesis of Ni-rich layered oxides. *J. Mater. Chem. A* **2019**, *7*, 513–519.

[53] Makimura, Y.; Zheng, S.; Ikuhara, Y.; Ukyo, Y. Microstructural Observation of $LiNi_{0.8}Co_{0.15}Al_{0.05}O_2$ after Charge and Discharge by Scanning Transmission Electron Microscopy. *J. Electrochem. Soc.* **2012**, *159*, A1070–A1073.

[54] Sun, H.-H.; Manthiram, A. Impact of Microcrack Generation and Surface Degradation on a Nickel-Rich Layered $Li[Ni_{0.9}Co_{0.05}Mn_{0.05}]O_2$ Cathode for Lithium-Ion Batteries. *Chem. Mater.* **2017**, *29*, 8486–8493.

[55] Jung, R.; Morasch, R.; Karayaylali, P.; Phillips, K.; Maglia, F.; Stinner, C.; Shao-Horn, Y.; Gasteiger, H. A. Effect of Ambient Storage on the Degradation of Ni-Rich Positive Electrode Materials (NMC811) for Li-Ion Batteries. *J. Electrochem. Soc.* **2018**, *165*, A132–A141.

[56] Mu, L.; Lin, R.; Xu, R.; Han, L.; Xia, S.; Sokaras, D.; Steiner, J. D.; Weng, T.-C.; Nordlund, D.; Doeff, M. M.; Liu, Y.; Zhao, K.; Xin, H. L.; Lin, F. Oxygen Release Induced Chemomechanical Breakdown of Layered Cathode Materials. *Nano Lett.* **2018**, *18*, 3241–3249.

[57] Li, J.; Downie, L. E.; Ma, L.; Qiu, W.; Dahn, J. R. Study of the Failure Mechanisms of $LiNi_{0.8}Mn_{0.1}Co_{0.1}O_2$ Cathode Material for Lithium Ion Batteries. *J. Electrochem. Soc.* **2015**, *162*, A1401–A1408.

[58] Tornheim, A.; Sharifi-Asl, S.; Garcia, J. C.; Bareño, J.; Iddir, H.; Shahbazian-Yassar, R.; Zhang, Z. Effect of electrolyte composition on rock salt surface degradation in NMC cathodes during high-voltage potentiostatic holds. *Nano Energy* **2019**, *55*, 216–225.

[59] Li, J.; Liu, H.; Xia, J.; Cameron, A. R.; Nie, M.; Botton, G. A.; Dahn, J. R. The Impact of Electrolyte Additives and Upper Cut-off Voltage on the Formation of a Rocksalt Surface Layer in $LiNi_{0.8}Mn_{0.1}Co_{0.1}O_2$ Electrodes. *J. Electrochem. Soc.* **2017**, *164*, A655–A665.

[60] Mukherjee, P.; Faenza, N. V.; Pereira, N.; Ciston, J.; Piper, L. F. J.; Amatucci, G. G.; Cosandey, F. Surface Structural and Chemical Evolution of Layered $LiNi_{0.8}Co_{0.15}Al_{0.05}O_2$ (NCA) under High Voltage and Elevated Temperature Conditions. *Chem. Mater.* **2018**, *30*, 8431–8445.

[61] Jung, S.-K.; Gwon, H.; Hong, J.; Park, K.-Y.; Seo, D.-H.; Kim, H.; Hyun, J.; Yang, W.; Kang, K. Understanding the Degradation Mechanisms of $LiNi_{0.5}Co_{0.2}Mn_{0.3}O_2$ Cathode Material in Lithium Ion Batteries. *Advanced Energy Materials* **2014**, *4*, 1300787.

[62] Hwang, S.; Kim, S. M.; Bak, S.-M.; Chung, K. Y.; Chang, W. Investigating the Reversibility of Structural Modifications of $Li_xNi_yMn_zCo_{1-y-z}O_2$ Cathode Materials during Initial Charge/Discharge, at Multiple Length Scales. *Chem. Mater.* **2015**, *27*, 6044–6052.

[63] Li, H.; Liu, D.; Zhang, L.; Qian, K.; Shi, R.; Kang, F.; Li, B. Combination Effect of Bulk Structure Change and Surface Rearrangement on the Electrochemical Kinetics of $LiNi_{0.80}Co_{0.15}Al_{0.05}O_2$ During Initial Charging Processes. *ACS Appl. Mater. Interfaces* **2018**, *10*, 41370–41379.

[64] Hwang, S.; Chang, W.; Kim, S. M.; Su, D.; Kim, D. H.; Lee, J. Y.; Chung, K. Y.; Stach, E. A. Investigation of Changes in the Surface Structure of $Li_xNi_{0.8}Co_{0.15}Al_{0.05}O_2$ Cathode Materials Induced by the Initial Charge. *Chem. Mater.* **2014**, *26*, 1084–1092.

[65] Liu, H.; Liu, H.; Seymour, I. D.; Chernova, N.; Wiaderek, K. M.; Trease, N. M.; Hy, S.; Chen, Y.; An, K.; Zhang, M.; Borkiewicz, O. J.; Lapidus, S. H.; Qiu, B.; Xia, Y.; Liu, Z.; Chupas, P. J.; Chapman, K. W.; Whittingham, M. S.; Grey, C. P.; Meng, Y. S. Identifying the chemical and structural irreversibility in $LiNi_{0.8}Co_{0.15}Al_{0.05}O_2$ – a model compound for classical layered intercalation. *J. Mater. Chem. A* **2018**, *6*, 4189–4198.

[66] Jung, R.; Strobl, P.; Maglia, F.; Stinner, C.; Gasteiger, H. A. Temperature Dependence of Oxygen Release from $LiNi_{0.6}Mn_{0.2}Co_{0.2}O_2$ (NMC622) Cathode Materials for Li-Ion Batteries. *J. Electrochem. Soc.* **2018**, *165*, A2869–A2879.

[67] Hatsukade, T.; Schiele, A.; Hartmann, P.; Brezesinski, T.; Janek, J. Origin of Carbon Dioxide Evolved during Cycling of Nickel-Rich Layered NCM Cathodes. *ACS Appl. Mater. Interfaces* **2018**, *10*, 38892–38899.

[68] Wandt, J.; Freiberg, A. T. S.; Ogrodnik, A.; Gasteiger, H. A. Singlet oxygen evolution from layered transition metal oxide cathode materials and its implications for lithium-ion batteries. *Materials Today* **2018**, *21*, 825–833.

[69] Renfrew, S. E.; McCloskey, B. D. Residual Lithium Carbonate Predominantly Accounts for First Cycle CO_2 and CO Outgassing of Li-Stoichiometric and Li-Rich Layered Transition-Metal Oxides. *J. Am. Chem. Soc.* **2017**, *139*, 17853–17860.

[70] Bartsch, T.; Strauss, F.; Hatsukade, T.; Schiele, A.; Kim, A.-Y.; Hartmann, P.; Janek, J.; Brezesinski, T. Gas Evolution in All-Solid-State Battery Cells. *ACS Energy Lett.* **2018**, *3*, 2539–2543.

[71] Ding, Y.; Deng, B.; Wang, H.; Li, X.; Chen, T.; Yan, X.; Wan, Q.; Qu, M.; Peng, G. Improved electrochemical performances of $LiNi_{0.6}Co_{0.2}Mn_{0.2}O_2$ cathode material by reducing lithium residues with the coating of Prussian blue. *Journal of Alloys and Compounds* **2019**, *774*, 451–460.

[72] Freiberg, A. T. S.; Roos, M. K.; Wandt, J.; de Vivie-Riedle, R.; Gasteiger, H. A. Singlet Oxygen Reactivity with Carbonate Solvents Used for Li-Ion Battery Electrolytes. *J. Phys. Chem. A* **2018**, *122*, 8828–8839.

[73] Buchner, F.; Fingerle, M.; Kim, J.; Späth, T.; Hausbrand, R.; Behm, R. J. Interaction of Ultrathin Films of Ethylene Carbonate with Oxidized and Reduced Lithium Cobalt Oxide—A Model Study of the Cathode|Electrolyte Interface in Li-Ion Batteries. *Advanced Materials Interfaces* **2019**, *6*, 1801650.

[74] Becker, D.; Cherkashinin, G.; Hausbrand, R.; Jaegermann, W. Adsorption of Diethyl Carbonate on $LiCoO_2$ Thin Films: Formation of the Electrochemical Interface. *J. Phys. Chem. C* **2014**, *118*, 962–967.

[75] Seong, W. M.; Yoon, K.; Lee, M. H.; Jung, S.-K.; Kang, K. Unveiling the Intrinsic Cycle Reversibility of a $LiCoO_2$ Electrode at 4.8-V Cutoff Voltage through Subtractive Surface Modification for Lithium-Ion Batteries. *Nano Lett.* **2019**, *19*, 29–37.

[76] Qian, Y.; Niehoff, P.; Börner, M.; Grützke, M.; Mönnighoff, X.; Behrends, P.; Nowak, S.; Winter, M.; Schappacher, F. M. Influence of electrolyte additives on the cathode electrolyte interphase (CEI) formation on $LiNi_{1/3}Mn_{1/3}Co_{1/3}O_2$ in half cells with Li metal counter electrode. *Journal of Power Sources* **2016**, *329*, 31–40.

[77] Lebens-Higgins, Z. W.; Sallis, S.; Faenza, N. V.; Badway, F.; Pereira, N.; Halat, D. M.; Wahila, M.; Schlueter, C.; Lee, T.-L.; Yang, W.; Grey, C. P.; Amatucci, G. G.; Piper, L. F. J. Evolution of the Electrode–Electrolyte Interface of $LiNi_{0.8}Co_{0.15}Al_{0.05}O_2$ Electrodes Due to Electrochemical and Thermal Stress. *Chem. Mater.* **2018**, *30*, 958–969.

[78] Petersburg, C. F.; Li, Z.; Chernova, N. A.; Whittingham, M. S.; Alamgir, F. M. Oxygen and transition metal involvement in the charge compensation mechanism of $LiNi_{1/3}Mn_{1/3}Co_{1/3}O_2$ cathodes. *J. Mater. Chem.* **2012**, *22*, 19993–20000.

[79] Niemöller, A.; Jakes, P.; Eichel, R.-A.; Granwehr, J. In operando EPR investigation of redox mechanisms in $LiCoO_2$. *Chemical Physics Letters* **2019**, *716*, 231–236.

[80] Manthiram, A.; Song, B.; Li, W. A perspective on nickel-rich layered oxide cathodes for lithium-ion batteries. *Energy Storage Materials* **2017**, *6*, 125–139.

[81] Gao, S.; Cheng, Y.-T.; Shirpour, M. Effects of Cobalt Deficiency on Nickel-Rich Layered $LiNi_{0.8}Co_{0.1}Mn_{0.1}O_2$ Positive Electrode Materials for Lithium-Ion Batteries. *ACS Appl. Mater. Interfaces* **2019**, *11*, 982–989.

[82] Liu, D.; Qian, K.; He, Y.-B.; Luo, D.; Li, H.; Wu, M.; Kang, F.; Li, B. Positive film-forming effect of fluoroethylene carbonate (FEC) on high-voltage cycling with three-electrode $LiCoO_2$/Graphite pouch cell. *Electrochimica Acta* **2018**, *269*, 378–387.

[83] Leanza, D.; Vaz, C. A. F.; Melinte, G.; Mu, X.; Novák, P.; El Kazzi, M. Revealing the Dual Surface Reactions on a HE-NCM Li-Ion Battery Cathode and Their Impact on the Surface Chemistry of the Counter Electrode. *ACS Appl. Mater. Interfaces* **2019**, *11*, 6054–6065.

[84] Zhang, X.-Q.; Cheng, X.-B.; Chen, X.; Yan, C.; Zhang, Q. Fluoroethylene Carbonate Additives to Render Uniform Li Deposits in Lithium Metal Batteries. *Advanced Functional Materials* **2017**, *27*, 1605989.

[85] Renfrew, S. E.; McCloskey, B. D. Quantification of surface oxygen depletion and solid carbonate evolution on the first cycle of $LiNi_{0.6}Mn_{0.2}Co_{0.2}O_2$ electrodes. *ACS Appl. Energy Mater.* **2019**, DOI: 10.1021/acsaem.9b00459.

[86] Arakawa, M.; Yamaki, J.-i. Anodic oxidation of propylene carbonate and ethylene carbonate on graphite electrodes. *Journal of Power Sources* **1995**, *54*, 250–254.

[87] Joho, F.; Novák, P. SNIFTIRS investigation of the oxidative decomposition of organic-carbonate-based electrolytes for lithium-ion cells. *Electrochimica Acta* **2000**, *45*, 3589–3599.

[88] Rasch, B.; Cattaneo, E.; Novák, P.; Vielstich, W. The influence of water on the oxidation of propylene carbonate on platinum—an electrochemical, in situ FT-ir and on-line MS study. *Electrochimica Acta* **1991**, *36*, 1397–1402.

[89] Metzger, M.; Marino, C.; Sicklinger, J.; Haering, D.; Gasteiger, H. A. Anodic Oxidation of Conductive Carbon and Ethylene Carbonate in High-Voltage Li-Ion Batteries Quantified by On-Line Electrochemical Mass Spectrometry. *J. Electrochem. Soc.* **2015**, *162*, A1123–A1134.

[90] Shkrob, I. A.; Zhu, Y.; Marin, T. W.; Abraham, D. Reduction of Carbonate Electrolytes and the Formation of Solid-Electrolyte Interface (SEI) in Lithium-Ion Batteries. 1. Spectroscopic Observations of Radical Intermediates Generated in One-Electron Reduction of Carbonates. *J. Phys. Chem. C* **2013**, *117*, 19255–19269.

[91] Sloop, S. E.; Pugh, J. K.; Wang, S.; Kerr, J. B.; Kinoshita, K. Chemical Reactivity of PF_5 and $LiPF_6$ in Ethylene Carbonate/Dimethyl Carbonate Solutions. *Electrochem. Solid-State Lett.* **2001**, *4*, A42–A44.

[92] Yoshida, H.; Fukunaga, T.; Hazama, T.; Terasaki, M.; Mizutani, M.; Yamachi, M. Degradation mechanism of alkyl carbonate solvents used in lithium-ion cells during initial charging. *Journal of Power Sources* **1997**, *68*, 311–315.

[93] Hayashi, K.; Nemoto, Y.; Tobishima, S.-i.; Yamaki, J.-i. Mixed solvent electrolyte for high voltage lithium metal secondary cells. *Electrochimica Acta* **1999**, *44*, 2337–2344.

[94] Sloop, S. E.; Kerr, J. B.; Kinoshita, K. The role of Li-ion battery electrolyte reactivity in performance decline and self-discharge. *Journal of Power Sources* **2003**, *119-121*, 330–337.

[95] Thompson, L. M.; Stone, W.; Eldesoky, A.; Smith, N. K.; McFarlane, C. R. M.; Kim, J. S.; Johnson, M. B.; Petibon, R.; Dahn, J. R. Quantifying Changes to the Electrolyte and Negative Electrode in Aged NMC532/Graphite Lithium-Ion Cells. *J. Electrochem. Soc.* **2018**, *165*, A2732–A2740.

[96] Späth, T.; Becker, D.; Schulz, N.; Hausbrand, R.; Jaegermann, W. Understanding the SEI Formation at Pristine Li-Ion Cathodes: Chemisorption and Reaction of DEC on $LiCoO_2$ Surfaces Studied by a Combined SXPS/HREELS Approach. *Advanced Materials Interfaces* **2017**, *4*, 1700567.

[97] Bolli, C.; Guéguen, A.; Mendez, M. A.; Berg, E. J. Operando Monitoring of F^- Formation in Lithium Ion Batteries. *Chem. Mater.* **2019**, *31*, 1258–1267.

[98] Teng, X.; Zhan, C.; Bai, Y.; Ma, L.; Liu, Q.; Wu, C.; Wu, F.; Yang, Y.; Lu, J.; Amine, K. In Situ Analysis of Gas Generation in Lithium-Ion Batteries with Different Carbonate-Based Electrolytes. *ACS Appl. Mater. Interfaces* **2015**, *7*, 22751–22755.

[99] Michan, A. L.; Parimalam, B. S.; Leskes, M.; Kerber, R. N.; Yoon, T.; Grey, C. P.; Lucht, B. L. Fluoroethylene Carbonate and Vinylene Carbonate Reduction: Understanding Lithium-Ion Battery Electrolyte Additives and Solid Electrolyte Interphase Formation. *Chem. Mater.* **2016**, *28*, 8149–8159.

[100] Strehle, B.; Solchenbach, S.; Metzger, M.; Schwenke, K. U.; Gasteiger, H. A. The Effect of CO_2 on Alkyl Carbonate Trans-Esterification during Formation of Graphite Electrodes in Li-Ion Batteries. *J. Electrochem. Soc.* **2017**, *164*, A2513–A2526.

[101] Petibon, R.; Xia, J.; Burns, J. C.; Dahn, J. R. Study of the Consumption of Vinylene Carbonate in $Li[Ni_{0.33}Mn_{0.33}Co_{0.33}]O_2$/Graphite Pouch Cells. *J. Electrochem. Soc.* **2014**, *161*, A1618–A1624.

[102] Downie, L. E.; Nelson, K. J.; Petibon, R.; Chevrier, V. L.; Dahn, J. R. The Impact of Electrolyte Additives Determined Using Isothermal Microcalorimetry. *ECS Electrochem. Lett.* **2013**, *2*, A106–A109.

[103] Seo, D. M.; Boyle, P. D.; Sommer, R. D.; Daubert, J. S.; Borodin, O.; Henderson, W. A. Solvate Structures and Spectroscopic Characterization of LiTFSI Electrolytes. *J. Phys. Chem. B* **2014**, *118*, 13601–13608.

[104] Dougassa, Y. R.; Jacquemin, J.; El Ouatani, L.; Tessier, C.; Anouti, M. Viscosity and Carbon Dioxide Solubility for $LiPF_6$, LiTFSI, and LiFAP in Alkyl Carbonates: Lithium Salt Nature and Concentration Effect. *J. Phys. Chem. B* **2014**, *118*, 3973–3980.

[105] Alvarado, J.; Schroeder, M. A.; Pollard, T. P.; Wang, X.; Lee, J. Z.; Zhang, M.; Wynn, T.; Ding, M.; Borodin, O.; Meng, Y. S.; Xu, K. Bisalt ether electrolytes: a pathway towards lithium metal batteries with Ni-rich cathodes. *Energy Environ. Sci.* **2019**, *12*, 780–794.

[106] Hoang, K.; Johannes, M. Defect Physics and Chemistry in Layered Mixed Transition Metal Oxide Cathode Materials: (Ni,Co,Mn) vs (Ni,Co,Al). *Chem. Mater.* **2016**, *28*, 1325–1334.

[107] Koyama, Y.; Arai, H.; Tanaka, I.; Uchimoto, Y.; Ogumi, Z. Defect Chemistry in Layered $LiMO_2$ (M = Co, Ni, Mn, and $Li_{1/3}Mn_{2/3}$) by First-Principles Calculations. *Chem. Mater.* **2012**, *24*, 3886–3894.

[108] Bi, Y.; Yang, W.; Du, R.; Zhou, J.; Liu, M.; Liu, Y.; Wang, D. Correlation of oxygen non-stoichiometry to the instabilities and electrochemical performance of $LiNi_{0.8}Co_{0.1}Mn_{0.1}O_2$ utilized in lithium ion battery. *Journal of Power Sources* **2015**, *283*, 211–218.

[109] Henrich, V. E.; Cox, P. A. Fundamentals of gas-surface interactions on metal oxides. *Applied Surface Science* **1993**, *72*, 277–284.

[110] Jeong, S.; Kim, J.; Mun, J. Self-Generated Coating of $LiCoO_2$ by Washing and Heat Treatment without Coating Precursors. *J. Electrochem. Soc.* **2019**, *166*, A5038–A5044.

[111] Crowe, R.; Badyal, J. P. S. Surface modification of poly(vinylidene difluoride) (PVDF) by LiOH. *J. Chem. Soc., Chem. Commun.* **1991**, *0*, 958–959.

[112] Moshtev, R.; Zlatilova, P.; Vasilev, S.; Bakalova, I.; Kozawa, A. Synthesis, XRD characterization and electrochemical performance of overlithiated $LiNiO_2$. *Journal of Power Sources* **1999**, *81*, 434–441.

[113] Aurbach, D. Review of selected electrode–solution interactions which determine the performance of Li and Li ion batteries. *Journal of Power Sources* **2000**, *89*, 206–218.

[114] Zhu, J.; Chen, G. Single-crystal based studies for correlating the properties and high-voltage performance of $Li[Ni_xMn_yCo_{1-x-y}]O_2$ cathodes. *Journal of Materials Chemistry A* **2019**, *7*, 5463–5474.

Appendices

A | Differential Electrochemical Mass Spectrometry

Differential electrochemical mass spectrometry (DEMS) was first described[1] as a technique "which allows the gaseous and volatile products of electrochemical reactions to be measured quantitatively and with high sensitivity." The data obtained from the DEMS is an analog to cyclic voltammetry (CV) – the faradaic current is proportional to the detected flow rates of gaseous species (sometimes called mass spectrometry CVs) – provided the electrochemical cell is scanned at a "reasonable "rate. This first DEMS was used to study electrochemical oxidation of ethanol,[1] CO adsorption on Pt,[2] and oxidation of propylene carbonate electrolytes,[3] to name a few.

Differential EMS is distinguished from EMS by the mode of detection. Previous authors used the name "differential" to refer to both the differential pumping – a two stage pumping mechanism – as well as to the measured time "differential," i.e., the rate of formation of gaseous species. With constant pumping, the effective flow of gaseous and volatile species is detected by the mass spectrometer. An EMS, however, does not constantly remove the gaseous species and allows them to accumulate. Thus, EMS directly measures the total amount of gas evolved while DEMS directly measures the rate of gas evolution.

The original DEMS read signals in a near continuous manner, giving small delays in detection due to residence time. The DEMS design in 209 Hildebrand is of a different design than the original DEMS. In contrast to a constant flow and constant pumping of gaseous species, 209 Hildebrand's is an integrated DEMS: one that allows gas to accumulate and only samples the headspace periodically. Allowing gases to accumulate in this manner enables longer experiments without significant electrolyte evaporation and detection of trace gases with increased sensitivity, at however the cost of decreased frequency of measurements and greater uncertainty in the voltage at which gases begin to evolve.

[1] Wolter, O.; Heitbaum, J. Differential Electrochemical Mass Spectroscopy (DEMS) – a New Method for the Study of Electrode Processes. *Berichte der Bunsengesellschaft für physikalische Chemie* **1984**, *88*, 2–6.

[2] Wolter, O.; Heitbaum, J. The Adsorption of CO on a Porous Pt-Electrode in Sulfuric Acid Studied by DEMS. *Berichte der Bunsengesellschaft für physikalische Chemie* **1984**, *88*, 6–10.

[3] Eggert, G.; Heitbaum, J. Electrochemical reactions of propylenecarbonate and electrolytes solved therein–a dems study. *Electrochimica Acta* **1986**, *31*, 1443–1448.

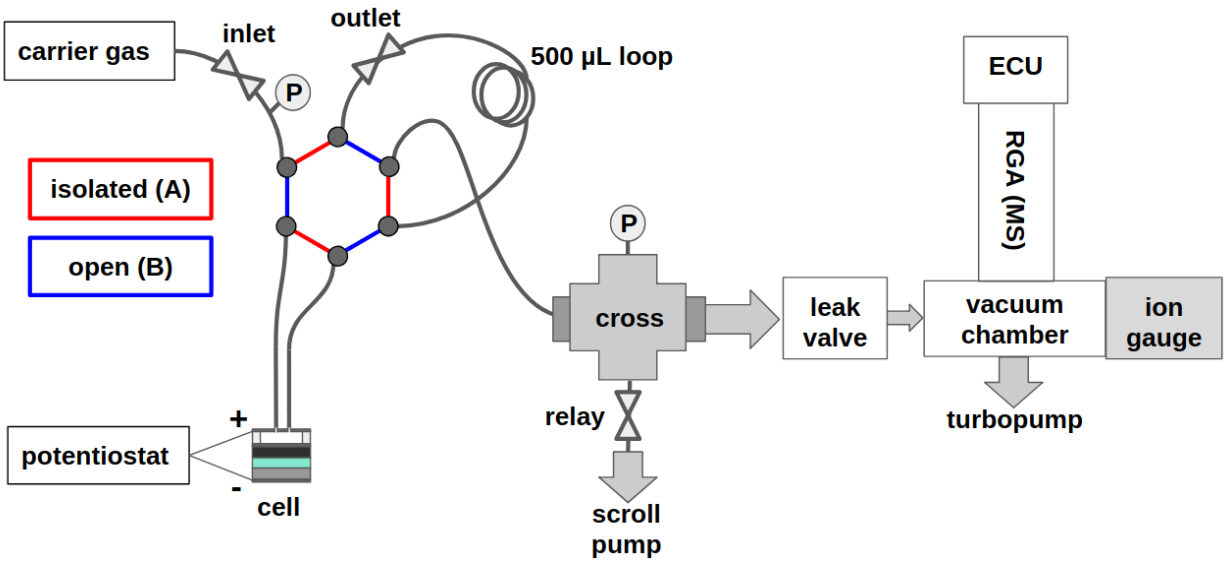

Figure A.1: DEMS schematic described in detail in Section A.1.

A.1 Setup

The DEMS is shown schematically above in Figure A.1.[4] During a DEMS measurement the system is open to the carrier gas: the valve marked "inlet" is left open and the valve marked "outlet" is closed. An electrochemical cell is connected via 1/16" capillaries to an electrically actuated 6-way valve. This 6-way valve has two positions: **A**, shown in red, wherein the electrochemical cell is isolated from the rest of the DEMS system and **B**, shown in blue, wherein the electrochemical cell is connected to the carrier gas upstream and the 500 µL transfer loop downstream.

To monitor pressure rise and/or decay, the cell stays in position **B** with the inlet and outlet valves closed such that the pressure transducer may read changes to the cell pressure. However for a DEMS measurement, the cell mostly stays isolated in **A** and gases are allowed to accumulate in the cell. While the cell is integrating, the rest of the system downstream of the outlet valve is pumped down, including the 500 µL transfer loop and the cross. When a measurement is made the cell is switched to position **B**, so that the gas expands into the 500 µL transfer loop at the carrier gas pressure. Next the scroll pump is switched off and the cell is switched back to position **A**. This allows the gas in the 500 µL transfer loop to expand into the cross. This gas is then leaked into the mass spectrometer vacuum chamber via a leak valve that is used to control the pressure in the vacuum chamber to be $5 - 10 \times 10^{-7}$ Torr. The mass spectrometer is a 4-point probe residual gas analyzer (RGA) that can measure mass per charge (m/z) ratios from 1 to 200 amu.

[4] portions of this adapted from the author's qualifying exam manuscript entitled *Transition Metal Oxides: Accommodating Lithium* submitted on September 22, 2015 and corresponding talk given on October 6, 2015

A.2 Residual Gas Analyzer (RGA) basics

Within the RGA a portion of the gas molecules are ionized, separated by the quadrupole mass-filter, and then detected as currents.[5] An RGA mass spectrum is then a collection of the measured ion currents for a set range of m/z's.

In the simplest mode of operation the ion currents are directly measured without any amplification (no mass dependence). This mode is termed the Faraday Cup mode. For more sensitive measurements, the Electron Multiplier mode can be used. An electron multiplier is a resistive glass tube that amplifies the signal by secondary electron emission, which is mass dependent (i.e., the multiplicative factor depends on the mass). When the electron multiplier is used the noise is lowered, however signal saturation at higher operating pressures is possible.

The ionizer causes multiple ions to be produced for a single molecule, giving rise to the fragmentation pattern. When, for example, CO_2 is ionized, it fragments mainly into m/z = 12, 16, 22, 28, and the principal fragment 44; the total signal for CO_2 is the sum of all of the ion currents of the signature fragments. For simplicity in analyzing DEMS data, we choose the most unique m/z (not necessarily the principal fragment) for each calibration. For detailed analyses of spectra, fragmentation patterns are needed to decouple the signals.

The baseline ion currents detected stem from limitations of the vacuum system or from sensitivity limits specified by the RGA settings. Hydrogen, water, carbon monoxide, nitrogen, oxygen, and carbon dioxide are inevitably present as the background at the ultimate vacuum limit in the RGA. The mass spectrum below in Figure A.2 is the background signal for a pressure of $\approx 10^{-9}$ Torr. Deviations from this background can indicate leaks, contamination, and/or aging of the RGA components.

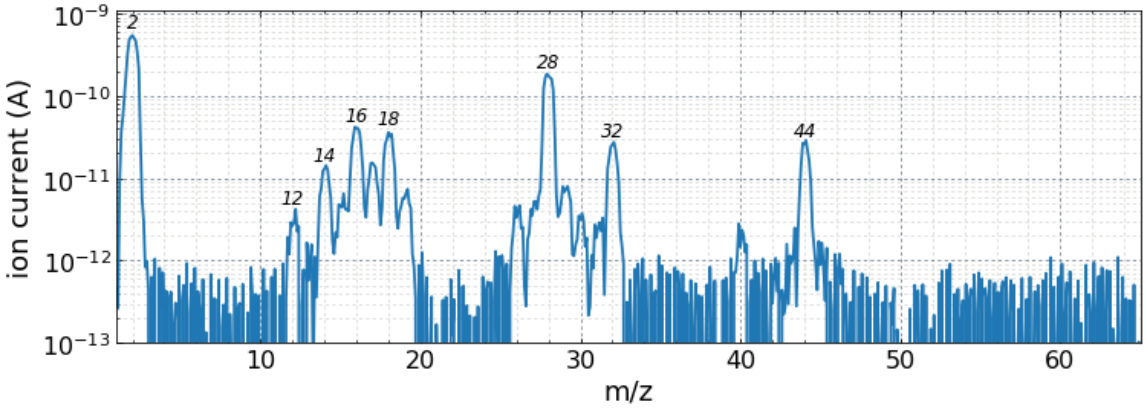

Figure A.2: Ultimate vacuum limit of our DEMS system.

[5]For diagrams and more details, see the Stanford Research Systems RGA manual: http://www.thinksrs.com/downloads/pdfs/manuals/RGAm.pdf

A.3 DEMS Calibration

The DEMS calibration exploits the fact that at low pressures (below $\approx 10^{-5}$ Torr), the RGA signal's response to a change in gas composition is linear. Using this, we want to relate the current detected by the RGA for a given m/z = z, termed the ion current I_z, to the unknown amount of moles of species j present in our electrochemical cell. While an increase in the ion current I_z above the baseline signal can indicate an increase in species j, to be quantitative we must know how much I_z increased above the baseline signal **relative** to the carrier gas ion current, I_c:

$$\{\text{increase in z}\} = \quad I_z/I_c - \text{baseline} = i_z - \text{baseline} = \tilde{i}_z, \tag{A.1}$$

where i_z represents the relative ion current, and $\tilde{i}_z$ the relative, residual (baseline subtracted) ion current of z. The form of the increase in signal z is analogous to the ratio of partial pressures of species j and the carrier gas:

$$\{\text{amount of j rel. to carrier gas c}\} = P_j/P_c = q_j, \tag{A.2}$$

where q_j, the ratio of the partial pressures of j and c, gives approximately the mole fraction of j for a dilute system.

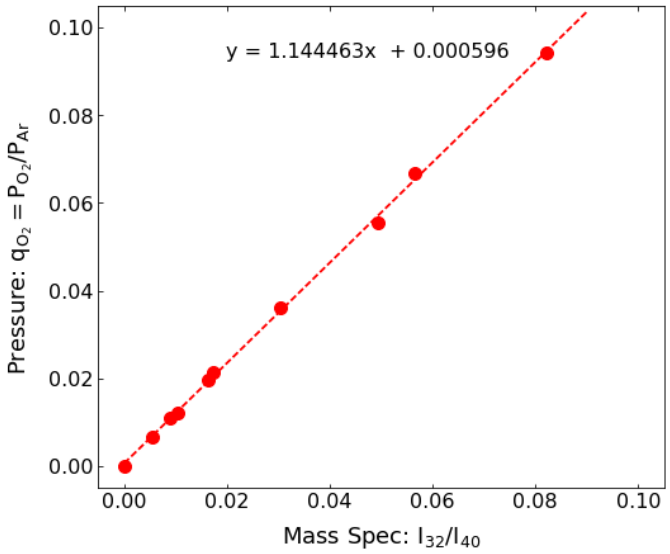

Figure A.3: Oxygen calibration in Argon as the carrier gas.

By mixing known pressure ratios of j and the carrier gas while recording the change in corresponding ion currents, we can fit linearly over a series of pressure ratios and obtain the calibration factor a_{jz} for each j, z pair, related as:

$$q_j \quad = P_j/P_c = a_{jz} \cdot \tilde{i}_z. \tag{A.3}$$

Figure A.3 above shows an example oxygen calibration. The RGA data is on the x-axis, plotting the ratio of I_{32} to the argon carrier gas I_{40}, and the pressure ratio of oxygen to argon

is on the y-axis. For most chemical species with a clear dominant mass fraction, excluding low masses like hydrogen, the slope between partial pressure ratios and ion current ratios of the calibration gas and carrier gas is nearly unity. This allows us to estimate quantities for uncalibrated species that are not present in a large number of samples or are toxic and not desired to be handled. Note that when calibrating the baseline does not need to be explicitly calculated, as the slope of the linear fit is the calibration factor $a_{O_2,32}$. The baseline is subtracted for each unique DEMS experiment.

The DEMS system is calibrated for volume and for concentrations ($\lesssim$ 10 mol%) of H_2, O_2, C_2H_4, CO, and CO_2 in Ar and N_2, allowing quantitative measurement of those specific gases. To increase the lifetime of the RGA's internal components, I_c is not directly measured. Instead a reference ion current, I_r, which can be from an isotope, fragment, or the doubly ionized carrier gas, is measured and multiplicative factor indirectly gives I_c. An example of such a reference ion current is m/z = 36 (^{36}Ar, $\approx$ 0.3 % natural abundance) when Ar (m/z = 40) is used as the carrier gas.

A.4 DEMS data collection and analysis

The mass spectra are collected in histogram mode, such that signals are recorded only for discrete m/z's. At each time point (referred to as cycle), n, the following are recorded:

$t(n)$, time (minutes)

$T(n)$, temperature (Celsius)

$P_{total}(n)$, the total pressure (Torr) of the carrier gas and the evolved gas

$I_r(n)$, carrier gas reference ion current (Amps)

$I_z(n)$ for $z = \{1, \ldots, 200\}$, ion currents for $m/z = z$, excluding the carrier and reference ion currents (Amps)

The basic analysis procedure for every cycle n collected for any mass per charge ratio z corresponding to species j is as follows. It should be noted that the order of calculations listed below is flexible and can be tailored by personal preference.

1. The inferred carrier gas ion current, $I_c(n)$, is calculated from the carrier gas reference ion current, $I_r(n)$, with the calibration A_{cr}:

$$I_c(n) = A_{cr} \cdot I_r(n) \tag{A.4}$$

2. The relative ion current for mass per charge ratio z, i_z, is obtained by dividing the ion current by the carrier ion current:

$$i_z(n) = I_z(n)/I_c(n) \tag{A.5}$$

3. The relative ion current baseline, $i_{zb}(n)$, is subtracted to get the residual relative ion current, $\tilde{i}_z(n)$:

$$\tilde{i}_z(n) = i_z(n) - i_{zb}(n) \tag{A.6}$$

4. By multiplying by the carrier gas pressure P_c and the calibration factor a_{jz} of the form given in Eqn. A.3 we get the partial pressure of species j at timepoint n:

$$\begin{aligned} P_j(n) = &\quad a_{jz} \quad \tilde{i}_z(n) \cdot P_c(n) \\ = &\qquad\quad q_j(n) \cdot P_c(n), \end{aligned} \tag{A.7}$$

5. However, the pressure we measure in the cell is the total pressure, not the pressure of the carrier gas. For almost all DEMS measurements, we are operating in the dilute case and $P_j \ll P_c$ and $P_j(n) = q_j(n) \cdot P_c(n) \approx q_j(n) \cdot P_{total}(n)$. For rare, extreme cases of significant gas evolution, assuming a dilute system will result in systematic overestimation of the partial pressures of a given chemical species. For this rare case there are two options: correct the pressure or approximate the mole fraction.

The pressure correction at each measurement is $(1 + \sum_{j'} q_{j'}(n))^{-1}$. To see this we can write the mole fraction of species j, n_j, as a function of the set of pressure ratios $\{q_{j'}\}$:

$$\begin{aligned} n_j(n) = &\quad \frac{P_j(n)}{P_{total}(n)} \\ = &\quad \frac{P_j(n)}{P_c(n)+\sum_{j'} P_{j'}(n)} \\ = &\quad \frac{q_j(n)\cdot P_c(n)}{P_c(n)+\sum_{j'} q_{j'}(n)\cdot P_c(n)} \\ = &\quad \frac{q_j(n)}{1+\sum_{j'} q_{j'}(n)} \end{aligned} \tag{A.8}$$

An alternative to specifically calculating the correction as above is to find a calibration factor that relates the mole fraction of species j, n_j, to the RGA signal $\tilde{i}_z$. Instead of the calibration like A.3, a calibration factor b_{jz} is used:

$$n_j(n) \approx b_{jz} \cdot \tilde{i}_z(n). \tag{A.9}$$

Word of caution! The calibration factor b_{jz} is from the linearization of the expression for the mole fraction of j for the binary mixture of j and the carrier gas, and this linearization depends on the range of the calibration performed.

This does not generally hold for non-dilute multicomponent mixtures. The relationship between q_j and n_j for a generic binary mixture is illustrated in Figure A.4.

Plotted on the x-axis is $Pj/Pc = \tilde{i}_z \cdot a_{jz}$, and the y-axis is the calculated mole fraction of j. The exact mole fraction function is plotted in blue with the solid black line representing q_j. In the dilute limit, near $q_j = 0$, $q_j \approx n_j$. The dashed line is the linearized fit for the mole

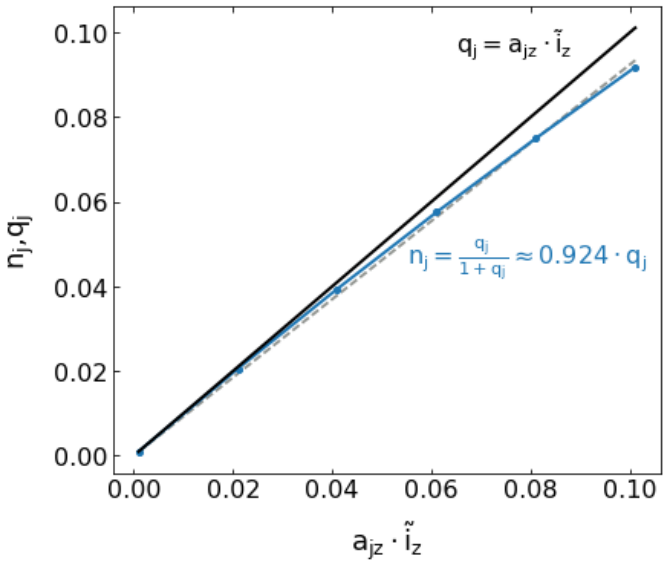

Figure A.4: Relationship between q_j and n_j.

fraction. Up to $q_j = 0.10$, when linearized with a forced intercept of zero, the mole fraction $n_j \approx 0.924 \cdot q_j$. As seen above in Table A.1, when using the mole fraction approximation for this range of calibration, the mole fraction of species j is underestimated in the dilute limit.

For a binary mixture of j and the carrier gas, the mole fractions obtained from the three methods for different $q_j = {}^{P_j}/_{P_c}$ are listed below. When comparing the dilute assumption to the actual mole fraction, we see that the error in the dilute assumption approximately scales with the amount of species j. Below $q_j = 1 \times 10^{-2}$ there is less than 1 % error. Only when the species j is $\approx$ 10 % of gas is the error from the dilute assumption large enough to be significant.

$q_j = a_{jz} \cdot \tilde{i}_z$	mole percent j (%)		
	dilute	pressure correction	mole fraction
1.00×10^{-5}	1.00×10^{-3}	1.00×10^{-3}	9.24×10^{-4}
1.00×10^{-4}	1.00×10^{-2}	1.00×10^{-2}	9.24×10^{-3}
1.00×10^{-3}	1.00×10^{-1}	9.99×10^{-2}	9.24×10^{-2}
1.00×10^{-2}	1.00	9.90×10^{-1}	9.24×10^{-1}
1.00×10^{-1}	10.0	9.09	9.24

Table A.1: Calculated mol% j for various methods.

To summarize, the three ways to calculate the partial pressure of species j, $P_j(n)$ are:

$$\text{dilute approximation:} \quad P_j(n) = q_j(n) \cdot P_{total}(n) \tag{A.10}$$

$$\text{pressure correction:} \quad P_j(n) = \frac{q_j(n)}{1 + \sum_j q_j(n)} \cdot P_{total}(n) \tag{A.11}$$

$$\text{mole fraction:} \quad P_j(n) = b_{jz} \cdot \tilde{i}_z \cdot P_{total}(n) = \frac{b_{jz}}{a_{jz}} \cdot q_j(n) \cdot P_{total}(n) \tag{A.12}$$

With practical DEMS calculations, the previous expressions are necessarily only an approximation, as not all volatile species are calibrated and can be accounted for. As an example, changes in temperature can wildly effect the partial pressure of the electrolyte in the headspace, though the electrolyte concentrations are still dilute.

6. With the partial pressure calculated from a method in equations A.10-A.12, P_j can be converted to µmol with the ideal gas law using the appropriate gas constant $R = 62.36$ L Torr mol^{-1} K^{-1}, the temperature $T(n)$, and the volume of the calibration loop, $v = 500\ \mu L$:

$$\mu mol_j(n) = \frac{P_j(n) \cdot v}{R \cdot (T(n) + 273.15)} \tag{A.13}$$

7. All of the above quantities were calculated at each cycle n. We wish to be able to know the cumulative as well as the rates of gas evolution. The molar evolution rate, $\dot{m}(t(n))$ in µmol min^{-1} can be calculated using the time between measurements, the cycle time Δt:

$$\dot{m}(t(n)) = \frac{d}{dt} m(t(n)) = \mu mol_j(n)/\Delta t. \tag{A.14}$$

And finally, $m(t(n))$, the total µmol of gas evolved up to time $t(n)$, is:

$$m(t(n)) = \sum_{n'=1}^{n} \mu mol_j(n'). \tag{A.15}$$

Again, it should be emphasized that the order of calculations presented above is not set in stone. Flexibility exists in when to divide by the carrier gas signal, when to apply baselines, and when to apply cell conditions (pressure and temperature). For the typical experimental conditions seen, the differences between different orders of operations will be minimal.

A.5 Worked Examples

This section goes over examples for Na-O_2 and Li-ion chemistries, temperature-induced fluctuations in the electrolyte background signal, and tips for uncalibrated gases.

A.5.1 A Na-O_2 cell This example looks at the gas evolution on charge of oxidation of NaO_2 deposited on a porous carbon electrode in an electrolyte comprised of sodium triflate ((sodium trifluoromethanesulfonate) in 1,2-dimethoxyethane (DME). DME has a high vapor pressure and its mass spectrum is below in Figure A.5.

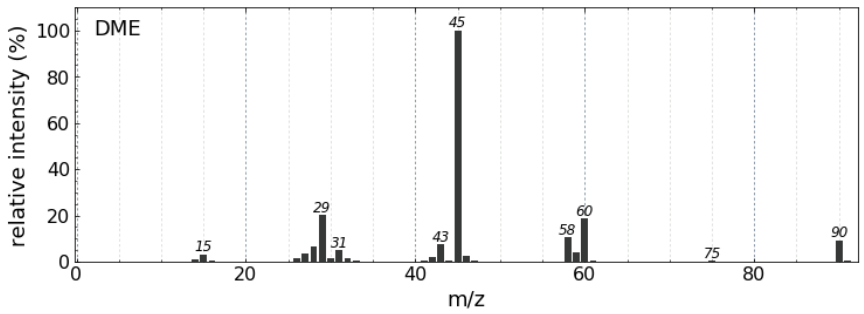

Figure A.5: Mass Spectrum of 1,2-dimethoxyethane. [6]

This cell is first discharged under O_2 to a capacity of 1 mAh. After discharge the O_2 headspace is then replaced with Ar. The DEMS measurement includes a rest period before charge, charge at 2 mA to a capacity of 1 mAh, and then a subsequent rest period.[7]

Plotted in Figure A.6 is the charge profile vs. Na/Na^+ and selected ion currents. The charge section is shaded in gray. For clarity, the electrolyte signals are only partially plotted in the inset (same scale). The electrolyte signals are plotted in more detail in Section A.5.4. From the DME spectrum we expect that m/z = 45, 29, 60, and 58 will be elevated. The baseline background signal is $\approx 1 \times 10^{-12}$ A, for comparison.

To see how much gas is evolved compared to the Ar carrier gas, we divide by the inferred I_{40} ion current (from I_{36}, Step 1) to get the relative ion current (Step 2). We can see that the main gas is O_2 (m/z = 32) with also H_2 (2) and CO_2 (44) evolved in small quantities at the end of the charge, as well as the unknown m/z = 75, which increases at the end of charge and remains elevated during rest after charge. As seen in the relative ion current plot, the O_2 signal is significant compared to the Ar carrier gas, with $i_{32} \approx 0.1$.

Next we calculate baselines (dashed lines in the bottom panel of Figure A.6). The best

[6] data taken from Ethane, 1,2-dimethoxy- in "Mass Spectra" in NIST Chemistry Webbook, doi:10.18434/T4D303, (2018).

[7] Data courtesy of J.E. Nichols

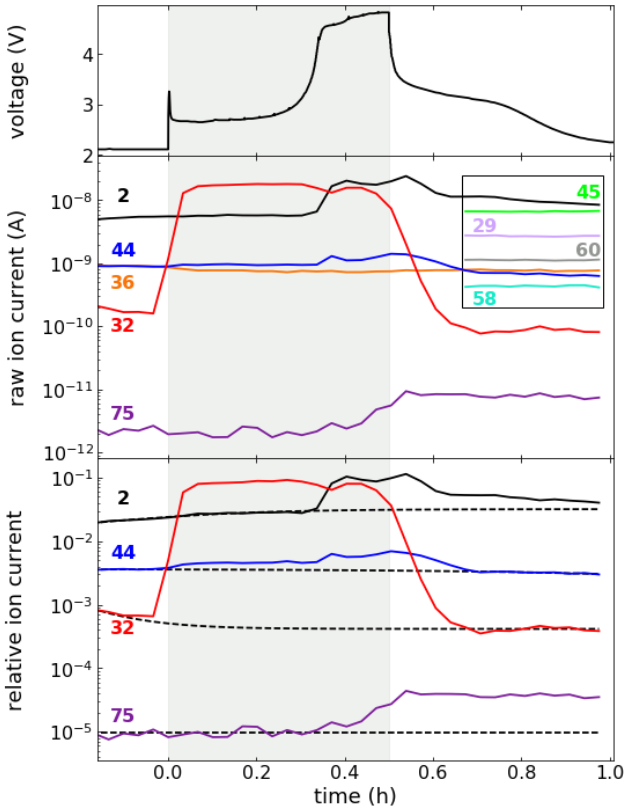

Figure A.6: A Na-O_2 cell (discharged to 1 mAh) charged at 2mA under Ar.

practice is to use the rest period before and after an electrochemical measurement to calculate the baseline, as done for m/z = 32 and 44, but this is not always practically possible. m/z = 2 and 75 remain elevated during the final rest and thus are calculated from only the initial rest. Common functions for baselines are constants and linear combinations of decaying exponentials.

	Q = 0.53 mAh				Q = 1 mAh			
	CO_2	H_2	O_2	e^-/O_2	CO_2	H_2	O_2	e^-/O_2
pressure correction	0.21	0.00	18.0	1.09	0.83	1.13	31.5	1.18
dilute	0.23	0.00	19.7	1.00	0.88	1.17	34.4	1.08

Table A.2: Cumulative gas evolution (in µmol) for Na-O_2.
For the Na-O_2 cell characterized in Figures A.6 and A.7 at roughly 50% and 100% state-of-charge. Q=0.53 mAh corresponds to the onset of the sharp voltage rise (sudden death) as in Figure A.7.

Subtracting the baselines as in Step 3 gives us the residual, relative ion currents. These are plotted for m/z = 2, 32, 44, and 75 above in the panel labeled "RGA" in Figure A.7. Per

Step 4 we next apply the calibration factors a_{jz} (Equation A.3) to get the partial pressure ratios for each gas (bottom panel "calibration"). The dashed curve indicates the sum of all of the partial pressure ratios. At the maximum, $q_{O_2} \approx 0.1$.

From Steps (5–7) we can apply the cell conditions (pressure and temperature) and the time step to get the cumulative and rates of gas evolution. Given the significant oxygen evolution anticipated from the 1 e^- oxidation of NaO_2, we expect that based on Table A.1, the difference in the pressure correction and dilute approximation will be about 10 %. This is seen in the calculated cumulative gas evolution is given in Table A.2 for both the dilute assumption and the pressure correction method.

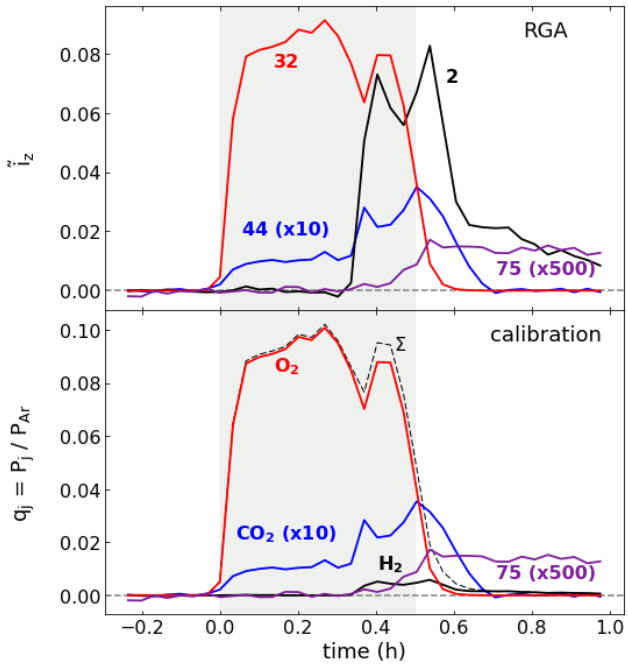

Figure A.7: Na-O_2 RGA signals to calibrated pressure ratios.

Without any pressure correction, prior to sudden death (Q = 0.53 mAh) the calculated e^-/O_2 is 1.00, compared to with the pressure correction of 1.09. From pressure rise measurements, and given that prior to sudden death (the sharp rise in voltage observed in Figure A.7 at t ≈ 0.3 h) the dominant gas is O_2 by a factor of ≈ 100, we expect that the e^-/O_2 to be 1.08 ± 0.02 before sudden death.[8] For large rates of gas evolution, it is best practice to compare pressure rise measurements with calculated DEMS results, as calibrations can shift with aging of the RGA components. The comparison between the pressure corrected DEMS measurement and the pressure rise measurement clearly demonstrate that the pressure correction provided more accurate gas evolution results for the Na-O_2 system due to the high rate of O_2 evolution observed at 2 mA for this ≈ 1 e^-/O_2 process. For high charge rates (> 0.5 mA) in metal-air systems, the pressure correction method is certainly warranted over the dilute method.

[8]Nichols, J. E.; McCloskey, B. D. The Sudden Death Phenomena in Nonaqueous Na-O_2 Batteries. *J. Phys. Chem. C* **2017**, *121*, 85–96.

The gas evolution rates are plotted below:

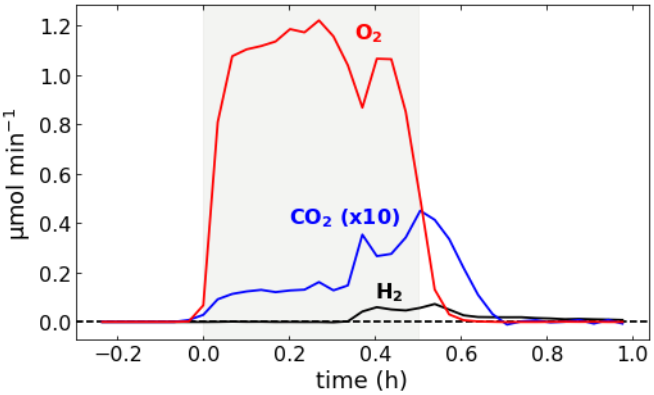

Figure A.8: Gas evolution rates for the Na-O_2 cell characterized in Figure A.6 and A.7.

As well as the cumulative gas evolution:

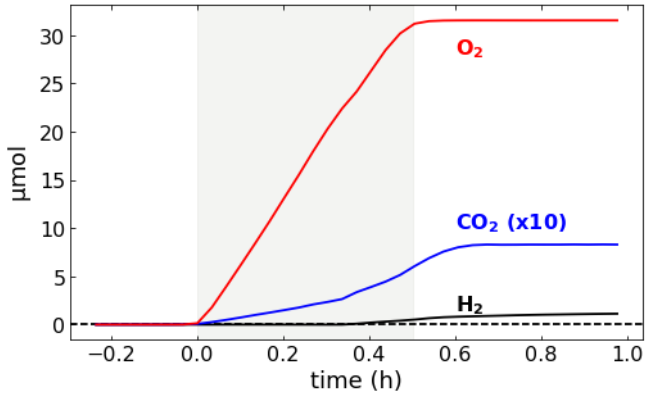

Figure A.9: Cumulative gas evolution for the Na-O_2 cell characterized in Figure A.6 and A.7.

The unknown m/z = 75 will be covered in more detail later in section A.5.4

A.5.2 A Ni-rich NMC Li-ion cathode material This example covers the outgassing during charge (delithiation) of a Li-ion cathode, a lithium nickel manganese cobalt (NMC) oxide. In the limit of high states of charge, there are several decomposition mechanisms that can evolve gas, such that tracing gas evolution during charge provides useful detail into these mechanisms.

For this example, the cathode is a Ni-rich NMC, NMC622, which when fully lithiated (discharged) has the formula $LiNi_{0.6}Mn_{0.2}Co_{0.2}O_2$, the electrolyte is 1 M LiTFSI in a carbonate blend of EC/DEC (1:1 v/v) with 100 ppm added H_2O, and the anode/reference is Li foil. After an initial rest period, the cathode is charged (delithiated) at a rate of 55.3

mA g^{-1} NMC622 (1 Li in 5 h) to 4.8 V vs. Li/Li^+ (removing $\approx$ 0.8 Li per formula unit), and then allowed to rest.

At the cathode, the carbonate electrolyte and Li_2CO_3 contaminants on the NMC surface can oxidize to form CO_2 and CO, starting at $\approx$ 3.8 V vs. Li/Li^+. At above 4.45 V, the oxide is unstable and lattice oxygen can be lost as O_2. At the Li anode, gaseous products stem from reduction reactions involving the carbonate electrolytes and any water contaminants. Two possible EC reduction reactions that evolve ethylene and either lithium carbonate (Li_2CO_3) or lithium ethylene dicarbonate [$(LiCO_3CH_2)_2$, LiEDC] are:

$$EC + 2\,Li^+ + 2\,e^- \longrightarrow C_2H_4 + Li_2CO_3\downarrow \tag{A.16}$$

$$2\,EC + 2\,Li^+ + 2\,e^- \longrightarrow C_2H_4 + LiEDC\downarrow \tag{A.17}$$

The difficulty in analyses of systems with CO_2, CO, and C_2H_4 using an RGA is the overlap in fragmentation patterns and the high inherent baseline for m/z = 28. In Table A.3 select relative intensities of the fragments are given for the RGA used in this study. **Note!** The fragmentation pattern for a molecule is specific to each ionizer and should be calculated for each RGA calibration.

m/z	44	28	27	26	25	16	12
CO_2	100	9.4	0	0	0	11.6	5.9
CO	0	100	0	0	0	2.8	6.4
C_2H_4	0	100	57.4	56.3	10.7	0	1.9

Table A.3: Relative intensities (%) for select fragments of CO_2, CO, and C_2H_4.

With this in mind, the ion currents for m/z = 26, 28, 32, 36, and 44 are plotted with the corresponding voltage profile in Figure A.10. First note that none of the selected ion currents are above m/z = 36, the ^{36}Ar signal. Calculating the inferred Ar signal and dividing by it, we get the relative ion currents (Steps 1–2), which are plotted in the lowest panel. The calculated baselines (Step 3) are plotted in dashed black. In contrast to the Na-O_2 example, we can see that gas evolution in this example is dilute, with the maximum $^{P_j}/_{P_{Ar}} \approx 10^{-3}$.

At the beginning of charge, m/z = 26 and 28 are elevated due to C_2H_4 evolution from Li plating at the anode (Equations A.16 and/or A.17). Next m/z = 44 increases due to CO_2 evolution from Li_2CO_3 and elecetrolyte decomposition. At higher potentials m/z = 32 increases due to lattice oxygen loss, as well as a corresponding increase in the m/z = 28 and m/z = 44 signals. During rest after charge, m/z = 44 and 32 fade, while m/z = 26 and 28 continue to increase. At above a certain state of delithiation, the NMC622 lattice is unstable and transition metal dissolution occurs, even during rest. The dissolved transition metals can migrate to the Li anode and plate, where a reduction reaction with the carbonate electrolyte can occur similarly to Equations A.16 and/or A.17, releasing C_2H_4.

As seen in Table A.3, for typical gas evolution in Li-ion batteries, m/z = 26 is a sufficiently

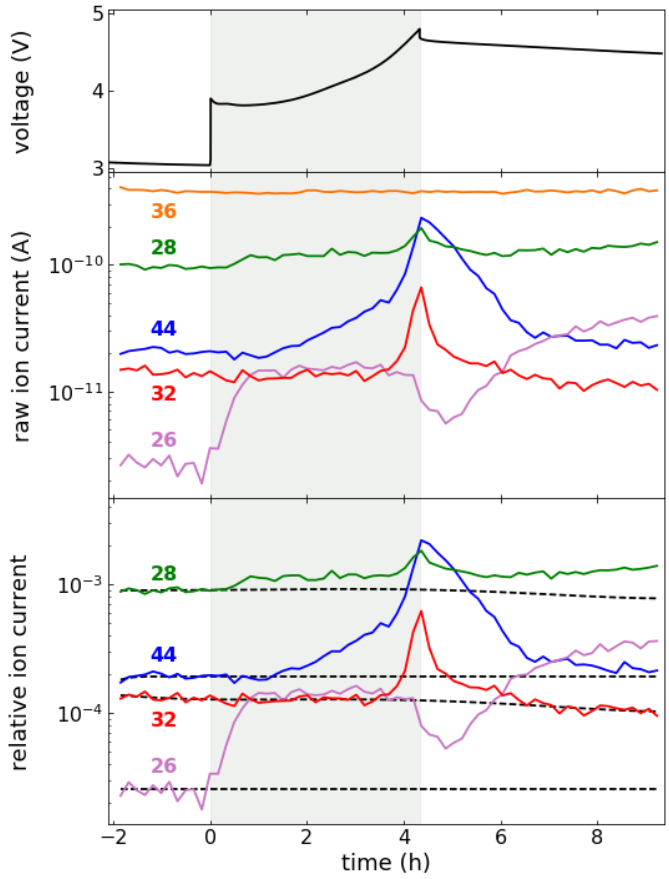

Figure A.10: NMC622 voltage, raw and relative ion currents during the first charge and rest.

unique identifier for C_2H_4 and m/z = 44 for CO_2. Thus to quantify any CO evolution, the CO_2 and C_2H_4 contribution to the m/z = 28 signal should first be removed before the CO calibration factor is applied. Due to the inherent high baseline signal for 28 (see Figure A.2), the calculated CO signal can be noisy relative to the other calculated gases.

After removing the baselines (Step 3), the scaling factor is applied to the baseline subtracted signals for $\tilde{i}_{44}$ and $\tilde{i}_{26}$ and subtracted from $\tilde{i}_{28}$. The scaling factor is determined by Table A.3, writing the fragment intensity as $f_j(z)$ for species j and the fragment m/z = z.

$$q_{CO} = a_{CO,28} \cdot \left(\tilde{i}_{28} - \frac{f_{CO_2}(28)}{f_{CO_2}(44)} \cdot \tilde{i}_{44} - \frac{f_{C_2H_4}(28)}{f_{C_2H_4}(26)} \cdot \tilde{i}_{26} \right) \tag{A.18}$$

$$= a_{CO,28} \cdot \left(\tilde{i}_{28} - 0.094 \cdot \tilde{i}_{44} - 1.776 \cdot \tilde{i}_{26} \right) \tag{A.19}$$

Below in Figure A.11 the full baseline subtracted ion current for 28 is plotted with the contribution from CO_2 and C_2H_4.

As a check, or when m/z = 28 is not available (if using N_2 as the carrier gas, for example), other ion currents could be used to calculate the CO signal. Taking the m/z = 12 C signal,

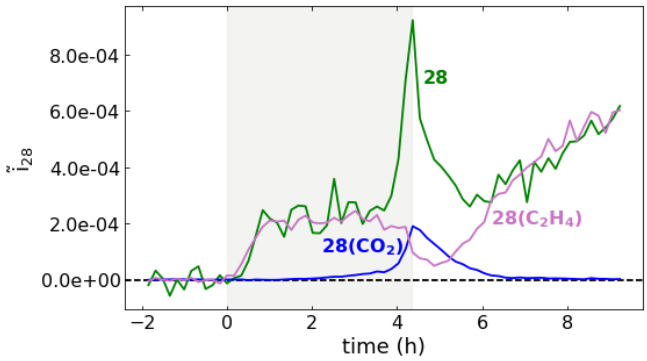

Figure A.11: Contributions to m/z = 28 ion current.

subtracting the portion of CO_2 and C_2H_4 given in Table A.3, and then scaling to get the CO signal will produce very similar results to the m/z = 28 method from above.

Applying the calibration factors, pressure, and temperature, the gas evolution rates are then:

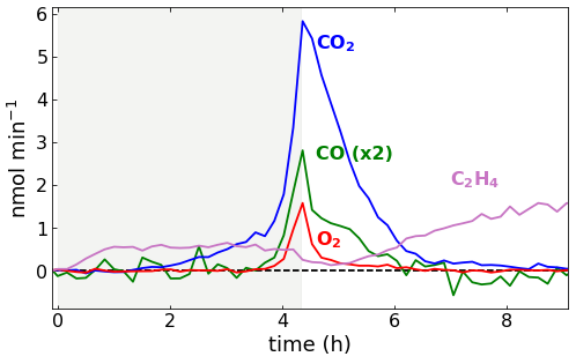

Figure A.12: NMC622 gas evolution rates.

As well as the cumulative gas evolution:

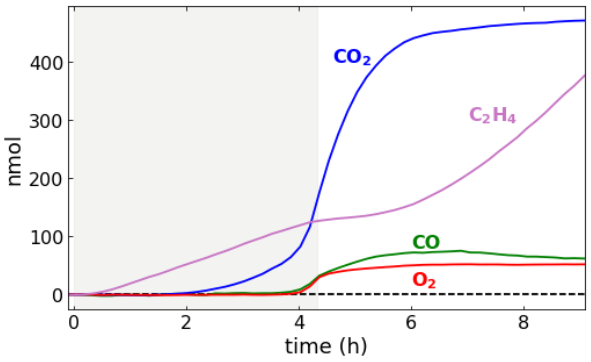

Figure A.13: NMC622 cumulative gas evolution.

For gas evolution originating from the cathode, the rates or cumulative evolution are often scaled by mass or surface area of the active oxide. For gas evolution originating from the Li anode, scaling by mass of the cathode is less informative, as the rates of evolution stemming from the anode are expected to scale with the current rate. The extent of the reduction reactions of the form of Equations A.16 and/or A.17 depends on the type of anode and its surface area. For a pure Li anode with low surface area, the C_2H_4 evolution is a small percent of the overall current.

For this example the C_2H_4 evolution rate during charge is ≈ 0.55 nmol min^{-1}. Assuming a 2 e^- process to produce C_2H_4, this corresponds to a parasitic current of 1.8 µA. For comparison, the current rate applied is 1.66 mA, or, the parasitic current only accounts for ≈ 0.1 % of the total applied current. During rest after charge, the C_2H_4 evolution increases in rate without an applied current, implying that a shuttling mechanism must occur. Even without knowledge of the exact mechanism of transition metal dissolution and plating, we could estimate the parasitic current assuming again a 2 e^- process to reduce EC.

A.5.3 Electrolyte volatility The previous two examples focused on relatively short experiments with nearly constant pressure and temperature. This example exhibits day/night fluctuations in the building temperature. These temperature fluctuations do not largely affect anything except the partial pressure of the electrolyte. As the electrolyte signals may have overlap with signals of interest, this may impact how baselines are calculated.

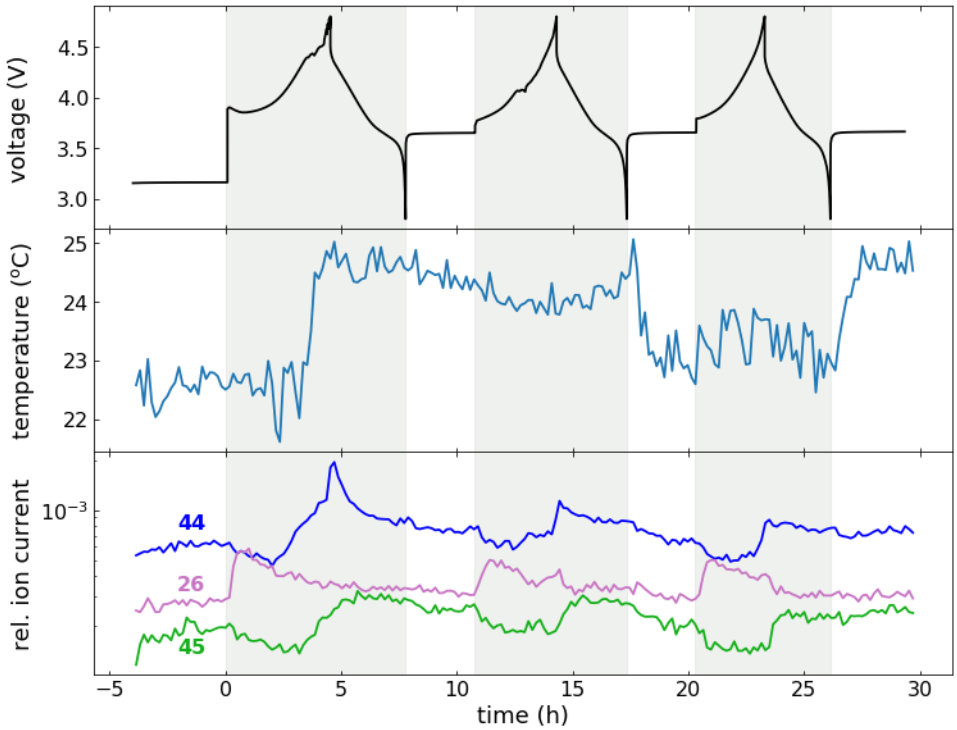

Figure A.14: NMC622 voltage, temperature, and ion currents for m/z = 44, 45, and 26.

Continuing with NMC622 from the previous example, in this experiment NMC622/Li with 1 M LiTFSI in EC/DEC (1:1, v/v) is cycled between 2.8–4.8 V for three cycles, with the whole experiment lasting about 36 hours. In Figure A.14 the voltage profile is plotted along with the recorded room temperature and relative ion currents for m/z = 44 and 45.

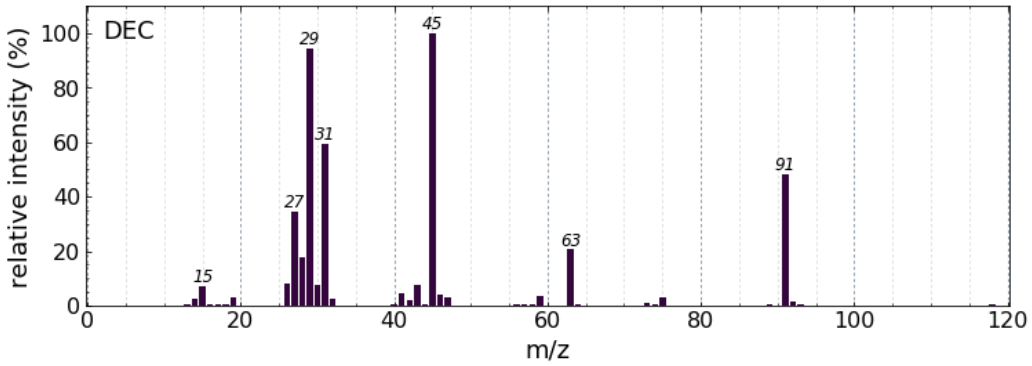

Figure A.15: Mass spectrum of diethyl carbonate. [9]

The dominant fragment for the mass spectrum of DEC is m/z = 45, as seen above in Figure A.15. Although there is no fragment corresponding to m/z = 44, there is inevitable overlap between adjacent discrete m/z values. The RGA is tuned to balance correct alignment at low and high m/z's, but offset and asymmetry are inevitable. It is apparent from Figure A.14 that the DEC electrolyte signal affects CO_2's dominant fragment of m/z = 44. Note that m/z = 29, 31, 63, and 91 follow the same shape of m/z = 45 but are not shown above.

Additionally plotted in Figure A.14 is the C_2H_4 signal from m/z = 26, to show that this phenomenon only affects the major electrolyte fragments. We can also see that though at the start of the experiment there appears to be a general correlation between the room temperature and the electrolyte signal, this does not hold near the end of the experiment. The thermocouple‘s measurement is not a good indicator of the actual cell temperature, as reactions and phase changes within the cell could change the actual internal temperature. This tells us that a simple temperature correction will not be sufficient for this experiment.

The normal best practice to calculate baselines is to use periods of rest, where no gas evolution is occurring, to fit a baseline. When applied to this particular example, we get a baseline that gives nonsensical results, appearing to show CO_2 consumption. Scaling an electrolyte fragment ion current to the rest periods in the CO_2 signal gives a better baseline calculation. This is illustrated below in Figure A.16, with the normal baseline calculation in the top panel labeled “automatic,” and the scaled signal from m/z = 45 in the bottom panel labeled “electrolyte.”

The inappropriateness of the automated baseline is most apparent in the calculated CO_2 properties. Applying the CO_2 calibration factor, pressure, and temperature we get the rate

[9]data taken from Diethyl carbonate in “Mass Spectra” in NIST Chemistry Webbook, doi:10.18434/T4D303, (2018).

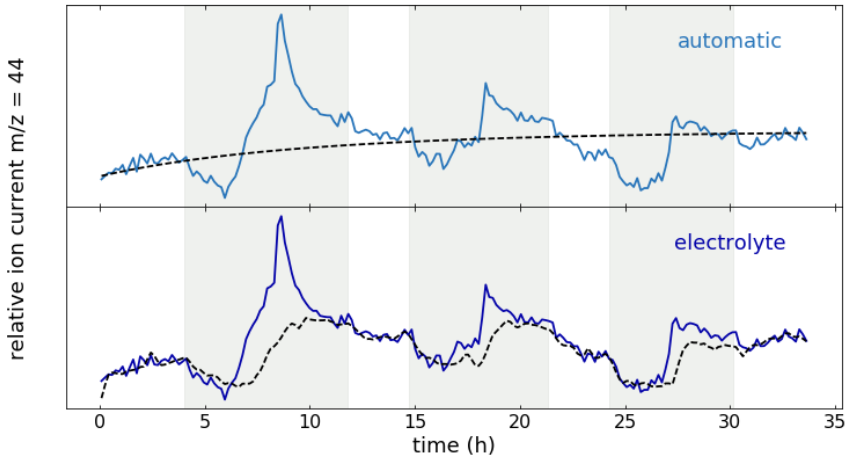

Figure A.16: NMC622 CO_2 baselines.

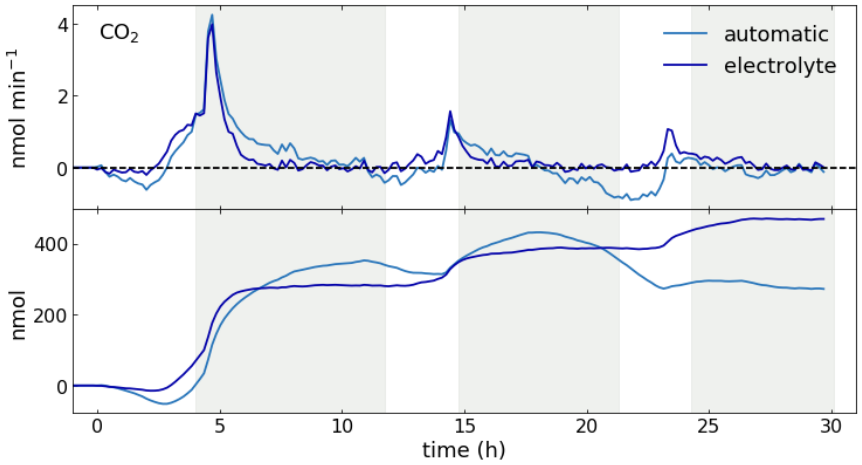

Figure A.17: NMC622 calculated CO_2 for baselines in Figure A.16.

and cumulative CO_2 as shown in Figure A.17. Although the difference in the rate of CO_2 evolution in the first cycle is not very different for the two different baselines, the cumulative CO_2 more readily shows the difference. For the automatic baseline, the calculated cumulative CO_2 frequently decreases, implying a consumption in CO_2, even though this is physically impossible due to the carrier gas pulses used in the DEMS measurement. The electrolyte baseline gives the expected CO_2 behavior: large CO_2 evolution in the first cycle, followed by less in the later cycles due to less Li_2CO_3 and electrolyte oxidation.

A.5.4 Uncalibrated gases For practical purposes the DEMS is calibrated for just a small set of gases. It is possible, however, to use published mass spectra for estimations. In addition to NIST, the RGA software (Stanford Research Systems) has a built-in library of limited spectra. As mentioned before, the exact fragmentation pattern is dependent on the ionizer and its settings, so any reference spectra available should be used only as an estimate for

fragmentation expected from the DEMS. As an example, below in Figure A.18 are the mass spectra with relative intensities comparing the fragmentation of C_2H_4 from NIST and the RGA library to that measured in 209 Hildebrand.

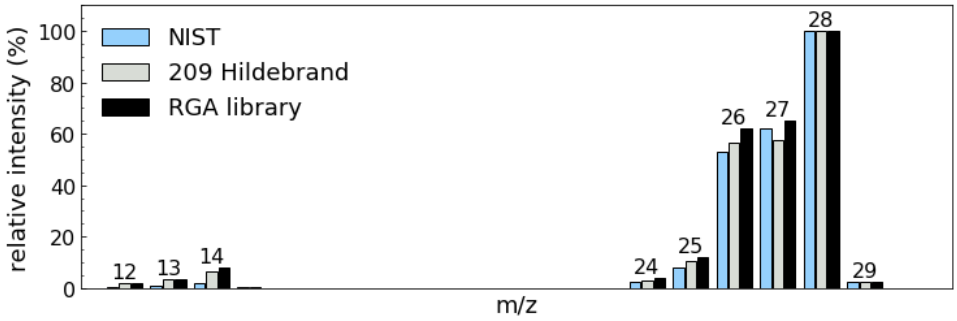

Figure A.18: C_2H_4 fragmentations. [10]

This shows that the NIST and/or RGA library fragmentation patterns can be used as a starting point for the estimation of uncalibrated gases.

CH_4 One example of an uncalibrated gas sometimes seen in DEMS measurements is CH_4. With the author not desiring to calibrate methane, methane has been estimated using the RGA library spectrum as a guide and a calibration factor (Equation A.3) of 1. Below in Figure A.19 is the spectrum for CH_4. Although a methyl fragment (15) is a fairly common fragment to see in various spectra, it is not normally a dominant fragment with 16 as in CH_4.

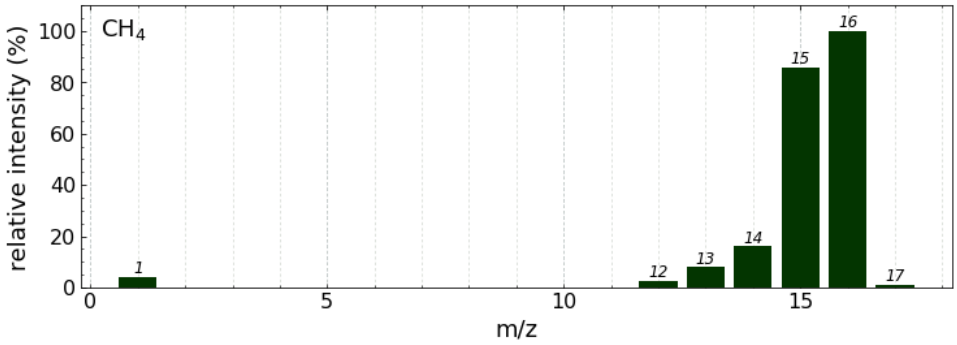

Figure A.19: Mass spectrum of methane. [11]

Returning to the example of Section A.5.2 of NMC622 with EC/DEC (1:1 v/v) 1 M LiTFSI with 100 ppm added H_2O, plotted below in Figure A.20 is m/z = 12, 15, 16, and 26.

CO and CO_2 evolution mostly account for the m/z = 12 signal. CO, CO_2, and O_2 at high voltages account for the peak near the end of charge for m/z = 16. At the beginning of charge,

[10] data taken from the RGA software library and Ethylene in "Mass Spectra" in NIST Chemistry Webbook, doi:10.18434/T4D303, (2018).

[11] data taken from the RGA software library

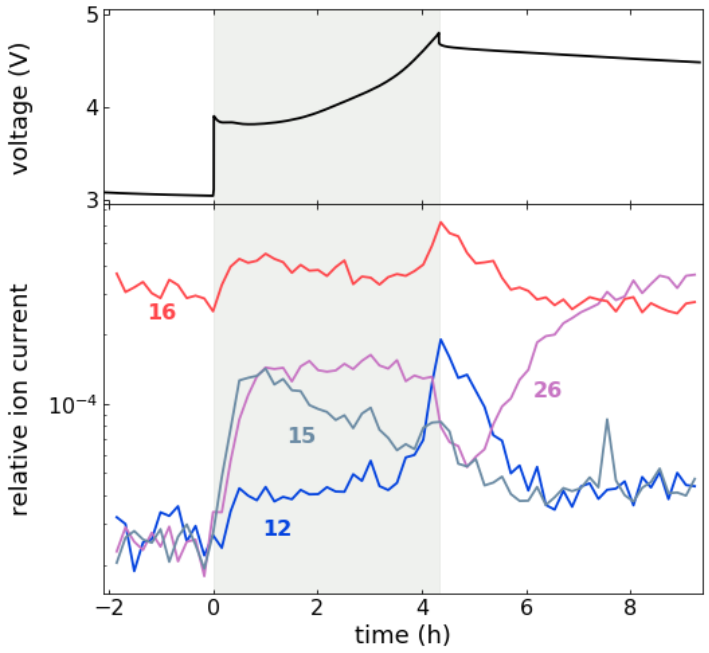

Figure A.20: NMC622 relative ion currents.

m/z = 15 peaks, not showing a constant evolution like C_2H_4. The baseline subtracted signals for m/z = 15 and 16 with the contributions from CO, CO_2, and O_2 removed are plotted below.

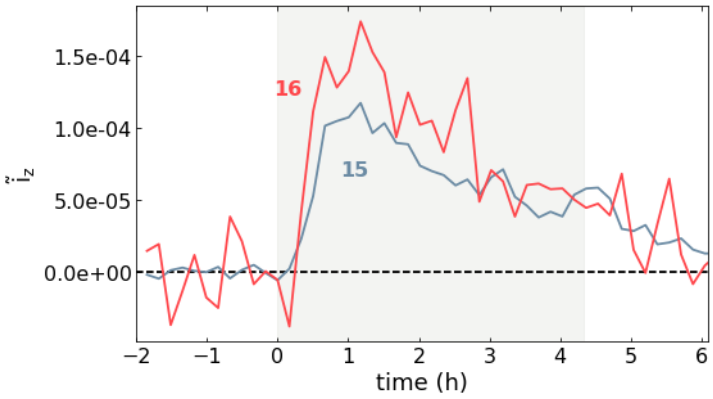

Figure A.21: NMC622 methane baseline subtracted ion currents.

This shows that the m/z = 15 signal is a good indicator of CH_4 evolution in this case. Taking the residual 16 signal and a calibration factor of 1, the approximate CH_4 quantities can be calculated just as for any calibrated gas. However, what is the source of the CH_4? For an equivalent experiment (same amount of all components) with instead only 10 ppm of added H_2O, the same rate of C_2H_4 is detected, however there is less methane evolved with less added H_2O, as shown below in Figure A.22.

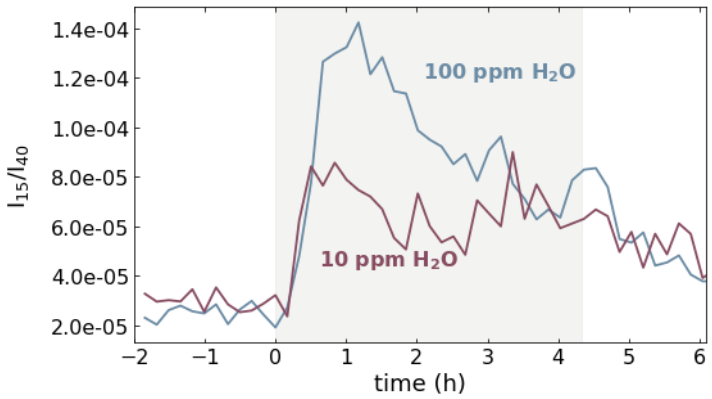

Figure A.22: NMC622 relative ion currents for m/z = 15 for added water.

Based on this, we anticipate that the CH_4 stems from a reduction reaction of the electrolyte involving water contaminants.

Na-O_2 cell: m/z = 75 Returning to the Na-O_2 example from Section A.5.1, as seen below in Figure A.6, H_2 and m/z = 75 remained elevated during rest after charge to sudden death. These elevated signals during rest imply a possible chemical reaction or a temperature increase. To gain some insight into what is occurring, the spectrum of DME from Figure A.5 will give valuable clues. The molecular weight of DME is 90 amu, and the loss of a methyl unit gives 75.

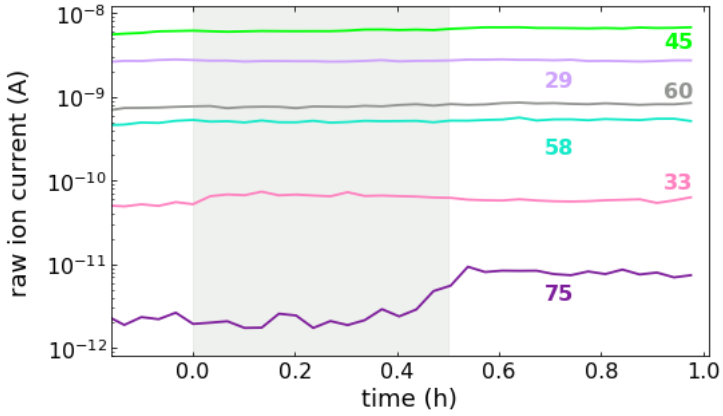

Figure A.23: DME fragments.

A few fragments that are expected to be elevated due to the volatility of DME are plotted for the entire DEMS experiment in Figure A.23. For all ion currents plotted, excluding for m/z = 75, the signals are constant before, during, and after charge. From the NIST spectrum of DME, the relative intensity of m/z = 75 to the main fragment of m/z = 45 is 0.4 %. If the elevated signal were from increased vapor pressure of DME (from increased cell temperature), we would expect to see a corresponding increase in the other electrolyte signals approximately proportional to their relative intensities. The absence of this increase rules out the likelihood of increased electrolyte volatility after sudden death.

Qualitatively, the DEMS data indicates that the elevated signals during rest after charge are likely from chemical reactions, possibly initiated by side reactions from sudden death. Further exploratory DEMS experiments, where ion currents up to m/z = 200 are recorded, could find any other elevated signals and help complement other further analyses.

B | ^{18}O-enrichment of Oxides

Throughout this dissertation ^{18}O-enriched materials were used to distinguish the Li-ion cathode material from the electrolyte. This Appendix goes over the enrichment details of the materials used in Chapter 2, but the remaining chapters used a very similar setup. After the basic procedure is given a set of guidelines for other materials and other temperatures is given.

B.1 Basic Enrichment Procedure

Exploiting that at high temperatures TMOs may exchange lattice oxygen with atmospheric oxygen ($O_O^\times \rightleftharpoons V_O^{\bullet\bullet} + 2e' + \frac{1}{2}O_2$), LMR/NMC were enriched with ^{18}O by the following procedure:

(i) a weighed sample ($\approx$ 0.5–1 g) of TMO powder was placed in a combustion boat (2mL, VWR) in a tube furnace (Lindberg Blue Mini Mite Tube Furnace, Thermo Scientific) with custom Swagelok end connections with heat-resistant O-rings (Markez Z1028, Marco Rubber),

(ii) the tube (Alumina, 20" length, 1" OD, Coorstek) headspace was purged with N_2,

(iii) a known volume of $^{18}O_2$ (97 at%, Sigma Aldrich) was dosed into the tube headspace,

(iv) the tube was sealed, allowing for volume expansion using a volume expansion membrane on one side of the tube,

(v) the sample was heated at 800 °C for 8 h and allowed to cool, and

(vi) the headspace was then tested for ^{16}O and ^{18}O content.

By comparing the ^{18}O content of the headspace before and after exchange, an oxygen balance on ^{18}O was performed to get an estimate for the upper bound of the total enrichment of the TMO lattices. The estimate is an upper bound as it does not take into account the ^{18}O in the

surface carbonate nor the ^{18}O in the CO_2 in the headspace from degradation of the Li_2CO_3, and it assumes that there is no exchange with the sample boat or tube, nor any losses or atmospheric contamination. The setup is leak tested but some exchange below detectable limits through the pressure expansion membrane cannot be excluded. The schematic in Figure B.1 visualizes the NMC and LMR oxygen balances, showing detailed calculations.

B.2 Other Enrichments

B.2.1 ^{18}O:TMO ratio. For NMC622, a ratio of $^{18}O_2$:NMC622 of 10 mL:200 mg was used throughout this dissertation. This ratio gives an approximate outer surface enrichment of 20 % ^{18}O. Other ratios will of course yield different surface enrichments, but one is limited by practicality and the total volume of the furnace headspace of $\gtrsim$ 100 mL. The $^{18}O_2$:N_2 ratio is also important for consideration of the surface oxygen defects, so proceed with caution.

B.2.2 Temperatures. For sensitive oxides (like $LiNiO_2$), temperatures lower than 800 °C may be used. Any temperature above 600 °C will yield similar results to 800 °C, with potentially slightly lower surface enrichments for the same ^{18}O:TMO ratio. Enrichments performed at 600 °C will yield surfaces that are uniformly enriched, as for 800 °C. Below 600 °C is not recommended unless absolutely necessary because the surface enrichments are not uniform, making the analysis as presented in Chapter 4 difficult, if not impossible. This may, however, be acceptable if one only wishes to distinguish the role of direct decomposition of surface Li_2CO_3, as the Li_2CO_3 enrichment distribution can be directly measured by a carbonate titration, as presented in Appendix C.

B.2.3 Non-oxide materials. Generally speaking, the enrichment temperature for non-oxide materials should be chosen to be $\approx$ 100 °C below the melting temperature, if applicable. For example for enriching pure Li_2CO_3, an enrichment temperature of 600–650 °C is appropriate to avoid the material melting (at 723 °C) and reforming in the combustion boat, leading to low yields.

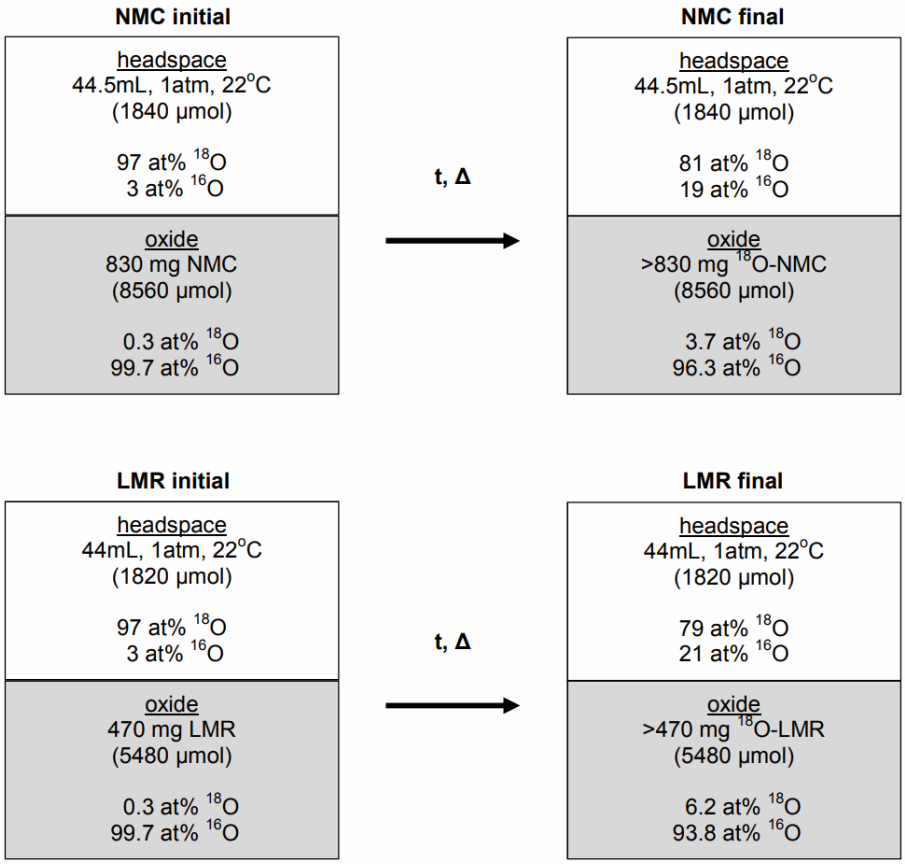

Figure B.1: ^{18}O enrichment of NMC and LMR.

Representative isotopic enrichment performed on NMC and LMR. Gas (headspace) and oxide isotope compositions are shown before and after the procedure.

591 µmol ^{18}O is removed from the NMC headspace and replaces ^{16}O in the NMC oxide. This gives an upper bound for the total ^{18}O content in the enriched NMC as < 3.7 %. From the DEMS data that is shown later we know the surface enrichment is 24 % ^{18}O, suggesting that the ^{18}O is concentrated on the surface of the NMC particles. This is confirmed by examining the distribution of ^{18}O in the oxygen released from the lattice, see Figure 2.4.

651 µmol ^{18}O is removed from the LMR headspace and replaces ^{16}O in the LMR oxide. This gives an upper bound for the total ^{18}O content in the enriched LMR as < 6.2 %. With a surface enrichment of 2 % ^{18}O (as seen in the DEMS data later), this suggests that the ^{18}O is more uniformly distributed in the LMR particles. This is confirmed by examining the distribution of ^{18}O in the oxygen released from the lattice, see Figure 2.7.

C | Carbonate and Peroxide Titration

This section details the use of an acid titration combined with gas analysis to detect and quantify surface compounds on lithium transition metal oxides. The method is first described as used in Chapter 2 and then expanded upon as used in the rest of the chapters.

C.1 Quantification of Li_2CO_3

In Chapter 2 we used a carbonate titration method based largely on prior literature[1],[2] to determine the amount of the surface contaminant Li_2CO_3 present on the surface of transition metal oxides (TMOs) by titrating LMR ($Li_{1.2}Ni_{0.15}Co_{0.1}Mn_{0.55}O_2$) and $LiNi_{0.6}Mn_{0.2}Co_{0.2}O_2$ (NMC622) powder with sulfuric acid, H_2SO_4. The LMR and NMC622 were enriched with ^{18}O, and We extended this method to also infer the ^{18}O-enrichment on the surface of LMR/NMC622. To perform the measurement, a known amount of LMR/NMC622 powder was placed in a glass bulb with capillaries that attach to the DEMS. Using a injection port with a septum, after a baseline was achieved for isotopes of CO_2, approximately 1 mL of 1–2 M H_2SO_4 was injected into the cell and stirred. The resultant CO_2 evolution was measured by sampling the headspace every two minutes until attenuation, taking several hours. All CO_2 fragments were monitored with time and integrated to get the total amount of surface Li_2CO_3, as based on the following reaction:

$$Li_2CO_3 + H_2SO_4 \longrightarrow Li_2SO_4 + H_2O + CO_2 \tag{C.1}$$

Though this method gives reliable total Li_2CO_3 content, it does not accurately measure the ^{18}O-enrichment.

[1] McCloskey, B. D. et al. Combining Accurate O_2 and Li_2O_2 Assays to Separate Discharge and Charge Stability Limitations in Nonaqueous Li-O_2 Batteries. *J. Phys. Chem. Lett.* **2013**, *4*, 2989–2993.

[2] Ottakam Thotiyl, M. M.; Freunberger, S. A.; Peng, Z.; Bruce, P. G. The Carbon Electrode in Nonaqueous Li-O_2 Cells. *J. Am. Chem. Soc.* **2013**, *135*, 494–500.

C.1.1 Oxygen exchange Our original assumption was that 1 mL of 1 M H_2SO_4 for $\lesssim 1$ µmol of Li_2CO_3 on LMR/NMC622 would be a sufficient excess of H^+ to push the equilibria far enough to minimize any isotopic exchange with water. However, by titrating with increasing H_2SO_4 molarities, a larger extent of ^{18}O was detected in the CO_2 released with no change in the total amount of Li_2CO_3 inferred. As seen in Table C.1, increasing the molarity of the H_2SO_4 solution coincides with an increase in the detected ^{18}O-content and a corresponding change in the CO_2 distribution. This trend is explained by an oxygen exchange with the initially natural abundance, predominantly $H_2{}^{16}O$, water in the lower molarity titration solutions: $H_2{}^{16}O + C^{18}O_2 \rightleftharpoons H_2C^{16}O^{18}O_2 \rightleftharpoons H_2{}^{18}O + C^{16,18}O_2$. This exchange was clearly inevitable at lower H_2SO_4 concentration for our particular titration setup. Other DEMS setups than our own, wherein all of the evolved gas is immediately removed instead of sampling a portion of the gas, likely will not observe this exchange to the same extent.

H_2SO_4 molarity	Distribution (%)			^{18}O (%)	µmol g^{-1}
	$C^{16,16}O_2$	$C^{16,18}O_2$	$C^{18,18}O_2$		
1 M	86.3	12.6	1.1	7.4	66.6 ± 0.3
3.5 M	79.9	18.6	1.5	10.8	67.0 ± 0.3
6 M	72.4	25.1	2.4	15.1	69.3 ± 0.3
10 M	70.0	27.3	2.7	16.4	68.6 ± 0.3

Table C.1: Carbonate titration by H_2SO_4 molarity for an ^{18}O-labeled NMC622.

Thus our previous method as used in Chapter 2 underestimated the ^{18}O-content of the surface Li_2CO_3, and, for the acid molarity we used, happened to give nearly identical results for the ^{18}O-content in the Li_2CO_3 compared to the CO_2 release detected by DEMS, which led us to the interpretation that the CO_2 released was predominantly directly that of Li_2CO_3 oxidation.

Additionally, from our previous titration results we concluded that the ^{18}O-labeling of Li_2CO_3 must be nonuniform as the distribution was not binomial. Writing the ^{18}O-enrichment fraction as z ($0 \leq z \leq 1$), uniformly distributed ^{18}O in the surface Li_2CO_3 predicts a distribution of ($C^{16,16}O_2$, $C^{16,18}O_2$, $C^{18,18}O_2$) detected in the titration as ($(1-z)^2$, $2z(1-z)$, z^2). For this batch of ^{18}O-NMC622, 1 M measures 7.4 % ^{18}O-enrichment which predicts a distribution of (85.8, 13.7, 0.5) of ($C^{16,16}O_2$, $C^{16,18}O_2$, $C^{18,18}O_2$), deviating from the measured distribution of (86.3, 12.6, 1.1). For the 10 M case, a measured 16.4 % ^{18}O-enrichment predicts a distribution of (69.9, 27.4, 2.7), which is in close agreement to the measured distribution of (70.0, 27.3, 2.7). This tells us that an ^{18}O exchange temperature of 800 °C gives a nearly uniform distribution of ^{18}O in the surface Li_2CO_3.

For practical purposes acid above 10 M was not tested. However, as shown in the 10 M panel in Figure C.1, the normalized molar flows collapse for all isotopes of CO_2 for the 10 M case. This is indicative that throughout the titration gas sampling there is no significant exchange with the natural abundance water, thus a higher molarity above 10 M is not predicted to give

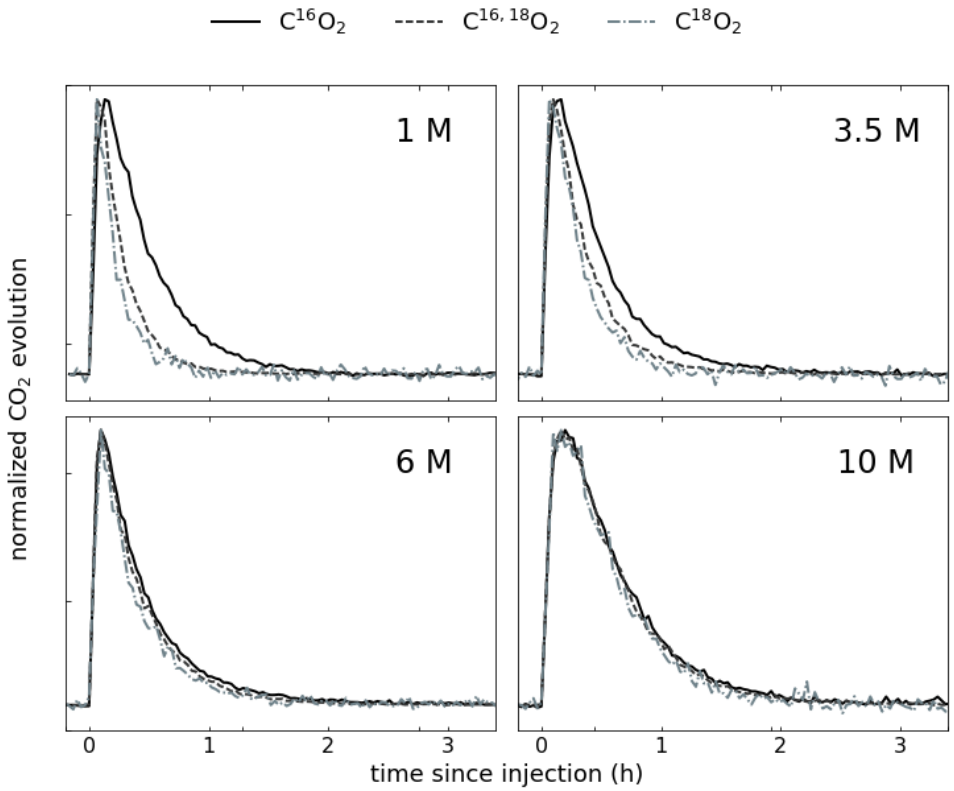

Figure C.1: Effect of H_2SO_4 molarity on detected isotopes of carbon dioxide.

Normalized $C^{16,16}O_2$, $C^{16,18}O_2$, and $C^{18,18}O_2$ evolution for 1, 3.5, 6, and 10 M H_2SO_4 titrations on an ^{18}O-NMC622 corresponding to the data given in Table C.1. 1 mL of the given molarity of H_2SO_4 was used for approximately 20 mg of ^{18}O-NMC622 ($\approx$ 0.6 µmol Li_2CO_3) in each titration. Each curve was normalized to the peak CO_2 evolution for that curve, noting that total CO_2 evolution follows the trend $C^{16,16}O_2 > C^{16,18}O_2 > C^{18,18}O_2$.

a significantly different distribution. Visually the exchange is apparent most dramatically in the 1 M panel in Figure C.1, showing a pronounced deviation in the curves of $C^{16,16}O_2$, $C^{16,18}O_2$, and $C^{18,18}O_2$. This deviation decreases with H_2SO_4 molarity, with only slight exchange in the 6 M case.

C.1.2 The updated interpretation of DEMS CO_2 results Given the updated ^{18}O-labeled Li_2CO_3 titration, how does this change the interpretation as given in Chapter 2? As mentioned in the previous section, the surface Li_2CO_3 ^{18}O-enrichment and isotopic distribution was underestimated by the lower molarity acid titration. With the incorrect titration we predicted a distribution of CO_2 evolution from the decomposition of Li_2CO_3 on the surface of a batch of ^{18}O-NMC622 to be (80, 18, 2). In the left panel of Figure C.2, this distribution is shown in the solid lines and the measured distribution of CO_2 evolved during the charge of ^{18}O-NMC622 to 4.8 V and subsequent rest is plotted in markers. There is an

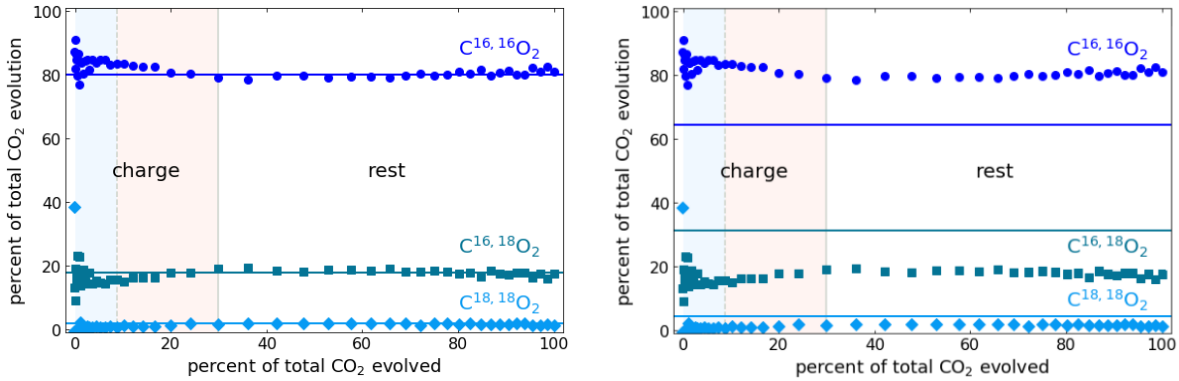

Figure C.2: Interpretations of CO_2 evolution for an ^{18}O-labeled NMC622.
Isotopes of CO_2 evolved during the first charge and rest for an ^{18}O-NMC622 material. In the left panel the incorrectly measured distribution of ^{18}O-Li_2CO_3 is shown in the solid lines. In the right panel the correctly measured distribution is given with the same CO_2 data.

apparent agreement between the incorrectly predicted surface Li_2CO_3 distribution from the 1 M titration and the detected CO_2.

However, when we plot the same DEMS data with the updated 10 M titration results in the right panel of Figure C.2, we see that there is a deviation throughout the whole charge and rest between the evolved CO_2 and that distribution predicted by the 10 M carbonate titration, before, during and after O_2 release. Specifically, the evolved CO_2 has a higher ^{16}O-content, or equivalently a lower ^{18}O-content, than the surface ^{18}O-Li_2CO_3. As the evolved O_2 from the ^{18}O-NMC622 has roughly the equivalent isotopic enrichment as the surface Li_2CO_3, this means that the natural abundance electrolyte must be the source of the ^{16}O.

Plotted with an x-axis of percentage of total CO_2 evolved, it becomes clear that the majority of the CO_2 is evolved during rest after charge. This CO_2 evolved during rest after charge has a nearly constant ^{18}O-enrichment. Even at low voltages there is electrolyte involvement in the evolved CO_2, occurring starting at $\approx$ 3.9 V, well below the onset of lattice oxygen at 4.45 V.

For the Li,Mn-rich (LMR) oxide we enriched with ^{18}O and reported on Chapter 2, we found that the O_2 released during charge to 4.8 V accounted for $\approx$ 0.3 % of the total lattice oxygen content and, with a lattice oxygen enrichment of 2 % ^{18}O, was only mildly enriched in ^{18}O. As the CO_2 released on charge had enrichment of $\approx$ 10 % ^{18}O, we concluded the origin of the CO_2 could not come from solely an electrolyte-^{18}O-LMR decomposition mechanism. Thus we speculated that the lattice O_2 release was not the majority mechanism for CO_2 evolution, and that surface Li_2CO_3 was a more important consideration for gas evolution. This was particularly supported by another report on an ^{18}O-LMR material where a similar distribution of ($C^{16,16}O_2$, $C^{16,18}O_2$, $C^{18,18}O_2$) was found [(87, 13, 0), with a total enrichment

of 6.5 % ^{18}O] for a, however, strikingly different lattice ^{18}O-enrichment of 15 %.[3]

As first discussed in Chapter 3, we can split the evolved CO_2 from ^{18}O-NMC622 into two components: that originating from direct Li_2CO_3 degradation and that of electrolyte-originating CO_2. For all anodic cut-off potentials 4.2 V and above, we found that the electrolyte portion of the CO_2 contained up to 5 % ^{18}O-enrichment.

With both materials considered, our interpretation is updated as:

(i) the total surface Li_2CO_3 tends to control the magnitude of CO_2 evolution

(ii) direct Li_2CO_3 decomposition accounts for a fraction of the evolved CO_2

(iii) CO_2 evolution has roughly constant ^{18}O-enrichment throughout the first charge and rest, before and after O_2 evolution

(iv) The electrolyte-originating CO_2, for EC/DEC-based electrolytes, is enriched in ^{18}O above natural abundance

(v) LMR and NMC622 exhibit similar CO_2 evolution behavior despite their different O_2 release

C.2 Quantification of Li_2O_2

To test Li_2O_2 decomposition in the presence of NMC622, Li_2O_2 was ground with NMC622 and titrated with pure H_2O, 3.5 M H_2SO_4, and 10 M H_2SO_4. In both 3.5 and 10 M the O_2 evolved suggested that reaction C.2 was the predominant net reaction. In pure H_2O, O_2 was evolved, but to a lesser extent, suggesting a mixture of the reactions C.3 and C.4 below.

$$Li_2O_2 + H_2O \rightleftharpoons 2\,LiOH + \frac{1}{2}\,O_2 \tag{C.2}$$

$$Li_2O_2 + 2\,H_2O \rightleftharpoons 2\,LiOH + H_2O_2 \tag{C.3}$$

$$H_2O_2 \rightleftharpoons H_2O + \frac{1}{2}\,O_2 \tag{C.4}$$

These titrations, and all titrations done in this work, were performed at room temperature without temperature control, so some hydrogen peroxide decomposition via reaction C.4 is expected.

[3] Luo, K. et al. Charge-compensation in 3d-transition-metal-oxide intercalation cathodes through the generation of localized electron holes on oxygen. *Nat Chem* **2016**, *8*, 684–691.

C.3 Controls for Interpretation of Electrochemically Modified TMOs

In this dissertation the peroxo/carbonate titrations were used to understand the effect of electrochemical modification on the surface of TMOs. To understand whether the differences observed compared to pristine TMOs are significant, a number of controls are needed. This section goes over the basic controls needed to interpret peroxo/carbonate titrations.

C.3.1 Effect of rinsing electrochemically modified electrodes with DMC In Chapters 3–5, extracted ^{18}O-NMC622 electrodes were rinsed with DMC to remove excess salt prior to titrating. Not desiring to titrate $LiPF_6$, LiTFSI-based electrolytes were used instead to study the effect of washing electrochemically modified ^{18}O-NMC622 electrodes. DMC-rinsed electrodes were dried under vacuum at room temperature and then stored in an Ar glovebox for several days to allow them to completely dry. Unrinsed electrodes were dried under vacuum more aggressively at room temperature and then stored in an Ar glovebox for several weeks to dry, monitoring the change in mass periodically. When the masses of the unrinsed electrodes remained steady they were then titrated.

For the cycled case, no large difference was observed for DMC-rinsed versus unrinsed 4.8–2.8 V-cycled electrodes: the remaining carbonate had a nearly identical ^{18}O-enrichment and distribution to the native Li_2CO_3 and the total amount left agreed with that predicted by gas analysis. This tells us that no significant carbonate-like decomposition products remained on the surface after discharge and that washing with DMC had no effect on the observable CO_2 evolved in the post-cycle titration. The CO_2 data for the unwashed LiTFSI 4.8–2.8 V-cycled ^{18}O-NMC622 compared to a washed $LiPF_6$ 4.8–2.8 V-cycled ^{18}O-NMC622 electrode is given in Table C.2.

For the charged electrodes, DMC rinsing yields significant differences in the titration results. As seen in Table C.3, when the electrode is not washed the entrained electrolyte in the charged ^{18}O-NMC622 electrode continues to mediate electrolyte and Li_2CO_3 decomposition, growing carbonate-like electrolyte decomposition products and reducing the native Li_2CO_3. We posit that this corrosive process involves the charged ^{18}O-NMC622 electrode, as the unwashed cycled ^{18}O-NMC622 electrode is not observed to exhibit extra Li_2CO_3 decomposition.

^{18}O-NMC622 4.8–2.8 V	Distribution (%)			^{18}O (%)	µmol g^{-1}
	$C^{16,16}O_2$	$C^{16,18}O_2$	$C^{18,18}O_2$		
initial native Li_2CO_3	*63.2 ± 0.3*	*32.4 ± 0.3*	*4.4 ± 0.1*	*20.6 ± 0.2*	*28.5 ± 1.7*
$LiPF_6$ DMC-rinsed: CO_2	82.9 ± 0.2	15.6 ± 0.2	1.5 ± 0.1	9.3 ± 0.1	25.0 ± 0.2
from Li_2CO_3	63.2 ± 0.3	32.4 ± 0.3	4.4 ± 0.1	20.6 ± 0.2	8.3 ± 0.3
from electrolyte	92.7 ± 0.4	7.3 ± 0.4	n/a	3.7 ± 0.2	16.7 ± 0.4
Post-cycle titration CO_2	67.2 ± 0.2	28.9 ± 0.2	3.9 ± 0.1	18.3 ± 0.2	22.8 ± 0.2
LiTFSI DMC-unrinsed: CO_2	84.7 ± 0.2	14.2 ± 0.1	1.1 ± 0.1	8.2 ± 0.1	24.2 ± 0.2
from Li_2CO_3	63.2 ± 0.3	32.4 ± 0.3	4.4 ± 0.1	20.6 ± 0.2	5.7 ± 0.2
from electrolyte	91.4 ± 0.2	8.6 ± 0.2	n/a	4.3 ± 0.1	18.5 ± 0.3
Post-cycle titration CO_2	64.9 ± 0.2	31.0 ± 0.2	4.1 ± 0.1	19.6 ± 0.1	22.3 ± 0.2

Table C.2: CO_2 evolution from DEMS and post-cycle titrations for ^{18}O-NMC622 for the first 4.8–2.8 V cycle both for DMC-rinsed $LiPF_6$ and not rinsed LiTFSI electrodes.

^{18}O-NMC622 4.8 V + 4 h rest	Distribution (%)			^{18}O (%)	µmol g^{-1}
	$C^{16,16}O_2$	$C^{16,18}O_2$	$C^{18,18}O_2$		
initial native Li_2CO_3	*63.2 ± 0.3*	*32.4 ± 0.3*	*4.4 ± 0.1*	*20.6 ± 0.2*	*28.5 ± 1.7*
LiTFSI no rinse: CO_2	82.1 ± 0.1	16.5 ± 0.1	1.4 ± 0.1	9.6 ± 0.1	17.1 ± 0.1
from Li_2CO_3	63.2 ± 0.3	32.4 ± 0.3	4.4 ± 0.1	20.6 ± 0.2	5.5 ± 0.2
from electrolyte	90.9 ± 0.2	9.1 ± 0.2	n/a	4.6 ± 0.1	11.6 ± 0.2
Post-charge titration CO_2	90.6 ± 0.1	8.5 ± 0.1	0.9 ± 0.1	5.2 ± 0.1	40.8 ± 0.2
from Li_2CO_3	63.2 ± 0.3	32.4 ± 0.3	4.4 ± 0.1	20.6 ± 0.2	8.5 ± 0.5
from electrolyte	97.8 ± 0.7	2.2 ± 0.7	n/a	1.1 ± 0.3	32.3 ± 0.5
LiTFSI DMC-rinse: CO_2	82.0 ± 0.2	16.6 ± 0.2	1.4 ± 0.1	9.7 ± 0.1	21.0 ± 0.2
from Li_2CO_3	63.2 ± 0.3	32.4 ± 0.3	4.4 ± 0.1	20.6 ± 0.2	6.7 ± 0.2
from electrolyte	90.9 ± 0.2	9.1 ± 0.2	n/a	4.5 ± 0.1	14.3 ± 0.3
Post-charge titration CO_2	73.7 ± 0.2	23.4 ± 0.1	2.9 ± 0.1	14.6 ± 0.1	20.9 ± 0.2
from Li_2CO_3	63.2 ± 0.3	32.4 ± 0.3	4.4 ± 0.1	20.6 ± 0.2	13.9 ± 0.6
from electrolyte	94.6 ± 1.7	5.4 ± 1.7	n/a	2.7 ± 0.9	7.0 ± 0.6

Table C.3: CO_2 evolution from DEMS and post-charge titrations for ^{18}O-NMC622-LiTFSI cells charged to 4.8 V and allowed to rest on the DEMS for 4 h. Electrodes were either rinsed with DMC after extraction or not rinsed before drying and titrating.

C.3.2 Effect of discharge cut-off potential All of the ^{18}O-NMC622 cycled electrodes presented in the main text were discharged to 2.8 V. For all anodic cut-off potentials it was found that the electrolyte decomposition products were largely removed from the surface due to the discharge process. To test whether the discharge cut-off potential affected the surface carbonate layer and the oxygen-depleted layer, we charged ^{18}O-NMC622 cells to 4.8 V; discharged them to 4.0, 2.8, and 2.0 V; and extracted and titrated them.

^{18}O-NMC622 4.8–2.8 V	Distribution (%)			^{18}O (%)	µmol g^{-1}
	$C^{16,16}O_2$	$C^{16,18}O_2$	$C^{18,18}O_2$		
4.0 V: CO_2 DEMS	81.4 ± 0.1	17.2 ± 0.1	1.4 ± 0.1	10.0 ± 0.1	24.3 ± 0.2
Post-cycle titration CO_2	67.2 ± 0.1	29.0 ± 0.1	3.8 ± 0.1	18.3 ± 0.3	22.3 ± 0.1
2.8 V: CO_2 DEMS	82.9 ± 0.2	15.7 ± 0.2	1.5 ± 0.1	9.3 ± 0.1	25.0 ± 0.2
Post-cycle titration CO_2	67.2 ± 0.2	28.9 ± 0.2	3.9 ± 0.1	18.3 ± 0.2	22.8 ± 0.2
2.0 V: CO_2 DEMS	82.2 ± 0.2	16.4 ± 0.2	1.4 ± 0.1	9.6 ± 0.1	21.0 ± 0.2
Post-cycle titration CO_2	64.6 ± 0.1	31.2 ± 0.1	4.2 ± 0.1	19.8 ± 0.1	22.4 ± 0.1

Table C.4: CO_2 from DEMS and post-cycle titration for ^{18}O-NMC622 charged to 4.8 V and discharged to 4.0, 2.8, and 2.0 V.

^{18}O-NMC622 4.8–2.8 V	Distribution (%)			^{18}O (%)	µmol g^{-1}
	$^{16,16}O_2$	$^{16,18}O_2$	$^{18,18}O_2$		
4.0 V: O_2 DEMS	64.0 ± 0.4	31.8 ± 0.3	4.2 ± 0.2	20.1 ± 0.3	3.1 ± 0.1
Post-cycle titration O_2	70.9 ± 0.3	25.7 ± 0.2	3.3 ± 0.2	16.2 ± 0.2	7.9 ± 0.1
2.8 V: O_2 DEMS	63.5 ± 0.4	32.3 ± 0.3	4.3 ± 0.2	20.4 ± 0.3	3.8 ± 0.1
Post-cycle titration O_2	69.9 ± 0.3	27.1 ± 0.2	3.0 ± 0.2	16.6 ± 0.3	8.5 ± 0.1
2.0 V: O_2 DEMS	63.8 ± 0.4	32.0 ± 0.4	4.2 ± 0.2	20.2 ± 0.3	3.4 ± 0.1
Post-cycle titration O_2	69.7 ± 0.3	27.6 ± 0.3	2.7 ± 0.3	16.5 ± 0.3	7.4 ± 0.1

Table C.5: O_2 from DEMS and post-cycle titration for ^{18}O-NMC622 charged to 4.8 V and discharged to 4.0, 2.8, and 2.0 V.

Tables C.4 and C.5 present the CO_2 and O_2 data, respectively, for gas evolution evolved during the cycle and the post-cycle titrations. There is not a large difference exhibited in the outgassing or the titration data for any of the cathodic cut-off potentials. Table C.6 gives the charge and discharge capacities for the three cathodic cut-off potentials and their final assumed formulas. Given that the titrations were similar for all three cathodic cut-off potentials, after a partial relithiation to $Li_{0.39}Ni_{0.6}Mn_{0.2}Co_{0.2}O_2$ the surface oxygen and carbonate is not largely affected by further relithiation.

^{18}O-NMC622 4.8–x V	charge capacity (Li units)	discharge capacity (Li units)	assumed x in $Li_xNi_{0.6}Mn_{0.2}Co_{0.2}O_2$
4.0	0.86	0.25	0.39
2.8	0.85	0.74	0.89
2.0	0.84	0.74	0.90

Table C.6: ^{18}O-NMC622 attained capacities for several cathodic cut-off potentials.

C.3.3 Effect of rest between charge and discharge As discussed in Chapter 3, charged and discharged ^{18}O-NMC622 exhibit contrasting surface carbonate morphologies, namely charged electrodes have significant carbonate-like electrolyte decomposition products on the surface, while the decomposition products are removed during discharge and not detected on cycled electrodes.

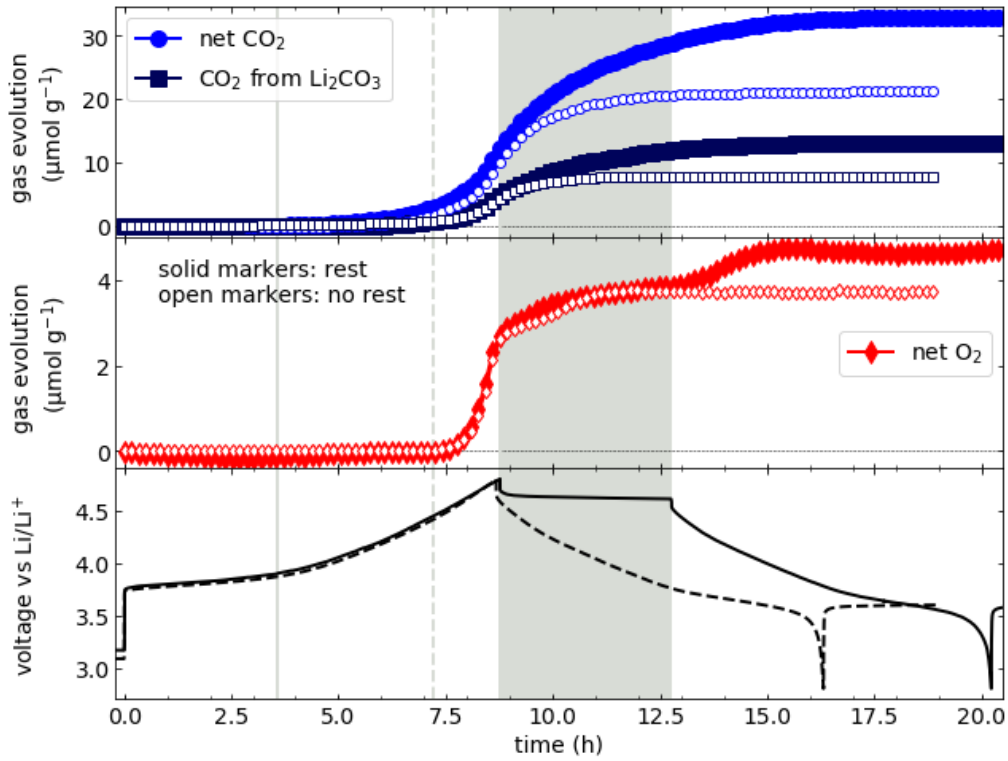

Figure C.3: Comparison of gas evolution and voltage profiles for ^{18}O-NMC622 cells charged to 4.8 V and either discharged immediately, or allowed to rest first for 4 h.

To understand the effect of rest at a high state of charge (with an open circuit potential > 4.6 V) on the evolution of the ^{18}O-NMC622 surface, cells were charged to 4.8 V at 0.1 Li^+ h^{-1} and either discharged immediately to 2.8 V or allowed to rest first for 4 h before discharge. The corresponding cumulative CO_2, O_2, and voltage profiles are shown in Figure C.3 Note that this is not the same batch of material as presented in Chapter 3, but was enriched with ^{18}O in nearly identical conditions.

The cells exhibited identical charge capacities, however the rested cell had a slightly lower discharge capacity (by 0.02 Li units). On charge the gases evolved are comparable however O_2 and CO_2 continue to evolve during the rest. Notably, more O_2 was evolved during discharge for the cell allowed to rest after charge compared to cell immediately discharged.

From the post-cycle titration data presented in Tables C.7 and C.8, we see there is not a large difference in the post-cycle surface carbonate layer between the rested and immediately discharged cell, with the only difference being more Li_2CO_3 is decomposed in the rested case, which is expected given that more CO_2 (both electrolyte and Li_2CO_3-originating) is evolved during the rest after charge. This indicates that even with extended electrolyte decomposition during rest, electrolyte decomposition products do not remain on the surface after discharge.

In contrast to the surface carbonate layer, however, the oxygen-depleted layer is altered due to the 4 h rest before discharge. As seen in Table C.8, the evolved O_2 for the immediately discharged and rested cells have comparable ^{18}O-enrichments, with the rested cell evolving $\approx$ 30 % more O_2. Due to the rest before discharge the disordered oxygen layer is increased in depth by also $\approx$ 30 % and also decreased in ^{16}O-content, implying greater penetration into the depth of the ^{18}O-NMC622 particle and loss of surface ^{18}O.

^{18}O-NMC622 4.8–2.8 V	Distribution (%)			^{18}O (%)	µmol g^{-1}
	$C^{16,16}O_2$	$C^{16,18}O_2$	$C^{18,18}O_2$		
no rest: CO_2	80.7 ± 0.2	17.7 ± 0.2	1.6 ± 0.1	10.4 ± 0.1	21.4 ± 0.2
Post-cycle titration CO_2	69.7 ± 0.2	26.9 ± 0.2	3.5 ± 0.1	16.9 ± 0.1	26.2 ± 0.2
4 h rest: CO_2	79.8 ± 0.2	18.4 ± 0.2	1.8 ± 0.1	11.0 ± 0.1	32.8 ± 0.2
Post-cycle titration CO_2	69.9 ± 0.2	26.9 ± 0.2	3.2 ± 0.1	16.6 ± 0.1	21.3 ± 0.2

Table C.7: CO_2 evolution from DEMS and post-cycle titrations for ^{18}O-NMC622 cells charged to 4.8 V and either discharged immediately, or allowed to rest first for 4 h.

^{18}O-NMC622 4.8–2.8 V	Distribution (%)			^{18}O (%)	µmol g^{-1}
	$^{16,16}O_2$	$^{16,18}O_2$	$^{18,18}O_2$		
no rest: O_2	64.6 ± 0.8	31.2 ± 0.7	4.2 ± 0.3	19.8 ± 0.4	3.7 ± 0.1
Post-cycle titration O_2	69.9 ± 0.6	27.2 ± 0.5	2.9 ± 0.5	16.5 ± 0.6	9.0 ± 0.2
4 h rest: O_2	63.8 ± 0.5	31.8 ± 0.4	4.4 ± 0.2	20.3 ± 0.3	4.8 ± 0.1
Post-cycle titration O_2	74.4 ± 0.4	24.3 ± 0.3	1.3 ± 0.3	13.5 ± 0.4	11.6 ± 0.1

Table C.8: O_2 evolution from DEMS and post-cycle titrations for ^{18}O-NMC622 cells charged to 4.8 V and either discharged immediately, or allowed to rest first for 4 h.

C.3.4 Effect of rest time after charge to 4.8 V All charged electrodes as presented in Chapter 3 were allowed to rest while monitoring the gas evolution for 4 h before being extracted. It was found that all charged electrodes above ≈ 4.2 V had less surface Li_2CO_3 than would be expected, had carbonate electrolyte decomposition products sorbed to the surface of the TMO, and evolved O_2 originating from the near-surface TMO lattice. To determine the effect of the length of the rest period after charge on the titration results, ^{18}O-NMC622 cells were charged to 4.8 V and extracted after 0 or 8 h rest.

As seen in Table C.9, after an initial growth in the electrolyte decomposition products, after extended rest the decomposition products are reacted/dissociated away.The O_2 titration results were not significantly different for different rest times after charge.

^{18}O-NMC622 4.8 V + 4 h rest	Distribution (%)			^{18}O (%)	µmol g^{-1}
	$C^{16,16}O_2$	$C^{16,18}O_2$	$C^{18,18}O_2$		
initial native Li_2CO_3	*63.2 ± 0.3*	*32.4 ± 0.3*	*4.4 ± 0.1*	*20.6 ± 0.2*	*28.5 ± 1.7*
0 h: CO_2 evolved	83.8 ± 0.4	14.9 ± 0.4	1.3 ± 0.1	8.8 ± 0.2	7.7 ± 0.2
from Li_2CO_3	63.2 ± 0.3	32.4 ± 0.3	4.4 ± 0.1	20.6 ± 0.2	2.2 ± 0.1
from electrolyte	92.8 ± 0.4	7.2 ± 0.4	n/a	3.6 ± 0.2	5.5 ± 0.2
Post-charge titration CO_2	86.0 ± 0.1	12.5 ± 0.1	1.5 ± 0.1	7.7 ± 0.1	43.8 ± 0.2
from Li_2CO_3	63.2 ± 0.3	32.4 ± 0.3	4.4 ± 0.1	20.6 ± 0.2	14.7 ± 0.6
from electrolyte	97.6 ± 0.6	2.4 ± 0.6	n/a	1.2 ± 0.3	29.1 ± 0.6
4 h: CO_2 evolved	81.9 ± 0.1	16.5 ± 0.1	1.6 ± 0.1	9.9 ± 0.1	31.5 ± 0.2
from Li_2CO_3	63.2 ± 0.3	32.4 ± 0.3	4.4 ± 0.1	20.6 ± 0.2	11.7 ± 0.3
from electrolyte	92.8 ± 0.3	7.2 ± 0.3	n/a	3.6 ± 0.1	19.7 ± 0.4
Post-charge titration CO_2	94.3 ± 0.1	5.2 ± 0.1	0.5 ± 0.1	3.1 ± 0.1	49.9 ± 0.2
from Li_2CO_3	63.2 ± 0.3	32.4 ± 0.3	4.4 ± 0.1	20.6 ± 0.2	5.2 ± 0.5
from electrolyte	97.9 ± 0.6	2.1 ± 0.6	n/a	1.0 ± 0.3	44.7 ± 0.5
8 h: CO_2 evolved	81.9 ± 0.1	16.5 ± 0.1	1.6 ± 0.1	9.9 ± 0.2	40.5 ± 0.2
from Li_2CO_3	63.2 ± 0.3	32.4 ± 0.3	4.4 ± 0.1	20.6 ± 0.2	15.2 ± 0.4
from electrolyte	93.1 ± 0.3	6.9 ± 0.3	n/a	3.5 ± 0.1	25.3 ± 0.4
Post-charge titration CO_2	91.1 ± 0.1	8.1 ± 0.1	0.8 ± 0.1	4.8 ± 0.1	34.4 ± 0.2
from Li_2CO_3	63.2 ± 0.3	32.4 ± 0.3	4.4 ± 0.1	20.6 ± 0.2	6.2 ± 0.5
from electrolyte	97.3 ± 0.6	2.7 ± 0.6	n/a	1.4 ± 0.5	28.2 ± 0.5

Table C.9: CO_2 evolution from DEMS and post-charge titrations for ^{18}O-NMC622 charged to the 4.8 V and allowed to rest on the DEMS for 0, 4, and 8 h.

D | Experimental Details

This section lists manufacturers and other experimental details that were not included in the main body of this dissertation or in the other appendices.

D.1 Electrolyte Preparations

This includes all electrolytes tested in this dissertation. The following electrolytes were prepared with 1 M $LiPF_6$ (Sigma, battery grade) as the salt concentration:

(i) ethylene carbonate (EC, BASF),

(ii) propylene carbonate (PC, Sigma),

(iii) dimethyl carbonate (DMC, BASF),

(iv) diethyl carbonate (DEC, BASF),

(v) EC/DEC 1:1 v/v,

(vi) EC/DEC 1:1 v/v with 2 vol% fluoroethylene carbonate (FEC, Daikin),

(vii) and EC/DEC 1:1 v/v with 2 vol% vinylene carbonate (VC, Daikin).

2 vol% corresponds to ≈ 30 µmol for each in our cell setup. A typical electrode tested has an active ^{18}O-NMC622 loading of ≈ 25–30 mg, so on the gas basis these additives account for ≈ 1000 µmol g^{-1} ^{18}O-NMC622.

The following were prepared with 1 M lithium bis(trifluoromethanesulfonyl)imide (LiTFSI, BASF) as the salt concentration:

(i) EC/DEC 1:1 v/v,

(ii) EC/DEC 1:1 v/v with 10 ppm ultrapure H_2O,

(iii) EC/DEC 1:1 v/v with 100 ppm ultrapure H_2O,

(iv) 1,2 dimethoxyethane (DME, BASF),

(v) and tetraethylene glycol dimethyl ether (TEGDME/tetraglyme, BASF).

D.2 Electrochemical Testing

D.2.1 Cathode preparation Cathodes were made by casting slurries (90 wt% active material, 5 wt% SP/graphite (TIMCAL), 5 wt% PVDF (Sigma) in n-methyl-2-pyrrolidone (NMP, Sigma) solvent) onto stainless steel mesh. In Chapter 2 electrode preparation was performed in ambient atmosphere but done to minimize TMO exposure to the ambient. In total, the TMO powders were exposed to ambient atmosphere at room temperature for roughly 30 minutes during electrode preparation. In the remaining chapters electrode preparation was performed exclusively in the glovebox Ar atmosphere to avoid reactions with the ambient H_2O and CO_2. In all cases, after casting electrodes in the box the cathodes were moved to an attached heated antechamber without air exposure and dried under vacuum at 120 °C.

D.2.2 Electrochemical cells Custom Swagelok cells were used as described previously without modification.[1],[2] Li foil was used as the reference/counter electrode. In Chapter 2, two sheets Celgard 2400 were used as the separator. In the remaining chapters, one sheet Celgard 2400 (polypropylene) and one sheet QMA (Whatman) were used as the separators for all electrolytes except EC and PC, which only used QMA as the separator (due to non-wetting of polypropylene). Cells were assembled in the glovebox and tested on a Bio-Logic VSP-series potentiostat. All cell potentials given in this work are versus Li/Li^+ unless stated otherwise.

[1]McCloskey, B. D. et al. Combining Accurate O_2 and Li_2O_2 Assays to Separate Discharge and Charge Stability Limitations in Nonaqueous Li-O_2 Batteries. *J. Phys. Chem. Lett.* **2013**, *4*, 2989–2993.

[2]McCloskey, B. D. et al. Solvents' Critical Role in Nonaqueous Lithium-Oxygen Battery Electrochemistry. *J. Phys. Chem. Lett.* **2011**, *2*, 1161–1166.